

**AN EXPERIMENTAL AND NUMERICAL STUDY  
ON EFFECTS OF PORE TO THROAT SIZE RATIO  
ON MACROSCOPIC TRANSPORT PARAMETERS  
IN POROUS MEDIA**

**A Thesis Submitted to  
the Graduate School of Engineering and Sciences of  
İzmir Institute of Technology  
in Partial Fulfillment of the Requirements for the Degree of**

**DOCTOR OF PHILOSOPHY**

**in Mechanical Engineering**

**by  
Türküler ÖZGÜMÜŞ**

**January 2015  
İZMİR**

We approve the thesis of **Türküler ÖZGÜMÜŞ**

**Examining Committee Members:**

---

**Prof. Dr. Moghtada MOBEDİ**

Department of Mechanical Engineering, Izmir Institute of Tecnology

---

**Prof. Dr. Semra ÜLKÜ**

Department of Chemical Engineering, Izmir Institute of Tecnology

---

**Prof. Dr. Aytunç EREK**

Department of Mechanical Engineering, Dokuz Eylül University

---

**Assist. Prof. Dr. H. Seçil ARTEM**

Department of Mechanical Engineering, Izmir Institute of Tecnology

---

**Assist. Prof. Dr. Murat Barışık**

Department of Mechanical Engineering, Izmir Institute of Tecnology

**28 January 2015**

---

**Prof. Dr. Moghtada MOBEDI**

Supervisor, Department of  
Mechanical Engineering, Izmir  
Institute of Tecnology

---

**Assist. Prof. Dr. Ünver ÖZKOL**

Co-Supervisor, Department of  
Mechanical Engineering, Izmir  
Institute of Tecnology

---

**Prof. Dr. Metin TANOĞLU**

Head of the Department of Mechanical  
Engineering

---

**Prof. Dr. Bilge KARAÇALI**

Dean of the Graduate School of  
Engineering and Sciences

## ACKNOWLEDGEMENTS

I would like to thank to my advisor, Prof. Dr. Moghtada MOBEDĪ for his supervision, guidance, patience and support during this study. Without his constant motivation, I would not have studied this effectively. I am also thankful to Assist. Prof. Dr. Ünver ÖZKOL for his guidance, contributions and recommendations, Prof. Dr. Semra ÜLKÜ and Assist. Prof. Dr. H. Seçil ARTEM for their valuable recommendations and contributions.

I would like to thank Özgür ÇEKMER who leaded me to İYTE and Prof. MOBEDĪ in the first place. I would like to thank the members of room 142 – especially to Eren UÇAR and Hasan ÇELİK - for their helps and supports.

I would like to thank Mechanical Engineer Ali DÖNMEZ for his valuable recommendations and contributions to the experimental part of the study and to my knowledge.

I also would like to thank Murat MİRZA, Sedat ÇELİK and Cenk ERBİL for their helps during my experimental study.

I would like to thank to BAP committee for the financial support on the study performed.

I would like to thank to TUBITAK for 2211 Scholarship for PhD Students.

Lastly, I would like to thank to my loveful husband Turgay and my daughter Tanura for their presence that enlighten my entire life.

.

## ABSTRACT

### AN EXPERIMENTAL AND NUMERICAL STUDY ON EFFECTS OF PORE TO THROAT SIZE RATIO ON MACROSCOPIC TRANSPORT PARAMETERS IN POROUS MEDIA

Heat and fluid flow in porous media are frequently encountered in natural and industrial applications, such as oil recovery, water supply management in hydrogeology, ground heat storage, nuclear waste disposals, and ground water flow modeling. Fluid flow and heat transfer analyses in porous media have gained recent attention. The theoretical analysis of heat and fluid flow in porous media is troublesome. That's why some methods were developed to overcome the difficulties. One of these methods is the macroscopic method in which the solid and fluid phases are combined and the porous media is represented as an imaginary continuum domain. For the application of the macroscopic method onto a porous medium, the macroscopic transport properties such as permeability and thermal dispersion of the corresponding medium should be known. Many parameters such as pore to throat size ratio, porosity, Reynolds number, solid-to-fluid thermal conductivity ratio influence the macroscopic transport parameters.

In this study, the fluid flow and heat transfer in porous media are examined numerically to determine the effects of pore to throat size ratio on permeability, interfacial convective heat transfer and thermal dispersion coefficients. The heat and fluid flow in periodic porous media consisting of rectangular rods are investigated. A representative elementary volume is considered and the continuity, Navier-Stokes and energy equations are solved to determine the velocity, pressure and temperature fields in the voids between the rods. It is shown that the pore to throat size ratio is a significant parameter which should be taken into account to suggest a wide applicable correlation. Based on obtained computational results, correlations for determination of Kozeny constant and interfacial heat transfer coefficient in terms of pore to throat size ratio and other related parameters are proposed. An experimental study was conducted to validate the numerical results of the present study. In the experimental part, a porous channel of square rods is used and the permeability and thermal dispersion coefficient are validated with the aid of experimental measurements. A good agreement between the experimental and numerical results is observed.

## ÖZET

### GÖZENEKLİ YAPILARDA GÖZENEK İLE BOĞAZ ARASINDAKİ BÜYÜKLÜK ORANININ MAKROSKOPİK TAŞINIM PARAMETRELERİNE ETKİSİ ÜZERİNE DENEYSEL VE TEORİK BİR ÇALIŞMA

Gözenekli ortamlarda akış ve ısı transferi ile hidrojeolojideki su kaynağı yönetimi ve zemin ısı depolama gibi birçok doğal ve endüstriyel uygulamada sıklıkla karşılaşılmaktadır. Bu sebepten gözenekli ortamlarda akış ve ısı transferi analizleri ilgi kazanmaktadır. Gözenekli ortamlarda akış ve ısı transferinin teorik analizi külfetlidir. Analizdeki zorlukları gidermek için bazı yöntemler geliştirilmiştir. Bu yöntemlerden birisi makroskopik yöntemdir. Makroskopik yöntemde gözenekli ortamdaki katı ve sıvı birleştirilmekte ve gözenekli yapı varsayımsal bir sürekli ortam olarak gösterilmektedir. Ancak makroskopik yöntemin uygulanabilmesi için gözenekli ortamın geçirgenlik ve ısıl dispersiyon katsayısı gibi makroskopik taşınım özelliklerinin bilinmesi gerekmektedir. Gözenek ile boğaz arasındaki büyüklük oranı, porozite, Reynolds sayısı, katı ile sıvı arası ısıl iletkenlik katsayısı oranı gibi birçok parametre makroskopik taşınım özelliklerini etkiler.

Bu çalışmada, gözenek ile boğaz arasındaki büyüklük oranının geçirgenlik, arayüz ısı transfer ve ısıl dispersiyon katsayıları gibi makroskopik taşınım özelliklerine etkisi sayısal olarak incelenmiştir. Dikdörtgen çubuklardan oluşan periyodik gözenekli bir ortamda akış ve ısı transferi incelenmiştir. Temsili bir birim hacim gözönüne alınmış ve süreklilik, Navier-Stokes ve enerji denklemleri çözülerek çubuklar arası boşluktaki hız, basınç ve sıcaklık dağılımları bulunmuştur. Gözenek ile boğaz arasındaki büyüklük oranının, makroskopik taşınım özelliklerinin doğru bir şekilde hesaplanabilmesi için dikkate alınması gereken, önemli bir parametre olduğu gösterilmiştir. Kozeny sabiti ve arayüz ısı transfer katsayısının bulunması için gözenek ile boğaz arasındaki büyüklük oranı ve diğer ilişkili parametrelere bağlı korelasyonlar önerilmiştir. Sayısal sonuçların geçerliliğini göstermek için deneysel bir çalışma yapılmıştır. Deneysel çalışmada, kare çubuklardan oluşan gözenekli bir kanal kullanılmış ve sayısal olarak bulunan geçirgenlik ve ısıl dispersiyon katsayıları doğrulanmıştır. Deneysel ve sayısal sonuçlar arasında iyi bir uyum gözlenmiştir.

# TABLE OF CONTENTS

LIST OF FIGURES .....	ix
LIST OF TABLES .....	xv
LIST OF SYMBOLS .....	xvii
CHAPTER 1. INTRODUCTION .....	1
1.1. The Aim of Study .....	3
1.2. The Outline of Thesis .....	4
CHAPTER 2. BACKGROUND OF MACROSCOPIC HEAT AND FLUID FLOW ANALYSIS IN POROUS MEDIA .....	6
2.1. Microscopic and Macroscopic Views of Porous Media.....	6
2.2. Microscopic Fluid Flow and Energy Equations .....	9
2.3. Volume Averaging Method.....	10
2.4. Traditional Macroscopic Flow Equations: Darcy and Forchheimer Motion Equations .....	11
2.5. General Forms of Macroscopic Motion Equations .....	15
2.6. Macroscopic Energy Equations.....	19
2.7. Equivalent Thermal Conductivity Models .....	24
CHAPTER 3. LITERATURE REVIEW .....	26
3.1. Literature Review on Permeability and Kozeny Constant .....	27
3.1.1. Review of Theoretical Studies on Determination of Permeability and Kozeny Constant .....	28
3.1.2. Review of Experimental Studies on Determination of Permeability and Kozeny Constant .....	43
3.2. Literature Review on Interfacial Convective Heat Transfer Coefficient .....	49
3.2.1. Review of Theoretical Studies on Determination of Interfacial Convective Heat Transfer Coefficient .....	49

3.2.2. Review of Experimental Studies on Determination of Interfacial Convective Heat Transfer Coefficient .....	56
3.3. Literature Review on Thermal Dispersion Coefficients.....	59
3.3.1. Review of Theoretical Studies on Determination of Thermal Dispersion Coefficients .....	59
3.3.2. Review of Experimental Studies on Determination of Thermal Dispersion Coefficients .....	65
3.3.2.1. Heat Addition/Removal at Lateral Boundaries .....	67
3.3.2.2. Heat Addition at Inlet/Outlet Boundary .....	76
3.3.2.3. Heat Addition inside Bed .....	82

CHAPTER 4. CONSIDERED DOMAIN, GOVERNING EQUATIONS AND BOUNDARY CONDITIONS.....	94
4.1. Considered Domain.....	94
4.2. Governing Equations and Boundary Conditions for Determination of Permeability and Kozeny Constant.....	96
4.3. Governing Equations and Boundary Conditions for Determination of Interfacial Convective Heat Transfer Coefficient.....	99
4.4. Governing Equations and Boundary Conditions for Determination of Thermal Dispersion Coefficients .....	102

CHAPTER 5. SOLUTION TECHNIQUE AND COMPUTATIONAL DETAILS .....	105
5.1. Numerical Procedure.....	105
5.1.1. Iterative Procedure for Obtaining Periodical Fluid Flow Boundaries.....	105
5.1.2. Iterative Procedure for Obtaining Periodical Thermal Boundaries for Determination of Interfacial Convective Heat Transfer Coefficient.....	107
5.1.3. Iterative Procedure for Obtaining Periodical Thermal Boundaries for Determination of Thermal Dispersion Coefficients .....	110
5.2. Computational Details.....	112
5.3. Grid Independency Tests.....	112

CHAPTER 6. EXPERIMENTAL STUDY, MATERIALS AND METHOD.....	114
6.1. Experimental Setup and Its Components .....	114
6.1.1. Components of Experimental Setup.....	114
6.1.2. Measurement and Control Devices .....	121
6.2. Experimental Procedure .....	123
6.2.1. Experiments with Empty Channel.....	124
6.2.2. Experiments with Porous Channel .....	128
 CHAPTER 7. RESULTS AND DISCUSSION .....	 131
7.1. Comparison of Numerical Model with Literature .....	131
7.2. Results for Permeability and Kozeny Constant.....	136
7.2.1. Darcy and Non-Darcy Regions .....	136
7.2.2. Effects of Pore to Throat Size Ratio on Kozeny Constant .....	138
7.3. Results for Interfacial Convective Heat Transfer Coefficient.....	148
7.3.1. Effects of Pore to Throat Size Ratio on Interfacial Nusselt Number .....	 149
7.3.2. Effects of Porosity on Interfacial Nusselt Number .....	155
7.4. Results for Thermal Dispersion.....	161
7.5. Experimental Results.....	171
 CHAPTER 8. CONCLUSION.....	 180
 REFERENCES.....	 184
 APPENDIX A. CALIBRATION OF PID CONTROLLERS AND DATA LOGGERS .....	  194



# LIST OF FIGURES

<b><u>Figure</u></b>	<b><u>Page</u></b>
Figure 1.1. Pores and throats in a metal foam.....	2
Figure 1.2. A rectangular fin array (a) real case (b) pores and throats in the array .....	3
Figure 2.1. Schematic views of porous media (a) ordered, (b) disordered porous media .....	7
Figure 2.2. Macroscopic and microscopic flows through a porous channel.....	8
Figure 2.3. A microscopic control volume in a porous structure.....	10
Figure 2.4. Flow through a bundle of capillary tubes .....	13
Figure 3.1. Kozeny constant comparison between some studies .....	34
Figure 3.2. The classification of the experimental studies performed for the determination of thermal dispersion .....	66
Figure 3.3. The schematic view of the experimental setups for the use of the heat addition/removal at the lateral boundaries method .....	70
Figure 3.4. Experimental setup of Bey and Eigenberger 2001 .....	75
Figure 3.5. The schematics of the experimental setups for the heating at the inlet boundary.....	77
Figure 3.6. The schematic of experimental setups in which the radiation heating method was used .....	79
Figure 3.7. The Reynolds number ranges in the reported experimental studies on the determination of the effective thermal conductivity .....	89
Figure 3.8. The comparison of reported correlations for determination of radial effective thermal conductivity ratios for (a) spherical (b) cylindrical (c) Raschig ring particles.....	93
Figure 4.1. Schematic view of the considered porous medium and the REV.....	94
Figure 4.2. REV's with pore to throat size ratios of 1.63, 3.04 and 7.46 for $\varepsilon = 0.7$ .....	95
Figure 5.1. The change of velocity profiles at the inlet and outlet through the iterative procedure to obtain periodic velocity distribution in the studied REV ( $\beta = 1.63$ , $\varepsilon = 0.7$ and $Re = 100$ ).....	106
Figure 5.2. The variation of Nu with Re for channel flow.....	109
Figure 5.3. The change of dimensionless temperature ( $\theta$ ) profiles at the inlet and	

outlet through the iterative procedure to obtain periodic temperature distribution in the studied REV ( $\beta = 1.63$ , $\varepsilon = 0.7$ and $Re = 100$ ) .....	110
Figure 5.4. The effect of number of grid on the obtained dimensionless pressure drop values for the REV with square rods ( $\varepsilon = 0.75$ and $Re = 100$ ) .....	113
Figure 5.5. The effect of number of grid on the obtained interfacial Nusselt numbers for the REVs with $\beta = 1.63$ and $7.46$ ( $\varepsilon = 0.9$ ) and the flow with $Re = 100$ .....	113
Figure 6.1. The schematic of the experimental setup.....	115
Figure 6.2. The complete views of the experimental setup (a) the side view, (b) the porous channel outlet view .....	115
Figure 6.3. A view of fan used in the experimental setup.....	116
Figure 6.4. Control panel of fan and preheater .....	116
Figure 6.5. The view of the honeycomb plate.....	117
Figure 6.6. Views of porous channel before placing the rods.....	118
Figure 6.7. Schematic view of the packed bed (porous inlet, test and outlet sections) .....	118
Figure 6.8. Outlet of the packed bed, a) wooden plates used for the placement of rods b) the located rods in the channel .....	118
Figure 6.9. Schematic view of porous channel (inlet, test and outlet sections) - top (or bottom) view .....	119
Figure 6.10. The holes for the velocity measurement – top view of the packed bed.....	120
Figure 6.11. The plate type heaters at the top wall of the porous test section and the equipment to fix the heaters to the wall .....	120
Figure 6.12. PID controllers and the electrical table (a) inside (b) cover door.....	122
Figure 6.13. Velocity measurement device (Testo 435-2) (a) main device, (b) hot wire probe and a magnetic mechanism for the velocity measurement .....	122
Figure 6.14. Data logger and its computer software .....	123
Figure 6.15. The coordinate axes considered for the velocity measurements .....	124
Figure 6.16. The velocity measurement locations at the inlet plane of porous channel and outlet plane of test section.....	124
Figure 6.17. The fluctuations in the measured velocities (a) $Re = 192$ , (b) $Re = 424$ .....	125

Figure 6.18. 5x10 grid used for the calculation of average velocity, temperature and mass flow rate.....	126
Figure 6.19. The fluctuations in the measured temperatures (a) Re = 192, (b) Re = 424 .....	127
Figure 6.20. Schematic view of the velocity and temperature measurement locations in the porous channel .....	129
Figure 6.21. A sample measured local velocity distribution in the porous channel (x = 500 mm and z = 1400 mm) .....	129
Figure 7.1. Comparison of the results of present study with the results of Lopez Penha et al. for Re = 1 and Re = 100 (a) Lopez Penha et al. 2011, (b) present study .....	132
Figure 7.2. Comparison of the results of present study with the results of Kuwahara et al. 1996 and Saada et al. 2006 for the change of dimensionless pressure drop with Re.....	133
Figure 7.3. Comparison of the obtained results with the study of Saada et al. for the change of dimensionless permeability with porosity .....	133
Figure 7.4. Comparison of the obtained results for the change of interfacial Nusselt number with the results of the reported studies .....	134
Figure 7.5. Comparison of the present results obtained for the longitudinal effective thermal conductivity with the results of reported studies (a) $\epsilon = 0.64$ and $k_s/k_f = 2$ and (b) $\epsilon = 0.64$ and $0.5$ , $k_s/k_f = 1$ .....	135
Figure 7.6. Comparison of the present results obtained for the transverse effective thermal conductivity with the results of reported studies $\epsilon = 0.75$ and $k_s/k_f = 1$ .....	136
Figure 7.7. The change of dimensionless pressure drop with Reynolds number for porous media with different ratios of pore to throat size ( $\epsilon = 0.7$ ).....	137
Figure 7.8. The variation of dimensionless permeability with pore to throat size ratio .....	138
Figure 7.9. The variation of $K/D^2$ with $\epsilon^3/(1-\epsilon)^2$ .....	140
Figure 7.10. The variation of dimensionless pressure drop with Re for various porosity and pore to throat size ratios.....	140
Figure 7.11. Streamlines and pressure contours in the porous media with $\beta = 7.46$ for porosities of a) 0.2, b) 0.3, c) 0.4, d) 0.5, e) 0.6, f) 0.7, g) 0.8, h) 0.9 .....	142

Figure 7.12. Streamlines and normalized pressure contours in porous media with $\varepsilon = 0.75$ and for pore to throat size ratios of a) 1.63, b) 2.21, c) 3.04, d) 4.44 .....	143
Figure 7.13. The change of dimensionless pressure gradient with porosity for porous media with different pore to throat size ratios.....	144
Figure 7.14. The variation of $K / d_h^2$ with porosity for different pore to throat size ratios .....	145
Figure 7.15. The variation of Kozeny constant with porosity for different pore to throat size ratios .....	146
Figure 7.16. The comparison of the predicted $16Kk_K / d_h^2$ values by using Eqs. (2.13), (2.14) and (7.2) with Kozeny-Carman permeability Equation .....	147
Figure 7.17. The streamlines (on the right) and temperature contours for $\beta = 1.63$ and $\varepsilon = 0.7$ and (a) $Re = 1$ , (b) $Re = 10$ , (c) $Re = 100$ .....	150
Figure 7.18. The variations of local interfacial Nusselt number along the solid-fluid interface for $\beta = 1.63$ and $\varepsilon = 0.7$ .....	151
Figure 7.19. The streamlines (on the right) and temperature contours for $\beta = 7.46$ and $\varepsilon = 0.7$ and (a) $Re = 1$ , (b) $Re = 10$ , (c) $Re = 100$ .....	152
Figure 7.20. The variations of local interfacial Nusselt numbers along the solid-fluid interface for $\beta = 7.46$ and $\varepsilon = 0.7$ .....	153
Figure 7.21. The change of interfacial Nusselt number with Reynolds number for porous structure with $\varepsilon = 0.7$ and different pore to throat size ratios.....	154
Figure 7.22. The variations of local interfacial Nusselt numbers along the solid-fluid interfaces with porosity for $\beta = 1.63$ and $Re = 1$ .....	155
Figure 7.23. The variations of local interfacial Nusselt numbers along the solid-fluid interfaces with porosity for $\beta = 1.63$ and $Re = 100$ .....	156
Figure 7.24. The change of interfacial Nusselt number with $Re$ for $\beta = 1.63$ and different porosities.....	157
Figure 7.25. The dimensionless temperature contours in porous media with $Re = 100$ , $\beta = 1.63$ and a) $\varepsilon = 0.75$ , b) $\varepsilon = 0.9$ .....	157
Figure 7.26. The variations of local interfacial Nusselt numbers along the solid-fluid interfaces with porosity for $\beta = 7.46$ and $Re = 1$ .....	158

Figure 7.27. The variations of local interfacial Nusselt numbers along the solid-fluid interfaces with porosity for $\beta = 7.46$ and $Re = 100$ .....	158
Figure 7.28. The change of interfacial Nusselt number with $Re$ for porous media with $\beta = 7.46$ .....	159
Figure 7.29. The comparison of the obtained numerical values of $Nu$ with the suggested correlation.....	160
Figure 7.30. The comparison of the suggested correlation with the reported values in literature for $\varepsilon = 0.75$ and $\beta = 2$ .....	161
Figure 7.31. The streamlines and dimensional temperature contours with longitudinal temperature gradient.....	163
Figure 7.32. The distributions of $(u'T')^*$ in the REV's .....	166
Figure 7.33. The variation of the longitudinal thermal dispersion with $\beta$ for different $Re$ a) $\varepsilon = 0.7$ , b) $\varepsilon = 0.8$ , c) $\varepsilon = 0.9$ .....	167
Figure 7.34. The streamlines and dimensional temperature contours with transverse temperature gradient for different REV's and two Reynolds numbers ....	168
Figure 7.35. The variation of the transverse thermal dispersion with Reynolds number for different $\beta$ a) $\varepsilon = 0.7$ , b) $\varepsilon = 0.8$ , c) $\varepsilon = 0.9$ .....	170
Figure 7.36. Experimental and numerical velocity profiles in empty channel for $Re = 192$ (a) empty channel inlet ( $z = 0$ ), (b) test section outlet ( $z = 1400$ mm).....	172
Figure 7.37. Experimental and numerical velocity profiles in empty channel for $Re = 329$ (a) empty channel inlet ( $z = 0$ ), (b) test section outlet ( $z = 1400$ mm).....	173
Figure 7.38. Experimental and numerical velocity profiles in empty channel for $Re = 424$ (a) empty channel inlet ( $z = 0$ ), (b) test section outlet ( $z = 1400$ mm).....	174
Figure 7.39. Experimental and numerical temperature profiles at the test section outlet in empty channel for $Re = 192$ .....	174
Figure 7.40. Experimental and numerical temperature profiles at the test section outlet in empty channel for $Re = 329$ .....	175
Figure 7.41. Experimental and numerical temperature profiles at the test section outlet in empty channel for $Re = 424$ .....	175
Figure 7.42. The experimental and numerical average velocity profiles in	

porous channel for $Re = 192$ .....	177
Figure 7.43. The experimental and numerical average velocity profiles in porous channel for $Re = 329$ .....	177
Figure 7.44. The experimental and numerical average velocity profiles in porous channel for $Re = 424$ .....	177
Figure 7.45. The experimental and numerical average temperature profiles in porous channel for $Re = 192$ .....	179
Figure 7.46. The experimental and numerical average temperature profiles in porous channel for $Re = 329$ .....	179
Figure 7.47. The experimental and numerical average temperature profiles in porous channel for $Re = 424$ .....	179
Figure A.1. Temperature calibration setup .....	194
Figure A.2. Modified temperature differences of PID controller with calibrator for random PID controllers. a) PID controller #2, b) PID controller #4....	195
Figure A.3. Modified temperature differences of channels of the data logger with calibrator with measurements taken with 5 Hz.....	196

## LIST OF TABLES

<b><u>Table</u></b>	<b><u>Page</u></b>
Table 3.1. Kozeny constant values found by Happel and Brenner .....	34
Table 3.2. Theoretical studies on the determination of permeability.....	38
Table 3.3. Theoretical studies on the determination of Kozeny constant .....	41
Table 3.4. Experimental studies on the determination of permeability .....	46
Table 3.5. Experimental studies on the determination of Kozeny constant.....	48
Table 3.6. Theoretical studies on the determination of interfacial convective heat transfer coefficient.....	53
Table 3.7. Experimental studies on the determination of interfacial convective heat transfer coefficient .....	57
Table 3.8. Theoretical studies on the determination of thermal dispersion coefficients.....	63
Table 3.9. The axial and/or radial effective thermal conductivity treatment in the reported experimental studies .....	68
Table 3.10. The lateral surface boundary conditions applied in studies with heat addition/removal at the lateral boundaries .....	69
Table 3.11. The properties of the packing particles used in the experimental studies on the determination of the effective thermal conductivity .....	84
Table 3.12. The features of the experimental setups used in the reported studies on the determination of the effective thermal conductivity .....	87
Table 3.13. The suggested correlations for the determination of the effective thermal conductivity .....	89
Table 4.1. The properties of fluid (air) used in numerical computations.....	95
Table 4.2. Geometric properties of investigated REVs.....	96
Table 4.3. The boundary conditions for the determination of thermal dispersion coefficients.....	103
Table 7.1. Minimum achievable porosities for the considered pore to throat size ratios .....	139
Table 7.2. The empirical coefficients for the determination of Kozeny constant....	147
Table 7.3. The empirical coefficients of the proposed correlation for the determination of the interfacial Nusselt number .....	160

Table 7.4. The Reynolds number, average velocity and mass flow rate values for the experiments in the empty channel .....	171
Table 7.5. Thermal dispersion coefficients that computed by using the numerical model.....	178



## LIST OF SYMBOLS

$A$	Area, $m^2$
$A^*$	Rod aspect ratio
$A_0$	Ratio of fluid-solid interfacial area to solid volume, $m^{-1}$
$A_{ss}$	Ratio of fluid-solid interfacial area to total volume, $m^{-1}$
$C$	Forchheimer coefficient
$c_p$	Specific heat, $kJ/kgK$
$d$	Diameter, $m$
$D$	Rod dimension, $m$
$H$	Convective heat transfer coefficient, $W/m^2K$
$H$	REV dimension, $m$
$k$	Thermal conductivity, $W/mK$
$\bar{k}_{dis}$	Thermal dispersion coefficient tensor, $W/mK$
$k_K$	Kozeny constant
$K$	Permeability, $m^2$
$L$	Characteristic length, $m$
$\dot{m}$	Mass flow rate, $kg/s$
$Nu$	Nusselt number
$p$	Pressure, $Pa$
$Pe$	Peclet number
$Pr$	Prandtl number
$q''$	Heat flux, $W/m^2$
$Re$	Reynolds number
$t$	Time, $s$
$T$	Temperature, $^{\circ}C$
$u$	Velocity in x direction, $m/s$
$\vec{u}$	Velocity vector, $m/s$
$u_D$	Darcian velocity, $m/s$
$v$	Velocity in y-direction, $m/s$
$V$	Volume, $m^3$

### **Greek Letters**

$\beta$	Pore to throat size ratio
$\varepsilon$	Porosity
$\theta$	Dimensionless temperature
$\mu$	Dynamic viscosity, Ns/m <sup>2</sup>
$\nu$	Kinematic viscosity, m <sup>2</sup> /s
$\rho$	Density, kg/m <sup>3</sup>
$\tau$	Tortuosity
$\varphi$	Any parameter

### **Subscripts**

b	Bulk
D	Diameter
dis	Dispersion
e	Equivalent
eff	Effective
f	Fluid
h	Hydraulic
L	Local
p	Particle
r	Radial (transverse)
ref	Reference
s	Solid
sf	Interfacial
w	Wall
xx	Longitudinal
yy	Transverse
zz	Longitudinal

# CHAPTER 1

## INTRODUCTION

A porous medium is a composite medium consisting of solid and voids. The voids can be interconnected (open cell) or disconnected (closed cell). The fluid flow and heat transfer in porous media are considerably studied in recent years due to their wide applications in both nature and technical areas. The application of transport in porous media is faced in almost all branches of engineering. Food and crop drying processes, chemical reactors, filters, membranes, gas separator adsorbent beds, nuclear reactors, and heat exchangers can be given as industrial examples in which transport in porous media appears as main topic. The flowing of water or petroleum through rocks and soil, air flowing in lung, blood flow in liver, biological tissues and veins or even flow of air in forests can be presented as examples for transport in porous media in nature.

In an open cell porous medium, fluid flows in the pores (or voids) between the particles. The mechanism of the flow through the pores is complex and the flow is three dimensional; hence pore level determinations of the velocity and the temperature fields are difficult. For this reason, some approaches are required to overcome the difficulties in analyzing heat and fluid flow in porous media. One of the most common methods is the macroscopic approach in which heat and fluid flow equations are established for a continuum domain involving the whole volume of the porous media although a discontinuity in the flow field exists due to the solid phase. This requires definitions for the volume averaged velocity, pressure, and temperature including both solid and fluid phases. Taking a volume integral of the continuity, momentum, and energy equations over a control volume in the domain yields the macroscopic governing equations for the continuum domain.

The application of volume averaging method on continuity, momentum and energy equations causes appearing of extra terms in corresponding equations. These terms involves macroscopic transport properties such as permeability, Forchheimer, thermal dispersion, thermal tortuosity and interfacial convective heat transfer coefficients. There are huge numbers of studies in the literature on the determination of

the macroscopic transport parameters for various porous media. The main aims in these studies generally were to understand the effects of the geometrical and/or flow properties such as porosity, Reynolds number, flow direction on the macroscopic transport parameters. Correlations and diagrams for determination of these effects were presented in the reported studies. Although the effects of many geometrical and flow parameters on macroscopic transport properties were studied and reported, still there are important parameters that have not been taken into account such as pore to throat size ratio.

The porous media structures considered in the present study are arrays of square or rectangular rods in inline arrangement. Mainly, the effects of pore to throat size ratio on the permeability, Kozeny constant, interfacial convective heat transfer and thermal dispersion coefficients are investigated. Additionally, the effects of porosity and Reynolds number on the aforementioned parameters and on Kozeny constant are examined. An experimental study was performed to validate the numerical model. The type of the porous structure is chosen as a fundamental geometry and a parametric study was performed to see the effects of pore to throat size ratio, porosity and Reynolds number on the aforementioned macroscopic transport parameters.

The pore to throat size ratio is an important parameter in porous media, whose effect can be encountered in many applications. For example, recently the interests in metal foams increase and they are produced to be employed in many heat exchanging applications. Pore and throat structures in a metal foam are shown in Figure 1.1. For the determination of the macroscopic transport parameters of metal foam, generally the ideal models are used since the investigation of the entire porous medium is very troublesome.



Figure 1.1. Pores and throats in a metal foam.

Another example for the effect of pore to throat size ratio on transport in porous media may be a fin array used for cooling of electronic equipment shown in Figure 1.2. There are long rectangular fins in the array and air flow through the fin array can be analyzed by using porous media models. Hence, the effect of pore to throat size ratio should be taken into account during design of this kind of fin arrays.

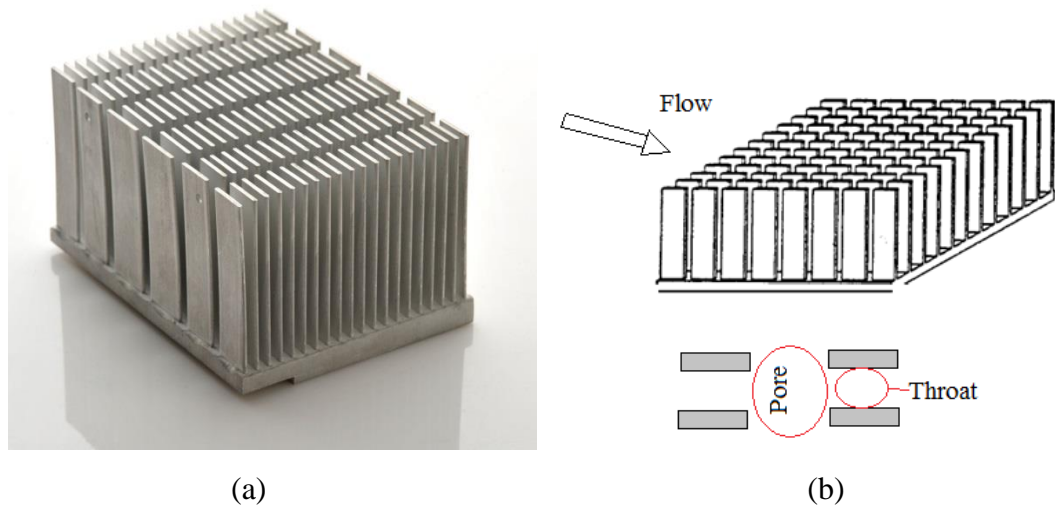


Figure 1.2. A rectangular fin array (a) real case (b) pores and throats in the array.

As it is well known, heat exchangers are widely used in industry. Most of the heat exchangers consist of long pipes. Porous media models can be used for analyzing of fluid flow and heat transfer between the pipes. Hence, the effect of pore to throat size ratio for design of heat exchangers should be considered. As a result, the effect of the pore to throat size ratio is encountered in many porous media applications; however, number of studies on this parameter is too limited

### 1.1. The Aim of Study

The aim of the present study is to investigate the effects of pore to throat size ratio on the fluid flow and heat transfer in porous media containing inline array of rectangular rods. The volume averaging method is used to determine the macroscopic transport parameters such as permeability, interfacial convective heat transfer and thermal dispersion coefficients. The applicability of Kozeny-Carman permeability equation for the considered porous media is examined and a correlation for the

determination of Kozeny constant based on the porosity and pore to throat size ratio of the considered medium is proposed. A correlation for the determination of the interfacial Nusselt number based on the same parameters is also presented.

An experimental study was performed to validate the numerical results. Although numerical studies on heat and fluid flow in packed beds with square rods are available in literature, no experimental study on the beds with square rods has been reported. Experimental studies were mostly done for unordered packed beds filled with spherical particles.

The present work is a parametric study to show the effects of pore to throat size ratio, Reynolds number, and porosity on the macroscopic transport parameters. A wide literature survey on the determination of macroscopic transport parameters, microscopic and macroscopic governing equations and boundary conditions and computation procedure are presented in details.

## **1.2. The Outline of Thesis**

The thesis is divided into eight chapters. In the first chapter an introduction to the subject and aim of study are presented.

In Chapter 2, basic concepts of porous media and background of microscopic and macroscopic methods are given. Microscopic governing equations for fluid flow and heat transfer and traditional macroscopic equations are presented. The derivation of the macroscopic fluid flow and heat transfer equations are written. The mathematical definitions of permeability, interfacial heat transfer coefficient and thermal dispersion and finally, a few words on the equivalent thermal conductivity models proposed in the literature are presented.

In Chapter 3, a literature review on the determinations of permeability, interfacial convective heat transfer and thermal dispersion coefficients is presented. Both theoretical and experimental studies are reviewed and the studies are summarized in tables.

In Chapter 4, the considered domain with the geometrical properties of the studied porous media is introduced. The governing equations solved to obtain the microscopic velocity, pressure and temperature distributions in the REV's and the

corresponding boundary conditions for the computation of the aforementioned macroscopic transport parameters are explained in detail.

Chapter 5 consists of the numerical procedure employed in the determination of the permeability, interfacial convective heat transfer coefficient and thermal dispersion coefficients. Computational details and grid independency tests of the computations are presented in this chapter as well.

In Chapter 6, the components of the experimental setup are introduced and the experimental procedure applied in the experimental part of the study is presented in detail.

The obtained results of the numerical and experimental parts of the present study are shown and explained in Chapter 7. The required discussions on the results are made and the proposed correlations for Kozeny constant and the interfacial convective heat transfer coefficient are reported in this chapter. Finally, the concluded remarks based on the obtained results are presented in Chapter 8.

## **CHAPTER 2**

# **BACKGROUND OF MACROSCOPIC HEAT AND FLUID FLOW ANALYSIS IN POROUS MEDIA**

A porous medium is a composite medium containing voids and solid particles. The mechanism of the flow through the pores is complex and the flow is three-dimensional; hence the pore level determination of velocity and temperature distributions is cumbersome and difficult. More appropriate approaches are required to overcome these difficulties in analysing the heat and fluid flow in porous media. One of the most common methods is the macroscopic approach which is explained in this chapter.

In this chapter, the microscopic and macroscopic methods for analysing fluid flow and heat transfer in the porous media are introduced. Firstly, an introduction to the microscopic point of view and the microscopic concepts of porous media are presented. Then, the microscopic fluid flow and heat transfer equations are introduced and explained. Finally, the traditional macroscopic equations are presented and the derivations of general forms of macroscopic momentum and energy equations are explained in detail.

### **2.1. Microscopic and Macroscopic Views of Porous Media**

In a porous medium, the fluid flows in the pores (or voids) between the particles. An open porous medium has interconnected voids and solid particles; hence the fluid flows in the voids. If there is periodicity in the porous structure, the medium is called as ordered or structured. If the structure is random, it is named as disordered (unstructured) porous medium (see Figure 2.1).

Disordered (randomly) packed beds are widely used in industrial processes, because of their low cost and ease of packing. But, pressure drops in these packed beds are usually much higher compared with the ordered packed beds, and the overall heat



transfer performances may be poor. Thus ordered packed beds are considered to be promising choices for the industrial applications (Yang et al. 2010).

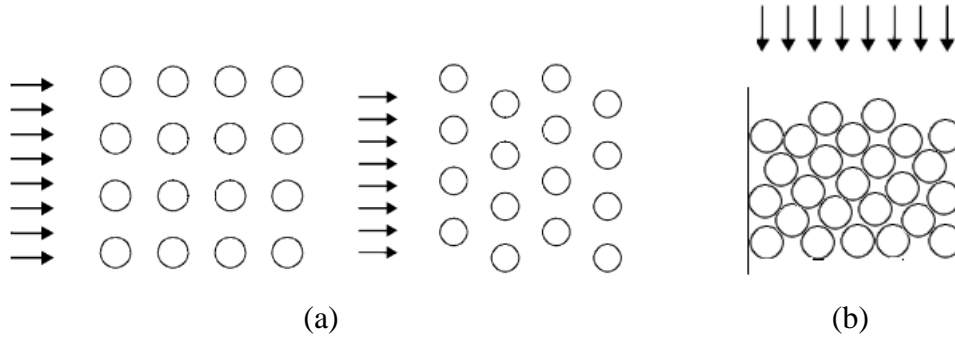


Figure 2.1. Schematic views of porous media (a) ordered, (b) disordered porous media

A basic property of a porous medium is porosity. The porosity is defined as the volume of the pores to the total volume of the porous media (see Eq. (2.1)).

$$\varepsilon = \frac{V_f}{V} \quad (2.1)$$

where  $V_f$  is the volume of the pores in the porous medium and  $V$  is the total volume. For the type of porous media in which some of the voids are closed to the fluid flow, the effective porosity value is defined to describe the volume in which the fluid flows.

As mentioned before, there are mainly two approaches to handle heat and fluid flow in porous media: microscopic and macroscopic approaches. In the microscopic approach, fluid motion in pores between particles is studied as it is. It can be studied by solving the continuity and Navier-Stokes equations. But it is cumbersome and difficult to analyze the heat and fluid flow for whole domain of a porous medium, microscopically. The microscopic approach is useful when a periodic structure is considered. On the other hand, in the macroscopic approach, heat and fluid flow is analyzed for a continuum domain by upscaling the microscopic parameters. Heat and fluid flow equations are established for a continuum domain involving the whole volume of porous medium in spite of discontinuity in the flow due to the solid phase and all properties of the domain are obtained as effective values. Volume integral of the

continuity, momentum and energy equations yields the governing equations for the whole of porous medium.

Figure 2.2 shows fluid flow in a channel filled with a porous medium. When fluid enters into the channel, fluid particles have 3D motion inside the pores. But macroscopically, flow through the porous column is unidirectional and the macroscopic velocity can be written as the ratio of volume flow rate to the cross-sectional area. This macroscopic velocity is also known as apparent, superficial or Darcian velocity. Because of the conservation of mass, this velocity should be constant through the channel (Nakayama 1995).

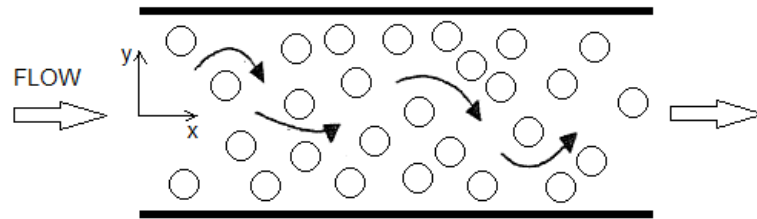


Figure 2.2. Macroscopic and microscopic flows through a porous channel.

Permeability is a macroscopic transport property used to obtain macroscopic velocity. Permeability is a measure of the allowance of the solid structure to fluid flow. It is independent of fluid properties and only depends on the properties of the solid structure of the considered porous medium (Nield and Bejan 2006).

There are industrial and natural processes in which heat transfer through porous media occurs while fluid flows through the voids. The heat transfer in porous media can also be analyzed macroscopically. Interfacial convective heat transfer and thermal dispersion coefficients are two macroscopic transport parameters that play important role on analyzing heat transfer in porous media.

Interfacial convective heat transfer coefficient represents the heat transfer between fluid and solid phases. It occurs when there is no local thermal equilibrium between two phases. When the interfacial convective heat transfer coefficient is studied, two phases in the porous medium should be considered, separately. Two energy equations (one for solid and another for fluid phase) should be solved to determine temperature field for the entire domain.

Thermal dispersion occurs in a porous medium due to non-uniform velocity and temperature fields, and thermal dispersion coefficients show the effects of these microscopic non-uniformities on macroscopic level. Thermal dispersion shows the enhanced heat transfer which occurs in response to the interaction between the local spatial fluctuations of velocity and temperature at the pore scale (Alshare et al. 2010). As flow velocity increases, thermal dispersion becomes a significant parameter in heat transfer through porous media, hence it is important to determine the values of thermal dispersion coefficients, accurately. Thermal dispersion depends on many parameters such as porosity, Reynolds and Peclet numbers, solid-to-fluid conductivity ratio etc. The shape of packing and type of porous media (ordered/disordered) affect thermal dispersion.

## 2.2. Microscopic Fluid Flow and Energy Equations

For an incompressible flow of Newtonian fluid with constant thermo-physical properties, the continuity and momentum equations, given in Eqs. (2.2) and (2.3), are used to obtain the velocity and pressure distributions in the pores of the considered porous medium.

$$\nabla \cdot \vec{u} = 0 \quad (2.2)$$

$$\rho_f \frac{\partial \vec{u}}{\partial t} + \rho_f (\vec{u} \cdot \nabla \vec{u}) = -\nabla p + \mu_f \nabla^2 \vec{u} \quad (2.3)$$

where  $\vec{u}$  is velocity vector,  $\rho_f$  and  $\mu_f$  are the density and dynamic viscosity of the fluid, respectively, and  $p$  is pressure. To obtain the microscopic temperature distribution in a porous medium, both solid and fluid phases should be considered separately and two microscopic energy equations should be taken into account. With the assumption of the negligible viscous dissipation, Eqs. (2.4) and (2.5) are microscopic energy equations for fluid and solid phases, respectively.

$$\rho_f c_{pf} \left( \frac{\partial T_f}{\partial t} + \nabla \cdot \vec{u} T_f \right) = k_f \nabla^2 T_f \quad (2.4)$$

$$\rho_s c_{ps} \frac{\partial T_s}{\partial t} = k_s \nabla^2 T_s \quad (2.5)$$

where  $T$  is temperature,  $c_p$  and  $k$  are specific heat capacity and thermal conductivity, respectively. The subscripts  $f$  and  $s$  refer to the fluid and solid phases. By using above governing equations (Eqs. (2.2)-(2.5)) with appropriate initial and boundary conditions, the velocity and pressure distributions in the pores and the temperature distributions in both solid and fluid phases can be obtained. However, for a porous medium consisting of huge number of pores and complex structure, the microscopic (or pore level) analysis by employing these equations may be difficult and time consuming. That's why; the macroscopic method which is explained in the following sections can be used to analyse fluid flow and heat transfer in porous media.

### 2.3. Volume Averaging Method

Volume averaging method is frequently used in macroscopic analysis of heat and fluid flow in porous media. In order to apply volume averaging method to a control volume within a porous medium, the characteristic length of the control volume ( $V^{1/3}$ ) should be chosen smaller than the macroscopic characteristic length ( $V_c^{1/3}$ ) (e.g. channel height), however it should be much larger than the microscopic characteristic length to find meaningful values (see Figure 2.3) (Nakayama 1995).

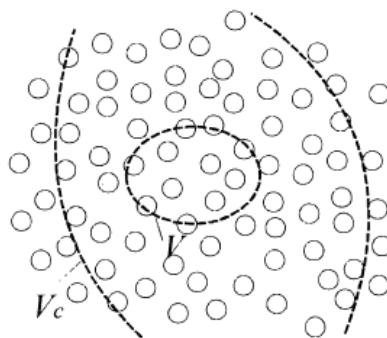


Figure 2.3. A microscopic control volume in a porous structure  
(Source: Nakayama 1995)

Volume averaging of a quantity over a control volume is calculated as follows:

$$\langle \varphi \rangle = \frac{1}{V} \int_V \varphi dV \quad (2.6)$$

where  $V$  is the volume of chosen control volume. By using Eq. (2.6), the macroscopic velocity is defined as below.

$$\langle \vec{u} \rangle = \frac{1}{V} \int_V \vec{u} dV \quad (2.7)$$

If an average value of a quantity for one of the phases is required, intrinsic averaging is used. For example, the average velocity in the fluid phase can be calculated from Eq. (2.8). This velocity can also be called as pore or interstitial velocity and it is proportional to the macroscopic velocity.

$$\langle \vec{u} \rangle^f = \frac{1}{V_f} \int_{V_f} \vec{u} dV \quad (2.8)$$

where  $V_f$  is pore volume. The relation between macroscopic and pore velocities is shown by Eq. (2.9) which is known as Dupuit-Forchheimer relation (Kaviany 1995).

$$\langle \vec{u} \rangle^f = \langle \vec{u} \rangle / \varepsilon \quad (2.9)$$

More details on the fundamentals and applications of volume averaging method can be found in the book of Whitaker (Whitaker 1999).

## **2.4. Traditional Macroscopic Flow Equations: Darcy and Forchheimer Motion Equations**

It is empirically discovered by Darcy (Darcy 1856, Kaviany 1995) that the macroscopic (Darcian) velocity through a column of porous medium is proportional to the pressure gradient and inversely proportional to the fluid viscosity. This relation is

called as Darcy's Law and its one-dimensional form is shown by Eq. (2.10). The proportionality constant  $K$  is called as permeability. The permeability is a tensor in which the diagonal terms show the permeability of the porous medium in principal directions. Permeability refers to the flow resistance inside the porous medium. It depends on the micro-structure of the solid phase and independent of the properties of the fluid (Nakayama 1995). Darcy's Law can be accurately used to obtain average velocity in a porous medium for low Reynolds number flows ( $Re_d < 1$ ,  $Re_d = \langle u \rangle d / \nu$ ) because it states a balance between viscous and pressure forces.

$$\langle u \rangle = -\frac{K}{\mu_f} \left( \frac{d\langle p \rangle^f}{dx} \right) \quad (2.10)$$

At higher Reynolds numbers, an additional quadratic term, which includes the flow inertia effects, was proposed by Dupuit (Dupuit 1863) and Forchheimer (Forchheimer 1901, Nakayama 1995). The resulting equation is called as Forchheimer extended Darcy's Law and its one dimensional form is given by Eq. (2.11). The first term on the right hand side accounts for the frictional drag (Darcy term) while the second term (Forchheimer) refers to the form drag.

$$-\frac{d\langle p \rangle^f}{dx} = \frac{\mu_f}{K} \langle u \rangle + \frac{C}{K^{1/2}} \rho_f \langle u \rangle^2 \quad (2.11)$$

where  $C$  is Forchheimer coefficient. As can be seen from Eqs. (2.10) and (2.11), in order to predict macroscopic velocity for a porous medium accurately, the permeability and Forchheimer coefficients should be well known. The most common equation for determination of permeability was derived according to Kozeny-Carman theory (Kozeny 1927, Carman 1937). The Kozeny-Carman theory and the derivation of Kozeny-Carman permeability equation are summarized in the following paragraphs. The average velocity for Hagen-Poiseuille flow in a channel with diameter of  $d_t$  can be found as:

$$\langle u \rangle^f = -\frac{1}{32\mu} \frac{d\langle p \rangle^f}{dx} d_t^2 \quad (2.12)$$

By using Dupuit-Forchheimer relation (Eq. (2.9)) and comparing Darcy's Law with Eq. (2.12), the permeability value for Hagen-Poiseuille flow in a channel can be found as  $K = d_t^2 \varepsilon / 32$ . Kozeny considered the medium as a bundle of capillary channels with the same radius as shown in Figure 2.4.



Figure 2.4. Flow through a bundle of capillary tubes  
(Source: Nakayama 1995)

By combining Hagen-Poiseuille velocity equation with Darcy's Law and using tortuosity concept, the following equation for permeability was proposed by Kozeny:

$$K = \frac{d_t^2 \varepsilon}{32\tau} \quad (2.13)$$

where  $\tau$  is tortuosity. Tortuosity can be defined as the ratio of the actual length of flow path in the porous medium to the length of flow path in the absence of porous medium (i.e., in clear fluid). The tortuosity can be thought as the effect of the microstructure of the porous medium (direction of the pores) on the macroscopic flow (Liu and Masliyah 2005). Tortuosity used in Eq. (2.13) may be understood as the correction to the pressure gradient which is defined for clear fluid (Kaviany 1995). The permeability equation of Kozeny was modified later by Carman and the so-called Kozeny-Carman equation was introduced to the literature and has been widely used. Kozeny-Carman equation which predicts the permeability reasonably well for the packed bed of spheres is presented as:

$$K = \frac{d_h^2 \varepsilon}{16k_K} \quad (2.14)$$

where  $d_h$  is the pore hydraulic diameter of the porous medium. The pore hydraulic diameter is defined as:

$$d_h = \frac{4\varepsilon}{A_0(1-\varepsilon)} \quad (2.15)$$

where  $A_0$  is the ratio of the fluid-solid interfacial area to the solid volume. The symbol of  $k_K$  in Eq. (2.14) is Kozeny constant which includes the effects of flow path, particle shape and their connections (i.e., tortuosity and shape effects) and given equal to a constant in Kozeny-Carman theory ( $k_K = 5$ ). For spherical particles, the Kozeny-Carman equation can be rewritten based on particle diameter as Eq. (2.16).

$$K = \frac{1}{36k_K} \frac{\varepsilon^3}{(1-\varepsilon)^2} d^2 \quad (2.16)$$

where  $d$  is the diameter of the spheres. On the other hand, for 2- or 3-dimensional cylinders Eq. (2.14) changes into Eq. (2.17).

$$K = \frac{1}{16k_K} \frac{\varepsilon^3}{(1-\varepsilon)^2} d^2 \quad (2.17)$$

where  $d$  is the diameter of the cylinders.

Ergun (Ergun 1952) studied gas flow through column of packed spheres experimentally and determined permeability and Forchheimer coefficients as follows:

$$K = \frac{1}{150} \frac{\varepsilon^3}{(1-\varepsilon)^2} d^2 \quad (2.18)$$

$$C = \frac{0.143}{\varepsilon^{3/2}} \quad (2.19)$$



Thus, Eq. (2.20) is called as Ergun's Equation.

$$-\frac{dp}{dx} = \frac{150(1-\varepsilon)^2 \mu_f \langle u \rangle}{\varepsilon^3 d^2} + \frac{1.75(1-\varepsilon) \rho_f \langle u \rangle^2}{\varepsilon^3 d} \quad (2.20)$$

As it was mentioned before, the drag term (Forchheimer term) becomes important for high Reynolds number flows. The Reynolds number used in the macroscopic fluid flow and heat transfer analysis generally has the following form:

$$\text{Re} = \frac{\rho_f \langle u \rangle L}{\mu_f} \quad (2.21)$$

where L is characteristic length which may be the dimension of the solid particles (d) or the dimension of the representative elementary volume etc. Another Reynolds number definition frequently used in the studies is given by Eq. (2.22). It might be useful to mention that for steady flow through porous media, the flow is assumed to remain laminar as long as  $\text{Re}_K < 300$  (Pedras and de Lemos 2001).

$$\text{Re}_K = \frac{\rho_f |\langle u \rangle| \sqrt{K}}{\mu_f} \quad (2.22)$$

The traditional macroscopic fluid flow equations are briefly explained in the previous paragraphs. The traditional equations were generally obtained intuitively by using the experimental observations. However, general forms of macroscopic fluid flow and heat transfer equations can be obtained theoretically by applying volume-averaging method on the corresponding microscopic equations. The macroscopic equations and the derivation procedure are presented in the following sections.

## 2.5. General Forms of Macroscopic Motion Equations

General macroscopic flow equations can be obtained by applying the volume averaging method on the continuity and Navier-Stokes equations by using below

equalities. The following relation can be used for intrinsic average of any multiplication  $\varphi_1\varphi_2$  (Nield and Bejan 2006).

$$\langle \varphi_1\varphi_2 \rangle^f = \langle \varphi_1 \rangle^f \langle \varphi_2 \rangle^f + \langle \varphi_1'\varphi_2' \rangle^f \quad (2.23)$$

Where the prime denotes the deviation of the intrinsic average value from the microscopic one, such that

$$\varphi' = \varphi - \langle \varphi \rangle^f \quad (2.24)$$

Eq. (2.23) can be rewritten in terms of the total volume averaged variables with using Dupuit-Forchheimer relation (Eq. 2.9) as follows.

$$\langle \varphi_1\varphi_2 \rangle = \frac{1}{\varepsilon} \langle \varphi_1 \rangle \langle \varphi_2 \rangle + \langle \varphi_1'\varphi_2' \rangle \quad (2.25)$$

Also, the following rules which are analogous to Leibnitz rule are used in the volume averaging procedure.

$$\langle \nabla \varphi \rangle = \nabla \langle \varphi \rangle + \frac{1}{V} \int_{A_{sf}} \varphi dA \quad (2.26)$$

$$\left\langle \frac{\partial \varphi}{\partial t} \right\rangle = \frac{\partial \langle \varphi \rangle}{\partial t} \quad (2.27)$$

where  $A_{sf}$  is the interfacial area between solid and fluid phases. By using these equalities, macroscopic governing equations can be directly derived from the microscopic equations. The macroscopic continuity equation can be obtained by applying volume averaging method to Eq. (2.2) which is the microscopic continuity equation.

$$\frac{1}{V} \int_V \nabla \cdot \vec{u} = \langle \nabla \cdot \vec{u} \rangle = 0 \quad (2.28)$$

The integration rule given by Eq. (2.26) is used on Eq. (2.28) to obtain Eq. (2.29).

$$\nabla \cdot \langle \vec{u} \rangle + \frac{1}{V} \int_{A_{sf}} \vec{u} dA = 0 \quad (2.29)$$

The second term vanishes since the flow cannot penetrate through the solid wall. Hence the macroscopic continuity equation is found as follows.

$$\nabla \cdot \langle \vec{u} \rangle = 0 \quad (2.30)$$

Microscopic momentum equation is given by Eq. (2.3). With a similar procedure explained for obtaining macroscopic continuity equation, the macroscopic momentum equation can also be found. Volume averaging of Eq. (2.3) yields:

$$\rho_f \left\langle \frac{\partial \vec{u}}{\partial t} \right\rangle + \rho_f \langle \vec{u} \cdot \nabla \vec{u} \rangle = -\langle \nabla p \rangle + \mu_f \langle \nabla^2 \vec{u} \rangle \quad (2.31)$$

This equation can be rewritten in the following form by using Eqs. (2.26) and (2.27):

$$\begin{aligned} & \rho_f \frac{\partial \langle \vec{u} \rangle}{\partial t} + \rho_f \left[ \frac{1}{\varepsilon} \langle \vec{u} \rangle \cdot \nabla \langle \vec{u} \rangle + \langle \vec{u}' \cdot \nabla \vec{u}' \rangle \right] \\ & = -\nabla \langle p \rangle - \frac{1}{V} \int_{A_{sf}} p dA + \mu_f \left[ \nabla^2 \langle \vec{u} \rangle + \frac{1}{V} \int_{A_{sf}} \nabla \vec{u} dA + \nabla \cdot \frac{1}{V} \int_{A_{sf}} \vec{u} dA \right] \end{aligned} \quad (2.32)$$

The last integration on the right hand side of Eq. (2.32) vanishes due to no flow penetration into solid. Since the pressure term in the momentum equations is related to the fluid phase, the Dupuit-Forchheimer relation can be used to change the total volume averaged pressure into the intrinsic volume averaged value.

$$\begin{aligned}
\rho_f \frac{\partial \langle \bar{\mathbf{u}} \rangle}{\partial t} + \rho_f \left[ \frac{1}{\varepsilon} \langle \bar{\mathbf{u}} \rangle \cdot \nabla \langle \bar{\mathbf{u}} \rangle + \langle \bar{\mathbf{u}}' \cdot \nabla \bar{\mathbf{u}}' \rangle \right] &= -\varepsilon \nabla \langle p \rangle^f - \frac{1}{V} \int_{A_{sf}} p dA \\
+ \mu_f \left[ \nabla^2 \langle \bar{\mathbf{u}} \rangle + \frac{1}{V} \int_{A_{sf}} \nabla \bar{\mathbf{u}} dA \right] &
\end{aligned} \tag{2.33}$$

With rearranging terms and dividing the whole equation to porosity, the macroscopic momentum equation becomes as follows.

$$\begin{aligned}
\rho_f \left( \frac{1}{\varepsilon} \frac{\partial \langle \bar{\mathbf{u}} \rangle}{\partial t} + \frac{1}{\varepsilon^2} \langle \bar{\mathbf{u}} \rangle \cdot \nabla \langle \bar{\mathbf{u}} \rangle \right) & \\
= -\nabla \langle p \rangle^f + \frac{\mu_f}{\varepsilon} \nabla^2 \langle \bar{\mathbf{u}} \rangle - \frac{1}{V} \int_{A_{sf}} p dA + \frac{\mu_f}{\varepsilon} \frac{1}{V} \int_{A_{sf}} \nabla \bar{\mathbf{u}} dA - \frac{1}{\varepsilon} \langle \bar{\mathbf{u}}' \nabla \cdot \bar{\mathbf{u}}' \rangle &
\end{aligned} \tag{2.34}$$

The last 3 terms on the RHS of Eq. (2.34) can be thought as an extra source terms since they do not exist in the microscopic momentum equations. The last term corresponds to the effects of inertia while other 2 terms (3<sup>rd</sup> and 4<sup>th</sup> on the RHS) together correspond to viscous effects. Vafai and Tien (Vafai and Tien 1981) stated that the last three terms in Eq. (2.34) correspond to Forchheimer-extended Darcy's Law in the following form.

$$\rho_f \left( \frac{1}{\varepsilon} \frac{\partial \langle \bar{\mathbf{u}} \rangle}{\partial t} + \frac{1}{\varepsilon^2} \langle \bar{\mathbf{u}} \rangle \cdot \nabla \langle \bar{\mathbf{u}} \rangle \right) = -\nabla \langle p \rangle^f + \frac{\mu_f}{\varepsilon} \nabla^2 \langle \bar{\mathbf{u}} \rangle + \vec{S} \tag{2.35}$$

$$\vec{S} = -\frac{\mu_f}{K} \langle \bar{\mathbf{u}} \rangle - \frac{C}{K^{1/2}} \rho_f |\langle \bar{\mathbf{u}} \rangle| \langle \bar{\mathbf{u}} \rangle \tag{2.36}$$

Thus the macroscopic momentum equation becomes as

$$\begin{aligned}
\rho_f \left( \frac{1}{\varepsilon} \frac{\partial \langle \bar{\mathbf{u}} \rangle}{\partial t} + \frac{1}{\varepsilon^2} \langle \bar{\mathbf{u}} \rangle \cdot \nabla \langle \bar{\mathbf{u}} \rangle \right) & \\
= -\nabla \langle p \rangle^f + \frac{\mu_f}{\varepsilon} \nabla^2 \langle \bar{\mathbf{u}} \rangle - \frac{\mu_f}{K} \langle \bar{\mathbf{u}} \rangle - \frac{C}{K^{1/2}} \rho_f |\langle \bar{\mathbf{u}} \rangle| \langle \bar{\mathbf{u}} \rangle &
\end{aligned} \tag{2.37}$$

The left hand side (LHS) terms are macroscopic convective inertia terms. The last three terms on the right hand side (RHS) are called as Brinkman (boundary friction), Darcy (porous viscous) and Forchheimer (porous inertia) terms, respectively (Nakayama 1995).

## 2.6. Macroscopic Energy Equations

For a porous medium with two phases as a solid phase and an incompressible Newtonian fluid flowing through the pores without considerable effect of viscous dissipation, the microscopic energy equations for the fluid and solid phases are given in Eqs. (2.4) and (2.5). To obtain the macroscopic energy equations for the fluid and solid phases of the porous media, volume averaging method can be used.

By applying volume averaging method on the microscopic energy equations, following equations for fluid and solid phases can be found as:

$$\rho_f c_{pf} \left( \left\langle \frac{\partial T}{\partial t} \right\rangle + \langle \nabla \cdot \vec{u} T \rangle \right) = k_f \langle \nabla^2 T \rangle \quad (2.38)$$

$$\rho_s c_{ps} \left\langle \frac{\partial T}{\partial t} \right\rangle = k_s \langle \nabla^2 T \rangle \quad (2.39)$$

Using the equalities given by Eqs. (2.26) and (2.27) on Eqs. (2.38) and (2.39), the macroscopic energy equations can be rewritten as follows.

$$\rho_f c_{pf} \left( \frac{\partial \langle T \rangle}{\partial t} + \nabla \cdot \langle \vec{u} T \rangle + \frac{1}{V} \int_{A_{sf}} \vec{u} T dA \right) = \quad (2.40)$$

$$k_f \nabla^2 \langle T \rangle + \nabla \cdot \frac{1}{V} \int_{A_{sf}} k_f T dA + \frac{1}{V} \int_{A_{sf}} k_f \nabla T dA$$

$$\rho_s c_{ps} \frac{\partial \langle T \rangle}{\partial t} = k_s \nabla^2 \langle T \rangle + \nabla \cdot \frac{1}{V} \int_{A_{sf}} k_s T dA + \frac{1}{V} \int_{A_{sf}} k_s \nabla T dA \quad (2.41)$$

The integration in the LHS of Eq. (2.40) vanishes because of the non-slip boundary condition at the solid-fluid interface. Since the temperature in both equations show the temperature of corresponding phases, the representation of intrinsic volume

averaged might be better and that's why Dupuit-Forchheimer relation is used to revise Eqs. (2.40) and (2.41). Additionally, Eq. (2.25) is used to re-write the second term on the LHS of Eq. (2.40).

$$\rho_f c_{p_f} \left( \varepsilon \frac{\partial \langle T \rangle^f}{\partial t} + \nabla \cdot \left[ \frac{1}{\varepsilon} \langle T \rangle \langle \bar{u} \rangle + \langle T' \bar{u}' \rangle \right] \right) = k_f \varepsilon \nabla^2 \langle T \rangle^f + \nabla \cdot \left[ \frac{1}{V} \int_{A_{sf}} k_f T dA \right] + \frac{1}{V} \int_{A_{sf}} k_f \nabla T \cdot dA \quad (2.42)$$

$$\rho_s c_{p_s} (1 - \varepsilon) \frac{\partial \langle T \rangle^s}{\partial t} = k_s (1 - \varepsilon) \nabla^2 \langle T \rangle^s + \nabla \cdot \left[ \frac{1}{V} \int_{A_{sf}} k_s T dA \right] + \frac{1}{V} \int_{A_{sf}} k_s \nabla T dA \quad (2.43)$$

The 2nd term on the LHS of Eq. (2.42) is rearranged with using macroscopic continuity equation and Dupuit-Forchheimer relation in the following way.

$$\begin{aligned} \nabla \cdot \left[ \frac{1}{\varepsilon} \langle T \rangle \langle \bar{u} \rangle + \langle T' \bar{u}' \rangle \right] &= \nabla \cdot \langle T \rangle^f \langle u \rangle + \nabla \cdot \langle T' \bar{u}' \rangle \\ &= \langle u \rangle \cdot \nabla \langle T \rangle^f + \langle T \rangle^f \nabla \cdot \langle u \rangle + \nabla \cdot \langle T' \bar{u}' \rangle = \langle \bar{u} \rangle \cdot \nabla \langle T \rangle^f + \nabla \cdot \langle T' \bar{u}' \rangle \end{aligned} \quad (2.44)$$

With rearranging the terms, the macroscopic equations in terms of intrinsic volume-averaged temperature values can be written as:

$$\rho_f c_{p_f} \left( \varepsilon \frac{\partial \langle T \rangle^f}{\partial t} + \langle \bar{u} \rangle \cdot \nabla \langle T \rangle^f \right) = k_f \varepsilon \nabla^2 \langle T \rangle^f + \nabla \cdot \left[ \frac{1}{V} \int_{A_{sf}} k_f T dA \right] + \frac{1}{V} \int_{A_{sf}} k_f \nabla T \cdot dA - \rho_f c_{p_f} \nabla \cdot \langle T' \bar{u}' \rangle \quad (2.45)$$

$$\rho_s c_{p_s} (1 - \varepsilon) \frac{\partial \langle T \rangle^s}{\partial t} = k_s (1 - \varepsilon) \nabla^2 \langle T \rangle^s + \nabla \cdot \left[ \frac{1}{V} \int_{A_{sf}} k_s T dA \right] + \frac{1}{V} \int_{A_{sf}} k_s \nabla T dA \quad (2.46)$$

Eq. (2.45) represents macroscopic form of energy equation for fluid phase, while Eq. (2.46) is for the solid phase. The first terms on the right hand sides of these equations represent the diffusion heat transfer in the fluid and solid phases. The second terms relate to the thermal tortuosity. The last term on the RHS of macroscopic energy

equation of fluid (see Eq. (2.45)) shows the thermal dispersion showing the additional diffusion heat transfer to the molecular diffusion. The third terms on the RHS of the macroscopic energy equations show the heat transfer between the solid surface and the fluid flowing in the voids and it can be calculated by using the interfacial convective heat transfer concept. Mathematically, the convective heat transfer between solid and fluid can be expressed by using the interfacial heat transfer coefficient.

$$h_{sf} A_{ss} (\langle T \rangle^s - \langle T \rangle^f) = \frac{1}{V} \int_{A_{sf}} \vec{n} \cdot k_f \nabla T dA = \frac{1}{V} \int_{A_{sf}} \vec{n} \cdot k_s \nabla T dA \quad (2.47)$$

where  $h_{sf}$  is the interfacial convective heat transfer coefficient and  $A_{ss}$  is the specific solid-fluid interfacial area (i.e.,  $A_{ss} = A_{sf}/V$ ). The interfacial convective heat transfer coefficient can be found by using Eq. (2.48) which directly comes from Eq. (2.47). When thermal equilibrium breaks down the interfacial convective heat transfer coefficient should be taken into account for the analysis of macroscopic heat transfer through porous medium.

$$h_{sf} = \frac{\frac{1}{V} \int_{A_{sf}} k_f \nabla T dA}{\langle T \rangle^s - \langle T \rangle^f} \quad (2.48)$$

It should be underlined that the interfacial convective heat transfer coefficient is calculated based on the macroscopic temperatures of the solid and fluid phases. Hence it is a macroscopic parameter and it is different from the convective heat transfer coefficient generally used in the heat transfer problems with clear fluid flow. By using definition of interfacial convective heat transfer coefficient, Eqs. (2.45) and (2.46) takes the following form:

$$\begin{aligned} \rho_f c_{p_f} \left( \varepsilon \frac{\partial \langle T \rangle^f}{\partial t} + \langle \vec{u} \rangle \cdot \nabla \langle T \rangle^f \right) &= k_f \varepsilon \nabla^2 \langle T \rangle^f + \nabla \cdot \left[ \frac{1}{V} \int_{A_{sf}} k_f T dA \right] \\ + h_{sf} A_{ss} (\langle T \rangle^s - \langle T \rangle^f) &- \rho_f c_{p_f} \nabla \cdot \langle T' \vec{u}' \rangle \end{aligned} \quad (2.49)$$

$$\rho_s c_{ps} (1 - \varepsilon) \frac{\partial \langle T \rangle^s}{\partial t} = k_s (1 - \varepsilon) \nabla^2 \langle T \rangle^s + \nabla \cdot \left[ \frac{1}{V} \int_{A_{sf}} k_s T dA \right] + h_{sf} A_{ss} (\langle T \rangle^s - \langle T \rangle^f) \quad (2.50)$$

If there is local thermal non-equilibrium in the porous medium, two energy equations given above should be solved in order to obtain the macroscopic temperature distribution for each phase. Local thermal equilibrium breaks down in the following situations as an example.

- At the entrance region of packed column where a hot gas flows at a high speed,
- Unsteady problems in which heat is transferred from one phase to another,
- Applications in which the temperature at the solid-fluid interface changes significantly with respect to time,
- Applications in which solid and fluid phases have significantly different heat capacities and thermal conductivities.

In spite of the above cases, there are many applications in which thermal equilibrium assumption between solid and fluid phases is valid. Quintard and Whitaker (Quintard and Whitaker 1995) developed the constraints that must be satisfied for the validity of the thermal equilibrium assumption; the details of these constraints can be seen in their study. If thermal equilibrium between two phases is valid, the equality of the macroscopic temperatures can be written as  $\langle T \rangle = \langle T \rangle^f = \langle T \rangle^s$  and the summation of Eqs. (2.45) and (2.46) yields Eq. (2.51) for a porous continuum domain.

$$\left( \rho c_p \right)_e \frac{\partial \langle T \rangle}{\partial t} + \rho_f c_{pf} \langle \vec{u} \rangle \cdot \nabla \langle T \rangle = k_e \nabla^2 \langle T \rangle + \nabla \cdot \left[ \frac{1}{V} \int_{A_{int}} (k_f - k_s) T dA \right] - \rho_f c_{pf} \nabla \cdot \langle T' \vec{u}' \rangle \quad (2.51)$$

Here,  $(\rho c_p)_e$  and  $k_e$  are the equivalent thermal capacitance and thermal conductivity of the porous continuum domain. These equivalent properties include porosity as well as both solid and fluid thermal properties and defined as below. The equivalent thermal conductivity is also called as stagnant thermal conductivity.



$$(\rho c_p)_e = (1 - \varepsilon)\rho_s c_{ps} + \varepsilon \rho_f c_{pf} \quad (2.52)$$

$$k_e = (1 - \varepsilon)k_s + \varepsilon k_f \quad (2.53)$$

As mentioned before, two distinctive terms appear in the macroscopic energy equation. The last two terms in the macroscopic energy equation (Eq. 2.51) have special names as tortuosity and thermal dispersion. These terms do not exist in the microscopic energy equations and they are resulted due to the volume averaging method. The thermal tortuosity term regards the change of the thermal diffusion path due to different thermal conductivities between the solid and the fluid. It is described as an elongation in the thermal path due to the existence of the solid particles (Hsu 2000). The thermal dispersion is caused by the non-uniformities of the pore level velocity and temperature fields, and the hydrodynamic mixing effects (Ozgunus et al. 2013). The term  $\rho_f c_{pf} \langle \bar{u}' T' \rangle$  is analogous to the turbulent heat flux in the turbulent convection heat transfer, which accounts for the contributions from mechanical dispersion, and can be modelled similarly by a gradient-type diffusion hypothesis (Nakayama 1995). Hence, the thermal dispersion term in Eq. (2.51) can be written in the form of a heat diffusion transport and defined by using the thermal dispersion coefficient ( $k_{dis}$ ) as follows:

$$-\rho_f c_{pf} \langle T' \bar{u}' \rangle = \bar{k}_{dis} \cdot \nabla \langle T \rangle^f \quad (2.54)$$

Thermal dispersion coefficient is a tensor because of the 3-D nature of heat transfer.

$$\bar{k}_{dis} = \begin{bmatrix} k_{dis,xx} & k_{dis,xy} & k_{dis,xz} \\ k_{dis,yx} & k_{dis,yy} & k_{dis,yz} \\ k_{dis,zx} & k_{dis,zy} & k_{dis,zz} \end{bmatrix} \quad (2.55)$$

By substituting Eq. (2.54) into Eq. (2.51) and neglecting the tortuosity term, the macroscopic energy equation takes the new form presented by Eq. (2.56).

$$(\rho c_p)_e \frac{\partial \langle T \rangle}{\partial t} + \rho_f c_{pf} \langle \bar{u} \rangle \cdot \nabla \langle T \rangle = \bar{k}_{eff} \nabla^2 \langle T \rangle \quad (2.56)$$

where  $k_{\text{eff}}$  is the effective thermal conductivity which is the summation of the equivalent thermal conductivity of the porous continuum domain and the thermal dispersion coefficient.

$$\bar{k}_{\text{eff}} = k_e + \bar{k}_{\text{dis}} = k_e + \begin{bmatrix} k_{\text{dis},xx} & k_{\text{dis},xy} & k_{\text{dis},xz} \\ k_{\text{dis},yx} & k_{\text{dis},yy} & k_{\text{dis},yz} \\ k_{\text{dis},zx} & k_{\text{dis},zy} & k_{\text{dis},zz} \end{bmatrix} = \begin{bmatrix} k_{\text{eff},xx} & k_{\text{eff},xy} & k_{\text{eff},xz} \\ k_{\text{eff},yx} & k_{\text{eff},yy} & k_{\text{eff},yz} \\ k_{\text{eff},zx} & k_{\text{eff},zy} & k_{\text{eff},zz} \end{bmatrix} \quad (2.57)$$

## 2.7. Equivalent Thermal Conductivity Models

It was mentioned in the previous section that the equivalent thermal conductivity of a porous medium can be found by using Eq. (2.53). Although the equation directly emerges as a result of the volume averaging method and the summation of two macroscopic energy equations under the local thermal equilibrium assumption, some researchers proposed that this equation is not proper for the determination of the equivalent thermal conductivity of porous media. That's why; several methods were proposed in literature for the determination of equivalent thermal conductivity of porous media (Hsu et al. 1994, Cheng et al. 1999, Chen and Peterson 2006, Kandula 2011). The thermal conductivity value of Eq. (2.53) relates to the thermal resistance of two medium (fluid and solid) in parallel connection (Nield and Bejan 2006). If a porous medium has the structure that shows the series connection characteristics in which the heat flows through both solid and fluid phases, Eq. (2.58), which is the weighted harmonic mean of the two thermal conductivities, can be used to find more accurate values for the equivalent thermal conductivity.

$$\frac{1}{k_e} = \frac{1-\varepsilon}{k_s} + \frac{\varepsilon}{k_f} \quad (2.58)$$

Eqs. (2.53) and (2.58) are the limiting models of the equivalent thermal conductivity that shows the upper and lower limits for equivalent thermal conductivity, respectively. Nield and Bejan also suggested that for practical purposes, the weighted geometric mean of two thermal conductivities (see Eq. (2.59)) gives a good estimate for

the equivalent thermal conductivity. The same equivalent thermal conductivity equation was used in many reported studies and found that it yields accurate results (Chua et al. 2004, Demir et al. 2009).

$$k_e = k_s^{1-\varepsilon} k_f^\varepsilon \quad (2.59)$$

## CHAPTER 3

### LITERATURE REVIEW

In this chapter, the literature review on the determination of the macroscopic transport properties of porous media is presented. The macroscopic transport properties such as permeability, interfacial convective heat transfer coefficient and thermal dispersion can be obtained theoretically and/or experimentally. Both theoretical and experimental studies on determination of the permeability, Kozeny constant, interfacial heat transfer and thermal dispersion coefficients are reviewed. For all studies reviewed in this chapter, the aim of studies and assumptions made in the studies are briefly explained. The correlations proposed by some of the researchers are presented. The tables are constructed to show the theoretical and experimental parameters of the studies. It should be noted that the studies on the pore scale analysis of heat and fluid flow in packed beds with random (disordered) particles can be found in the literature as well as studies with periodical porous media.

Firstly, the literature review on the determination of permeability and Kozeny constant is presented. Numerical and experimental studies on the determination of permeability and Kozeny constant are presented in two subsections. The literature studies on the interfacial convective heat transfer are reviewed in Section 3.2. Theoretical studies are summarized in a Table with considered porous media, range of the studied parameters and the proposed Nusselt number correlations. Another table is also prepared to show the experimental studies on the determination of interfacial convective heat transfer coefficient. Experimental setups and conditions are presented for the reviewed studies.

Finally, the theoretical and experimental studies on the determination of thermal dispersion are reviewed. A table is included to present the considered porous media, range of the studied parameters and the obtained correlations for the determination of thermal dispersion, theoretically.

In the last section, experimental approaches for the determination of the effective thermal conductivity, which directly relates to thermal dispersion via Eq.

(2.57), are explained and the reported experimental studies are also presented for each method, separately. Based on the thermal boundary condition and heat source type, each method is also classified into subgroups. These subgroups are explained in the related sections in detail as well. The experimental parameters used for the determination of thermal dispersion are summarized in tables.

### **3.1. Literature Review on Permeability and Kozeny Constant**

In this section, the literature studies on determination of permeability and Kozeny constant are reviewed. These two parameters are related to each other since Kozeny constant is used to determine the permeability by using Kozeny-Carman equation. Firstly, the theoretical studies on the determination of permeability and Kozeny constant are explained in detail. One of the fundamental studies on theoretical determination of Kozeny constant was performed by Happel and Brenner (Happel and Brenner 1986). They found Kozeny constant for two porous media consisting of spheres and cylinders for wide range of porosity. Table 3.1 shows the change of Kozeny constant with porosity for different flow types. As can be seen, Kozeny constant value increases with porosity. Furthermore, Figure 3.1 shows the variation of Kozeny constant with porosity according to different researchers. The value of Kozeny constant differs considerably with the structure of porous media and employed model.

Based on the performed literature review, two tables are provided to summarize the theoretical studies (Tables 3.2 and 3.3). Table 3.2 is presented to show the porous media structures used in the numerical studies for determination of permeability, the considered porosity ranges. In some of these studies, a limit Reynolds number for validation of Darcy's Law was proposed. Table 3.3 shows the considered porous media for determination of Kozeny constant with the proposed values or correlations.

Finally, the literature review on the determination of permeability and Kozeny constant by employing experimental methods is presented. Table 3.4 shows the schematic views of experimental setups along with the experiment conditions for determination of permeability. Table 3.5 presents the summary of literature on the experimental determination of Kozeny constant. In this table, the reported Kozeny constant values and proposed correlations with figure of experimental setup and conditions are given.

### **3.1.1. Review of Theoretical Studies on Determination of Permeability and Kozeny Constant**

Based on Table 3.2 and 3.3 given in this section, brief information about each study is also presented in the following part. Petrasch et al. (Petrasch et al. 2008) applied a computer tomography based methodology to determine permeability, Forchheimer coefficient and interfacial heat transfer coefficient in reticulate porous ceramics. A 3-D digital representation of material sample was generated by X-ray tomographic scans and a square duct was assumed to encircle the sample medium. Finite volume direct pore-level numerical simulation was used with unstructured tetrahedral mesh discretization. Ansys-Cfx code was used for 3-D incompressible problem. Fluid flow equations were solved for Reynolds numbers between 0.2 and 200. A uniform inlet velocity and temperature profile and an outlet pressure were given as boundary conditions. Periodicity was not assumed. The non-dimensional pressure profile was averaged over the pore space in the cross-sections perpendicular to the main flow direction. The permeability and Forchheimer coefficients obtained from these solutions were compared to the values predicted by conduit flow model, hydraulic radius theory, drag models, fibrous bed correlations and local porosity theory based models. The mean dimensionless pressure gradient was found almost constant up to Reynolds number of 2 (Darcy regime), while the influence of the Forchheimer term increases at high Reynolds numbers.

Kuwahara et al. (Kuwahara et al. 1996) studied a macroscopically uniform flow passing through a lattice of square rods placed regularly in an infinite space. The macroscopic flow angle was varied every 5 degree to investigate geometrical effects. Due to periodicity of the model, only one structural unit was taken as calculation domain. A fully implicit scheme is employed with the hybrid differencing scheme for the advection terms. 45x45 non-uniform grid arrangement was used. Porosity was varied from 0.1 to 0.96. It is found that the macroscopic pressure drop for a fixed mass flow rate is insensitive to the macroscopic flow direction for low Reynolds flows, while it becomes sensitive to the flow direction as the Reynolds number grows high. The dimensionless pressure gradient stays constant for Reynolds numbers lower than 10, irrespective of the flow angle. A sharp increase of the pressure gradient was observed as Reynolds number goes beyond 10 where Forchheimer effect becomes effective.

Gamrat et al. (Gamrat et al. 2008) studied banks of square rods in aligned and staggered arrangement with porosity range of 0.44 to 0.98. Periodicity was assumed and a single structural cell was taken as calculation domain. Reynolds numbers between 0.05 and 40 were considered. FLUENT was used to solve the equations. Darcy's Law was used to estimate permeability as a function of Reynolds number. A constant value of permeability was found for single porosity value and it was said that the permeability was generally higher for the aligned arrangement for the same porosity value. The variation of Forchheimer coefficient with porosity was investigated. It is found that the Forchheimer coefficient slightly increased when the porosity was decreased for both arrangements. The inertia effects were found to be more pronounced for the staggered arrangement.

Lopez Penha et al. (Lopez Penha et al. 2011) studied an array of staggered square rods in an infinite space. The dependence of permeability on the Reynolds number, porosity and the flow direction was investigated. Reynolds numbers from 1 to 600 and porosities from 0.25 to 0.75 were considered. The anisotropy of the apparent permeability was investigated by considering flow along the three coordinate axes. A parameter study was performed for the staggered arrangement of the rods to comprehend the relationship of the apparent permeability and the microscopic fluid flow. The effect of solid particles on the fluid flow was modeled using a source term in the momentum equation. It was confirmed that the Forchheimer extended Darcy's Law is valid for predicting macroscopically steady and uniform flow through the staggered arrangement.

Teruel and Rizwan-uddin (Teruel and Rizwan-uddin 2009) studied a representative elementary volume of a porous medium containing square cylinders of staggered arrangement. Reynolds numbers between  $10^{-3}$  and  $10^5$  were considered and porosities between 0.05 and 0.95 were simulated for each Reynolds number. Solutions for Reynolds numbers below 200 were obtained by solving 2-D Navier-Stokes equations numerically. Reynolds averaged Navier-Stokes equations were used to examine the turbulent regime. The Forchheimer coefficient was found to be weakly dependent on the Reynolds number and strongly dependent on the porosity if the flow is fully turbulent. The variation of permeability with porosity was investigated and the comparison with Carman- Kozeny equation was made. Additionally, the value of Kozeny constant was proposed as 8.1875. It was mentioned that the numerical results were align with the predicted values by using Kozeny-Carman equation for low

porosities. However, for high porosities they observed that the numerically computed permeability values become different from the values that predicted by Kozeny-Carman equation. The numerically obtained permeability values became lower. Hence, it was agreed that the Kozeny constant should be porosity dependent. On the other hand, they said that the proposed Kozeny constant value could be used for porosities lower than 0.95 with some error.

Yazdchi et al. (Yazdchi et al. 2011) studied the microstructure of fibrous porous media to obtain the macroscopic permeability. A finite element based model for viscous, incompressible flow through a regular array of cylinders was employed with ANSYS. At the inlet and outlet of the REV pressure was defined and at the top and bottom periodic boundary condition was set. The effect of porosity was studied. Also particle shape (with using elliptic cylinders instead of circle ones), orientation and unit cell staggered angle were varied. The results were compared with the Carman-Kozeny equation and the Kozeny factor dependence on the microstructural parameters. It was found that at high porosities the shape of particles did not affect much the normalized permeability, but at low porosities the effect was more pronounced. It was observed that the circles had the lowest and horizontal ellipses the highest normalized permeability. It was said that the permeability increases with increasing aspect ratio until it reached the permeability of slab flow. Additionally, some literature correlations relating permeability with porosity were summarized in this study.

Nakayama et al. (Nakayama et al. 2002) studied 2-D square rods placed in an infinite medium. Anisotropy was created by varying the vertical distance between rods, i.e. the structural unit dimensions were changed. Structural unit height to length ratio of 1, 3/2 and 2 were examined. Periodic boundary condition was used at the inlet and outlet of the structural unit. The Reynolds number range was between 1 and 600. It was said that the presence of the anisotropy in the structure nearly halves the permeability for the fixed porosity and rod size. The mean Forchheimer coefficient was found to be fairly insensitive to the degree of the anisotropy in the structure.

Papathanasiou et al. (Papathanasiou et al. 2001) studied square and hexagonal arrays of 2-D cylinders. Both uniform size cylinders and varying size cylinders were considered. The porosity range was from 0.3 to 0.6. The Reynolds numbers lower than 160 were considered. The results were compared with the predictions of Ergun and Forchheimer equations. It was observed that in the limit of creeping flow ( $Re < 1$ ) the Forchheimer equation was in excellent agreement with the results of numerical



computations. The Forchheimer equation was found to be accurately describing the parameters when the Forchheimer coefficient was taken a value as a function of porosity.

Tamayol and Bahrami (Tamayol and Bahrami 2009) investigated the permeability of ordered porous media analytically. Both normal flow and parallel flow were examined. A repeated structural unit was considered. Triangular, square and hexagonal arrays of cylinders were considered. The effects of unit cell aspect ratio and fibers diameter on the permeability were also investigated. It was found that, in case of rectangular fibers arrangement, the permeability is a function of geometrical parameters such as porosity, fiber diameter and unit cell aspect ratio. It is claimed that the normal permeability decreases with increasing aspect ratio while the parallel permeability remains constant. It was also found that the normal and parallel permeability values are functions of square of fiber diameter.

Liu et al. (Liu et al. 2009) studied the equivalent permeability of fractured porous media. A mathematical model which consisted of square blocks placed in an array with vertical and horizontal fractures between the blocks was proposed. The Brinkman extended Darcy's equation was used to analyze the flow. Horizontal flow was assumed in a structural unit with periodic boundary conditions. It was found that the model was valid for all macroscopic flow directions. The numerical solutions of microscopic equations were used to examine the analytical expression for the permeability and 2-D mathematical model was extended to 3D in which cubic blocks were placed in a cubic arrangement. The expressions obtained for 2-D and 3-D permeabilities were found to agree well with results in the literature.

Sahraoui and Kaviany (Sahraoui and Kaviany 1992) investigated the hydrodynamic boundary condition at the solid-fluid interface of a porous media insisting 2-D cylinders. Both slip and no-slip boundary conditions were examined. The study was performed for different flow directions, porosity, Reynolds number and particle arrangements. Permeability values as a function of distance from the interface were calculated. It was found that the lowest permeability values were at the interfaces while with increasing distance permeability becomes constant. Different variations of permeability were found at the neighborhood of the interface, depending on porosity.

Saada et al. (Saada et al. 2006) studied microscopic flow in a periodic structure consisting square and plus shaped rods. Both inline and staggered arrangements were considered. Dimensionless forms of governing equations were solved. Porosity range

was chosen between 0.1 and 0.9 while Reynolds numbers lower than 150 were considered. The Forchheimer-extended Darcy's Law was used to obtain permeability and Forchheimer coefficient with calculated macroscopic pressure loss. Dimensionless pressure drop values were equal to a constant for  $Re$  below 10 and they were increased for  $Re > 10$ . Change of dimensionless permeability ( $K/H^2$ ) with porosity was found in good agreement with Sahraoui and Kaviany (Sahraoui and Kaviany 1992) whereas some difference from Ergun's (Ergun 1952) values was found for high porosities. Forchheimer coefficient was found varying inversely proportional with the porosity. This coefficient became nearly constant for certain  $Re$  and it was found that the limiting value was in good agreement with Ergun's value (Ergun 1952).

Alshare et al. (Alshare et al. 2010) studied laminar steady and unsteady fluid flow and heat transfer for a periodic array of square rods. The calculations were made for different structural unit aspect ratios. Finite volume approach was used with SIMPLER algorithm. Macroscopic flow directions were changed from  $0^\circ$  to  $90^\circ$ . Reynolds numbers between 1 and 1000 were considered. The variations of pressure gradient, permeability and Forchheimer coefficient with flow angle were analyzed. It was found that the permeability of the isotropic porous medium is uniform, independent of the flow angle; however, the permeability varies linearly between two principal permeabilities for the anisotropic medium. It was also found that the permeability decreases with increasing solid volume fraction. It was shown that the apparent permeability has a maximum value along the principal axes and decreases with either increasing flow angle or increasing  $Re$ .

Yu (Yu 2008) reviewed the theories, methods, mathematical models, achievements and open questions in the field of the flow through fractal porous media by referencing numerous papers in this area. Some of the literature models with the modifications to Kozeny-Carman equation were summarized in this study. Based on the theoretical base for fractal analysis of flow in porous media, the flow resistance, permeabilities for both Newtonian and non-Newtonian flows, and Kozeny-Carman equation, its modifications and Kozeny constants were reviewed and discussed. It was concluded that the fractal geometry and technique may be used to analyze the flow in fractal porous media and determine the transport properties.

Wu and Yu (Wu and Yu 2007) proposed a fractal model for resistance of flow through the porous media. The model was expressed as a function of the pore-throat ratio, porosity, the properties of fluid, the pore/capillary and the particle sizes, Reynolds

number and the fractal dimensions of porous media. They stated that there is no empirical constant in their model and the model was constructed with parameters that have clear physical meaning. The model was found to be in good agreement with the experimental results. It was cautioned that the correct determination of the geometrical parameters included into the the fractal model presented in their study might be critical for the accuracy of the model.

Xu and Yu (Xu and Yu 2008) derived an analytical expression for the permeability in the homogeneous porous media based on the fractal characters of porous media and the capillary model. The proposed model was expressed as a function of the fractal dimensions, porosity and the maximum pore size. Linear scaling law between the dimensionless permeability and porosity was found. A correlation that relates permeability with porosity and the geometrical dimensions of fractal medium was proposed. It was found that the model is more effective in determining the permeability than the traditional methods and models. A comparative graphics (Figure 3.1) showing the variation of Kozeny constant with porosity obtained by different researchers was presented. They mentioned that Carman reported the value as  $4.8 \pm 0.3$  for uniform spheres in his experimental study. It was mentioned that the Kozeny constant is actually not a constant and depends strongly on porosity and the microstructures of pores and capillaries. The analytical Kozeny-Carman constant was found with the assumption of square geometrical model. The proposed Kozeny constant was expressed based on porosity and fractal dimensions.

Happel and Brenner (Happel and Brenner 1986) made a theoretical study with different flows and particle arrangements. Flow parallel to cylinders, flow perpendicular to cylinders, flow through random orientation of cylinders and flow through spheres were studied. The proposed results of Happel and Brenner indicate that for the porosities between 0.4 and 0.7, Kozeny constant was found between 4.5 and 5.8 for both cylinders and spheres. But at higher porosities, Kozeny constant increases sharply with porosity (Table 3.1). They proposed a relation for the determination of Kozeny constant for parallel flow along the cylinders.

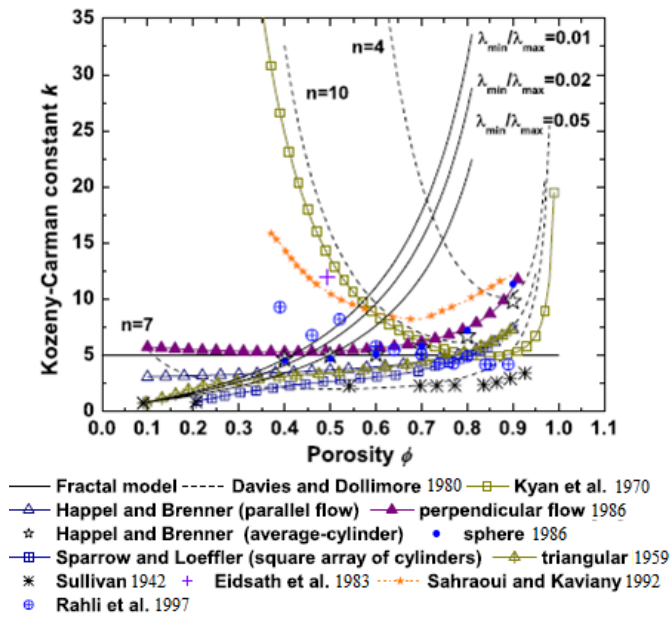


Figure 3.1. Kozeny constant comparison between some studies (Xu and Yu 2008)

Table 3.1. Kozeny constant values found by Happel and Brenner (Happel and Brenner 1986)

$\varepsilon$	Flow parallel to cylinders	Flow perpendicular to cylinders	Flow through random cylinders	Flow through spheres
0.4	3.44	5.28	4.66	4.54
0.5	3.67	5.38	4.97	4.74
0.6	3.96	5.62	5.07	5.11
0.7	4.42	6.19	5.60	5.79
0.8	5.23	7.46	6.72	7.22
0.9	7.31	11.03	9.79	11.34
0.99	31.1	53.83	46.25	71.63

Davies and Dollimore (Davies and Dollimore 1980) investigated the variation of Kozeny constant with porosity under sedimentation conditions, theoretically. Additionally, the experimental data from the literature for silica gel-dry xylene, emery powder-diethyl phthalate, glass-aqueous  $ZnSO_4$ , tapioca-hydrocarbon oil, kaolinite-water couples were analyzed in the study. It was observed that the Kozeny constant is different from its originally given value of 5 and also much greater than this value at high porosities. It was found that Kozeny constant does not monotonically change with porosity; it has a minimum for some value of porosity, which depends on the components of suspension. An equation which relates Kozeny constant with porosity was proposed.

Eidsath et al. (Eidsath et al. 1983) predicted Kozeny constant for various arrangements of square blocks and cylinders. In their numerical study, finite element method was used to solve the governing equations. The comparison between the experimental studies in the literature was done for the pressure drop through the porous media. Kozeny constant was found as 6.3 for in-line arrangement of blocks with porosity of 0.37.

Kaviany (Kaviany 1995) presented the details of Kozeny-Carman theory and reviewed some of the literature studies on the determination of Kozeny constant. It was mentioned that the experimental Kozeny constant value of 5 is acceptable for porosities lower than 0.7; however, much larger values of Kozeny constant was obtained theoretically for larger porosities. The variation of Kozeny constant with porosity, obtained by different researchers was presented for cylindrical particles and for various flow arrangements. Sahraoui and Kaviany (Sahraoui and Kaviany 1992) observed that the local permeability near the interface could not be computed by the aid of Kozeny-Carman equation.

Nakayama et al. (Nakayama et al. 2007) theoretically studied the determination of the equivalent diameter and the Reynolds number related with this diameter to generalize the correlations of macroscopic transport parameters available in the literature for tube flows and cross flows over banks of cylinders. The Kozeny constant was given as 7.5 for the square cylinders in cross-flow, 9.5 for the cubes and 9 for the circular cylinders in cross-flow in their study.

Vidal et al. (Vidal et al. 2009) studied the flow through spherical particles and blocks. The highly polydispersed spherical particle packings were constructed with Monte-Carlo methods. The simulations were done with lattice-Boltzmann method. The experimental data were obtained by using the blocks made of calcium carbonate powders compressed at different levels. Porosity values between 0.2 and 0.75 were considered. It was observed that with increasing poly-dispersivity, the permeability values predicted by Kozeny-Carman equation became higher than the numerically obtained values. An expression which relates Kozeny constant with the size distribution and compression level was proposed and Kozeny constant varies between 4.9 and 7.1 for the considered porous media.

Koponen et al. (Koponen et al. 1997) studied a porous medium constructed with randomly placed identical obstacles (square or rectangular particles) with unrestricted overlap. Porosity range of 0.38 to 0.95 was considered. Kozeny-Carman permeability

equation was found to be valid within porosity range from 0.7 to 0.9. They made a modification to Kozeny-Carman equation such that the porosity was changed with effective porosity defined as the ratio of the volume of the conducting pores to the total volume. The effective porosity value was defined empirically, based on porosity and percolation threshold porosity. Kozeny constant values between 6.5 and 10.4 were found, numerically.

The change of Kozeny constant with porosity was also investigated by Heijs and Lowe (Heijs and Lowe 1995) for a random array of spheres and a clay soil. The numerical study was done by using lattice-Boltzmann method. The structure of the clay soil was obtained by tomography imaging. The porosity of the porous medium constructed with random spheres was chosen as 0.6. The comparison of the obtained results with the experimental studies was satisfactory. Kozeny-Carman equation was found to be less accurate for the determination of the permeability of the soil rather than the random spheres.

Karimian and Straatman (Karimian and Straatman 2008) numerically studied pressure drop and heat transfer through metal foam structure. Laminar, periodic fluid flow in idealized pore geometry for a wide range of geometry parameters was considered. The model developed for pressure drop was based on Kozeny-Carman theory. A modified-Kozeny constant was used in their developed numerical model and the variation of modified-Kozeny constant obtained in the study with porosity was found to be consistent with that reported in literature for other types of pore geometry. For high porosity values, modified- Kozeny constant was found increasing with increasing porosity.

Liu and Hwang (Liu and Hwang 2012) proposed a 3D finite element method for solving fluid flow through fibrous porous media. The applicability of Kozeny-Carman permeability equation for complex 3D structures was investigated. A representative volume element was used as computational domain for modeling the repeated microstructure. Kozeny constants for various structures such as cross-ply fibers, 3D non-woven fibers, woven fiber tows, cross-fly fiber tows, square and hexagonal blocks for porosities between 0.3 and 0.95 were found and graphically presented.

Plessis and Woudberg (Plessis and Woudberg 2008) analyzed flow through the cube blocks to investigate the applicability of Ergun's equation for the prediction of permeability. The Blake-Kozeny constant ( $36k_K$ ) values proposed in some literature studies were compared and it was observed that the model used in the study predicts a

sudden increase of Blake-Kozeny constant for porosities higher than 0.8 while many of the researchers gave constant values for all porosities. Porosity dependence of Kozeny's constant was studied for porosities between 0.3 and 0.7. It was found that for this porosity range the Kozeny constant was between 5, although a slight change was observed. The change of Kozeny constant with porosity for this range was found to be less dramatic than the change predicted by Happel and Brenner (Happel and Brenner 1986).

Drummond and Tahir (Drummond and Tahir 1984) theoretically solved the motion equations for triangular, square and hexagonal arrays of cylinders in parallel and perpendicular flow. After exhaustive analytical calculations some values of Kozeny constant were obtained for porosities between 0 and 1. With comparing the formula given by Happel and Brenner (Happel and Brenner 1986), it was observed that the Kozeny constant values were very close for the case of triangular arrangement while the increase rate of Kozeny constant with porosity decreases for square and hexagonal arrangements.

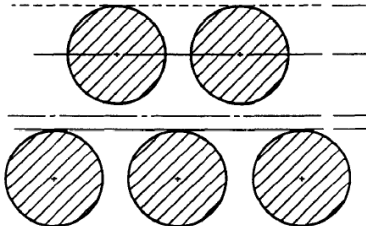
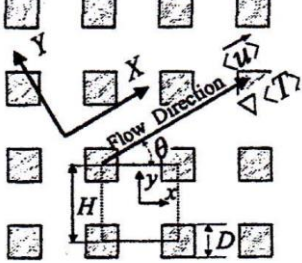
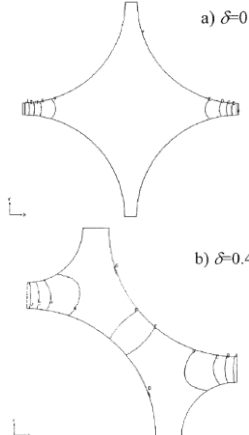
Singh and Mohanty (Singh and Mohanty 2000) used lattice-Boltzmann method to simulate 3D fluid flow in correlated porous media. The effects of porosity and spatial correlation on permeability were studied. Kozeny constant was expressed as a function of the correlation length. The modified-Kozeny constant was found to decrease with increasing correlation length for low correlation lengths; however, it was found to be nearly constant for higher correlation lengths.

Chen and Papathanasiou (Chen and Papathanasiou 2006) studied transverse flow through unidirectional arrays of randomly placed fibers, computationally. The porous media was created by using Monte Carlo procedure. Porosity range of 0.45 to 0.8 was considered and minimum inter-fiber distance was changed between 10 to 100 % of fiber radius. The study was performed in order to explain the effect of fiber spatial characteristic on the scatter of the Kozeny constant observed in real fiber beds in the experimental studies. It was found that for high porosities Kozeny constant was nearly constant for variable mean nearest neighbor inter-fiber spacing. With decreasing porosity, the decrease of Kozeny constant with increasing mean nearest neighbor inter-fiber spacing was observed. It was mentioned that the computationally found Kozeny constant values was consistent with the available experimental and numerical values in the literature. It was found that the increase of non-uniformity in fiber packing increases the Kozeny constant for the considered porosity range.

The summary of reviewed theoretical studies on the determination of the permeability is given in Table 3.2. In the table, the investigated porous media in the theoretical studies, considered porosity ranges and the obtained Reynolds number limit under which the Darcy's Law is valid are presented along with the employed Re definitions.

Additionally, Table 3.3 shows some details of the available theoretical studies on the determination of Kozeny constant. The considered porous media and proposed Kozeny constants and available correlations are displayed in the table.

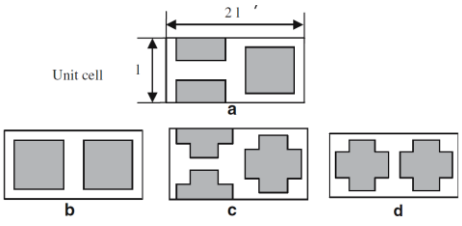
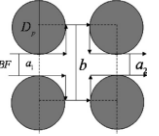
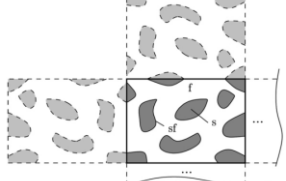
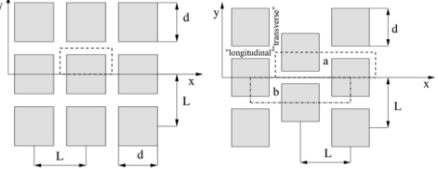
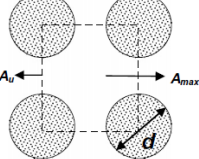
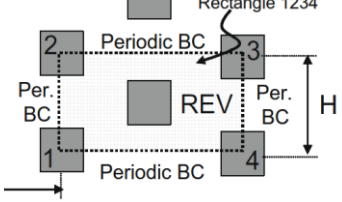
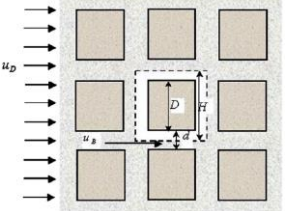
Table 3.2. Theoretical studies on the determination of permeability

Study	Investigated porous medium	Porosity range	Re limit for the validity of Darcy's Law	Definition of Reynolds number
Sahraoui and Kaviany 1992		0.48-0.8	3	$Re = \frac{\rho \langle u \rangle H}{\mu}$
Kuwahara et al. 1996		0.1-0.96	10	$Re = \frac{\rho \langle u \rangle H}{\mu}$
Papathanasiou et al. 2001		0.3-0.6	1	$Re_K = \frac{\rho \langle u \rangle K^{1/2}}{\mu}$

(Cont. on next page)



**Table 3.2. (cont.)**

<p>Nakayama et al. 2002</p>	<p>Same with Kuwahara et al.1996</p>	<p>0.75, 0.833, 0.875</p>	<p>10</p>	<p><math>Re = \frac{\rho\langle u \rangle H}{\mu}</math></p>
<p>Saada et al. 2006</p>		<p>0.1-0.9</p>	<p>10</p>	<p><math>Re = \frac{\rho\langle u \rangle H}{\mu}</math></p>
<p>Wu and Yu 2007</p>		<p>-</p>	<p>-</p>	<p>-</p>
<p>Petrasch et al. 2008</p>		<p>0.858</p>	<p>2</p>	<p><math>Re_{d_{nom}} = \frac{\rho\langle u \rangle d_{nom}}{\mu}</math></p>
<p>Gamrat et al. 2008</p>		<p>0.44- 0.98</p>	<p>1</p>	<p><math>Re_K = \frac{\rho\langle u \rangle K^{1/2}}{\mu}</math></p>
<p>Xu and Yu 2008</p>		<p>0.1-0.95</p>	<p>-</p>	<p>-</p>
<p>Teruel and Rizwan-uddin 2009</p>		<p>0.05- 0.95</p>	<p>10</p>	<p><math>Re = \frac{\rho\langle u \rangle H}{\mu}</math></p>
<p>Liu et al. 2009</p>		<p>0.08- 0.84</p>	<p>-</p>	<p><math>Re = \frac{\rho\langle u \rangle H}{\mu}</math></p>

(Cont. on next page)

**Table 3.2. (cont.)**

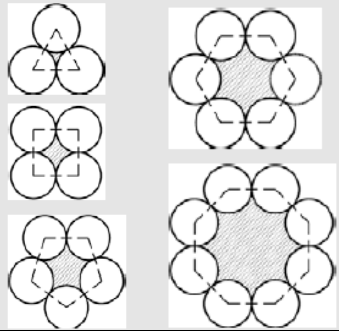
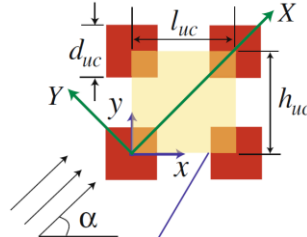
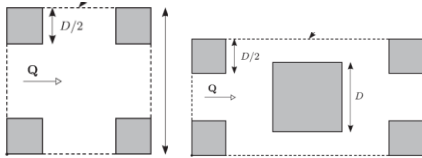
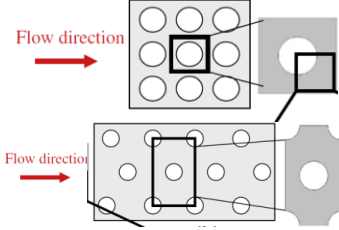
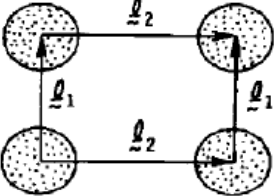

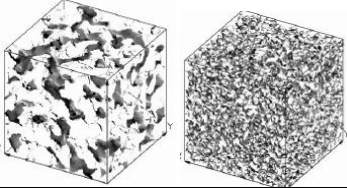
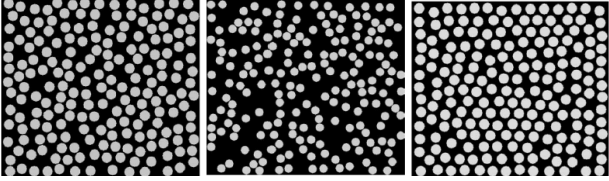
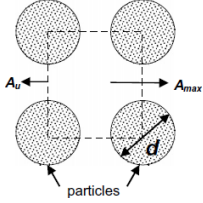
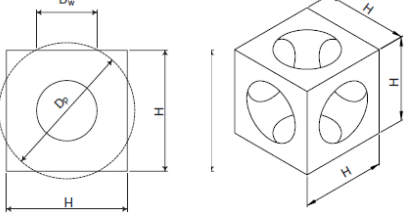
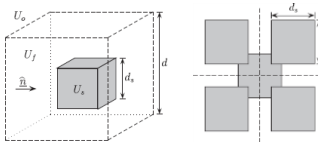
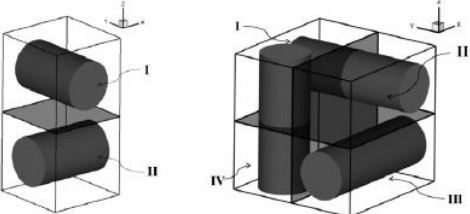
<p>Tamayol and Bahrami 2009</p>		<p>0.094- 0.512</p>	<p>-</p>	<p>-</p>
<p>Alshare et al. 2010</p>		<p>0.75- 0.875</p>	<p>10</p>	<p><math>Re = \frac{\rho\langle u\rangle H}{\mu}</math></p>
<p>Lopez Penha et al. 2011</p>		<p>0.25-0.75</p>	<p>10</p>	<p><math>Re = \frac{\rho\langle u\rangle H}{\mu}</math></p>
<p>Yazdchi et al. 2011</p>		<p>0.2-1</p>	<p>-</p>	<p>-</p>
<p>Notes:</p> <p><math>Re_{d_{nom}} = \frac{\rho\langle u\rangle d_{nom}}{\mu}</math>, <math>d_{nom}</math> is the nominal dimension of the porous medium</p> <p><math>Re = \frac{\rho\langle u\rangle H}{\mu}</math>, H is the dimension of the REV</p> <p><math>Re_K = \frac{\rho\langle u\rangle K^{1/2}}{\mu}</math></p>				

Table 3.3. Theoretical studies on the determination of Kozeny constant

Study	Porous medium	Proposed constant or relationship
Davies and Dullimore 1980	Beds of sedimenting spheres/fluidized beds	$k_K = 1/[2\varepsilon^{n-3}(1-\varepsilon)]$
Eidsath et al. 1983		Table presentation
Drummond and Tahir 1984	Parallel flow for triangular, square and hexagonal arrays of cylinders	Table presentation
Happel and Brenner 1986	Parallel flow along cylinders, Cross flow through cylinders, flow through random orientation of spheres, flow through spheres	<p>For parallel flow along cylinders:  <math>k_K = 2\varepsilon^3/(1-\varepsilon)/</math>  <math>\left(2\ln\left(\frac{1}{1-\varepsilon}\right) - 3 + 4(1-\varepsilon) - (1-\varepsilon)^2\right)</math></p> <p>For cross flow through cylinders:  <math>k_K = 2\varepsilon^3/(1-\varepsilon)/</math>  <math>\left(2\ln\left(\frac{1}{1-\varepsilon}\right) - (1 - (1-\varepsilon)^2)/(1 + (1-\varepsilon)^2)\right)</math></p> <p>Table presentations</p>
Heijs and Lowe 1995	Random spheres and soil sample	<p>For spheres of radius 2.5, <math>k_K = 2.79</math>                      radius 3.5, <math>k_K = 3.62</math>                      radius 4.5, <math>k_K = 3.80</math></p>
Koponen et al. 1997		$6.5 < k_K < 10.4$

(Cont. on next page)

**Table 3.3. (cont.)**

<p>Singh and Mohanty 2000</p>		<p>Graphical presentation</p>
<p>Chen and Papathanasiou 2006</p>		<p>Graphical presentations</p>
<p>Nakayama et al. 2007</p>	<p>Square rods, cubes, cylinders</p>	<p><math>k_K = 7.5</math> for square rods in cross flow  <math>k_K = 9.5</math> for cubes  <math>k_K = 9</math> for circular cylinders in cross flow</p>
<p>Xu and Yu 2008</p>		<p>Graphical presentation</p>
<p>Karimian and Straatman 2008</p>		<p>Graphical presentations</p>
<p>Plessis and Woudberg 2008</p>		<p>Graphical and table presentations</p>
<p>Teruel and Rizwan-uddin 2009</p>	<p>Cross flow, staggered square cylinders</p>	<p><math>kK = 8.1875</math> for <math>\varepsilon &lt; 55</math></p>
<p>Liu and Hwang 2012</p>		<p>Graphical presentations</p>

### **3.1.2. Review of Experimental Studies on Determination of Permeability and Kozeny Constant**

Based on the Tables 3.4 and 3.5 summarize the studies on experimental determination of permeability and Kozeny constant, following part is presented to give brief information about each study. Sano et al. (Sano et al. 2009) investigated the effective permeability of fluid saturated porous media consisting of small and large glass spherical particles. Water flowed upward through vertical packed bed filled with particles of different sizes. Experiments were conducted at Reynolds numbers of Darcy region. Pressure drops between inlet and outlet sections were measured for different flow rates. The results were compared with numerical results of Liu-Sano-Nakayama model (Liu et al. 2009) and a good agreement was found. Hence, the constructed mathematical model by the same researchers was confirmed by using experimental data and it was concluded that this theoretical model could be used estimate the permeability of porous media consisting of obstacles of different sizes.

Rodriguez et al. (Rodriguez et al. 2004) studied permeability and porosity relationship for glass and natural fiber mats. Glycerin and water mixture was used as fluid in the experimental setup. Difference of pressure was measured between the location where the fully-developed velocity profile had found and the front of the flow (at atmospheric pressure) near the outlet. The measurements were done at high pressure in order to have a constant permeability value (it was observed that at low pressures permeability increased with increased injection pressure for fiber mats). In order to obtain a unidirectional flow, fiber mats were placed in a prismatic bed. Darcy's law was used to find permeability. It was said that the same relationship for glass mats that was given in the literature was discovered for natural fiber mats. The experimental permeability values were fitted by the Kozeny-Carman equation with two fitting parameters: the Kozeny constant and the exponent of the porosity. The obtained permeability values for natural fiber mats were greater than the values of glass fiber mats for the same porosity.

Dias et al. (Dias et al. 2007) studied packed beds filled with glass spheres. Water-glycerol solution was used in the experiments. It was mentioned that, in the region of minimum porosity of particulate binary mixtures, heat transfer and permeability were found to be higher than packed beds with mono-sized packing with

the same small size particles. It was commented that it is possible to achieve a permeability enhancement with dense and loose packing. Permeability was said to be increased by a factor of two, if the size ratio between small and large spheres stays in the range 0.3-0.5. Dias et al. (Dias et al. 2008) additionally investigated the permeability of binary packings of spherical glass particles with different size ratios. A water-glycerol solution was used as fluid. The permeability was calculated using the measured flow velocity at fixed pressure drop in the laminar regime and the Reynolds number was less than 0.1. It was found that Kozeny constant is a function of particle size ratio. It is said that the permeability of binary mixtures modeled by Kozeny-Carman equation could be considerably different from the experimental values. It was concluded that to obtain accurate results for the permeability, tortuosity should change with a negative power of porosity and this power was defined as a function of the packing content and particle size ratio.

Han et al. (Han et al. 2000) was developed a new measurement technique for permeabilities of anisotropic fiber performs with high fiber content. In this method pressures at four different locations were measured and used in permeability calculations. The experimental device was able to measure permeability in three ways: parallel flow, radial flow and transverse flow; hence, the permeability values in different directions could be determined. It was said that, with using this technique, the permeability of an individual layer in a multi-layered preform could be determined using miniature pressure transducers. Fiber mats and silicone oil were used as packing particles and fluid.

Dukhan and Patel (Dukhan and Patel 2008) studied unidirectional air flow through several isotropic open-cell aluminum foam samples having different porosities and pore densities. Darcian velocities between 0.75 and 3 m/s were considered. Both permeability and Forchheimer coefficient were determined. It was proposed that Ergun's correlation is a good fit for the linear pressure drop as a function of the Darcian velocity, provided that an appropriate equivalent particle diameter is used. An appropriate particle diameter was investigated considering the viscous shear and the form drag. It was proposed that the equivalent particle diameter for foams is the reciprocal of the surface area density.

Paek et al. (Paek et al. 2000) investigated the permeability of aluminum foams. Porosities of the foams were between 0.89 and 0.96. The static pressure difference between the inlet and outlet of the test tube in which the foam placed was measured. It

was said that the permeability is substantially affected by porosity and cell size. It was observed that the permeability increases as cell size increases. It was also observed that the permeability first increases with increasing porosity; however, after reaching a maximum, it decreases with increasing porosity. An empirical correlation was proposed for the friction factor based on permeability and inertia effect.

Ergun (Ergun 1952) made an experimental study with a packed bed. The bed was randomly packed with spherical particles of different materials as glass, iron, lead and copper. Additionally, studies of other researchers with particle types of sphere, cylinder, Raschig ring and berl saddle were summarized and compared. Air, N<sub>2</sub>, CO<sub>2</sub>, H<sub>2</sub> and CH<sub>4</sub> were chosen as the flowing fluids. Different configurations of fluid and particles were experimented. The value of 150 is proposed for Blake-Kozeny constant which equals to  $36k_K$  for packed bed of spheres, which results in approximately 4.17 for  $k_K$ .

Pacella et. al. (Pacella et al. 2011) studied the permeability of hollow fiber bundles for porosities between 0.45 and 0.55, experimentally. Flow of glycerol solution through fabric fibers commonly used in the devices like blood oxygenators and artificial lungs were examined in the experiments. Different arrangements of fibers as parallel, perpendicular and angled stackings were employed. It was observed that the permeability values found from Kozeny-Carman equation with a constant Kozeny value might differ up to 50% from the experimentally predicted permeabilities. A linear relation between Kozeny constant and porosity was proposed for the determination of Blake-Kozeny constant which equals to  $36k_K$  for spheres.

Kyan et al. (Kyan et al. 1970) studied the flow of a single-phase fluid through a bed of random fibers. Experimentally, glass, nylon and Dacron fibers were used. Glycerol solutions and water were used. It was found that Kozeny constant increases rapidly for porosities higher than 0.9. A relation between Kozeny constant and porosity for the low velocity flows in fibrous beds was proposed. The constants in the proposed equation account for the effect of fiber deflection on pressure drop and the effect of stagnant space in a fibrous bed on flow. It was mentioned that the effects of these parameters have no parallels in a granular bed.

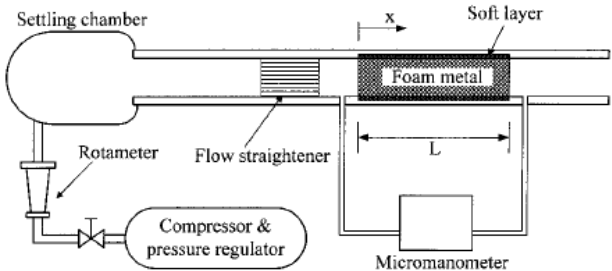
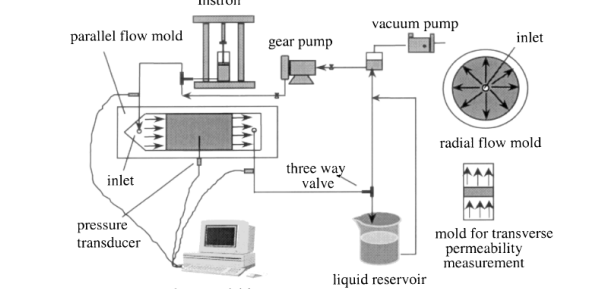
Li and Gu (Li and Gu 2005) studied fluid flow through fibrous and granular beds. A geometric method for the fibrous beds and an experimental method for the granular beds were used to determine the Kozeny constant, respectively. Polypropylene fibers and nylon fibers were used for the fibrous beds and polypropylene particles were

used for the granular beds. Crude oil, mineral oil and water were used a fluid. Both single and two phase flows were considered. The pressure drop through the bed was accurately predicted by employing Kozeny-Carman equation for the single phase. For the two-phase flow, a small increase of pressure drop was observed comparing with single-phase flow. They proposed the value of 12.81 for Kozeny constant.

Mathavan and Viraraghavan (Mathavan and Viraraghavan 1992) investigated the applicability of Kozeny-Carman equation for peat beds, experimentally. Standard mineral oil in water emulsion was used as fluid and six different flow rates were considered. Pressure drop through the bed was measured at 6 different locations. It was concluded that the average values obtained by using Kozeny-Carman permeability equation could be used to measure overall coalescence in a peat bed.

The experimental studies on the determination of permeability are summarized in Table 3.4. The constructed experimental setups and the experimental conditions are presented in this table. The experimental studies on the determination of Kozeny constant along with the employed setups and conditions are summarized in Table 3.5. The obtained Kozeny constant values or the proposed correlations are also presented in this table.

Table 3.4. Experimental studies on the determination of permeability

Study	Experimental setup	Experimental conditions
Paek et al. 2000		Solid: Aluminum foam Fluid: Air $0.89 \leq \varepsilon \leq 0.96$ Cell diameters: 0.65, 1.25, 2.5 mm
Han et al. 2000		Solid: Fiber mats Fluid: Silicone oil Flow rate: 7 l/min $\varepsilon = 0.45$

(Cont. on next page)



**Table 3.4. (cont.)**

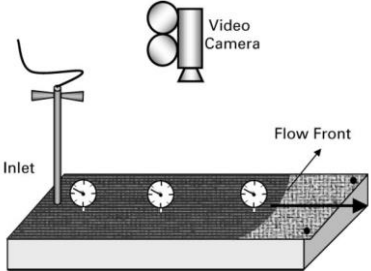
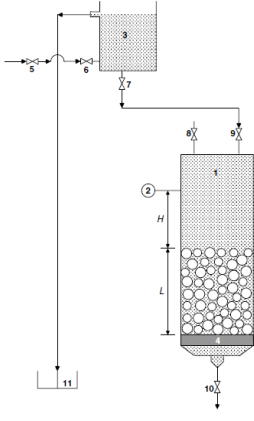
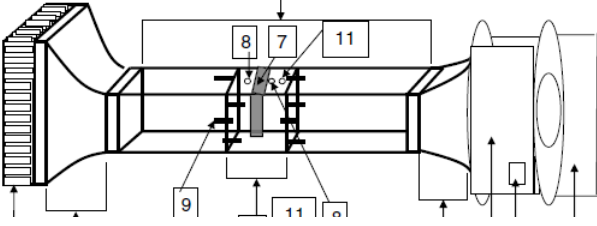
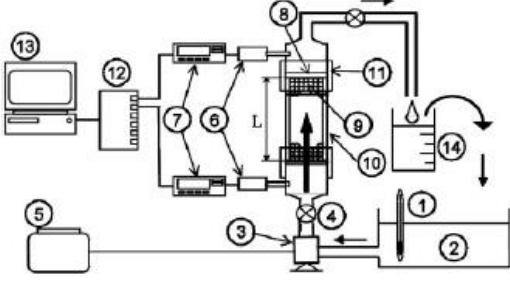
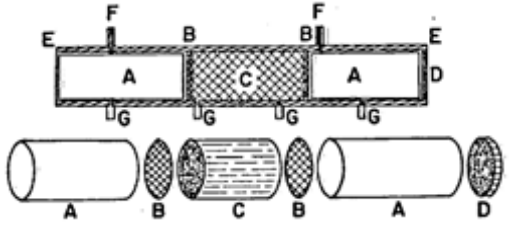
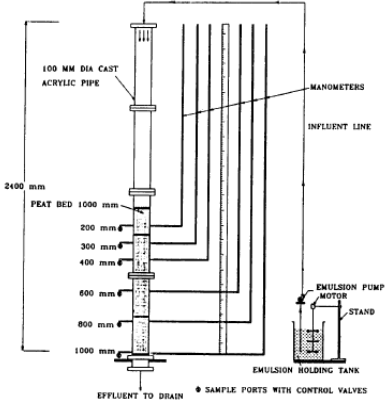
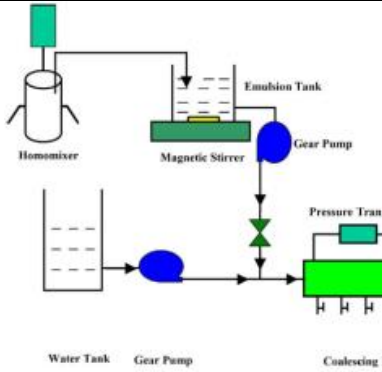
<p>Rodriguez et al. 2004</p>		<p>Solid: Glass and natural fiber mats Fluid: glycerin-water mixture Bed dimensions: <math>4 \times 200 \times 500 \text{ mm}^3</math> <math>0.45 \leq \varepsilon \leq 0.9</math></p>
<p>Dias et al. 2007</p>		<p>Solid: Soda-lime glass spheres Fluid: water Bed dimensions: <math>A = 0.08 \times 0.08 \text{ m}^2</math>, <math>L = 0.4 \text{ m}</math> Length of packing section: <math>0.1\text{-}0.15 \text{ m}</math> <math>d = 0.019, 0.115, 0.15, 0.3375, 0.875, 1.125, 2, 3, 4, 5, 6 \text{ mm}</math> <math>0.1 \leq \delta \leq 1.0</math> <math>0.3 \leq \varepsilon \leq 0.5</math></p>
<p>Dias et al. 2008</p>	<p>Same with [26]</p>	<p>Same with [26]</p>
<p>Dukhan and Patel 2008</p>		<p>Solid: Open-cell aluminum foams Fluid: Air <math>0.67 \leq \varepsilon \leq 0.92</math> <math>0.75 \text{ m/s} &lt; \langle u \rangle &lt; 3 \text{ m/s}</math></p>
<p>Sano et al. 2009</p>		<p>Solid: glass spheres of different sizes Fluid: water <math>D_i = 39 \text{ mm}</math> <math>d = 0.5, 1, 2.3, 5 \text{ mm}</math> <math>0.001 \text{ m/s} &lt; \langle u \rangle &lt; 0.01 \text{ m/s}</math> <math>0.4 \leq \varepsilon \leq 0.9</math></p>
<p>Notes: <math>D</math> is the bed (tube) diameter, <math>d</math> is the particle diameter, <math>u_D</math> is the Darcian velocity, <math>A</math> is the cross-sectional area of the bed, <math>L</math> is the length of the bed, <math>\delta</math> is the ratio of the diameters of the small and large particles.</p>		

Table 3.5. Experimental studies on the determination of Kozeny constant

Study	Experimental setup	Experimental Conditions and proposed Kozeny Constant
Ergun 1952	-	Spheres BK = 150
Kyan et al. 1970		Solid: Glass, Dacron an nylon fibers Fluid: Water and aqueous glycerol solution Fiber diameter: 8-28 $\mu\text{m}$  $k_K = \left[ 62.3 \left( \sqrt{\frac{2\pi}{1-\varepsilon}} - 2.5 \right)^2 (1-\varepsilon) + 107.4 \right] \times \varepsilon^3 / 16\varepsilon^6 (1-\varepsilon)^4$
Mathavan and Viraraghavan 1992		Solid: Horticultural peat beds Fluid: Oil in water emulsion kK = 3.4
Li and Gu 2005		Solid: Fibrous beds of polypropylene and nylon fibers and granular beds of polypropylene particles Fluid: Instow crude oil, mineral oil and tap water kK = 12.81
Vidal et al. 2009	-	Solid: Isometric natural ground calcium carbonate Fluid: Nitrogen 4.9 < k <sub>K</sub> < 7.1

(Cont. on next page)

**Table 3.5. (cont.)**

Pacella et. al. 2011		<p>Solid: Hollow fiber membranes of Celgard® microporous polypropylene oxygenator fibers          Fluid: Aqueous glycerol solution          Fiber diameters:  <math>D_o = 300 \mu\text{m}</math>, <math>D_i = 240 \mu\text{m}</math> &amp; <math>D_o = 193 \mu\text{m}</math>, <math>D_i = 139 \mu\text{m}</math>          Fiber density: 35, 54, 61 fibers/in.  <math>BK = 542\varepsilon - 128</math> (Blake-Kozeny constant which equals to <math>36k_K</math> for spheres)</p>
----------------------	--	--------------------------------------------------------------------------------------------------------------------------------------------------------------------------------------------------------------------------------------------------------------------------------------------------------------------------------------------------------------------------------------------------------------------------------------------------------------------------------------------------------

## 3.2. Literature Review on Interfacial Convective Heat Transfer Coefficient

In this section, the reported studies on the determination of interfacial convective heat transfer coefficient are reviewed. Firstly, the theoretical studies on the determination of interfacial convective heat transfer coefficient are reviewed in detail and then the experimental studies are explained. The reviewed studies are also summarized by tables. Table 3.6 shows the type of porous media, the range of Reynolds number and porosity, assumptions and conditions used in the performed theoretical studies. The resulting correlations for the interfacial Nusselt number are also presented in the same table. The experimental setups and the experimental parameters with the reported correlations are summarized in Table 3.7.

### 3.2.1. Review of Theoretical Studies on Determination of Interfacial Convective Heat Transfer Coefficient

Table 3.6 summaries the studies performed on theoretical determination of interfacial heat transfer coefficient for a porous medium. However, in order to have better idea about these studies, following part is also prepared to give brief information about each study. Petrasch et al. (Petrasch et al. 2008) employed direct pore-level numerical simulations to estimate the interfacial heat transfer coefficient in addition to permeability in their study. A Nusselt number correlation was derived and compared with experimental correlations. The temperature of the solid-fluid interface was

specified as constant and the square duct walls are assumed adiabatic. Computations were done for Prandtl numbers of 0.1, 0.5, 1 and 10. Viscous dissipation was neglected. The local Nusselt number was found dropping to an almost constant value near the inlet.

Gamrat et al. (Gamrat et al. 2008) performed a study to determine the interfacial Nusselt numbers of banks of square rods in inline and staggered arrangements for low Reynolds number flows ( $0.05 < Re < 40$ ). Both constant wall temperature and constant volumetric heat source were considered as thermal boundary conditions. Peclet numbers between 0.01 and 1000 and Prandtl numbers between 1 and 100 were considered. For constant wall temperature boundary condition, continuously decreasing difference between the fluid and the wall temperature along the system was created some computational difficulties and low Peclet numbers could not be investigated. In the case of uniform volumetric source heating, positive linear temperature gradient was created in the flow direction. It was shown that the heat transfer in the array of rods was insensitive to thermal boundary condition at the interface for the highest values of Reynolds and Prandtl numbers and porosity. It was observed that the Nusselt number was more influenced by the enhanced convective effect for the staggered arrangement. It was found that the heat transfer performance was slightly higher for the staggered arrangement, especially for small porosity values. Nusselt correlations were suggested for the aligned and staggered arrangements. It was concluded that the thermal boundary condition used for the solid phase affects the heat transfer between the solid and fluid phases in the thermal non-equilibrium condition.

Nakayama et al. (Nakayama et al. 2002) studied the interfacial heat transfer coefficient in their previously explained study in Section 3.1.1. In the heat transfer part of their study, a constant temperature which was different than the temperature of the flowing fluid was chosen for the temperature of the rods. Periodic boundary conditions were used at the inlet and outlet boundaries. It was observed that for the flow in the longitudinal direction, the interfacial Nusselt number does not change very much with Reynolds number; however, a slight decrease was seen near  $Re = 10$ . A correlation was proposed for the Nusselt number with the correlation coefficients that depend on the degree of the anisotropy of the medium and the flow direction. The coefficients decrease with increasing the degree of the anisotropy.

Kuwahara et al. (Kuwahara et al. 2001) studied square rods in staggered arrangement to determine the interfacial convective heat transfer coefficient. All rods were taken isothermal and maintained at a constant temperature which was different

than the mean temperature of the fluid. Due to the periodicity of the problem, a single structural unit was taken into consideration. The Reynolds number was varied from 0.01 to 1000 and the porosity from 0.36 to 0.96. Prandtl number was varied from 0.01 to 100. Computations were made to obtain a correlation for interfacial Nusselt number for wide range of porosities. It was mentioned that the predictions of the correlation was consistent with the experimental data in the literature.

Yang et al. (Yang et al. 2010) studied ordered packed beds with ellipsoidal or non-uniform spherical particles. A rectangular channel with large number of particles was considered. 3-D Navier-Stokes equations and RNG  $k-\epsilon$  turbulence model with scalable wall function were used. The channel walls were kept adiabatic and the temperature of particle surfaces was set constant. A representative packed channel composed of 8 packed cells was chosen as the computational domain. 6 different kinds of packed cells with three kinds of packing forms (simple cubic, body center cubic and face center cubic) and 3 types of particle shapes (sphere, flat ellipsoidal and long ellipsoidal) were used in computations. Also both uniform and non-uniform size spherical particles were used in body center packing. The effects of packing form and particle shape were examined. Comparison between the flow and heat transfer performances of uniform and non-uniform packed beds was made. It was found that, with proper selection of packing form and particle shape, the pressure drop can be decreased and the heat transfer performances can be improved compared to the random packed beds. It is mentioned that both packing form and particle shape had important effects on flow and heat transfer characteristics. With spherical particles, the overall heat transfer efficiency of simple cubic packing was the highest. With same packing form, long ellipsoidal particles were shown the best overall heat transfer performance. A Nusselt number correlation was proposed while the constants were found for different combinations.

Pathak and Ghiaasiaan (Pathak and Ghiaasiaan 2011) studied heat transfer coefficient during laminar pulsating flow through porous media. 2-D flow in periodic arrays of square cylinders was considered with sinusoidal time variation of flow as the inlet boundary condition. Porosities between 0.64 and 0.84, frequencies between 0 and 100 Hz and Reynolds numbers between 70 and 980 were studied. It was found that the analysis of a single structural unit was not sufficient for pulsating flow. Therefore, six structural units in the direction of flow were used. The solid-fluid interface temperature was held constant. It was observed that Nusselt number increases with increasing

Reynolds number and Womersley number (which shows the relation of pulsatile flow frequency with viscous effects) and it decreases with increasing porosity.

In their previously introduced study, Alshare et al. (Alshare et al. 2010) focused on the effects of the representative elementary volume (REV) aspect ratio, macroscopic flow direction and Reynolds number on the interfacial convective heat transfer coefficient for the inline arrangement of square rods. Constant heat flux at the interfaces was chosen as the temperature boundary condition. The variation of the interfacial Nusselt number with Reynolds number for different structural unit aspect ratios for periodic array of square rods was showed. It was observed that the interfacial convective heat transfer coefficient does not change much with Reynolds number for flow in the longitudinal direction while it increases with Reynolds number for flow in the direction with  $45^\circ$  angle. The heat transfer coefficients were found to have minimal values when the flow was issued along the principal axes, since the flow resembles channel flow.

Saito and de Lemos (Saito and de Lemos 2005) determined the interfacial heat transfer coefficient numerically for an infinite porous medium in which fully-developed flow condition prevails. Laminar flow conditions were considered for particle based Reynolds number range of 4 to 400 and porosity range of 0.44 to 0.9. An array of square rods in staggered arrangement was considered and the rods were assumed isothermal. The results found by Kuwahara et al. (Kuwahara et al. 2001) were confirmed. Saito and de Lemos (Saito and de Lemos 2006) additionally determined the interfacial convective heat transfer coefficient for the turbulent flow regime in the same porous medium. High and low Reynolds  $k$ - $\epsilon$  turbulence models were used in conjunction of a two-energy equation model. They proposed a correlation for the interfacial Nusselt number in terms of porosity, Reynolds and Prandtl numbers for the Reynolds numbers between  $10^4$  and  $10^7$ .

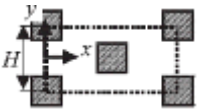
Lopez Penha et al. (Lopez Penha et al. 2012) studied fully-developed flow through the square rods for both inline and staggered arrangements to determine the macroscopic transport parameters. A constant volumetric heat generation in the rods was considered for the various solid-to-fluid thermal conductivity ratios and Reynolds numbers. Periodic representative elementary volumes of the porous media were considered and a finite volume based algorithm was used to solve the governing equations. Their results indicated that the interfacial Nusselt number is approximately constant for the solid-to-fluid thermal conductivity ratios higher than 100 while it varies

significantly for lower values. It was mentioned that as thermal conductivities approach the same order of magnitude, the temperature gradients across the interface diminish and consequently, Nu decreases with decreasing solid-to-fluid thermal conductivity ratio.

Teruel and Diaz (Teruel and Diaz 2013) simulated the fluid flow through square rods in staggered arrangement. Laminar, steady flow with Peclet numbers between 1 and  $10^3$  and porosities between 0.55 and 0.95 were considered. A single REV for the computational domain and  $h_{sf}$  was calculated as a function of the REV's location in the porous media to show its dependency on position. It was concluded that that single REV simulations were not sufficient to compute  $h_{sf}$ . A method that allows capturing the microscopic fluctuations of  $h_{sf}$  was proposed by employing single REV values.

Nakayama et al. (Nakayama et al. 2003) developed a numerical model for 3D fluid flow and heat transfer through a bank of long cylinders in yaw. Similar to some studies mentioned before, a single structural unit was chosen as the computational domain. It was shown that under macroscopically uniform flow, 3D governing equations could be reduced to quasi-3D forms, in which all derivatives associated with the axis of the cylinder can be either eliminated or replaced by other determinable expressions. The effects of porosity, degree of anisotropy, Reynolds number and macroscopic flow direction on the interfacial heat transfer coefficient were investigated. A correlation for the interfacial Nusselt number based on aforementioned parameters was proposed.

Table 3.6. Theoretical studies on the determination of interfacial convective heat transfer coefficient

Study	Porous Medium	Studied Parameters and Proposed Correlation
Kuwahara et al. 2001		$10^{-2} \leq Re \leq 10^3$ $10^{-2} \leq Pr \leq 10^2$ $0.36 \leq \varepsilon \leq 0.96$ $Nu_D = \left(1 + \frac{4(1-\varepsilon)}{\varepsilon}\right) + \frac{1}{2}(1-\varepsilon)^{1/2} Re_D^{0.6} Pr^{1/3}$

(Cont. on next page)

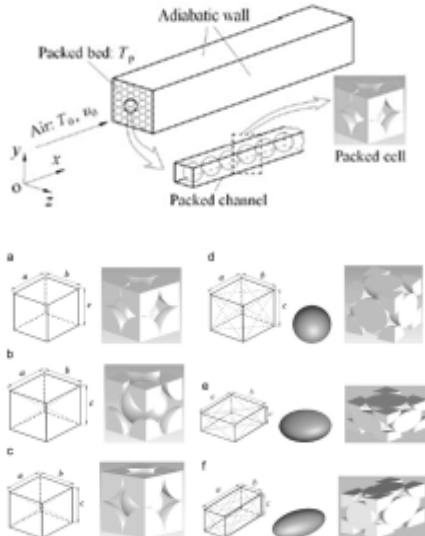
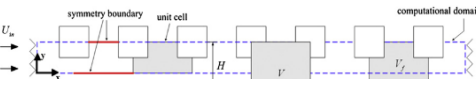
**Table 3.6. (cont.)**

Nakayama et al. 2002	Table 3.2	$10^{-2} \leq Re \leq 10^3$ $Pr = 1$ $\varepsilon = 0.75, 0.833, 0.875$  $Nu = c_{f1} \cos^2 \alpha + c_{f2} \sin^2 \alpha + d_{f1}^{0.3} Re^{0.6} Pr^{1/3}$  $c_{f1}, c_{f2}$ and $d_{f1}$ are coefficients that depend on porosity $\alpha$ is flow angle
Nakayama et al. 2003	Same with Kuwahara et al. 1996	$10^{-2} \leq Re \leq 6.103$ $\varepsilon = 0.75, 0.833$ and $0.875$  $Nu = \left( c_{f1}^{n_c} \cos^2 \alpha + c_{f2}^{n_c} \cos^2 \beta + c_{f3}^{n_c} \cos^2 \gamma \right)^{1/n_c} + d_{f1} \sin^{2/n_d} \gamma Re^{0.6} Pr^{1/3}$  All coefficients depend on porosity
Saito and Lemos de 2005	Same with Kuwahara et al. 2001	$4 \leq Re_D \leq 400$ $0.44 \leq \varepsilon \leq 0.9$ $Pr = 1$
Saito and de Lemos 2006	Same with Kuwahara et al. 2001	$10^4 \leq Re_D \leq 10^7$ $0.44 \leq \varepsilon \leq 0.9$ $Nu_D = 0.08 \left( \frac{Re_D}{\varepsilon} \right)^{0.8} Pr^{1/3}$  for $10^4 < \frac{Re_D}{\varepsilon} < 2 \cdot 10^7$
Gamrat et al. 2008	Table 3.2	$0.05 \leq Re_D \leq 40$ $1 \leq Pr \leq 100$ $0.44 \leq \varepsilon \leq 0.98$  For inline arrangement: $Nu_D = 3.02(1 - \varepsilon)^{0.278} \exp(2.54(1 - \varepsilon)) + (0.44(1 - \varepsilon) + 0.092) Re_D^{0.5} Pr^{0.2}$ For staggered arrangement: $Nu_D = 3.02(1 - \varepsilon)^{0.278} \exp(2.54(1 - \varepsilon)) + (1.093(1 - \varepsilon) + 0.357) Re_D^{0.5} Pr^{0.2}$
Petrasch et al. 2008	Table 3.2	$0.2 \leq Red_{nom} \leq 200$ $0.1 \leq Pr \leq 10$ $\varepsilon = 0.858$  $Nu_{d_{nom}} = 1.559 + 0.595 Re_{d_{nom}}^{0.5626} Pr^{0.472}$

(Cont. on next page)



**Table 3.6. (cont.)**

<p>Yang et al. 2010</p>		$0.281 \leq \varepsilon \leq 0.492$ $1 \leq Re \leq 5000$ $Pr = 0.7$ $Nu_{d_p} = a_1 + a_2 Pr^{1/3} Re^n \left( \frac{d_p}{d_h} \varepsilon \right)^n$ <p>a1, a2 and n are model constants that depend on porosity</p>
<p>Alshare et al. 2010</p>	<p>Table 3.2</p>	$1 \leq Re \leq 1000$ $\varepsilon = 0.75 \text{ and } 0.875$ <p>Graphical presentation</p>
<p>Pathak and Ghiaasiaan 2011</p>		$70 \leq Re \leq 980$ $0.64 \leq \varepsilon \leq 0.84$ $0 < f \leq 100 \text{ Hz}$ <p>For <math>W &lt; 2700</math></p> $Nu = 20.85 Re^{0.0873} (1 - \varepsilon)^{0.4014}$ $(\exp(-0.000045W) + 0.0001W)$ <p>For <math>W \geq 2700</math></p> $Nu = 20.999 Re^{0.14} (1 - \varepsilon)^{0.0189}$ $\cdot \exp(-0.00005W)$ $- 4.07 \ln(Re)$ $- (\varepsilon - 2.74)(\varepsilon + 1.47)$ <p>Where <math>W = \omega H^2 / \nu</math> and <math>\omega</math> is angular frequency.</p>
<p>Lopez Penha et al. 2012</p>	<p>Same with Lopez Penha 2011</p>	$0.01 \leq Re \leq 200$ $\varepsilon = 0.75$ $Pr = 1$ $1 \leq ks/kf \leq 104$ <p>Graphical presentation</p>
<p>Teruel and Diaz 2013</p>	<p>Same with Teruel and Riwanuddin 2009</p>	$1 \leq Pe \leq 103$ $0.55 \leq \varepsilon \leq 0.95$ <p>Graphical presentation</p>

### **3.2.2. Review of Experimental Studies on Determination of Interfacial Convective Heat Transfer Coefficient**

According to Table 3.7, the experimental studies for the determination of the interfacial convective heat transfer coefficient are summarized in this section. There is scarce number of experimental studies on the determination of interfacial heat transfer coefficient and available studies are explained in the following paragraphs.

Yang et al. (Yang et al. 2012) was made an experimental study for the validation of the previously made numerical computations (Yang et al. 2010). The interfacial heat transfer coefficient was determined. The effects of packing form and particle shape were investigated. Air was chosen as flowing fluid in the experimental setup. Glass ellipsoidal and uniform/non-uniform size steel spherical particles were used in the packed bed. Reynolds numbers higher than 100 were investigated. Before entering the bed air was heated. After the bed temperature had reached a certain value the heater was turned off and it was waited for packed bed to reach steady temperature. Then cold air was flowed through the bed and the temperature of the bed was cooled to ambient temperature. During the cooling of the bed, the experimental measurements were made. Volume flow rate of air, pressure difference across the test section and temperatures of air and particles were measured. In order to reduce wall effects, the heat transfer characteristics were only examined for the central packed channel. It was assumed that no local thermal equilibrium existed between fluid and particles and also the temperatures only changed along the flow direction and time. Measured temperatures were used in analytical solution to find heat transfer coefficient. Comparison between experimental and numerical results was made. It was found that the numerical model proposed in Yang et al. 2010 is sufficient for heat transfer predictions in ordered packings. But it was found that it might not be appropriate for the pressure drop estimations, especially for low porosity values. Also it was found that Wakao's equation might overpredict the Nusselt number for the ordered porous medium. It was mentioned that with simple cubic packing of ellipsoidal particles, the pressure drop can be greatly reduced and the heat transfer characteristics can be improved.

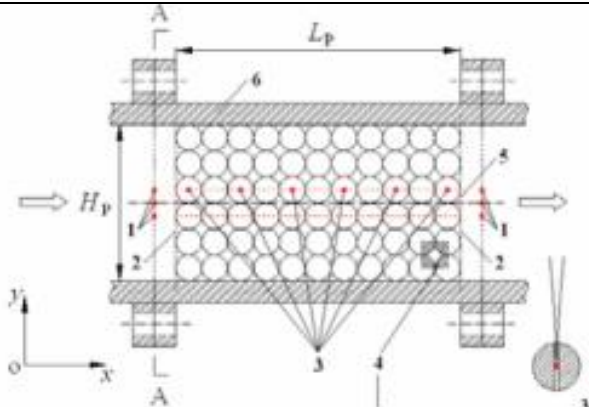
Saidi et al. (Saidi et al. 2006) investigated the heat transfer coefficient for a packed bed of shredded materials at low Peclet numbers. It was mentioned that the Nusselt number correlations derived for spherical particles overestimate the rate of heat

transfer in the packed beds with shredded materials. Both numerical simulations and experimental study were performed. The data obtained from experimental measurements were used in the numerical simulations and a power law formulation was applied. A correlation was proposed based on Peclet number.

Özdemir and Özgüç (Özdemir and Özgüç 1997) studied the hydrodynamic and heat transfer characteristics of a porous medium consisting of wire screen meshes. The convection heat transfer experiments for the determination of Nusselt number were performed for the uniform heat flux boundary condition. The variation of Nusselt number with Peclet and Darcy numbers was determined for both thermally developing and fully-developed flows and correlations were proposed for both flow types.

Schröder et al. (Schröder et al. 2006) studied the heating of the randomly packed beds. The packed bed was filled with slate particles and wooden cubes. Local measurements were done for particle and gas temperatures. A special arrangement of the test particles was used to exclude the effects of heat conduction. The variations of gas temperature and flow rate were taken into consideration and the heat transfer coefficient was determined by using the temperature measurements. It was observed that the increasing flow rate increases the heat transfer coefficient. The radiation heat transfer was taken into account numerically by solving the equations of a one-dimensional particle model and it was observed that under 500 °C, the influence of radiation is negligible.

Table 3.7. Experimental studies on the determination of interfacial convective heat transfer coefficient

Study	Experimental setup	Experimental Conditions
Yang et al. 2012		<p>Solid: Glass ellipsoidal or steel spherical particles (ordered)            Fluid: Air  <math>d_p = 9, 12 \text{ mm}</math>  <math>0.26 \leq \epsilon \leq 0.477</math>  <math>10^2 \leq Re_{dh/\phi} \leq 10^4</math></p>

(Cont. on next page)

**Table 3.7. (cont.)**

<p style="writing-mode: vertical-rl; transform: rotate(180deg);">Özdemir and Özgüç 1997</p>		<p>Solid: 20 wire screen meshes          Fluid: water  <math>\varepsilon = 0.732, 0.7832</math></p> <p>For fully-developed flow:  <math>Nu_L = 0.2211</math>  <math>\times (Pe_d \sqrt{Da})^{0.5992}</math>          for <math>10 \leq Pe_d \leq 50</math></p> <p>for thermally developing flow:  <math>Nu_x = 1.4842 Pe_d^{0.7884}</math>  <math>\times (x/L)^{-0.2751}</math>          for <math>10 \leq Pe_d \leq 50</math></p>
<p style="writing-mode: vertical-rl; transform: rotate(180deg);">Saidi et al. 2006</p>		<p>Solid: Shredded tobacco material          Fluid: Air  <math>\varepsilon = 0.8</math></p> <p><math>Nu_{d_p} = 0.015 + 0.11 Pe_{d_p}^{0.73}</math>          for <math>Pe_{d_p} &lt; 25</math></p>
<p style="writing-mode: vertical-rl; transform: rotate(180deg);">Schröder et al. 2006</p>		<p>Solid: Bed of slate particles and wooden cubes          Fluid: Nitrogen  <math>d_p = 9.5 \text{ mm (wood), } 5.7 \text{ mm (porous slate), } 6.995 \text{ mm (aluminum spheres)}</math></p>

### **3.3. Literature Review on Determination of Thermal Dispersion Coefficients**

In this section, the studies performed on the determination of the thermal dispersion in porous media are reviewed. There are two subsections containing the reviews of the theoretical and experimental studies. Theoretical studies are summarized in Table 3.8 with the available correlations for the determination of thermal dispersion. Additionally, the considered porous media and the ranges of parameters are provided in the same table. The experimental studies are reviewed in detail and also a classification of the experimental procedures for the determination of thermal dispersion is proposed. Based on this classification, the reviewed experimental studies are separated and the experimental procedures are explained for each branch of the classification. Several tables are provided to present the assumptions, experimental conditions, particle and bed properties and available correlations. Additionally, the considered Reynolds number ranges and the available correlations are compared in figures.

#### **3.3.1. Review of Theoretical Studies on Determination of Thermal Dispersion Coefficients**

Kuwahara et al. (Kuwahara et al. 1996) applied a macroscopically linear temperature gradient perpendicularly to the flow direction to obtain the transverse dispersion coefficient for the square rods in inline arrangement. Some details of this study are presented in Section 3.1.1. Reynolds numbers between  $10^{-2}$  and  $10^3$  and solid-to-fluid thermal conductivity ratios between 2 to 100 were considered. Prandtl number was taken as 0.71. It was found that the isotherms obtained at low Reynolds numbers show a typical pattern for the case of pure thermal conduction whereas for the high Reynolds number flows the temperature patterns become very complex as a result of thermal dispersion. Correlations for the determination of the transverse thermal dispersion coefficient were proposed. It was mentioned that the resulting correlation for high Peclet numbers is consistent with available experimental data.

Kuwahara and Nakayama (Kuwahara and Nakayama 1999) studied a macroscopically uniform flow passing through a lattice of regularly placed square rods in an infinite space. Macroscopically linear temperature gradient was applied in parallel

and perpendicular to the flow direction to obtain longitudinal and transverse thermal dispersion conductivities. The Reynolds number was varied from 0.01 to 1000, solid-to-fluid thermal conductivity ratio from 2 to 100 and the porosity from 0.1 to 0.96. Prandtl number was set to 0.71 and 10. The macroscopic flow angle was varied every 5 degree to investigate geometric effects on the dispersion coefficients. For the transverse dispersion conductivity above the correlations proposed in the study of Kuwahara et al. (Kuwahara et al. 1996) were mentioned confirmed. Correlations for the longitudinal dispersion conductivity were proposed. It was said that the longitudinal dispersion is substantially higher than the transverse dispersion. The predicted apparent conductivities were found in good agreement with experimental data. Later, Nakayama and Kuwahara (Nakayama and Kuwahara 2005) developed an algebraic model to determine thermal dispersion conductivity. The microscopic and macroscopic governing equations were used together to obtain a transport equation for the dispersion heat flux. With using definitions of permeability and Forchheimer coefficient in Ergun's equation, a relation was obtained for longitudinal thermal dispersion. It was mentioned that thermal dispersion in the longitudinal direction increases with square of Peclet number for the low Peclet numbers; however, it changes with Pe for high Pe range. It was said that the results of this algebraic relation for longitudinal thermal dispersion was in good agreement with previous numerical studies of these researchers and some other theoretical studies.

Yang and Nakayama (Yang and Nakayama 2010) investigated the effects of tortuosity and thermal dispersion on the effective thermal conductivity, analytically. A general expression for the equivalent thermal conductivity of porous medium was derived and this value was compared with numerical and experimental studies in the literature. Then using two energy equations for solid and fluid phases with volume averaging method, a general expression for the thermal dispersion was found. It was shown that the interfacial heat transfer between the solid and fluid phases and thermal dispersion were closely related. It was claimed that for small Peclet numbers longitudinal thermal dispersion was proportional with  $Pe^2$  and there was a transition zone between laminar and turbulent regimes where longitudinal thermal dispersion was proportional with  $Pe^{1.4}$ . Correlations were proposed for transverse and longitudinal thermal dispersion conductivities for laminar and turbulent regimes.

Jeong and Choi (Jeong and Choi 2011) investigated longitudinal thermal dispersion in 2D arrays of uniformly distributed circular and square cylinders and

uniformly distributed spheres and cubes by using lattice Boltzmann method. The effects of  $Re$ ,  $Pr$  and porosity were examined. Reynolds numbers between 0.1 and 100 and Prandtl numbers between 0.1 and 20 were considered. It was said that the in-line arrangement yielded higher dispersion than the staggered arrangement. It was also claimed that the dispersion depends more on the arrangement than the shape of particles. Thermal dispersion was found increasing with increasing Peclet number. New correlations were proposed for 2D and 3D cases.

Xu et al. (Xu et al. 2010) studied periodic array of parallel plates to determine the thermal dispersion, analytically. Three cases were considered as a) transient heat transfer due to an arbitrary initial temperature distribution within the fluid, b) steady heat transfer with constant heat flux on all plate surfaces, and c) steady heat transfer with constant wall temperatures. Steady-state laminar flow of an incompressible fluid was considered for all cases. For the first two cases thermal dispersion was found to change with  $Pe$  according to  $1+C'Pe$ , where coefficient  $C'$  is independent of  $Pe$ . For the last case  $C'$  is a function of  $Pe$ . It was explained that thermal dispersion is not a property of the porous medium depending only on pore structure, porosity and the underlying fluid flow. It was explained that the thermal dispersion can be influenced by the type of thermal setting imposed on the medium since the imposed heat source condition contributes the temperature non-uniformity in the channel. It was advised that thermal dispersion of a porous medium obtained using one type of thermal setting should be used carefully when the thermal boundary conditions are changed.

Pedras and de Lemos (Pedras and de Lemos 2008) studied the heat transfer in a periodic array of elliptic rods in an infinite porous medium. Two different solid-to-fluid thermal conductivity ratios were considered. Turbulence flow was assumed and a low  $Re$   $k-\varepsilon$  model was used. Both longitudinal and transverse thermal dispersion conductivities were computed. Temperature gradients were imposed by either using constant temperature at cell boundaries or constant heat flux at top and bottom boundaries. A highly non-uniform grid was used. Peclet numbers from 1 to 4000 and porosities from 0.6 to 0.9 were considered. It was claimed that the type of boundary condition has little influence on the longitudinal thermal dispersion value and only a slight effect on transverse thermal dispersion. Longitudinal dispersion was found to be less sensitive to the variations of porosity, conductivity ratio and porous structure. Some correlations were proposed.

Saada et al. (Saada et al. 2006) investigated thermal dispersion in a periodic structure consisting square and plus shaped rods in inline and staggered arrangements. Some details of this study are presented in Section 3.1.1. Local fluctuations of microscopic velocity and temperature were used to obtain thermal dispersion. Peclet numbers between 0.1 and 1000, and solid-fluid thermal conductivity ratios between 0.1 and 1000 were considered. It was said that depending on the nature of the porous medium, the thermal dispersion may have significant effect on heat transfer, especially in the longitudinal direction for a highly conducting fluid and certain values of Pe. Both transverse and longitudinal thermal dispersion conductivities were computed for various porosities, Reynolds and Peclet numbers and solid-to-fluid conductivity ratio values. It is found that for the same rod shape the longitudinal thermal dispersion was higher for inline arrangements while the transverse one is higher for the staggered arrangement.

Sahraoui and Kaviany (Sahraoui and Kaviany 1994) considered two-dimensional periodic arrangement of cylinders and determine the longitudinal and transverse total thermal diffusivities which includes both molecular diffusion and thermal dispersion coefficients by considering the slip and no-slip temperature boundary conditions. It was proposed that the ratio of total thermal diffusivity in the longitudinal direction to the thermal conductivity of the fluid change with the square of Peclet number for inline arrangement while for the staggered arrangement the ratio increases with Peclet number. It was also observed that the total thermal diffusivity is almost equal to the stagnant thermal conductivity of the porous medium and the thermal dispersion is negligible comparing with the stagnant thermal conductivity for low Peclet numbers.

Alshare et al. (Alshare et al. 2010) investigated the change of thermal dispersion in an array of square rods with inline arrangement by changing the representative elementary volume (REV) aspect ratio. Both transverse and longitudinal thermal dispersion conductivities were studied. It was found that the dispersion values are dependent on both Peclet number and flow angle. The thermal dispersion coefficient in the flow direction was found to be much larger than the thermal dispersion in the transverse direction to the flow. It was observed that the dispersion depends more on the arrangement than the shape of particles. The results for longitudinal thermal dispersion were found in good agreement with Sahraoui and Kaviany (Sahraoui and Kaviany 1994) and Saada et al. (Saada et al. 2006).



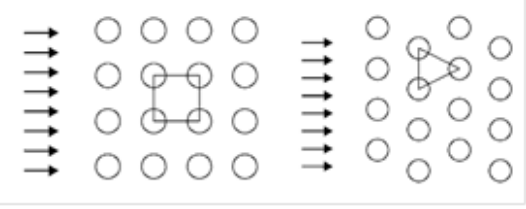
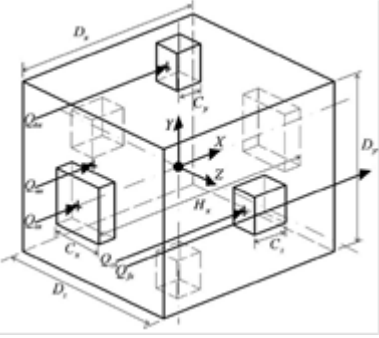
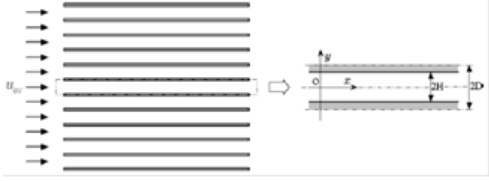
In the previously explained study of Pathak and Ghiaasiaan (Pathak and Ghiaasiaan 2011), the thermal dispersion during laminar pulsating flow through porous media was studied in addition to the interfacial heat transfer coefficient. Thermal dispersion was found to be strongly dependent on porosity, Reynolds number and flow pulsation frequency. The thermal dispersion conductivity was found to be much larger than the molecular thermal conductivity. It was observed that the thermal dispersion conductivity is a periodic function of time and the usefulness of the concept of thermal dispersion conductivity in pulsating flow is questionable. A correlation relating thermal dispersion with Re number, porosity and Womersley number ( $W = \omega L^2/\nu$ ) was proposed.

Table 3.8. Theoretical studies on the determination of thermal dispersion coefficients

Study	Porous Medium	Studied Parameters and Proposed Correlation
Sahraoui and Kaviany 1994	Same with Sahraoui and Kaviany 1992	$10^{-2} \leq Pe \leq 10^3$ $10^{-2} \leq k_s/k_f \leq 10^3$ $0.5 \leq \varepsilon \leq 0.95$
Kuwahara et al. 1996	Table 3.2	$10^{-2} \leq Re \leq 10^3$ $0.1 \leq \varepsilon \leq 0.96$ $Pr = 0.71$ $2 \leq k_s/k_f \leq 100$ $\frac{k_{dis,YY}}{k_f} = 0.022 \frac{Pe_D^{1.7}}{(1-\varepsilon)^{1/4}} \text{ for } Pe_D < 10$ $\frac{k_{dis,YY}}{k_f} = 0.052(1-\varepsilon)^{1/2} Pe_D \text{ for } Pe_D > 10$
Kuwahara and Nakayama 1999	Same with Kuwahara et al. 1996	<p>Same with Kuwahara et al. 1996</p> $\frac{k_{dis,XX}}{k_f} = 0.022 \frac{Pe_D^2}{(1-\varepsilon)} \text{ for } Pe_D < 10$ $\frac{k_{dis,XX}}{k_f} = 2.7 \frac{Pe_D}{\varepsilon^{1/2}} \text{ for } Pe_D > 10$

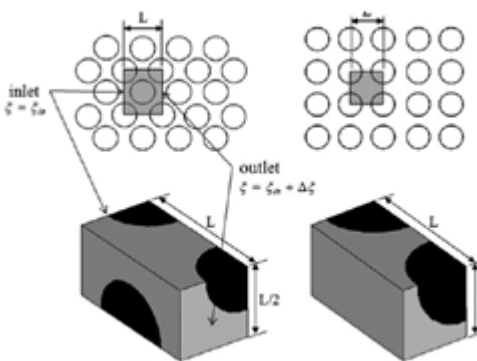
(Cont. on next page)

**Table 3.8. (cont.)**

<p>Nakayama and Kuwahara 2005</p>	<p>-</p>	$\frac{k_{dis,XX}}{k_f} \cong \frac{4.5 \left( \frac{\varepsilon}{150(1-\varepsilon)^{1/2}} \right) Pe_d^2}{Pr + \left( \frac{1.75}{150(1-\varepsilon)} \right) Pe_d}$
<p>Saada et al. 2006</p>	<p>Table 3.2</p>	<p> <math>Re \leq 150</math>  <math>0.1 \leq Pe \leq 103</math>  <math>0.1 \leq \varepsilon \leq 0.9</math>  <math>0.1 \leq k_s/k_f \leq 103</math> </p>
<p>Pedras and de Lemos 2008</p>		<p> <math>1 \leq Pe \leq 4000</math>  <math>0.6 \leq \varepsilon \leq 0.9</math>  <math>k_s/k_f = 2</math> and <math>10</math> </p> $\frac{k_{dis,XX}}{k_f} = 3.45 \cdot 10^{-2} Pe^{1.65}$ $\frac{k_{dis,YY}}{k_f} = 1.55 \cdot 10^{-4} Pe^{0.94}$
<p>Yang and Nakayama 2010</p>		<p> <math>0.1 \leq Pe_D \leq 10^4</math>  <math>Pr = 0.71</math> and <math>7.02</math>  <math>k_s/k_f = 2.3</math> and <math>53.28</math>                      For laminar regime:                 </p> $\frac{k_{dis,XX}}{k_f} = 0.15 \frac{Pe_D^2}{2 + 1.1Pe_D^{0.6} / Pr^{0.27}}$ $\frac{k_{dis,YY}}{k_f} = 0.0075 \frac{Pe_D^2}{2 + 1.1Pe_D^{0.6} / Pr^{0.27}}$ <p>                     For turbulent regime:                 </p> $\frac{k_{dis,XX}}{k_f} = 1.5Pe_D$ $\frac{k_{dis,YY}}{k_f} = 0.075Pe_D$
<p>Xu et al. 2010</p>		
<p>Alshare et al. 2010</p>	<p>Table 3.2</p>	<p> <math>1 \leq Re \leq 10^3</math>  <math>0.1 \leq Pe \leq 10^3</math>  <math>0.75 \leq \varepsilon \leq 0.875</math> </p>

(Cont. on next page)

**Table 3.8. (cont.)**

<p>Pathak and Ghiaasiaan 2011</p>	<p>Table 3.6</p>	<p>Table 3.6  <math>D_T^* = (A \cdot \ln(\text{Re}) - 37.7)</math>  <math>\times (1 - 0.00000001W^2 - 0.00008W)</math>  <math>/(1.2558 + 0.0004 \text{Re})^{((\varepsilon - 0.64)/0.11)}</math>  <math>A = 10.35</math> for <math>W &lt; 2700</math>  <math>A = 10.8</math> for <math>W \geq 2700</math></p>
<p>Jeong and Choi 2011</p>		<p><math>0.1 \leq \text{Re} \leq 100</math>  <math>0.1 \leq \text{Pr} \leq 20</math>  <math>0.44 &lt; \varepsilon &lt; 0.85</math></p> <p><math>\frac{k_{dis,XX}}{k_f} = \exp(-C_2) Pe^{C_1}</math>  <math>C_2 = \exp(a_2)(k_f / k_s)^{a_1}</math></p> <p>For 2D:  <math>a_1 = -0.1554 + 0.1595\varepsilon</math>  <math>a_2 = 1.783 - 1.775\varepsilon + 1.716\varepsilon^2</math></p> <p>For 3D staggered arrangement:  <math>a_1 = -0.0772 + 0.0856\varepsilon</math>  <math>a_2 = 0.897 + 1.617\varepsilon - 0.591\varepsilon^2</math></p> <p>For 3D inline arrangement:  <math>a_1 = -0.129 + 0.1341\varepsilon</math>  <math>a_2 = 1.291 - 0.2471\varepsilon + 0.6992\varepsilon^2</math></p>

### 3.3.2. Review of Experimental Studies on Determination of Thermal Dispersion Coefficients

In this section, the experimental studies on the determination of the effective thermal conductivity, which is the summation of the thermal dispersion coefficient and molecular thermal conductivity, are presented in detail. Because of the compact structure of the porous media, the thermal dispersion coefficient cannot be obtained directly from the experimental measurements and the effective thermal conductivity is investigated to see the variation of thermal dispersion coefficients in a specific porous medium since the equivalent thermal conductivity is a constant for a porous medium with unmoving solid particles (i.e., constant porosity). Different porous shapes were used in the performed studies and the employed porous materials show variety as well. Some researchers preferred to determine the effective thermal conductivity under steady

state circumstances while the others used transient state. Generally, thermal equilibrium condition was assumed for the determination of the effective thermal conductivity.

Basically all the experimental methods follow the same procedure. Experiments on the determination of the effective thermal conductivity are generally performed by measuring the temperatures at various locations inside a packed bed when a heat input was imposed. The heat source used to generate the temperature gradient in the bed was applied inside the packed bed or imposed at the bed boundaries. To determine the effective thermal conductivity which includes both the equivalent thermal conductivity of the porous medium and the thermal dispersion conductivity, the following procedure is followed:

- A temperature gradient in the packed bed is generated by using a heat source/sink.
- Temperatures at the different packed bed locations are measured.
- The macroscopic energy equation is solved for the packed bed. In the most of the studies, analytical methods were used to obtain the solution of the macroscopic energy equation.
- Finally, the effective thermal conductivity for the considered packed bed is found by the comparison of the temperature fields obtained from the analytical solution and the measurements.

Analysis of the related literature shows that the experimental studies can be classified into three groups (Figure 3.2):

- 1) Heat addition/removal at the lateral boundaries,
- 2) Heat addition at the inlet/outlet boundary,
- 3) Heat addition inside the bed.

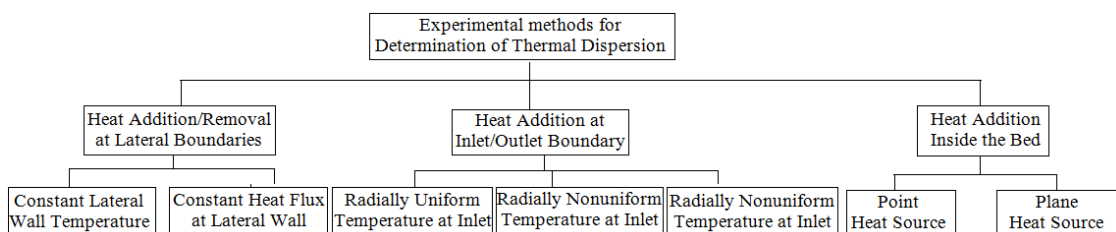


Figure 3.2. The classification of the experimental studies performed for the determination of thermal dispersion

In the following subsections, these approaches are explained and the reported experimental studies are also presented for each method, separately. Based on the thermal boundary condition and heat source type, each method is also classified into subgroups. These subgroups are explained in the following sections in detail as well.

Heat addition/removal at constant temperature lateral boundaries was mostly preferred in the literature due to the ease of application, probably. The spherical particles were favorable shape in the performed studies and air was mostly used. In the most of the studies, the shape of the bed was cylindrical to provide an axisymmetrical condition. The studies were performed for a wide range of particle-based Reynolds numbers. It is important to note that no laminar/turbulent distinction was taken into account for the suggested correlations. Peclet number is the main independent parameter in the suggested correlations, however there are correlations established based on Reynolds number only.

The present review indicates that although the thermal dispersion conductivity plays an important role in the convective heat transfer in porous media, the number of the performed experimental studies on the thermal dispersion is limited. The proposed correlations are also limited and mostly established for the spherical particle beds.

### **3.3.2.1. Heat Addition/Removal at Lateral Boundaries**

In this approach, the temperature gradient in the bed is provided by imposing uniform temperature or heat flux at the lateral boundaries of the packed bed. The imposed temperature at the bed boundary should be different than the fluid inlet temperature to create the temperature gradient in the bed. The cylindrical packed beds were mostly used to provide an axisymmetrical condition. The use of the axisymmetrical packed bed provides advantages such as checking of the measured temperature at different locations and the simplification of the macroscopic energy equation. Steady state heat addition/removal at the lateral boundaries was performed in the most of the studies. In the all studies that are discussed in this section, thermal equilibrium condition was assumed for the determination of the effective thermal conductivity. Hence, the comparison of the solution of the steady state macroscopic energy equation with the experimentally achieved temperature profiles at steady state yielded the effective thermal conductivity value. The macroscopic energy equation

presented by Eq. (3.1) was used to determine the temperature distribution in the bed for the most experimental studies in which the cylindrical bed was used.

$$(\rho c_p)_f \langle u \rangle \frac{\partial \langle T \rangle}{\partial z} = k_{eff,r} \left[ \frac{\partial^2 T}{\partial r^2} + \frac{1}{r} \frac{\partial \langle T \rangle}{\partial r} \right] + k_{eff,zz} \frac{\partial^2 T}{\partial z^2} \quad (3.1)$$

where  $k_{eff,r}$  and  $k_{eff,zz}$  are the radial (transverse) and the axial (longitudinal) effective thermal conductivities, respectively. The axial diffusion was neglected in some studies. Some researchers preferred to include axial heat diffusion while the value of the axial effective thermal conductivity was calculated based on the previously reported correlations. The assumptions for the components of the effective thermal conductivity tensor are summarized in Table 3.9 for all the studies reviewed in this section.

The imposed boundary conditions for Eq. (3.1) are:

- Convective heat transfer or constant heat flux at the lateral surface,
- Uniform temperature at the inlet,
- Constant temperature that equals to the lateral wall temperature at the outlet (if it is required),
- Symmetry at the center of the packed bed.

The lateral boundary conditions that used in the studies that employ the heat addition/removal at the lateral boundaries method are summarized in Table 3.10.

Table 3.9. The axial and/or radial effective thermal conductivity treatment in the reported experimental studies

Study	$k_{eff,zz}$			$k_{eff,r}$		
	calculated	neglected	a reported correlation was used	calculated	neglected	a reported correlation was used
Bunnell et al. 1949	X			X		
Kwong and Smith 1957		X		X		
Yagi et al. 1960	X				X	
Vortuba et al. 1972	X				X	
Gunn and Khalid 1975	X			X		
Gunn and De Souza 1974	X				X	

(Cont. on next page)

**Table 3.9. (cont.)**

Clement and Jorgensen 1983	X			X		
Vortmeyer and Adam 1984	X				X	
Levec and Carbonell 1985	X			X		
Borkink and Westerterp 1992a, 1992c		X		X		
Borkink and Westerterp 1992b	X			X		
Dixon and van Dongeren 1998			X	X		
Thomeo and Freire 2000		X		X		
Demirel et al. 2000		X		X		
Bey and Eigenberger 2001		X		X		
Elsari and Hughes 2002	X				X	
Dekhlyar et al. 2002		X		X		
Smirnov et al. 2003a, 2003b, 2004		X		X		
Metzger et al. 2004	X			X		
Testu et al. 2005, 2007	X			X		
Wen and Ding 2006			X	X		
Jorge et al. 2010			X	X		

Table 3.10. The lateral surface boundary conditions applied in studies with heat addition/removal at the lateral boundaries

<b>Study</b>	<b>Constant lateral wall temperature</b>	<b>Constant heat flux</b>
Bunnell et al. 1949	X	
Kwong and Smith 1957	X	
Gunn and Khalid 1975	X	
Borkink and Westerterp 1992a, 1992b, 1992c	X	
Dixon and van Dongeren 1998	X	
Thomeo and Freire 2000	X	
Demirel et al. 2000		X
Bey and Eigenberger 2001	X	
Dekhlyar et al. 2002		X
Smirnov et al. 2003a, 2003b, 2004	X	
Wen and Ding 2006	X	
Jorge et al. 2010	X	

In Figure 3.3, the schematic view of an experimental setup that summarizes the main components of the apparatus used in the experimental studies is shown. As seen from Figure 3.3, the fluid with a specified mass flow rate firstly enters to the pre-heating section to increase the fluid temperature to a specified value. The preheating section is also filled with the studied porous medium. Then, it passes through the calming section providing fully developed velocity field. After the calming section, it enters to the main section whose lateral surface temperature is different than the fluid inlet temperature. In this section (test section), the temperatures at different points of the bed (longitudinal or transverse) are measured. Based on the obtained local temperature, longitudinal or

transverse temperature profiles can be obtained. In some studies, the preheating or the calming sections were not involved in the setup.

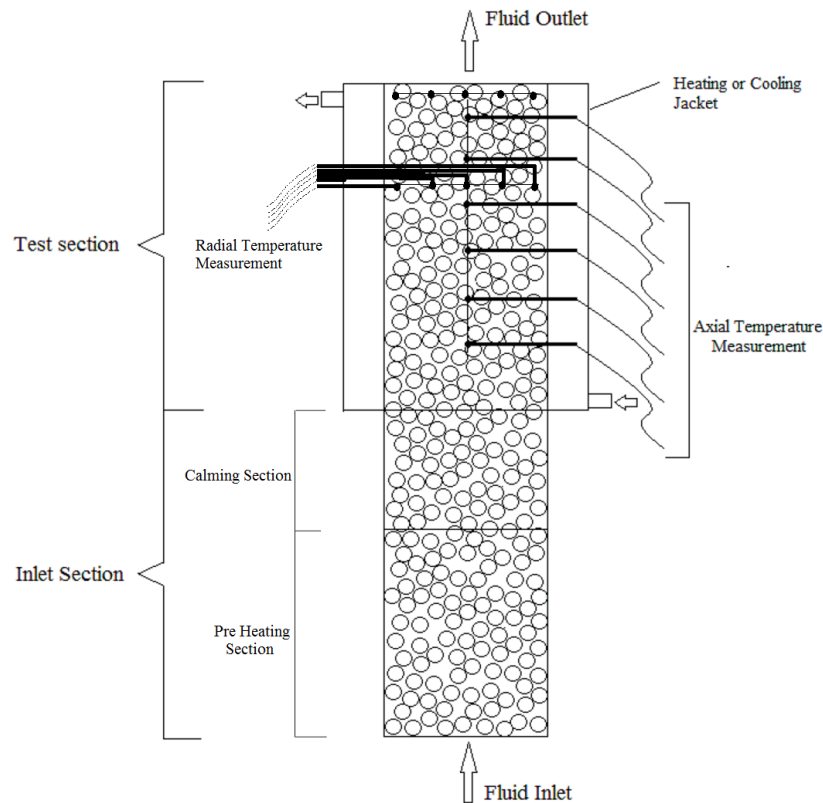


Figure 3.3. The schematic view of the experimental setups for the use of the heat addition/removal at the lateral boundaries method

The available reported studies, which used heat addition/removal at the lateral boundaries method, are briefly explained below.

Smirnov et al. (Smirnov et al. 2003a) studied heat transfer in the cylindrical packed beds filled with steel and glass spheres, ceramic cylinders, and ceramic and copper Raschig rings. The performed study was done for the range of Reynolds numbers from 250 to 2250. The heat diffusion in the axial direction was neglected. The heat removal at the lateral boundary was done by circulating water in an annular jacket. In the study, the effective thermal conductivity and the related wall heat transfer coefficient were found. A model with a linear variation of the radial effective thermal conductivity in the vicinity of the wall was proposed for the description of the radial heat transfer in the packed bed. A correlation for the radial effective thermal conductivity was proposed.



Smirnov et al. (Smirnov et al. 2003b) also studied 4-hole and 52-hole cylindrical pellets, 6-spoke wheels and 3-hole trilobed particles as packing with the same experimental setup that was used in the previous study (Smirnov et al. 2003a). All particles were made of ceramic. Reynolds number range of 400 to 2300 was examined. It was claimed that the shape of the particles used in the packed bed can significantly improve the radial heat transfer and reduce the pressure drop. It was remarked that the proposed model can describe the radial thermal conductivity for all type of particles used in the study without requiring any additional empirical parameters except the value of the convective heat transport parameter  $K$ .

Smirnov et al. (Smirnov et al. 2004) also performed another study and investigated the heat transfer in a cylindrical packed bed filled with copper and ceramic particles with various shapes (cylinder, Raschig ring, six-spoke wheels etc.). In the performed experiments, Reynolds number was greater than 300. The values of the convective heat transport parameter used in the proposed correlation for different shapes of copper and ceramic particles were found.

Thomeo and Freire (Thomeo and Freire 2000) studied the heat transfer in a cylindrical packed bed filled with glass spheres. Air flow with Reynolds numbers between 60 and 190 was studied. The air temperature was reduced at the main test section having heat removal at the lateral boundary by imposing constant wall temperature. The axial diffusion was neglected. A correlation was not proposed for the determination of the radial effective thermal conductivity.

Demirel et al. (Demirel et al. 2000) studied air flow in a rectangular duct filled with polyvinyl chloride Raschig rings for Reynolds numbers with the range of 200 – 1200, and polystyrene spheres for Reynolds numbers with the range of 200 – 1450. The bed was placed horizontally and a uniform heat flux with the range of 50 - 170 W/m<sup>2</sup> was applied at the top wall while the other surfaces were insulated. Instead of the theoretical solution for the determination of the temperature distribution, a third order polynomial function was assumed to predict the temperature distribution in the bed. The coefficients of the polynomial function were obtained by using the experimental data. The correlations for the determination of the transverse effective thermal conductivity of two packings as Raschig rings and spheres were suggested.

Bunnell et al. (Bunnell et al. 1949) investigated the heat transfer in a cylindrical packed bed with alumina cylinders. Reynolds numbers with the range between 30 and 100 were studied. The lateral surface of the bed was held at a constant temperature (100

°C) that was lower than the inlet air temperature (400 °C) by using boiling water circulation in the jacket of the bed. Thermocouples were placed in such a way that both fluid and solid temperatures were measured in the radial direction. The effective thermal conductivities for the radial and the axial directions were assumed equal and the solution Eq. (3.1) was obtained under this assumption. A correlation for the determination of the effective thermal conductivities was proposed.

Wen and Ding (Wen and Ding 2006) studied a cylindrical packed bed of glass spheres with air as the fluid. Re with the range between 100 and 700 were considered. The whole lateral surface of the packed bed was heated and maintained at constant wall temperature. The thermocouples were distributed both in the axial and the radial directions. The temperature difference between solid and fluid phases was checked. The study was performed for both transient and steady-state conditions. In the transient conditions, only the temperature distribution variations with time inside the bed were investigated. The radial effective thermal conductivity and the wall heat transfer coefficient were determined by the comparison of the steady-state experimental results with the analytical solution of Eq. (3.1). The axial effective thermal conductivity was directly calculated from Eq. (3.2) which was proposed by Wakao et al. (Wakao et al. 1978):

$$\frac{k_{eff,zz}}{k_f} = \frac{k_e}{k_f} + 0.5 \text{Re Pr} \quad (3.2)$$

It was declared that the correlations of the radial effective thermal conductivity of Bunnell et al. (Bunnell et al. 1949) and Demirel et al. (Demirel et al. 2000) provide well predictions.

Dixon and van Dongeren (Dixon and van Dongeren 1998) studied a cylindrical packed bed with spherical particles of porous ceramic, nylon and steel. The effects of the tube (packed bed) and the particle diameters on the heat transfer were investigated for the fixed tube-to-particle diameter ratios of 4 and 8. The Re interval was between 100 and 900. Steam was circulated in the jacket of the tested section to provide constant wall temperature. Both the axial and the radial temperature measurements were achieved. Eq. (3.1) and its boundary conditions were used to find an analytical expression for the temperature distribution through the bed. For the axial effective thermal conductivity, the following equation was used:

$$\frac{k_{eff,zz}}{k_f} = \frac{k_s}{k_f} + 0.5 \text{RePr} \quad (3.3)$$

where  $k_s/k_f$  was taken as 18, 8 and 4 for steel, porous ceramic and nylon packings, respectively. The radial effective thermal conductivity and the wall Nusselt number values were found for various Reynolds numbers. It was found that the radial effective thermal conductivity can be described based on the value of tube-to-particle diameter ratio rather than the individual tube and particle diameters.

Borkink and Westerterp (Borkink and Westerterp 1992a) studied a cylindrical packed bed with glass spheres of two different diameters as 3.7 mm for the Peclet number range of 60 – 300 and 7.2 mm for the Peclet number range of 100 – 800. Moreover, porous alumina cylinders for  $50 < \text{Pe} < 450$  and porous alumina Raschig rings for  $100 < \text{Pe} < 450$  were studied. The study was performed for three stainless steel beds with different inner diameters. Air was used as fluid phase. The experimental setup was constructed to measure both the radial and the axial temperature values throughout the packed bed. Hot air entered to the bed while cooling of the fluid was made by the lateral walls with constant temperature. No calming section was involved in the setup. For the steady state, the radial temperature profile was measured near the top section of the bed. Dimensionless form of Eq. (3.1) was solved and the axial conduction was neglected. A correlation that relates the radial effective thermal conductivity with the Peclet number, the particle shape and the number of particles on the tube (packed bed) diameter was obtained.

The same packed bed setup (Borkink and Westerterp 1992a) was studied for Pe between 150 and 2100 by the same researchers (Borkink and Westerterp 1992b). Similar to the previous study, the dimensionless form of Equation (3.1) without the axial dispersion was solved. Based on the obtained results, it was declared that the inlet boundary condition in the modeling of the radial effective thermal conductivity is very important. If the inlet temperature profile is assumed to be radially flat, although the actual profile is curved, an axial dispersion may occur. The radial effective thermal conductivity and the wall heat transfer coefficient were found to be strongly cross-correlated and both parameters were found to be independent of the tube diameter.

Furthermore, the same experimental setup was used with alumina cylinder packings (Borkink and Westerterp 1992c). Reynolds numbers between 70 and 600 were

considered. The dimensionless form of Equation (3.1) with the axial conduction was solved, numerically. The influences of the inlet and the outlet boundary conditions on the solution were investigated. The values of the axial effective thermal conductivity, the radial effective thermal conductivity and the wall heat transfer coefficient were found for various Reynolds numbers and bed diameters. These results were obtained with the assumption of a parabolic temperature profile at the inlet. It was declared that the inclusion of the axial thermal dispersion in the heat balance does not significantly influence the description of the heat transport in wall cooled or heated packed bed if the correct radial inlet temperature profile is selected and the employed Reynolds numbers exceed 50.

Kwong and Smith (Kwong and Smith 1957) studied two different sizes of the cylindrical packed beds with air and ammonia. The packing materials were steel and alumina spheres. Non-heated calming section was not involved in the study, but the inlet temperature measurements were taken at about 18 cm above the actual inlet of the bed to reduce entrance disturbances. To find theoretical temperature distribution, Equation (3.1) was solved, numerically. The term for the axial heat transfer by diffusion was neglected. The radial effective thermal conductivity values were found for Reynolds numbers between 50 and 450.

Bey and Eigenberger (Bey and Eigenberger 2001) studied the packed bed (tube) with glass and ceramic spheres, and ceramic ring packings with tube-to-particle diameter ratios between 3.3 and 11. The studied Reynolds number range was between 50 and 900 for the spheres and between 0 and 2500 for the rings. The experiments were conducted with the packing materials between two parallel plates of different temperatures (Figure 3.4). By this way, instead of solving Eq. (3.1) with aforementioned boundary conditions (in the case of the cylindrical beds), the radial effective thermal conductivity and the wall heat transfer coefficient were described by using Eqs. (3.4) and (3.5) where  $q_w''$  is the wall heat flux and  $h_w$  is the wall heat transfer coefficient. The results of Eqs. (3.4) and (3.5) were compared with the experimental data.

$$q_w'' = k_{eff,r} \frac{dT}{dx} \quad (3.4)$$

$$q_w'' = h_w [T_w - T(r = R)] \quad (3.5)$$

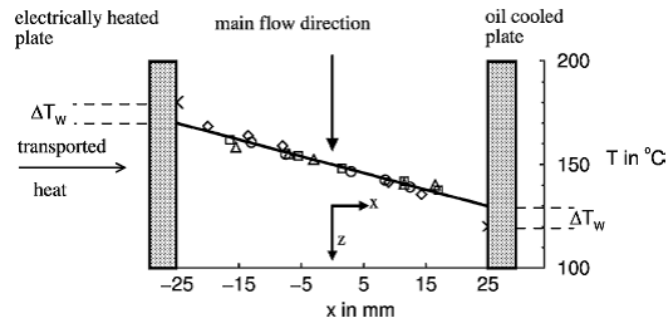


Figure 3.4. Experimental setup of Bey and Eigenberger 2001

It was claimed that the value of the radial effective thermal conductivity can be well described by the correlation developed by Bauer and Schlünder (Bauer and Schlünder 1977) (Eq. (3.6)), where  $K_r$  is a correlation constant.  $K_r$  values for different tube-to-particle diameters were shown in diagrams in their study.

$$\frac{k_{eff,r}}{k_f} = \frac{k_e}{k_f} + \frac{Pe}{K_r} \quad (3.6)$$

Jorge et al. (Jorge et al. 2010) studied a cylindrical packed bed filled with cylindrical particles. Air was used as fluid. The packing material was an industrial catalyst made of nickel supported on alumina. Reynolds numbers between 87 and 290 was studied. The radial effective thermal conductivity and the wall heat transfer coefficient were estimated from the steady state data while the characteristic bed time constant was estimated from the transient data of the experiments. The test section was heated by using a steam jacket and the uniform temperature at the lateral surface was checked. A new correlation was proposed for the radial effective thermal conductivity. Equation (3.1) was numerically solved to obtain the temperature distribution. A correlation developed by Dixon and Cresswell (Dixon and Cresswell 1979) (Eq. (3.7)) was used for the determination of the axial effective thermal conductivity, where  $G$  is the superficial mass flow rate.

$$k_{eff,zz} = Gc_{pf}d_p \left[ \frac{0.5}{1+9.7\varepsilon/Pe} + \frac{0.73\varepsilon + k_s/k_f}{Pe} \right] \quad (3.7)$$

Dekhtyar et al. (Dekhtyar et al. 2002) studied a cylindrical packed bed of glass spheres. The fluids were water and 47% aqueous solution of glycerin. Reynolds number range of 3 to 700 was examined. Constant heat flux at the surface boundary was used in the experimental setup. Equation (3.1) was solved without considering the axial component of diffusion heat transfer to obtain an analytical expression for the temperature profile. In the obtained analytical solution, temperature depends on  $r^2$  and  $x$ . A parabolic temperature profile was assumed in the packed bed and then Eq. (3.8) was found by using the parabolic temperature profile.

$$k_{eff,r} = \frac{q_w''}{D \partial T / \partial (r^2)} \quad (3.8)$$

The radial effective thermal conductivity was calculated from Equation (3.8) with using the temperature data from the experiment ( $D$  is the tube diameter). A correlation was obtained for the radial effective thermal conductivity ratio. It was claimed that the proposed correlation was adequate for the turbulent range whereas some stratification of data was observed for the low Reynolds number regions. It was also mentioned that the effective thermal conductivity ratio is proportional to the square root of the Peclet number for the Reynolds numbers below 100.

Gunn and Khalid (Gunn and Khalid 1975) studied air flowing cylindrical packed beds with glass and metallic particles. The investigated Reynolds number range was between 1 and 400. The packed bed had an unheated inlet section and then the lateral walls were heated by steam. Eq. (3.1) was used to obtain the analytical solution. The determination of the axial and the radial thermal dispersion conductivities was achieved. The results were shown by the graphics of the axial and the radial Peclet numbers constructed with the dispersion conductivities versus Reynolds number.

### **3.3.2.2. Heat Addition at Inlet/Outlet Boundary**

Heat addition at the inlet/outlet boundary approach used most frequently in the early studies of the heat transfer in porous media. A review of those studies can be found in the book of Kaviany (Kaviany 1995). In some studies, mass transfer experiments were conducted based on this method and the effective thermal conductivity values were obtained by analogy between the heat and mass transfer

(Delgado 2007). Generally, thermal equilibrium condition was assumed for the determination of the effective thermal conductivity. In this method, the bed can be heated at the inlet or outlet boundaries to provide a temperature gradient. A sample experimental setup for the heat addition at the inlet/outlet boundary is provided and shown in Figure 3.5, schematically. Similar to the heat removal/addition at the lateral boundaries (Figure 3.3), the experimental setup consists of a calming section and a test section. There is an electrical heater array at the inlet of test section and the temperature of the bed increases at the inlet boundary of the bed. In some cases, the heat step input was provided by pumping the fluids from two different reservoirs at the different temperatures. The lateral boundary of the bed is insulated. Then, temperature distributions in longitudinal and transverse directions in the bed is measured and plotted. Our literature review shows that two methods can be applied for the heat addition at the inlet boundary. The methods used for the heat addition at the inlet/outlet boundaries are explained below. The first and the second methods are used for the heating at the inlet boundary while the third method is used for the heating at the outlet boundary.

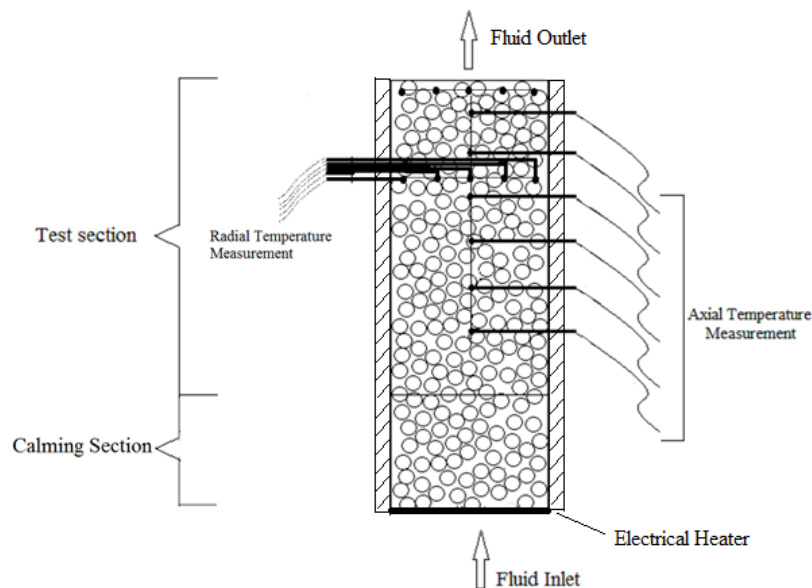


Figure 3.5. The schematics of the experimental setups for the heating at the inlet boundary

A) In the first method used for the heating at the inlet boundary, temperature gradient can be generated by a heat source and applied at the bed inlet plane. The effect of the temperature gradient at the bed inlet plane is propagated through the bed and then it is measured. A temperature gradient in the radial direction of the bed can be obtained by partial heating of the inlet section of the packed bed. Generally, steady condition is conducted to determine the thermal dispersion. The transverse and longitudinal components of the effective thermal conductivity can be found by comparing theoretical solution of Equation (3.9) with temperature measurements.

$$(\rho c_p)_f \langle u \rangle \frac{\partial \langle T \rangle}{\partial z} = k_{eff,yy} \frac{\partial^2 \langle T \rangle}{\partial y^2} + k_{eff,zz} \frac{\partial^2 \langle T \rangle}{\partial z^2} \quad (3.9)$$

where  $k_{eff,yy}$  and  $k_{eff,zz}$  are the transverse and the longitudinal (axial) effective thermal conductivities, respectively. The imposed boundary conditions are:

- Radially uniform or non-uniform temperature at the inlet,
- Zero heat flux at the lateral boundaries,
- Symmetry at the center of the packed bed,
- No diffusion heat flux at the outlet.

B) In the second method used for the heating at the inlet boundary, transient experiments were conducted by using radially uniform temperature at the inlet of the packed bed. A step change, a pulse heat input, or a sinusoidal temperature variation in time can be imposed at the bed inlet and consequently the outlet air temperature varies with time. For a step change, a sudden temperature change is applied at the bed inlet boundary and then the inlet temperature remains constant. For a pulse heat input, a finite amplitude pulse is applied by the heater and it is repeated periodically. With a similar arrangement, a sinusoidal change in temperature can also be achieved. The measurements are made for temperature in the downstream temperature and/or time lag difference between the waves at the inlet and outlet of the packed bed. The walls of the bed are insulated and consequently the axial conductive and convective heat transports become dominant. Because of these assumptions, one-dimensional transient form of the macroscopic energy equation (Eq. (3.10)) can be used to obtain the theoretical solution of the temperature in the bed.



$$(\rho c_p)_e \frac{\partial \langle T \rangle}{\partial t} + (\rho c_p)_f \langle u \rangle \frac{\partial \langle T \rangle}{\partial z} = k_{eff,zz} \frac{\partial^2 \langle T \rangle}{\partial z^2} \quad (3.10)$$

Following initial and boundary conditions can be implemented for the boundaries:

- For the inlet boundary condition, a time dependent temperature can be used (e.g. sinusoidal wave with constant amplitude),
- A uniform temperature for the initial condition,
- The measured outlet temperatures can be used.

C) The third method is used for heating at the outlet boundary. Heating at the outlet of the packed bed can be done by using an infrared lamp. Thus, the radiation heating from the external of the bed is used to create the temperature gradient inside the bed. Eq. (3.9) is considered to obtain the theoretical temperature distribution. Figure 3.6 displays the schematic view of the experimental setups used in the studies in which the radiation heating method was applied. Eq. (3.9) is used without heat diffusion in the transverse direction to obtain the analytical temperature distribution in the packed bed.

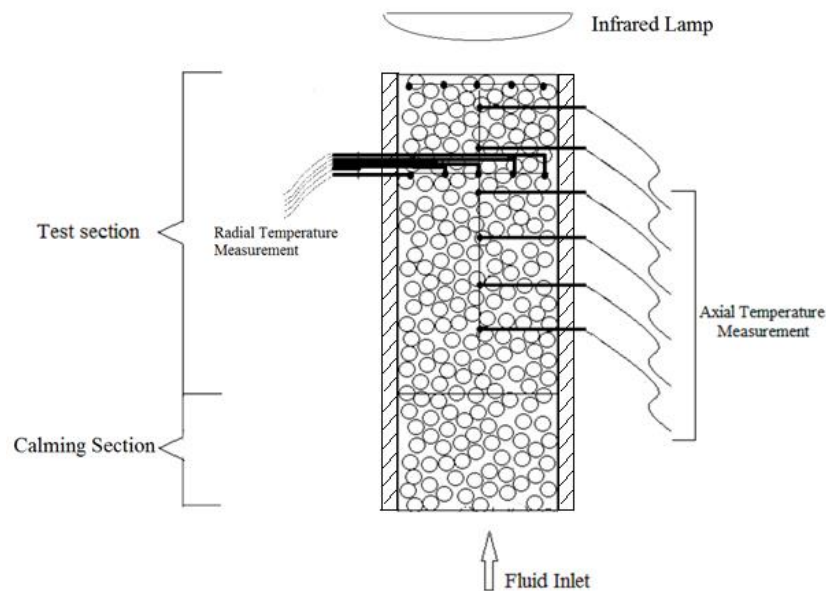


Figure 3.6. The schematic of experimental setups in which the radiation heating method was used.

Gunn and De Souza (Gunn and De Souza 1974) studied the thermal frequency response of the packed beds by using a similar method as described above. The packing materials were glass, steel and lead spheres. Air was used as fluid and the Reynolds number range between 0.05 and 330 was studied. A grid heater was placed at the inlet of the packed bed and sinusoidal heating was applied via this heater. Low thermal conductivity materials were used at the walls of the packed bed; hence, the radial heat transfer was kept small compared to the axial heat transfer. The axial dispersion coefficient and the fluid-particle heat transfer coefficient were found by a non-linear regression. The experimental frequency response was observed to be mostly influenced from the thermal dispersion at Reynolds numbers less than 1.

Clement and Jorgensen (Clement and Jorgensen 1983) studied the axial and the radial dispersion coefficients under non-reacting and reacting conditions. A cylindrical packed bed with Pt-impregnated alumina pellets as packing was used. The lateral walls were insulated. At the beginning of the experiments, the packed bed was allowed to reach the steady state. After some time, a periodical temperature pulse was applied at the bed inlet. Then the transient measurements were done. Three steady state temperature profiles were examined with different inlet conditions. All experiments were conducted for Reynolds number of 10. Thus the values of dispersion coefficients for this Reynolds number were found. Dimensionless, 2-D and cylindrical form of Eq. (3.10) was solved analytically to obtain the temperature distribution in the bed. It was concluded that for non-reacting conditions, in order to obtain accurate values of the axial thermal dispersion coefficients, it is necessary to include the radial thermal dispersion in spite of the insulation at lateral walls.

Levec and Carbonell (Levec and Carbonell 1985) investigated the thermal response of a rectangular packed bed due to step temperature changes. Water was used as fluid. Peclet number range from 10 to 1000 was studied. The packing was urea formaldehyde spheres. A flow distributor was used at the setup to provide uniform velocity. Transient experiments were conducted by employing a step temperature change in water. Fluid and solid temperatures were measured separately at six axial locations as a function of time. Transverse diffusion was neglected and the axial effective thermal conductivity values were obtained. Thermal non-equilibrium was considered and the macroscopic energy equations for the solid and the fluid phases were solved, separately. It was mentioned that there are three factors affecting the axial effective thermal conductivity: firstly conduction, secondly hydrodynamic dispersion,

and finally the heat exchange between solid and fluid. In their study, some steady experiments were conducted to measure the transverse effective thermal conductivity. For these measurements non-uniform temperature at the inlet was used by contributing different temperatures at the two halves of the packed bed. Eq. (3.9) was used to obtain the transverse effective thermal conductivity values with neglecting axial diffusion.

Elsari and Hughes (Elsari and Hughes 2002) investigated the axial effective conductivity for a cylindrical packed bed with different packing materials. Air, nitrogen and carbon dioxide were used as fluid in the study. The packing materials were steel ball bearings, copper chromite and chromia alumina cylinders, alumina hollow cylinders and alumina spheres. Two types of the packed beds were used as a glass bed and a thin walled steel bed. The lateral surfaces of the beds were insulated. Heat input was given at the outlets of the beds by using an infra-red lamp of 375 W. Eq. (3.9) was first considered with using uniform temperatures at the inlet and outlet and with neglecting radial conduction. Additionally, in order to calculate the radial heat losses Eq. (3.11) was used. It was observed that the axial effective thermal conductivity strongly depends on particle size.

$$(\rho c_p)_f \langle u \rangle \frac{\partial \langle T \rangle}{\partial z} + k_{eff,zz} \frac{\partial^2 \langle T \rangle}{\partial z^2} + \frac{4h_w}{D} (\langle T \rangle - T_i) = 0 \quad (3.11)$$

where  $h_w$  is the wall heat transfer coefficient,  $D$  is the tube diameter and  $T_i$  is the inlet gas temperature.

Yagi et al. (Yagi et al. 1960) studied a cylindrical packed bed with insulated walls for low Reynolds numbers. Glass and metal spherical particles were used as packing materials. The packed bed was heated from the top by an infrared lamp. The axial effective thermal conductivity values were obtained by using Eq. (3.9). The radial diffusion was neglected. A correlation that related the axial effective thermal conductivity with the Peclet number and the dimensionless stagnant thermal conductivity was found.

Vortuba et al. (Vortuba et al. 1972) studied an experimental setup similar to that used by Yagi et al. (Yagi et al. 1960) in order to determine the axial effective thermal conductivity. Reynolds number range from 0.1 to 1000 was studied for air, oxygen and nitrogen. The packing particles were glass, iron, lead, alumina, sand and duracryl spheres, ceramic Raschig rings, alumina cylinders and irregular particles. 250 W

infrared lamp was used to heat the packed bed from the top. The temperature measurements were done at the packed bed axis. Radial measurements were also done, but no measurable radial temperature gradient was found. To obtain analytical temperature profiles, Eq. (3.9) was used with neglecting radial heat diffusion. A correlation for the axial effective thermal conductivity was obtained.

Vortmeyer and Adam (Vortmeyer and Adam 1984) studied heat transfer in cylindrical packed beds filled with spherical particles. The experiments were conducted with spherical particles of low thermal conductivity, such as catalyst support material Al<sub>2</sub>O<sub>3</sub> or plastic, with glass spheres of moderate thermal conductivity and metal (steel, bronze, brass) spheres of high thermal conductivity. Air was used as fluid phase. Radial heat losses were included to the analytical solution by using Eq. (3.11). A correlation for the axial effective thermal conductivity was derived. Additionally, the experimental results of Kunii and Smith (Kunii and Smith 1961) were analyzed to include the effects of different gases and another relation was obtained for the axial effective thermal conductivity of packed beds with glass spherical packings.

### 3.3.2.3. Heat Addition Inside Bed

In this approach, a plane or a point heat source is placed inside the packed bed. Time dependent or steady heat sources can be used. Usually rectangular packed beds were used. A wire that is placed perpendicular to the fluid flow can be thought as a point source or several wires in the same plane can be considered as a plane heat source inside the packed bed. Furthermore, a heated spherical particle can be used as a heat addition source in the bed. Both the axial and the transverse components of the effective thermal conductivity can be determined if the thermocouples distributed throughout the packed bed.

The governing equation, which should be solved to determine the axial and the transverse effective thermal conductivities, is given by Eq. (3.12).

$$(\rho c_p)_e \frac{\partial \langle T \rangle}{\partial t} + (\rho c_p)_f \langle u \rangle \frac{\partial \langle T \rangle}{\partial z} = k_{eff,zz} \frac{\partial^2 \langle T \rangle}{\partial x^2} + k_{eff,yy} \frac{\partial^2 \langle T \rangle}{\partial y^2} + s \quad (3.12)$$

where  $k_{eff,zz}$  and  $k_{eff,yy}$  are the axial and the transverse effective thermal conductivities and  $s$  is the source strength. The boundary conditions for this equation

can be

- Constant temperature at the inlet,
- Thermally developed outlet (zero temperature gradient),
- Insulation at the lateral boundaries.
- The initial condition can be a uniform reference temperature.

Metzger et al. (Metzger et al. 2004) investigated transient heat transfer in a rectangular packed bed filled with glass spheres. Water flow from the top to the bottom in the packed bed with constant inlet temperature and the Peclet numbers below 130 were considered. The experimental setups are shown in Figure 3.7. Two different configurations of the heat sources were analyzed in the study. A single wire near the inlet of the packed bed was used as a point heat source (Figure 3.7a) and a plane heat source was made by wires placed in the same plane (Figure 3.7b). Thirteen thermocouples in the downstream measured the temperature response to a step heat input. Ordinary least squares and Gauss-Markov methods were used to estimate unknown effective thermal conductivity values in the analytical solution of Eq. (3.12). Monte Carlo simulations were done to assess the estimation errors. As a result of these simulations, it was claimed that the axial effective thermal conductivity has been estimated with higher accuracy whereas the lateral one has lower accuracy. A correlation was proposed for the axial effective thermal conductivity.

Testu et al. (Testu et al. 2005) studied the same experimental setup for the line heater shown in Figure 3.7a. Air was used as fluid phase and glass spheres and ceramic grains with internal porosity were used as the packing particles. The Peclet number range between 10 and 70 were studied. Eq. (3.9) was used to obtain the analytical temperature distribution. The medium was approximated as infinite. The ordinary least squares method was used to predict the unknown coefficients of the analytical solution with using the experimental temperature data. Both the axial and the transverse effective thermal conductivities were obtained. Some diagrams were constructed for the axial and the transverse effective thermal conductivities of the packed bed filled with spheres for various Peclet numbers. It was also claimed that the thermal equilibrium assumption is valid even for the fluid and the packing materials of different thermophysical properties.

Testu et al. (Testu et al. 2007) examined the setup in Figure 3.7a with glass spheres. Both air and water were used as fluid. Water flow was examined for Reynolds numbers below 18 while air flow was examined for Reynolds numbers between 12 and 100. The same procedure in the study of Testu et al. (Testu et al. 2005) was followed. It

was claimed that the size of the beads has no effect on the dispersion in air. The correlations were constructed for the axial and the transverse effective thermal conductivity values of water and air flows. Furthermore, another correlation was claimed to be valid to predict the axial effective thermal conductivity values for both fluids.

The packing particles that used for the construction of the packed beds of porous media in the reviewed studies on the determination of the effective thermal conductivity are summarized in Table 3.11. The particles shapes, materials and dimensions of the particles are provided in this table for all the explained studies in this section. The shapes and dimensions of the packed beds used in the reviewed studies on the determination of effective thermal conductivity are summarized in Table 3.12. Additionally, the chosen fluids that flow through the packed beds are provided in this table.

Table 3.11. The properties of the packing particles used in the experimental studies on the determination of the effective thermal conductivity

<b>Study</b>	<b><i>Sphere</i></b>	<b><i>Cylinder</i></b>	<b><i>Raschig ring</i></b>	<b><i>Others</i></b>
Bunnell et al. 1949	-	Alumina 3.175 mm (d and l)	-	-
Kwong and Smith 1957	Steel 6.35 mm and 3.97 mm Alumina 6.35 mm and 9.525 mm	-	-	-
Yagi et al. 1960	Glass Metal	-		Broken pieces of limestone
Vortuba et al. 1972	Glass 0.45, 2.25, 3.9, 6.5 mm Iron 5, 5.15 mm Lead 2.25 mm Duracryl 1.3 mm Alumina 3.4 mm Sand 0.25 mm	Alumina d=5.4 mm l=4 mm	Ceramic do=l=6.5 mm, t=3.5 mm	Irregular particles 0.5 mm<d<2 mm

(Cont. on next page)

**Table 3.11. (cont.)**

Gunn and De Souza 1974	Glass 0.275, 0.46, 1.15, 2.2, 3, 6 mm Steel 3.16, 6.32 mm Lead 0.8 mm	-	-	-
Gunn and Khalid 1975	Lead 1 mm, 7 mm Nickel 6.8 mm Steel 6.4 mm Glass 0.5 mm, 1.2 mm, 3 mm, 6 mm	-	-	-
Clement and Jorgensen 1983	-	Pt-impregnated alumina 3.7 mm (d and l)	-	-
Vortmeyer and Adam 1984	Al <sub>2</sub> O <sub>3</sub> 5, 6 mm, Plastic 6 mm Glass 5, 8 mm Steel 2<d<10 mm Bronze 6 mm Brass 6 mm	-	-	-
Levec and Carbonell 1985	Urea Formaldehyde 2.5, 5.5 mm	-	-	-
Borkink and Westerterp 1992a, 1992c	Glass 3.7 mm and 7.2 mm	Porous alumina d=6.4 mm and l=5.2 mm	Porous alumina d <sub>o</sub> =8.5 mm, t=5.4 mm, l=8.6 mm	-
Borkink and Westerterp 1992b	-	Same with 1992a	-	-
Dixon and van Dongeren 1998	Porous ceramic, nylon, steel 3.275 mm <d< 24.95 mm	-	-	-

(Cont. on next page)

**Table 3.11. (cont.)**

Thomeo and Freire 2000	Glass 3.1 mm	-	-	-
Demirel et al. 2000	Polystyrene 48 mm, 38 mm, 29 mm	-	Polyvinyl chloride dp = 38.5 mm, 32.6 mm	-
Dekhyyar et al. 2002	Glass 0.9, 3.2, 8.9 mm	-	-	-
Elsari and Hughes 2002	Stainless steel 3.17 mm Alumina 6.4 mm	Copper chromite d=3.26 mm l=3.62 mm Chromia alumina d=4.07 mm l=4.18 mm	Alumina t=6 mm, do=l=8 mm	-
Smirnov et al. 2003a	Steel 16 mm Glass 19 mm	Ceramic 10 mm (d and l) 19 mm (d and l)	Ceramic 14 mm (do and l) and t=3.5 mm Copper 14 mm (do and l) and t=1 mm	-
Smirnov et al. 2003b	-	-	-	4-hole and 52-hole cylindrical pellets, 6-spoke wheels, 3-hole trilobed particles
Metzger et al. 2004	Glass 2 mm	-	-	-
Smirnov et al. 2004	-	Ceramic d=14 mm and l=9 mm d=9 mm and l=19 mm Same with 2003a	Same with 2003a	Ceramic wheel with six holes, ceramic 52-hole block, ceramic 4-hole pellet
Wen and Ding 2006	Glass 5 mm	-	-	-

(Cont. on next page)



**Table 3.11. (cont.)**

Testu et al. 2005, 2007	Glass 2 mm	-	-	-
Note: $d$ , $d_o$ and $d_p$ are particle, outer and equivalent diameters while $l$ and $t$ are the length and the thickness, respectively.				

Table 3.12. The features of the experimental setups used in the reported studies on the determination of the effective thermal conductivity

Study	Bed shape		Tube-to-particle diameter ratio	Employed fluid
	<i>Cylindrical</i>	<i>Rectangular</i>		
Bunnell et al. 1949	$D_i=50.8$ mm $L=965.2$ mm	-	16	Air
Kwong and Smith 1957	$D_i=50.8, 101.6$ mm	-	Btw 5 and 26	Air Ammonia
Yagi et al. 1960	$D_i=50, 68$ mm	-	-	Air
Vortuba et al. 1972	$D_i=26$ mm	-	Btw 3.85 and 104	Air, O <sub>2</sub> , N <sub>2</sub>
Gunn and De Souza 1974	$L=30$ and 60 mm	-	-	Air
Gunn and Khalid 1975	$D_i=95.25$ mm $L=304.8$ mm	-	Btw 13.5 and 190.5	Air

(Cont. on next page)

**Table 3.12. (cont.)**

Dekhtyar et al. 2002	Di=52 mm L=531 mm	-	Btw 5.8 and 58	Water 47% aqueous solution of glycerin
Elsari and Hughes 2002	Di=25 mm L=230 mm	-	Btw 3.9 and 8	Air, N2, CO2
Smirnov et al. 2003a, 2003b, 2004	Di=84 mm L=1130 mm (330 mm heating, 150 mm calming, 650 mm cooled test sections)	-	Btw 4 and 5.25	Air
Metzger et al. 2004	-	L=400 mm H=100 mm w=200 mm	-	Water
Wen and Ding 2006	Di=41 mm L=1100 mm	-	8.2	Air
Testu et al. 2005, 2007	-	Same with Metzger et al. 2004	-	Air/Water
Jorge et al. 2010	Di=60 mm L=650 mm (250 mm calming, 400 mm heating test sections)	-	~16	Air
Di is the inner diameter, L is the length, H is the height and w is the width of the tubes				

Figure 3.7 shows the ranges of the studied Reynolds numbers by different researchers. A wide range of Reynolds numbers was studied. Most of the researchers preferred to study on the Reynolds numbers less than 1000. This may be due to the possibility of the occurrence of turbulent flow. The solution of the macroscopic turbulent energy equation in the voids between the particles is not easy because in addition to unknown effective thermal conductivities in different directions, the turbulent thermal diffusivity should also be predicted. The suggested correlations for the

determination of the effective thermal conductivities are presented in Table 3.13. The validity conditions for the correlations are provided in the table as well.

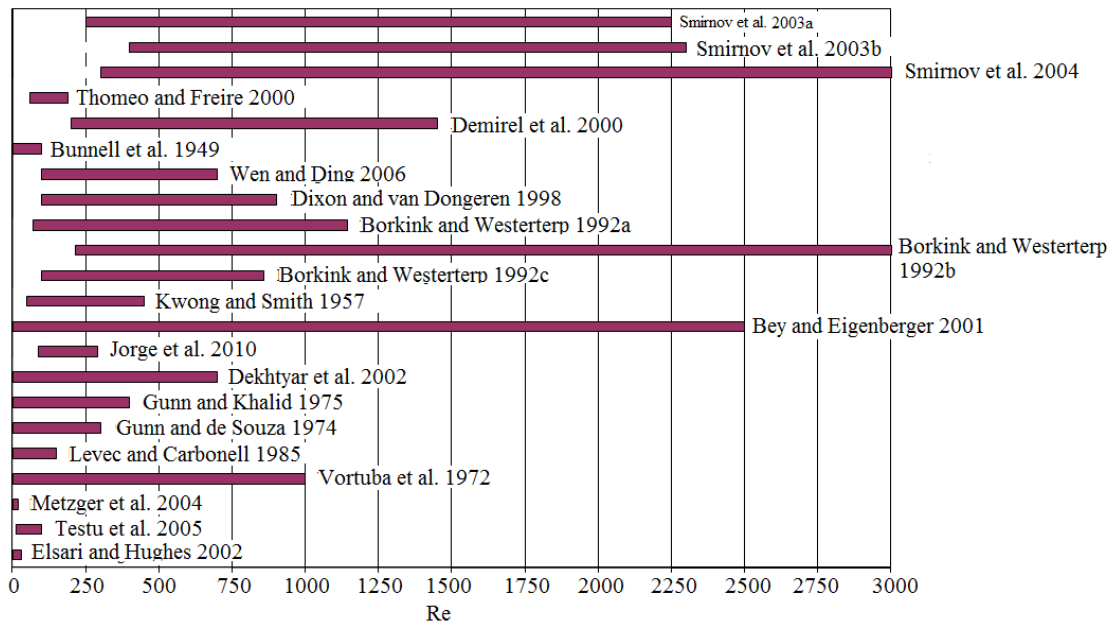


Figure 3.7. The Reynolds number ranges in the reported experimental studies on the determination of the effective thermal conductivity

Table 3.13. The suggested correlations for the determination of the effective thermal conductivity

Studies	Correlation	Constant values and validation conditions
Bunnell et al. 1949	$\frac{k_{eff,zz}}{k_f} = \frac{k_{eff,r}}{k_f} = 5.0 + 0.061Re$	For alumina cylinders
Yagi et al. 1960	$\frac{k_{eff,zz}}{k_f} = \frac{k_e}{k_f} + \delta Pe$	$\delta=0.8$ for glass beads $\delta=0.7$ for metal spheres
Vortuba et al. 1972	$\frac{k_{eff,zz}}{Gc_p d_p} = \frac{k_e/k_f}{Re Pr} + \frac{14.5}{d_p \left(1 + \frac{C_3}{Re Pr}\right)}$	G is mass flow rate, C3 is experimental parameter

(Cont. on next page)

**Table 3.13. (cont.)**

Elsari and Hughes 1957	$\frac{k_{eff,zz}}{k_f} = 7.24 + 8.49Pe$	Steel ball bearings
	$\frac{k_{eff,zz}}{k_f} = 4.25 + 7.20Pe$	Copper chromite cylinder
	$\frac{k_{eff,zz}}{k_f} = 3.24 + 6.47Pe$	Chromia alumina cylinder
	$\frac{k_{eff,zz}}{k_f} = 9.68 + 3.21Pe$	Alumina hollow cylinder
	$\frac{k_{eff,zz}}{k_f} = 8.63 + 3.12Pe$	Alumina spheres
Vortmeyer and Adam 1984	$\frac{k_{eff,zz}}{k_f} = \frac{k_e}{k_f} + \frac{g\nu Re/d_p}{1+h\nu Re/d_p}$	g=1420, 1060, 600 s/m and h=70, 96, 110 s/m for metal, glass, and catalyst, respectively. $\nu$ is kinematic viscosity
	$\frac{k_{eff,zz}}{k_f} = \frac{k_e}{k_f} + \frac{k\nu RePr/d_p}{1+p\nu Re/d_p}$	For glass spheres and any gases. k and p are experimental parameters found for CO <sub>2</sub> , air and He.
Borkink and Westerterp 1992a	$\frac{k_{eff,r}}{k_f} = \frac{k_e}{k_f} + \frac{Pe}{B}$	ke/kf= 4.7 and B=8.8 for 3.7-mm-diameter spheres and N=13.5 ke/kf=6.2 and B=10.9 for 7.2-mm-diameter spheres and 7<N<14 ke/kf=4 and B=7.6 for cylinders and 8<N<17 ke/kf=4.5 and B=4.2 for Raschig rings and 8≤N≤16 N is number of particles on a diameter
Demirel et al. 2000	$\frac{k_{eff,r}}{k_f} = 2.894 + 0.068 Re$	For polyvinyl chloride Raschig rings
	$\frac{k_{eff,r}}{k_f} = 10.432 + 0.0481 Re$	For polystyrene spheres
Bey and Eigenberger 2001	$\frac{k_{eff,r}}{k_f} = \frac{k_e}{k_f} + \frac{Pe}{K_r}$	K <sub>r</sub> is empirical constant and its values were given in graphics
Dekhtyar et al. 2002	$\frac{k_{eff,r}}{k_f} = 0.083 Re Pr$	For glass spheres

(Cont. on next page)

**Table 3.13. (cont.)**

Smirnov et al. 2003a	$\frac{k_{eff,r}}{k_f} = \frac{k_e}{k_f} + K \cdot \text{Re Pr}$	<p>K=0.089 for steel spheres          K=0.091 for glass spheres          K=0.146 for 10-mm-diameter ceramic cylinders          K=0.14 for 19-mm-diameter ceramic cylinders          K=0.16 for 3.5-mm-diameter ceramic Raschig rings          K=0.21 for 1-mm-diameter copper Raschig rings</p>
Smirnov et al. 2004	Same correlation with Smirnov et al. 2003a	<p>K=0.14 for ceramic cylinder of D. 14 mm and L. 9 mm          K=0.16 for ceramic cylinder of D. 9 mm and L. 19 mm          K=0.17 for ceramic wheel w. thickness 2 mm          K=0.23 for ceramic wheel w. thickness 1 mm</p>
Metzger et al. 2004	$\frac{k_{eff,zz}}{k_f} = \frac{k_e}{k_f} + 0.073Pe^{1.59}$	For water and glass spheres $k_e \cong 0.86 \text{ W/mK}$
Jorge et al. 2010	$\frac{k_{eff,r}}{k_f} = \frac{k_e}{k_f} + 0.16 \text{Re Pr}$	<p>For nickel supported on alumina cylinders</p> <p>Where <math>\frac{k_e}{k_f} = \left( \frac{k_s}{k_f} \right)^n</math>  <math>n = 0.28 - 0.757 \log \varepsilon - 0.057 \log(k_s / k_f)</math>          (Krupiczka 1967)</p>
Testu et al. 2007	$\frac{k_{eff,zz}}{k_f} = \frac{k_e}{k_f} + 1.61 \text{Re}^{1.59}$	Water, $0 < \text{Re} < 18$
	$\frac{k_{eff,zz}}{k_f} = \frac{k_e}{k_f} + 0.126Pe^{1.45}$	Air, $12 < \text{Re} < 100$
	$\frac{k_{eff,zz}}{k_e} = 1 + \frac{k_f}{k_e} \varepsilon (1 - \varepsilon) \text{Re}^{1.5}$ $\times \left[ \frac{8.87(\text{Pr} - 0.7) - 0.543(\text{Pr} - 7.02)}{6.32} \right]$	Both water and air
	$\frac{k_{eff,yy}}{k_f} = 6.4 + 0.113Pe$	Air, $12 < \text{Re} < 130$
	$\frac{k_{eff,yy}}{k_f} = \frac{k_e}{k_f} + 0.04Pe$	Water, $0.5 < \text{Re} < 18$

In Figure 3.8, the comparison of the change of radial (or transverse) effective thermal conductivity ratios, found by using the proposed correlations in Table 3.13, with Reynolds number is shown. The radial effective thermal conductivity ratios are calculated for air. The variation of the radial effective thermal conductivity with Reynolds number for sphere, cylinder and Raschig ring particle beds with Reynolds number are shown in Figure 3.8a, 3.8b and 3.8c, respectively. The range of the experimented Reynolds numbers is considered in this diagram and the results are not extended out of the reported range. Figure 3.8a shows the variation of the radial effective thermal conductivity ratio with Reynolds number for the beds with the spherical particles. The experimental results of the beds with the spherical particles have good agreement with each other. As can be seen from the figure, the obtained experimental results for low Reynolds numbers (i.e.  $Re < 400$ ) have excellent agreement. However by the increase of Reynolds number, the consistency between the results decreases. This might be due to the occurrence of turbulent flow and the increasing effects of the surface roughness of the particles as well as the particle arrangement in the packed bed. Figure 3.8b shows the change of the radial effective thermal conductivity ratio for the cylindrical particle beds. Four correlations on the cylindrical particle beds could be found in the literature. A good consistency between the correlations can be observed. Finally, Figure 3.8c illustrates the change of  $k_{er}/k_f$  with  $Re$  for Raschig ring particles. The correlations of different studies do not align with each other. This difference between the results of the correlations might be due to the different shapes of the experimented Raschig rings and the different bed porosities because of the different thicknesses of Raschig rings. For instance, Bey and Eigenberger (Bey and Eigenberger 2001) performed experiments with thick Raschig rings ( $d_o=5$ ,  $d_i=2.2$ , and  $L = 5$  mm). However, Sminov et al. (Smirnov et al. 2003a) used relatively thin Raschig rings ( $d_o=14$ ,  $d_i=13$ , and  $L = 14$  mm). The comparison between the axial effective thermal conductivity correlations cannot be made because of the diversity of the employed packing particles and fluids.

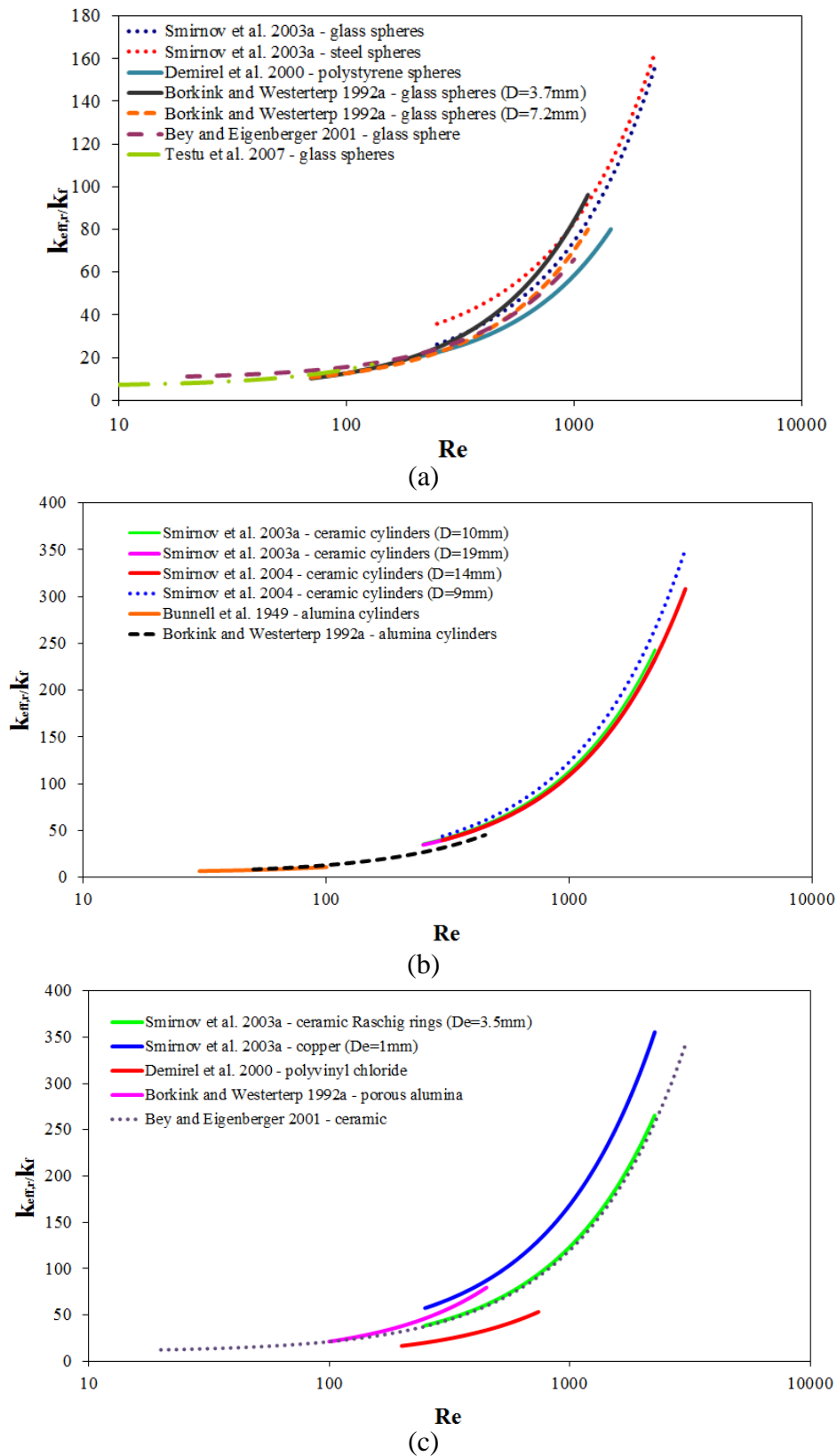


Figure 3.8. The comparison of reported correlations for determination of radial effective thermal conductivity ratios for a) spherical b) cylindrical c) Raschig ring particles

## CHAPTER 4

### CONSIDERED DOMAIN, GOVERNING EQUATIONS AND BOUNDARY CONDITIONS

In this chapter, the considered porous media for the determination of the effects of pore to throat size ratio on the macroscopic transport parameters are presented. The governing equations used in the numerical simulations and the employed boundary conditions are explained in detail. The full forms of the governing equations for fluid flow and heat transfer are previously presented in Chapter 2. In this chapter, the equations employed to obtain microscopic velocity, pressure and temperature distributions in the present study are given. Additionally, the boundary conditions required for the solution of the microscopic equations are presented.

#### 4.1. Considered Domain

The considered porous medium and the representative elementary volume (REV) that used as computational domain are shown in Figure 4.1. The square or rectangular rods are assumed very long in  $z$ -direction; hence, two-dimensional model can be used.

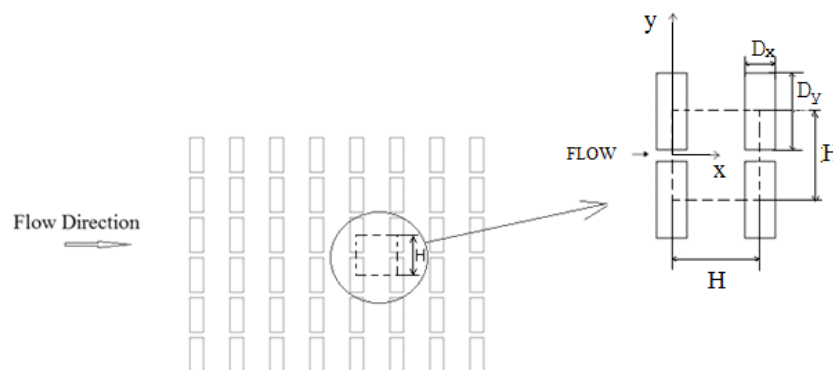


Figure 4.1. Schematic view of the considered porous medium and the REV.



The considered porous media are infinite media consisting rectangular rods. A periodic REV with the dimensions  $H \times H$  ( $10 \times 10 \text{ mm}^2$ ) is considered to investigate the throat effect.  $10 \times 10 \text{ mm}^2$  is chosen because of the dimensional analysis applied in the numerical study and it does not change the obtained results if the dimension  $H \times H$  is chosen different with considering the units of other parameters accordingly (see Table 4.1). The dimension of the REV is held constant for all cases. The square or rectangular particles are placed with in-line arrangement. The particles are rectangular with dimensions  $D_x$  and  $D_y$ . The pore to throat size ratio is defined as  $\beta = H / (H - D_y)$  and its value is changed between 1.63 and 7.46. Some sample REVs showing the change of particle shapes and pore to throat size ratio for the same porosity are shown in Figure 4.2.

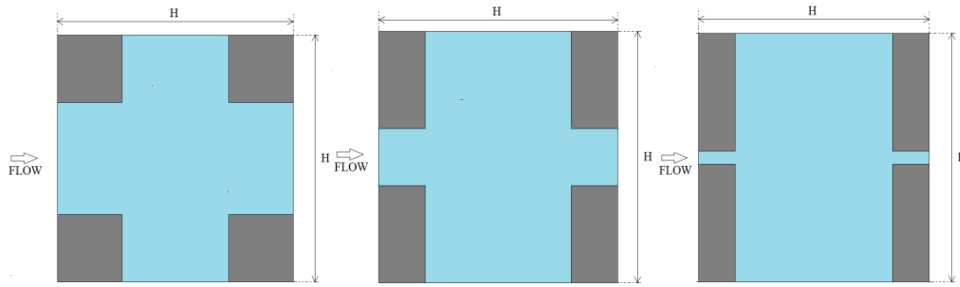


Figure 4.2. REVs with pore to throat size ratios of 1.63, 3.04 and 7.46 for  $\epsilon = 0.7$ .

The fluid flowing through the medium is assumed to be Newtonian and incompressible with constant properties. The properties of the fluid are given in Table 4.1. The geometrical properties of the considered REVs are given in Table 4.2. For all studied REVs in the present study, the porosity range of 0.7 to 0.9 is considered. The investigated flows remained in the laminar regime and the macroscopic flow is unidirectional. The REV is taken from an infinite region so the flow is fully-developed and periodical.

Table 4.1. The properties of fluid (air) used in numerical computations

$\rho_f$ (kg/m <sup>3</sup> )	1.205
$\mu_f$ (kg/m·s)	$1.821 \cdot 10^{-5}$
$k_f$ (W/m·K)	0.0258
$c_{p,f}$ (J/kg·K)	1006.43

Table 4.2. Geometric properties of investigated REV's

	$\beta=1.63$	$\beta=2.21$	$\beta=3.04$	$\beta=4.44$	$\beta=7.46$
$\varepsilon = 0.7$					
$A^*$	0.5	1	1.5	2	2.5
$D_x/H$	0.776	0.547	0.446	0.388	0.346
$D_y/H$	0.388	0.547	0.670	0.776	0.866
$d_h/H$	1.207	1.276	1.250	1.207	1.155
$d_p/H$	0.776	0.820	0.804	0.776	0.742
$\varepsilon = 0.75$					
$A^*$	0.6	1.2	1.8	2.4	3
$D_x/H$	0.646	0.456	0.372	0.323	0.289
$D_y/H$	0.388	0.547	0.670	0.776	0.866
$d_h/H$	1.454	1.492	1.434	1.368	1.300
$d_p/H$	0.727	0.746	0.717	0.684	0.650
$\varepsilon = 0.8$					
$A^*$	0.75	1.5	2.25	3	3.75
$D_x/H$	0.518	0.365	0.297	0.259	0.231
$D_y/H$	0.388	0.547	0.670	0.776	0.866
$d_h/H$	1.775	1.751	1.645	1.553	1.459
$d_p/H$	0.665	0.657	0.617	0.582	0.547
$\varepsilon = 0.9$					
$A^*$	1.5	3	4.5	6	7.5
$D_x/H$	0.260	0.182	0.149	0.129	0.115
$D_y/H$	0.388	0.547	0.670	0.776	0.866
$d_h/H$	2.802	2.458	2.193	1.991	1.827
$d_p/H$	0.467	0.410	0.366	0.332	0.305

## 4.2. Governing Equations and Boundary Conditions for Determination of Permeability and Kozeny Constant

For the determination of permeability, the fluid flow through the REV is analyzed by using microscopic continuity and momentum equations. Steady flow is assumed. Also, computations are done with governing equations in 2-D with the assumption of very long rods (in z-direction). Hence, the microscopic governing equations that are solved to determine the microscopic velocity and pressure distributions in the REV's are given as follows. For the determination of permeability and Kozeny constant, the flows in the Darcy region (low Reynolds number flows) are considered.

$$\frac{\partial u}{\partial x} + \frac{\partial v}{\partial y} = 0 \quad (4.1)$$

$$\rho_f \left( u \frac{\partial u}{\partial x} + v \frac{\partial u}{\partial y} \right) = -\frac{\partial p}{\partial x} + \mu_f \left( \frac{\partial^2 u}{\partial x^2} + \frac{\partial^2 u}{\partial y^2} \right) \quad (4.2)$$

$$\rho_f \left( u \frac{\partial v}{\partial x} + v \frac{\partial v}{\partial y} \right) = -\frac{\partial p}{\partial y} + \mu_f \left( \frac{\partial^2 v}{\partial x^2} + \frac{\partial^2 v}{\partial y^2} \right) \quad (4.3)$$

For the solution of Eqs. (4.1), (4.2) and (4.3) the boundary conditions for velocities at the boundaries of REV and at the fluid-solid interfaces are required. In order to obtain the periodical conditions an iterative procedure, which is explained in detail in Chapter 5, is applied to solve these governing equations. At the final step of the iterative procedure, a velocity profile  $f(y)$  which fulfils the requirement of periodicity of the flow is provided for the  $u$ -velocity at the fluid inlet boundary and  $v$  velocity is chosen as zero at the same boundary. At the solid-fluid interfaces no-slip boundary condition is applied. The velocity gradient at the fluid outlet boundary is assumed zero, hence no diffusion transport exists. Mathematically, the defined boundary conditions can be presented as follows.

On the fluid-solid  
interfaces and on the walls:

$$u = v = 0 \quad (4.4)$$

For the top and the bottom  
boundaries:

$$\frac{\partial u}{\partial y} = \frac{\partial v}{\partial y} = 0 \quad (4.5)$$

For the inlet boundary:

$$u = f(y), v = 0 \quad (4.6)$$

For the outlet boundary:

$$\frac{\partial u}{\partial x} = \frac{\partial v}{\partial x} = 0 \quad (4.7)$$

For the studied Reynolds numbers, the Darcy's Law (Eq. (2.10)) is valid and it can be made dimensionless by rearranging the parameters in the following way:

$$\frac{H^2}{K} = -\frac{H}{\rho \langle u \rangle^2} \text{Re} \frac{d \langle p \rangle^f}{dx} \quad (4.8)$$

where  $Re = \rho_f H \langle u \rangle / \mu_f$ . Eq. (4.8) is the dimensionless form of Darcy's Law and the term at the right hand side is called as the dimensionless macroscopic pressure drop through the porous medium while  $H^2/K$  is the inverse of dimensionless permeability. As can be seen from Eq. (4.8) there is a linear relationship between the dimensionless pressure drop and inverse of dimensionless permeability. This relation is only accurate in the Darcian region ( $Re < 1$ ), although it is observed that the applicability of this equation can be expanded to  $Re < 10$  with considerable accuracy. Since the permeability only depends on the porous structure and independent of the fluid and flow properties, its value for a REV should be a constant independent of Reynolds number. However, for high  $Re$ , the inertia effects become important and the Forchheimer term contributes to the dimensionless pressure drop. Hence, the obtained permeability value for the high  $Re$  becomes the apparent permeability if Darcy's Law is used without considering the Forchheimer term. On the other hand, the value of dimensionless pressure drop should be identical for all values of  $Re$  below 10 while some differences can be observed while approaching  $Re = 10$ .

It should be also underlined that the non-dimensional form of Darcy's law is constructed with the representative elementary volume dimension,  $H$ . Since Darcy's law is a macroscopic flow equation, the usage of the macroscopic dimension,  $H$ , for the non-dimensionalisation is appropriate and it is also provide convenience for the comparison of the permeabilities of the considered REVs.

The volume averaged values in the dimensionless form of Darcy's law may be obtained by applying the volume averaging on the microscopic velocity and pressure values.

$$\langle u \rangle = \int_V u dV \quad (4.9)$$

$$\langle p \rangle^f = \int_{V_f} p dV \quad (4.10)$$

Macroscopic velocity and pressure values found by using volume averaging integrations can be substituted into Eq. (4.8) and the permeability value can be computed by plotting the dimensionless pressure drop versus inverse of permeability for the considered REV.

In order to find Kozeny constant, Kozeny-Carman equation is employed with the computed permeability values. The pore hydraulic diameters of the REV are computed with using Eq. (2.15).

As mentioned before, Reynolds number is defined as follows for the computations.

$$\text{Re} = \frac{\langle u \rangle H}{\nu} \quad (4.11)$$

As can be seen from Eq. (4.11), Reynolds number is based on REV dimension. Some of the reasons for this selection are mentioned in the previous text. Since the macroscopic transport parameters are found in this study and the dimension of the REV is held constant, it is both useful and necessary to use H as the characteristic length in Reynolds number definition. For the microscopic investigations, pore hydraulic diameter can be used; however, it is not chosen in this study. Additionally, the definition given in Eq. (2.22) can be used; but it is not suitable for the analysis explained in the present study. The selection of H for the characteristic length is also seen in many reported studies (Nakayama et al. 2002, Alshare et al. 2010, Lopez Penha et al. 2012).

### **4.3. Governing Equations and Boundary Conditions for Determination of Interfacial Convective Heat Transfer Coefficient**

For the determination of the interfacial convective heat transfer coefficient, in addition to the motion equations, the microscopic form of energy equation of fluid is solved with the assumption of steady state. The governing equations are solved for  $1 \leq \text{Re} \leq 100$  for these computations. Macroscopically, local thermal non-equilibrium between solid and fluid phases is assumed. A uniform and constant temperature distribution is assumed in the solid phase and the energy equation for the solid phase is not taken into account.

$$\rho_f c_{pf} \left( u \frac{\partial T}{\partial x} + v \frac{\partial T}{\partial y} \right) = k_f \left( \frac{\partial^2 T}{\partial x^2} + \frac{\partial^2 T}{\partial y^2} \right) \quad (4.12)$$

For the solution of Eq. (4.12), temperature boundary conditions at the boundaries of REV and at the interfaces of solid and fluid phases are required. Considering the REV in Figure 4.1, the boundary conditions for the microscopic energy equation for fluid phase are chosen as symmetry for the top and the bottom of the REV. Periodic temperature profiles are generated for the inlet and outlet boundaries. The temperature gradient at the fluid outlet boundary is assumed zero, hence no diffusion transport exists. At the interface of the solid and fluid phases, the equality of temperature is assumed. The employed boundary conditions mathematically can be written as follows:

$$\text{In the solid phase:} \quad T_s = \text{constant} \quad (4.13)$$

$$\text{On the fluid-solid} \\ \text{interfaces:} \quad T = T_s \quad (4.14)$$

$$\text{For the top and the bottom} \\ \text{boundaries:} \quad \frac{\partial T}{\partial y} = 0 \quad (4.15)$$

$$\text{For the inlet boundary:} \quad T = g(y) \quad (4.16)$$

$$\text{For the outlet boundary:} \quad \frac{\partial T}{\partial x} = 0 \quad (4.17)$$

The function  $g(y)$  is the temperature profile which provides thermal periodicity of the REV. To obtain this function, another iterative procedure, which is explained in Chapter 5, is applied. By applying these boundary conditions and solving the microscopic energy equation for the REV with periodic boundaries, the microscopic temperature distribution in the fluid phase is obtained. Then, Eq. (2.48) can be used to compute the value of the interfacial convective heat transfer coefficient of the considered REV.

As can be seen from Eq. (2.48), macroscopic temperatures of both phases are required to compute the interfacial convective heat transfer coefficient. The macroscopic temperature of the solid phase equals to the chosen reference temperature

and the macroscopic temperature of the fluid phase can be calculated by using intrinsic volume averaging on the microscopic temperature.

$$\langle T \rangle^s = T_{ref} \quad (4.18)$$

$$\langle T \rangle^f = \frac{1}{V_f} \int_{V_f} T dV \quad (4.19)$$

The interfacial Nusselt number can be defined as follows:

$$Nu = \frac{h_{sf} H}{k_f} \quad (4.20)$$

Although different characteristic lengths such as hydraulic diameter and particle height may be employed to define Nusselt number for the studied porous structure, the dimension of the REV is selected. The same characteristic length is also selected in many reported studies (Nakayama et al. 2002, Alshare et al. 2010, Lopez Penha et al. 2012). Furthermore, a local interfacial heat transfer coefficient is defined based on the macroscopic temperature differences between the solid and fluid phases in order to explain the change of the convective heat transfer with  $Re$ ,  $\varepsilon$  and  $\beta$ .

$$h_L = \frac{\vec{n} \cdot k_f \nabla T}{(\langle T \rangle^s - \langle T \rangle^f)} \quad (4.21)$$

where  $\nabla T$  is the local temperature gradient through the solid–fluid interface. Hence, the local interfacial Nusselt number (relates to the interfacial Nusselt number at any point of the solid–fluid interface),  $Nu_L$ , is defined as:

$$Nu_L = \frac{h_L H}{k_f} \quad (4.22)$$

The interfacial Nusselt number can be calculated directly from Eqs. (2.48) and (4.20), or by the determination of the area based average of the local interfacial Nusselt number calculated by using Eq. 4.22.

#### 4.4. Governing Equations and Boundary Conditions for Determination of Thermal Dispersion Coefficients

For the determination of thermal dispersion coefficients in the longitudinal and transverse directions, microscopic energy equations for both phases are considered in addition to fluid motion equations with steady state assumption. These computations are done for the range of Re from 1 to 100.

$$\rho_f c_{pf} \left( u \frac{\partial T}{\partial x} + v \frac{\partial T}{\partial y} \right) = k_f \left( \frac{\partial^2 T}{\partial x^2} + \frac{\partial^2 T}{\partial y^2} \right) \quad (4.23)$$

$$k_s \left( \frac{\partial^2 T}{\partial x^2} + \frac{\partial^2 T}{\partial y^2} \right) = 0 \quad (4.24)$$

For the solution of these equations in order to obtain the microscopic temperature distribution throughout the REV, boundary conditions at both solid and fluid boundaries of the REV and at the interfaces of fluid and solid phases are required. At the solid-fluid interfaces, the equalities of temperature and heat flux are set. At the fluid outlet boundary change of temperature gradient is set to zero, which means no diffusive transport at this boundary. The aforementioned boundary conditions are common for the computations of both the longitudinal and transverse dispersion coefficients. However, boundary conditions for other boundaries are chosen different as to create macroscopic temperature gradient along the desired direction. For the computation of the longitudinal thermal dispersion coefficient, zero change of the temperature gradients in the y direction are chosen as boundary conditions for top and bottom boundaries. The temperature values at the solid boundaries at the inlet and outlet of the REV are set constants as  $T_{\text{ref}}$  and  $T_{\text{ref}} + \Delta T$ , respectively. Here,  $T_{\text{ref}}$  is a chosen reference temperature and  $\Delta T$  is the imposed macroscopic temperature difference value. Hence, a macroscopic temperature difference between inlet and outlet solid boundaries (along the longitudinal direction) is imposed by using this boundary condition. For the fluid inlet boundary, a temperature profile  $g(y)$ , which is obtained by using an iterative procedure (see Chapter 5), is chosen as the temperature boundary condition.  $g(y)$  profile fulfils the temperature periodicity of the REV and additionally helps to create the macroscopic linear temperature gradient of  $\Delta T$  between the inlet and outlet boundaries



of the REV. Different boundary conditions are set for the computation of the transverse thermal dispersion coefficient because of the desired temperature difference in the transverse direction. Constant temperature values are provided to the top and bottom boundaries by using  $T_{ref}$  and  $\Delta T$ . Hence, the macroscopic temperature gradient in the transverse direction is created. For the solid boundaries at the inlet and outlet of the REV, a linear temperature profile  $h(y)$  is set to provide the linear change along transverse direction. For the fluid inlet boundary, the same temperature profile  $h(y)$  is chosen as temperature boundary condition. Mathematically, the defined boundary conditions can be presented as given in Table 4.3.

Table 4.3. The boundary conditions for the determination of thermal dispersion coefficients

At the solid-fluid interfaces:	$T_f = T_s, \vec{n}_{fs} \cdot (k_f \nabla T_f) = \vec{n}_{fs} \cdot (k_s \nabla T_s)$		(4.25)
At the fluid outlet boundary:	$\frac{\partial T}{\partial x} = 0$		(4.26)
	For the computation of longitudinal thermal dispersion coefficient	For the computation of transverse thermal dispersion coefficient	
At the top and bottom boundaries:	$\frac{\partial T}{\partial y} = 0$	$T(y = -H/2) = T_{ref}$ $T(y = H/2) = T_{ref} + \Delta T$	(4.27)
At the solid boundaries of inlet and outlet :	$T(x = 0) = T_{ref}$ $T(x = H) = T_{ref} + \Delta T$	$T(x = 0) = h(y)$ $T(x = H) = h(y)$	(4.28)
At the fluid inlet boundary:	$T = g(y)$	$T = h(y)$	(4.29)

By using aforementioned boundary conditions and solving microscopic energy equations, the microscopic temperature distributions in the solid and fluid phases are obtained. For the computation of longitudinal and transverse thermal dispersion coefficients, Eqs. (4.30) and (4.31), which come directly from the equality given by Eq. (2.54), can be used.

$$k_{dis,xx} = \frac{-\rho_f c_{pf} \langle T'u' \rangle}{\nabla \langle T \rangle^f} \quad (4.30)$$

$$k_{dis,yy} = \frac{-\rho_f c_{pf} \langle T'v' \rangle}{\nabla \langle T \rangle^f} \quad (4.31)$$

where subscripts xx and yy show the longitudinal and transverse directions. The volume averaged value of the multiplication of temperature and velocity fluctuations can be found by using Eqs. (4.32) and (4.33).

$$\langle T'u' \rangle = \frac{1}{V} \int_v (T - \langle T \rangle^f)(u - \langle u \rangle^f) dV \quad (4.32)$$

$$\langle T'v' \rangle = \frac{1}{V} \int_v (T - \langle T \rangle^f)(v - \langle v \rangle^f) dV \quad (4.33)$$

## **CHAPTER 5**

# **SOLUTION TECHNIQUE AND COMPUTATIONAL DETAILS**

In this chapter, the numerical solution procedure employed for solution of the governing equations is explained in detail. Iterative procedures are employed to obtain the hydraulically and thermally periodical boundary conditions for the considered REV. The details of iterative procedures, computational method and employed parameters are presented in this chapter. The performed grid independency checks for the numerical computation of the macroscopic transport parameters are also presented.

### **5.1. Numerical Procedure**

In this section the iterative procedures employed to obtain periodical heat and fluid flow are explained in details. Different iterative procedures are applied to determine flow and temperature boundaries. It should be mentioned that the iterative procedure to obtain thermally periodical boundaries for determination of interfacial convective heat transfer coefficient is different than that for thermal dispersion.

#### **5.1.1. Iterative Procedure for Obtaining Periodical Fluid Flow Boundaries**

The boundary conditions for the motion equations, presented in Section 4.2, are the periodical boundary conditions which are found by using an iterative procedure. Hence, the function  $f(y)$  (see Eq. (4.6)) chosen for the fluid inlet boundary provides hydraulic periodicity for the inlet and outlet boundaries of the considered REV. The iterative procedure is employed in the following way.

- At the beginning of the iterative procedure, a fully developed velocity profile is defined for the fluid inlet boundary.
- After solving the governing equations and obtaining the microscopic velocity and pressure distributions in the REV, the outlet velocity profile is substituted to the inlet boundary.
- This iterative procedure continues until the same velocity distribution at the inlet and outlet boundaries are obtained.
- Additionally, the value of permeability is calculated at each iteration step and iterative procedure also continues until negligible change of the value of permeability is observed between the successive steps.

The obtained inlet and outlet velocity distributions for the REV with pore to throat size ratio of 1.63, porosity of 0.7 and the flow with Reynolds number of 100 is shown in Figure 5.1 as an example. The obtained velocity profiles are shown in the upper left corner and they seem similar at the first look. However, the detail of the velocity profiles (larger graph) indicates that the inlet and outlet velocity profiles differ from each other for the first two steps of this computation. Then, the velocity profile at the fluid outlet boundary of the third run becomes similar to the inlet profile.

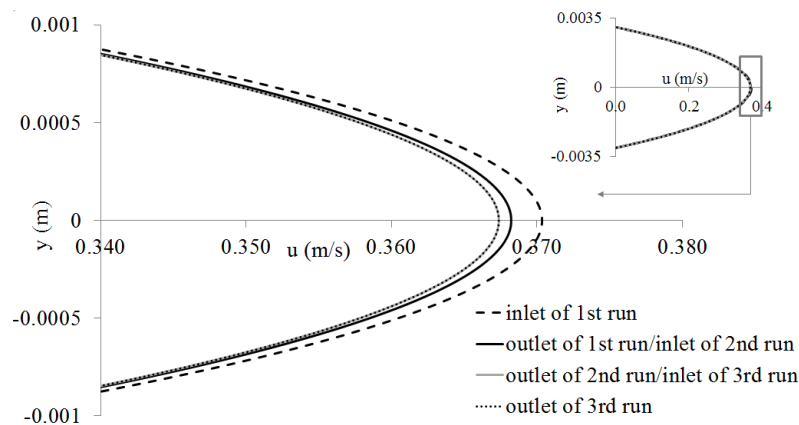


Figure 5.1. The change of velocity profiles at the inlet and outlet through the iterative procedure to obtain periodic velocity distribution in the studied REV ( $\beta = 1.63$ ,  $\varepsilon = 0.7$  and  $Re = 100$ ).

Additionally, the relative difference of the permeability values obtained for the successive iterations become acceptable. Since the value of permeability should not be

changed if the hydraulic periodicity for the flow field is achieved. Eventually, the periodicity of the flow boundaries is assumed to be valid. After these boundary conditions are reached, the computations of the permeability and Kozeny constant for the considered REV are completed as the explained way in Section 4.2.

### **5.1.2. Iterative Procedure for Obtaining Periodical Thermal Boundaries for Determination of Interfacial Convective Heat Transfer Coefficient**

The governing equations and the boundary conditions to obtain the microscopic temperature distribution in order to determine the interfacial convective heat transfer coefficient are presented in the previous chapter. To compute the interfacial convective heat transfer coefficient of the considered REV, periodical temperature boundaries should be exist at the inlet and outlet boundaries of the REV since it is taken from infinite periodical porous medium. Hence, the boundary conditions given in Section 4.3 are the periodical boundary conditions. The function  $g(y)$  (see Eq. (4.16)), which is imposed at the inlet fluid boundary, is the temperature profile which provides thermal periodicity of the inlet and outlet boundaries of the REV. This function is found by the following method.

- At the beginning of this iterative procedure, a uniform temperature which is different from the solid temperature is defined for the fluid inlet boundary
- The temperature field for the entire fluid domain is obtained by solving the energy equation for fluid.
- The temperature profile at the inlet for the subsequent computation is determined from the dimensionless temperature profile at the outlet boundary of the recent iteration.
- The iterative process continues until no change in the dimensionless temperature distribution between the inlet and outlet and no variation of the interfacial Nusselt number are observed since if a thermally fully-developed convection heat transfer is valid, no change of the dimensionless temperature and interfacial convective heat transfer should

be observed in the sequential REV's through the flow direction in the porous medium.

The dimensionless temperature is defined by Eq. (5.1).

$$\theta(y) = \frac{T(y) - T_s}{T_b - T_s} \quad (5.1)$$

where  $T_s$  and  $T_b$  are the solid and bulk temperatures, respectively.  $T_b$  is defined as follows.

$$T_b = \frac{\int_{-(H-D_y)/2}^{(H-D_y)/2} uT dy}{\int_{-(H-D_y)/2}^{(H-D_y)/2} u dy} \quad (5.2)$$

The applicability of this periodic condition for the determination of the interfacial convective heat transfer coefficient is checked by considering the forced convection in a channel with walls at constant temperature. A short channel segment with height of  $H$  and length of  $2H$  in an infinitely long channel is considered to validate the applicability of  $\theta_{inlet} = \theta_{outlet}$  as a fully-developed and periodical temperature boundary condition. Iterative procedures are applied to obtain the fully-developed flow and temperature distributions. Nusselt number is computed for various Reynolds numbers. As a result of this procedure Figure 5.2 is obtained for the variation of Nusselt number. Additionally, the results of Kuwahara et al. (Kuwahara et al. 2001), Gamrat et al. (Gamrat et al. 2008) and Shah and London (Shah and London 1978) for the channel flow  $Nu$  are shown in the figure. As can be seen from the figure, There are some differences between the present results and the results of Kuwahara et al. and Gamrat et al. for  $1 \leq Re \leq 10$ , but the difference is not exceed 2% for any of the considered Reynolds numbers. The results are well agreed with the results of Shah and London. It is also seen that Nusselt number approaches its fully developed value, 7.54, as  $Re$  increases, which is an expected situation and validates the computation procedure.

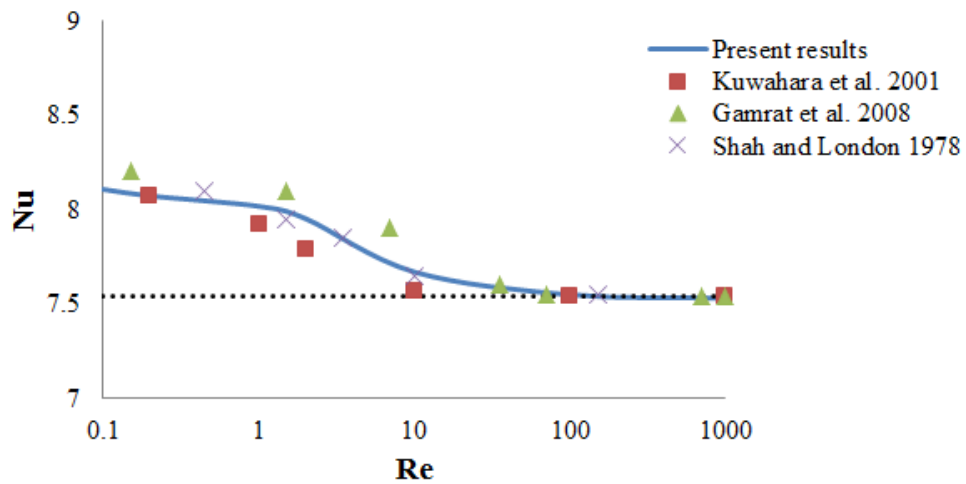


Figure 5.2. The variation of Nu with Re for channel flow

Similar to the channel segment, the periodicity of the temperature boundaries for the considered REV is succeeded by applying an iterative process. The change of the dimensionless temperature profiles at the inlet and outlet of the REV through the iterative procedure for obtaining a periodical temperature field is shown in Figure 5.3 for the REV with pore to throat size ratio of 1.63, porosity of 0.7 and the flow with  $Re = 100$  as an example. At the beginning of the iterative procedure, a uniform temperature profile for the inlet of the REV (i.e., the inlet of 1st run) is assigned to the program. Then, the dimensionless temperature profile at the outlet of the REV is calculated based on the computed outlet temperature profile. The inlet temperature profile is calculated from the dimensionless outlet temperature profile according to the equality of inlet and outlet dimensionless temperature profiles and the computation is repeated with the new inlet temperature profile. The iterative procedure is terminated when the dimensionless temperature profiles at the inlet and outlet of the REV become identical and the change of the interfacial Nusselt number becomes negligible (e.g. the inlet and outlet temperature profile of the 5th run).

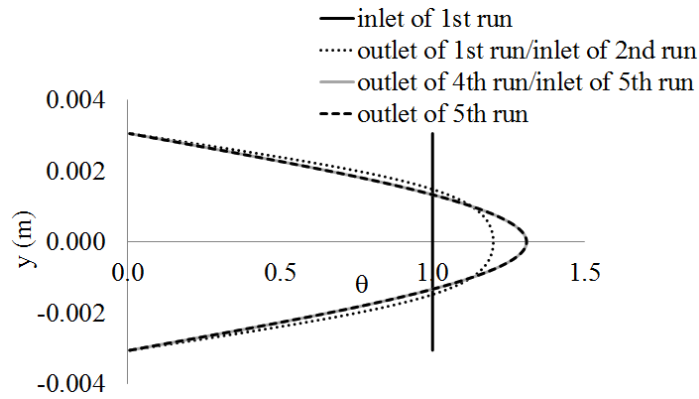


Figure 5.3. The change of dimensionless temperature ( $\theta$ ) profiles at the inlet and outlet through the iterative procedure to obtain periodic temperature distribution in the studied REV ( $\beta = 1.63$ ,  $\varepsilon = 0.7$  and  $Re = 100$ ).

### 5.1.3. Iterative Procedure for Obtaining Periodical Thermal Boundaries for Determination of Thermal Dispersion Coefficients

The boundary conditions used for the determination of the thermal dispersion coefficients are different from the boundary conditions used for the determination of interfacial heat transfer coefficient. The solid particles are assumed to have constant temperature for the computation of the interfacial heat transfer coefficient and additionally, the periodicity condition mentioned in Section 5.1.2 is used directly to provide inlet temperature profiles in the iterative procedure. On the other hand, the temperature of the solid particles are not constant in the computation of thermal dispersion and the energy equation for solid phase is solved along with the energy equation of fluid with the proper boundary conditions to obtain the temperature distribution in the REVs. Again, an iterative procedure is applied to obtain the final temperature distribution for the computation of the thermal dispersion coefficients. Similarly, the periodicity of the temperature boundaries is provided for both the longitudinal and transverse thermal dispersion; however, different iterative methods and periodicity conditions are applied.

For the determination of longitudinal thermal dispersion coefficient the following iterative method is used to provide periodic boundary condition to the REVs and determine  $g(y)$  function (see Eq. (4.29)). For the calculation of the longitudinal



thermal dispersion, as it was mentioned in the previous chapter, the temperature values at the solid boundaries of the inlet and outlet of the REV are set as  $T_{\text{ref}}$  and  $T_{\text{ref}} + \Delta T$ , respectively. In order to provide the same  $\Delta T$  for the fluid inlet and outlet boundaries, the iterative procedure is performed in the following way.

- A uniform fluid temperature for the inlet boundary is selected and the temperature profile at the outlet boundary is obtained.
- The macroscopic temperature difference ( $\Delta T$ ) is subtracted from the obtained outlet fluid temperature profile and then used as the inlet boundary condition.
- The procedure continues until the following condition is satisfied:

$$T(H, y) - T(0, y) = \Delta T \quad (5.3)$$

The last temperature profile which satisfies Eq. (5.3) is shown by  $g(y)$ . The temperature profile of  $g(y)$  fulfils the microscopic temperature periodicity of the REV and additionally helps to create a macroscopic linear temperature gradient through the flow direction/between the inlet and outlet boundaries.

For the calculation of the transverse thermal dispersion the macroscopic temperature gradient is desired to be in the transverse direction. That is why; constant and uniform temperatures are applied to the bottom and top boundaries (including symmetry and solid boundaries) as  $T_{\text{ref}}$  and  $T_{\text{ref}} + \Delta T$ , respectively. A linear temperature profile  $h(y)$  (see Eq. (4.29)), which is a 1st order function of  $y$ -direction that changes from  $T_{\text{ref}}$  to  $T_{\text{ref}} + \Delta T$ , is provided to the entire inlet boundary including both solid and fluid boundaries. The same temperature profile is also set to the outlet solid boundary. Hence, the macroscopically linear temperature gradient is generated along the transverse direction. The periodicity of the temperature distributions in the REVs are created automatically by using the aforementioned boundary conditions. After completing the iterative procedures for the computation of the longitudinal and transverse thermal dispersion coefficients, the equality of the dimensionless temperatures, which are calculated by Eq. (5.1), of the inlet and outlet fluid boundaries are achieved as a natural result.

## 5.2. Computational Details

The microscopic fluid flow and energy equations are solved for the considered REV, computationally. The grid size is chosen as 500x250 for the half of the REV which is employed as the computational domain. A commercial code based on the finite volume method is used to solve the governing equations (ANSYS/Fluent 12). The power law scheme is employed for the discretization of the convection terms in the momentum and energy equations. SIMPLE (Semi-Implicit Method for Pressure Linked Equations) method is used for handling the pressure-velocity coupling. The residual convergence criteria are set to  $10^{-9}$  for flow equations and  $10^{-12}$  for temperature. For velocity and temperature boundary conditions used in the iterative procedure, UDFs are provided to the computational program. A computer with Intel Core Duo processor (2.13 GHz, 1066 MHz, 3MB) and 4 GB RAM is used for the numerical computations. A typical computation time with flow equations is approximately 15 hours considering the iterative procedure. The solution of the energy equations considering iterative procedures had taken much less computational time (about 2.5 hours).

## 5.3. Grid Independency Tests

Grid independency tests are applied to select the best grid size for the accurate computation of permeability, interfacial convective heat transfer and thermal dispersion coefficients. Firstly, the computation of flow equations is made with different grid sizes that are changed from 50x25 to 1000x500. The change of dimensionless pressure drop with grid size is shown in Figure 5.4 for the REV with square rods ( $\varepsilon = 0.75$ ) and the flow with  $Re = 100$ . The dimensionless pressure drop values (Eq. 4.8) are computed after the periodicity of the flow field is achieved for all the considered grid sizes. This REV is used for the comparison of the present results with the results in the literature studies. Hence, the accurate computation of the flow field is important. As can be seen from the figure, the dimensionless pressure drop becomes constant for grid sizes larger than 250x500. Actually, for low Reynolds number flows, lower grid sizes are capable of capturing the accurate dimensionless pressure drop values, which is directly related with permeability. However, the computations of the interfacial convective heat transfer and

thermal dispersion coefficients are made for high Reynolds numbers as well as lower ones. Hence, 250x500 grid size is chosen for the computations.

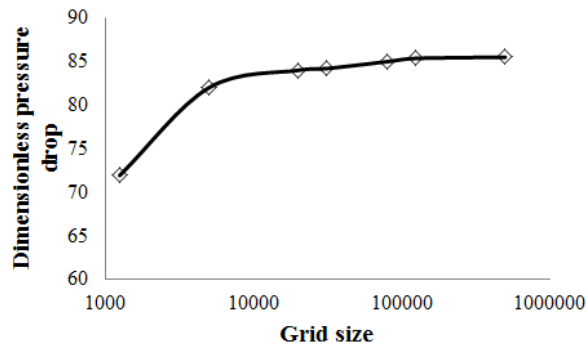


Figure 5.4. The effect of number of grid on the obtained dimensionless pressure drop values for the REV with square rods ( $\epsilon = 0.75$  and  $Re = 100$ ).

The grid independency study is also done for the computation of the interfacial heat transfer coefficient. Two extreme cases with  $\beta = 1.63$  and  $\beta = 7.46$  when  $\epsilon = 0.9$  and  $Re = 100$  are considered and the results are displayed in Figure 5.5. As can be seen, the employed grid number is sufficient to discretize the computational domain to achieve an accurate value for the interfacial Nusselt number. Hence, it is concluded that the grid size is sufficient to solve the flow and energy equations.

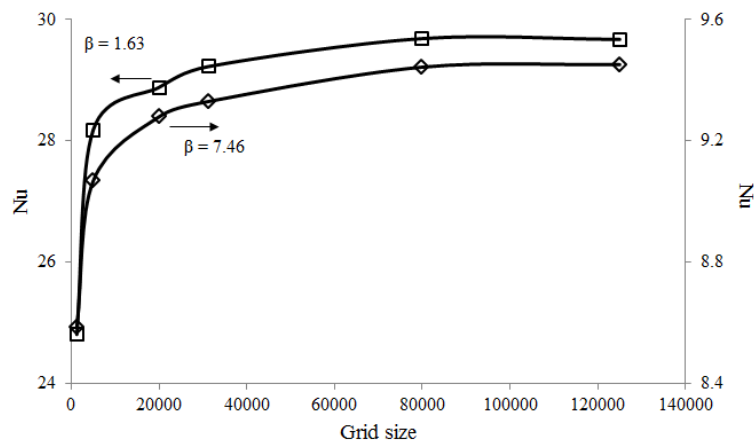


Figure 5.5 The effect of number of grid on the obtained interfacial Nusselt numbers for the REVs with  $\beta = 1.63$  and  $7.46$  ( $\epsilon = 0.9$ ) and the flow with  $Re = 100$ .

## **CHAPTER 6**

### **EXPERIMENTAL STUDY, MATERIALS AND METHOD**

In this chapter, the experimental setup used for the validation of permeability and thermal dispersion coefficients is explained in details. The experimental conditions, the materials and the procedure of the experiments are presented with tables and pictures. In the first section, the experimental setup is introduced and explained. In the second section, the preparation of the experiments is presented and finally, the experimental procedure is reported.

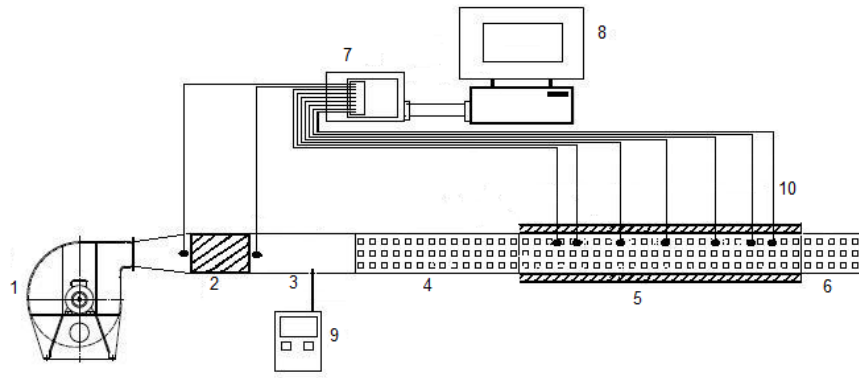
#### **6.1. Experimental Setup and Its Components**

In this section, the experimental setup and its components are explained in detail. The size of the components and setup, and the features of measurement devices are presented. The setup and devices used in the setup are shown by pictures.

The schematic of the experimental setup is shown in Figure 6.1 and the setup picture is presented in Figure 6.2. As can be seen from both pictures, the experimental setup mainly consists of a fan, a long clear channel section to provide the fully-developed velocity distribution, a porous channel constructed with long square rods, plate type heaters at the top and bottom surfaces of the test section of the porous channel and measurement and control devices. The detailed information on the components of the experimental setup is given in the following sections.

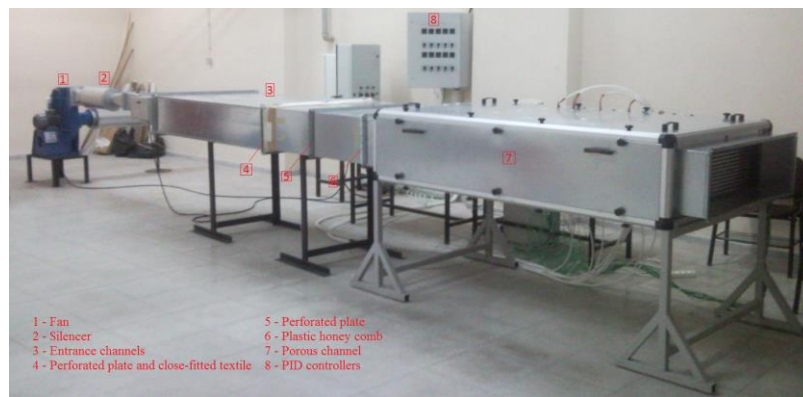
##### **6.1.1. Components of Experimental Setup**

The experimental setup consists of a fan, a preheater and a long rectangular channel system which consists of clear entrance and porous channels. These components of the experimental setup are explained in the following paragraphs separately.



- |                                                              |                           |
|--------------------------------------------------------------|---------------------------|
| 1. Fan                                                       | 6. Exit section of column |
| 2. Preheater                                                 | 7. Data logger            |
| 3. Velocity development section                              | 8. Computer               |
| 4. Entrance section of column                                | 9. Flow transducer        |
| 5. Test section of column (with heaters at top-bottom walls) | 10. Thermocouples         |

Figure 6.1. The schematic of the experimental setup.



- |                                               |                        |
|-----------------------------------------------|------------------------|
| 1 - Fan                                       | 5 - Perforated plate   |
| 2 - Silencer                                  | 6 - Plastic honey comb |
| 3 - Entrance channels                         | 7 - Porous channel     |
| 4 - Perforated plate and close-fitted textile | 8 - PID controllers    |

(a)



- |                   |
|-------------------|
| 1 - Data logger   |
| 2 - Thermocouples |
| 3 - Computer      |

(b)

Figure 6.2. The complete views of the experimental setup (a) the side view, (b) the porous channel outlet view

Fan: The air flow was provided with a fan which has nominal flow rate of 600 m<sup>3</sup>/h and pressure drop of 1.5 kPa. A frequency converter is used to change the mass flow rate, so the experiments could be done for different mass flow rates (Reynolds numbers). The fan and its control panel are shown in Figures 6.3 and 6.4.



Figure 6.3. A view of fan used in the experimental setup



Figure 6.4. Control panel of fan and preheater

Preheater: A preheater is located in the experimental setup to provide air at constant temperature at the inlet of the packed bed. Hence any fluctuations of the room temperature would not affect the experimental results. The maximum power of the preheater is 10 kW.

Channels: A channel system is placed after the fan and diffuser. The air from the fan flows through these channels and finally returns back to the room from the outlet. As can be seen from Figures 6.1 and 6.2, the first channel is a clear channel named as the entrance channel and it is placed between the diffuser and porous channel. The second channel is the porous channel (i.e., packed bed) that is after the entrance channel with the cross-section of 300x1000 mm<sup>2</sup> and total length of 1800 mm in the flow

direction. It is filled with long aluminum rods with square cross-section in inline arrangement. There are some materials such as perforated plates, a close-fitted textile and a plastic honey comb (see Figure 6.5) inserted in different location of the entrance channel to provide uniform velocity.



Figure 6.5. The view of the honeycomb plate

Porous channel (Packed bed): The pictures of the porous channel when no square rods exist are shown in Figure 6.6. As can be seen, it is a rectangular channel whose width is highly wider than its height. The schematic of the porous channel is shown in Figure 6.7 to present the size of the channel and the arrangement of the square rods. Porous channel has length of 1800 mm and cross-sectional area of  $300 \times 1000 \text{ mm}^2$ . The width of channel is larger than its height in order to reduce the effects of the side walls and convert the 3D flow into 2D. The porous channel (packed bed) was filled by placing square rods inside. The aluminum (6082) square cylinder rods with cross-section of  $10 \times 10 \text{ mm}^2$  and length of 1 m are placed perpendicular to the flow. The rods are placed with 10 mm intervals between each other in the parallel and perpendicular directions to the main flow. The number of rod rows perpendicular to flow is 15 and number of rows along the flow direction is 90. Total number of rods is 1350. The porosity of the channel is 0.75 with this placement of the rods. In order to place the square rods, wooden plates were inserted to the vertical side walls of the porous channel (see Figure 6.8).



Figure 6.6. Views of porous channel before placing the rods

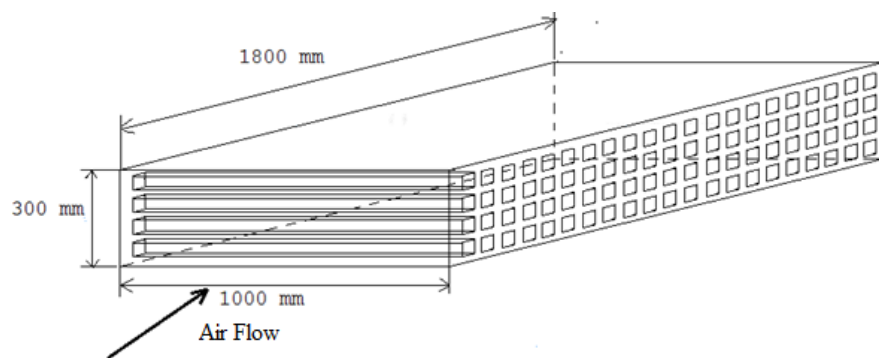


Figure 6.7. Schematic view of the packed bed (porous inlet, test and outlet sections)



Figure 6.8. Outlet of the packed bed, a) wooden plates used for the placement of rods  
b) the located rods in the channel

Porous channel has three sections as inlet, test and outlet sections with length of 500, 900 and 400 mm, respectively. The location of these sections is shown in Figure 6.9 and details are presented below.



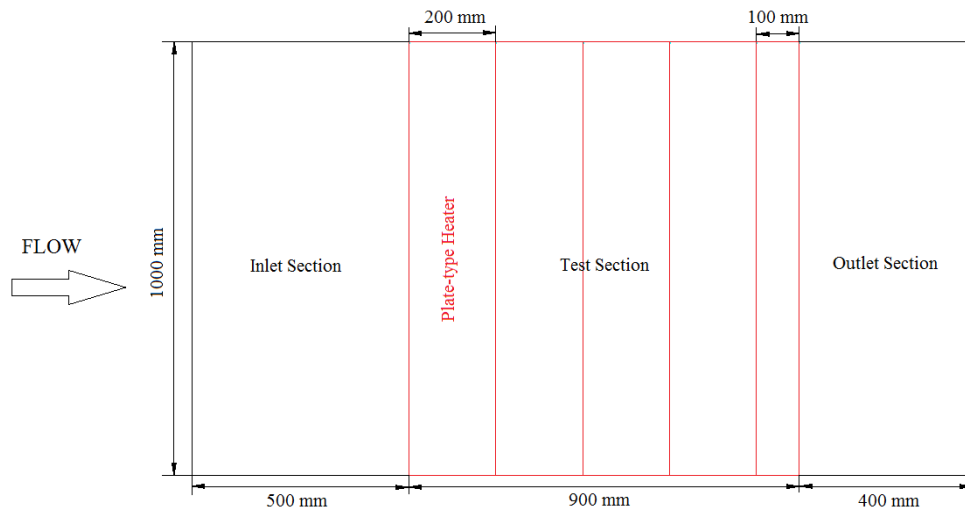


Figure 6.9. Schematic view of porous channel (inlet, test and outlet sections) - top (or bottom) view

The porous inlet section is placed after the entrance channel. It is filled with the square rods. The inlet section of the porous channel is unheated and insulated. The length of this section is 500 mm and the cross-sectional area is the same with the entrance channel as  $300 \times 1000 \text{ mm}^2$ . The porous inlet section can also be called as calming section. The aim of this section is to provide a periodic flow before entering of air into the test section. The experimental measurements were done at the next section (test section) without considering the inlet effect. In the porous inlet channel, 15 rods are placed perpendicular to air flow while 25 rods are placed in parallel direction to air flow. Total number of rods is 375 in the inlet section. Totally 10 holes with diameter of 10 mm in two different rows are drilled at the inlet section to measure air velocity and temperature at different locations as shown in Figure 6.10.

Porous test section is located after the inlet section of the packed bed. The test section has the same structure with the porous inlet section. The main difference is the plate type heaters placed at the top and bottom walls of the test section (see Figure 6.11). The heating of air was done in this section by using top and bottom heaters. The plate type heaters are electrical resistance heaters with the inlet voltage of 220 V.

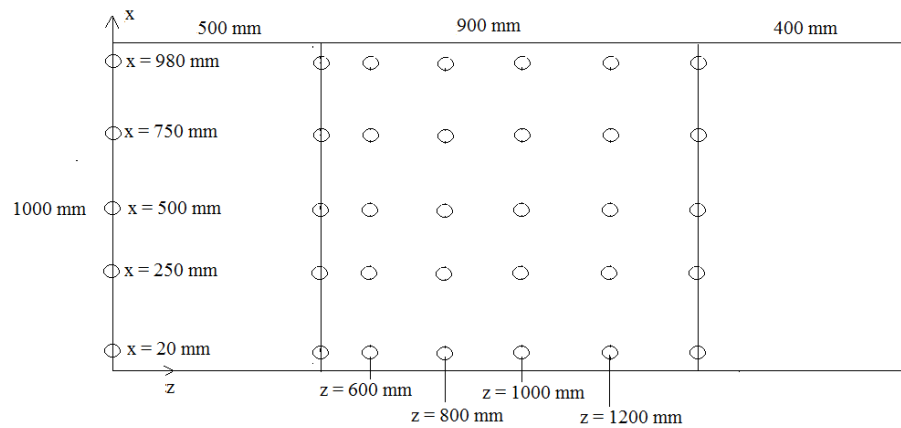


Figure 6.10. The holes for the velocity measurement – top view of the packed bed

Total of 10 plate type heaters (5 on top and 5 on bottom wall) are used to heat the top and bottom surfaces. Total of 13.5 kW power (6.75 kW for each wall) is supplied to the test section when the heaters are fully operated. Heaters were tightly fixed to the top and bottom walls to reduce the contact resistance between the wall and the heater surface. The power of each plate type heater was controlled by PID controllers, automatically.

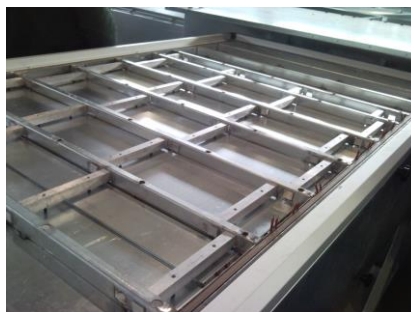


Figure 6.11. The plate type heaters at the top wall of the porous test section and the equipment to fix the heaters to the wall.

It should be mentioned that the aluminum rods with the same dimensions were placed inside the test section. 15 rods were placed in the direction perpendicular to the flow and 50 rods were placed in the direction parallel to the flow. Total of 750 rods were placed inside the test section. For the velocity and temperature measurement 25 holes in 5 rows with diameter of 10 mm were drilled at the top wall as seen from Figure 6.10.

Porous outlet section is the last section of the porous channel. Air flows through the porous outlet section and then it is dispersed into the room. The outlet section has the same structure with the rest of the porous channel. The length of the outlet section is 400 mm. Aluminum rods were placed in the outlet section to get rid of the end effects. Total number of rods in the outlet section is 225. The walls of the outlet section are insulated.

### **6.1.2. Measurement and Control Devices**

Several measurement and control devices were used during the experiments for the determination of the permeability and thermal dispersion of the packed bed. Mainly, the velocity and temperature measurements were done at different locations in the porous channel. These measurements were done to calculate the mass flow rate and the macroscopic temperatures. The detailed explanation of the devices is given in the following paragraphs.

**PID Controllers and Electrical Table:** For controlling the power of plate type heaters placed on the top and bottom walls of the test section, ENDA 4420 model PID controllers were used. There are 10 plate type heaters on the walls of the test section and each of them were controlled by different PID controller. The PID control was planned to regulate the power supplied to the heaters in order to achieve constant wall temperature value chosen by the user. The thermocouples were fixed on the top and bottom walls of channel and at the midpoints of heaters. The measured temperature signals were processed by the PID controllers. PID controllers compare the measured temperature with set temperature and regulate the electrical power input in order to achieve the set temperature. If the measured temperature is smaller than the set temperature, the power input to the heaters is allowed by PID controllers. PID controllers were placed into an electrical table. The electrical table, which is shown in Figure 6.12, also consists of contactors, fuses and solid state relays. Solid state relays (SSR) were placed in the control panel to increase the speed of the control process.

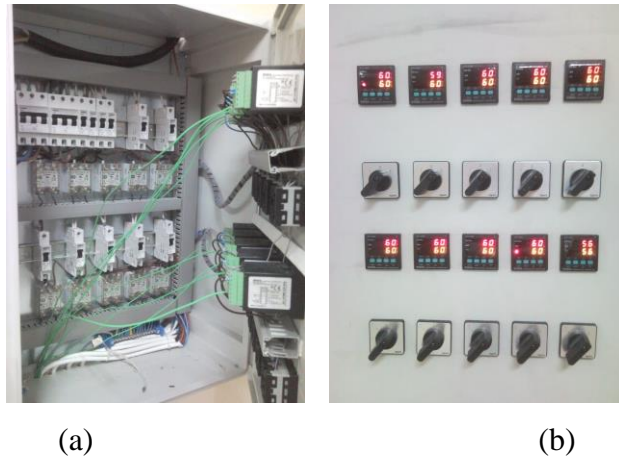


Figure 6.12. PID controllers and the electrical table (a) inside (b) cover door

Velocity Measurement Device: Testo 435-2 multi-function instrument was used to measure the air velocities at different locations. The instrument is shown in Figure 6.13. The measurement range of this device is from 0 to +20 m/s and the resolution is 0.01 m/s. A hot wire probe was used with the measurement device. The velocity measurement probe was inserted inside the channel from the holes drilled on the top wall and the velocity measurements were done at different positions through the all principal axes. To achieve accurate velocity measurements and prevent the motion of sensor, a magnetic mechanism was used and it is shown in Figure 6.13b.



Figure 6.13. Velocity measurement device (Testo 435-2) (a) main device, (b) hot wire probe and a magnetic mechanism for the velocity measurement

Temperature Measurement: For the temperature measurements in the channel, K type (NiCr-Ni) thermocouple wires were used. The diameter of the wires is 0.5 mm

and wires have Teflon insulation around them. The operating temperature range is from - 25 to + 200 °C. As mentioned before, 10 thermocouples were used to measure the top and bottom wall temperatures of the test section and the generated signals were transferred to the PID controllers. The temperature measurements in the porous channel were also made by using thermocouples. In order to collect measured temperature, Agilent 34972-A model data logger with 34908-A modules with 120 channels (3 modules with 40 channels) were used. The temperature values collected by data logger can be transferred and saved by a computer using software (see Figure 6.14).



Figure 6.14. Data logger and its computer software

## 6.2. Experimental Procedure

After calibration of temperature measuring devices, the experiments in order to validate the numerically calculated permeability and thermal dispersion coefficients were started. Three different mass flow rates (i.e. three different Reynolds numbers) were chosen for experiments. After completing experiments for the empty channel, the rods were placed into the porous channel and the main experiments were conducted. All of the experimental measurements were performed in the steady state condition. Velocity measurements were done at least 2 hours of fan work and temperature measurements were done after 4 hours of heating. The steady state conditions were also checked with the measured values at different times and also the energy input values measured by electricity meters. The details of experimental procedure are presented in the following two sections.

## 6.2.1. Experiments with Empty Channel

The procedures of taking the experimental measurements in empty channel are explained in the following paragraphs step by step.

a) Air velocity was measured by using the velocity measurement device. The hot wire probe was inserted into the empty channel from the holes drilled at the top wall. The coordinate axes considered for the measurements are shown in Figure 6.18. Velocity measurements were done at the inlet plane of the empty channel ( $z = 0$ ) and outlet plane of the test section ( $z = 1400$  mm) in 5 different horizontal and 10 different vertical locations perpendicular to the air flow (total of 50 locations per plane). The velocity measurement positions in  $xy$  plane are shown in Figure 6.19. Considering a plane perpendicular to the main flow direction, there are 2 holes near the side walls of the porous channel at the  $x = 12$  and  $988$  mm locations and 3 more holes at  $x = 250$ ,  $500$  and  $750$  mm locations.

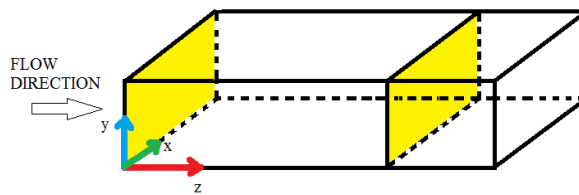


Figure 6.15. The coordinate axes considered for the velocity measurements

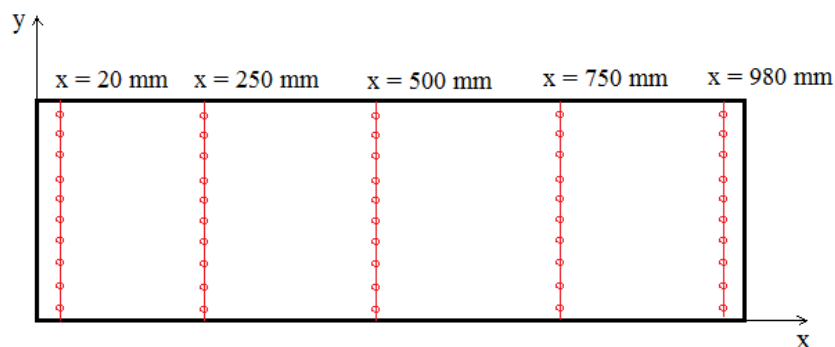
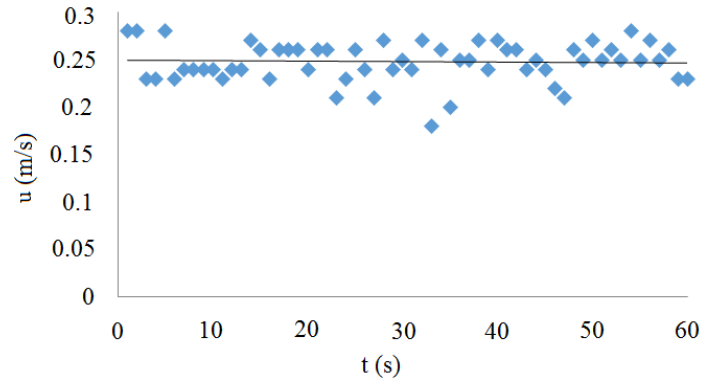


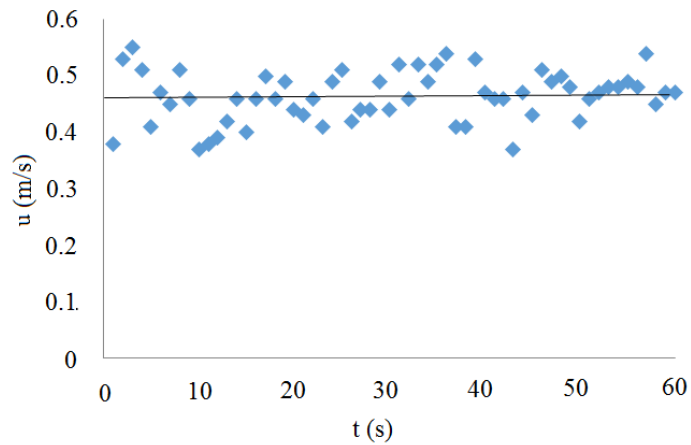
Figure 6.16. The velocity measurement locations at the inlet plane of porous channel and outlet plane of test section

The velocity measurements were conducted with data collecting frequency of 1 Hz. Two sample measurements that show the fluctuations of velocity values for  $Re =$

192 and 424 for points near the wall during the data collecting interval of 1 minute are shown in Figure 6.20. The time averaged value of measured velocity during 1 minute was used as the measured velocity value of the corresponding position.



(a)



(b)

Figure 6.17. The fluctuations in the measured velocities (a)  $Re = 192$ , (b)  $Re = 424$

b) In order to obtain mass flow rate, the planes perpendicular to the air flow were divided into  $5 \times 10$  grids that are shown in Figure 6.21. The time averaged velocities of the grid centers were obtained and then the average velocity, Reynolds number and the mass flow rate are calculated by using Eqs. (6.1), (6.2) and (6.3).

$$u_m = \frac{\sum_{i=1}^{50} u_i A_i}{\sum_{i=1}^{50} A_i} \quad (6.1)$$

$$\text{Re} = \frac{u_m H}{\nu} \quad (6.2)$$

$$\dot{m} = \rho u_m A \quad (6.3)$$

where  $u_m$  is the average velocity,  $u_i$  is the velocity along the main flow direction (z-direction, see Figure 6.30) at the  $i^{\text{th}}$  cell center,  $A_i$  are area of the  $i^{\text{th}}$  cell,  $H$  is the representative elementary volume dimension of the porous medium,  $\dot{m}$  is the mass flow rate,  $\rho$  is the density of air and  $A$  is the total cross-sectional area of the channel.

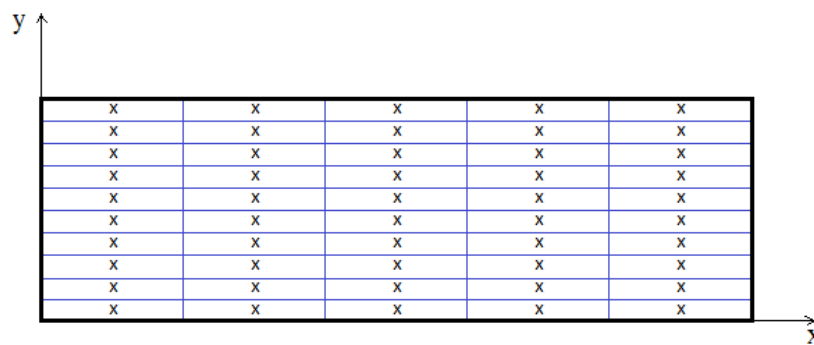


Figure 6.18. 5x10 grid used for the calculation of average velocity, temperature and mass flow rate

The velocity measurements were conducted for 3 different mass flow rate that adjusted by using the regulating switch of the fan. All measurements were repeated twice on different days and there was no considerable change between the measurements. The average of the two measurements was used for the calculations.

c) The temperatures were measured at the same locations that the velocity measurements were performed for all considered Reynolds numbers. For the temperature measurements in the empty channel a thermocouple connected to data logger was fixed in a slim pipe to provide support to the wire. Similar to the velocity measurement, the thermocouple in the pipe was inserted from the holes on the top wall of the empty channel and the temperature measurements were done at different y-locations. Total of 50 measurements for the inlet and outlet planes were taken at the same locations shown in Figure 6.19. Temperature measurements in empty channel were done with 10 Hz data collecting frequency in 10 second. Two samples of the fluctuations that were observed in the temperature measurements are shown in Figure



6.22. The fluctuations remained in  $\pm 0.05$  °C interval which is ignorable. The time averaged values of measured temperatures was used as the measured temperature of the corresponding location.

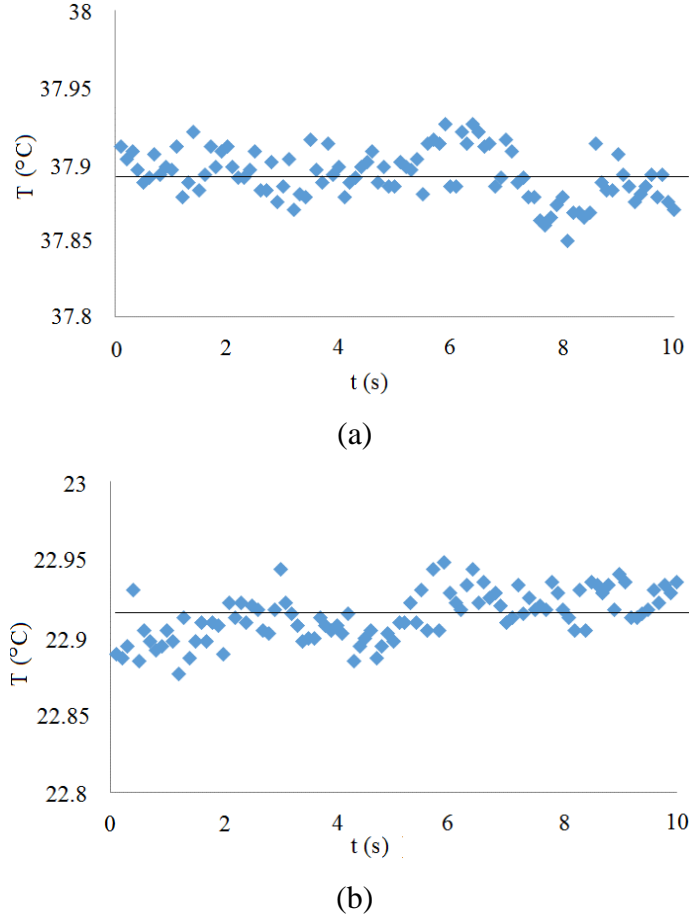


Figure 6.19. The fluctuations in the measured temperatures (a)  $Re = 192$ , (b)  $Re = 424$ .

The temperature measurements were repeated on separate days for all considered Reynolds numbers and no considerable change was observed. The average of two measurements was employed in the calculations.

d) In order to calculate the mass-weighted (bulk) temperature, the following formula is employed.

$$T_b = \frac{\sum_{i=1}^{50} u_i T_i}{\sum_{i=1}^{50} u_i} \quad (6.4)$$

where  $T_i$  is the measured temperature at the  $i^{\text{th}}$  cell center.

## 6.2.2. Experiments with Porous Channel

The velocity and temperature measurements were performed with the empty channel as explained in the previous section. After completing the experiments with empty channel, aluminum rods were placed to create the porous channel. Velocity and temperature measurements were done in the porous channel by employing the procedures employed for the experiments with the empty channel. The additional procedures employed for the porous channel are explained in the following text.

a) The velocity measurements were performed to calculate the mass flow rate and to validate the permeability value obtained in the numerical part of the study. To compute the mass flow rate, the velocity measurements were done at the entrance channels since the rods create fluctuations in the velocity in the porous channel.

b) The velocity measurements in the porous channel were performed at the REV centers and at the midpoint of the two adjacent rods as shown in Figure 6.23. Then the macroscopic velocity of  $i^{\text{th}}$  REV was obtained by the following relation:

$$u_{D,i} = \frac{u_{top,i}V_{top,i} + u_{center,i}V_{center,i} + u_{bottom,i}V_{bottom,i}}{V} \quad (6.5)$$

where  $u$  and  $V$  are measured velocity and volume, respectively. The subscripts top, bottom and center correspond to the measurement locations in the  $i^{\text{th}}$  REV. For the top and bottom voids between the particles in the REVs, the volume is  $(H - D) \cdot (H - D) / 2$  while for the central measurement its value is  $H \cdot (H - D)$ . A sample velocity measurement between the rods is shown in Figure 6.24. The velocity is made dimensionless by dividing the measured velocity values to the channel average velocity. The effects of rods on the velocity distribution can be clearly seen from the figure since the velocity values between the rods are smaller than the velocities measured at the center of the REVs.

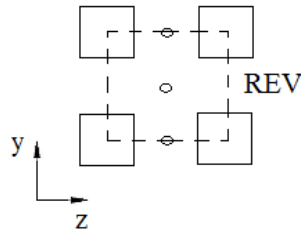


Figure 6.20. Schematic view of the velocity and temperature measurement locations in the porous channel

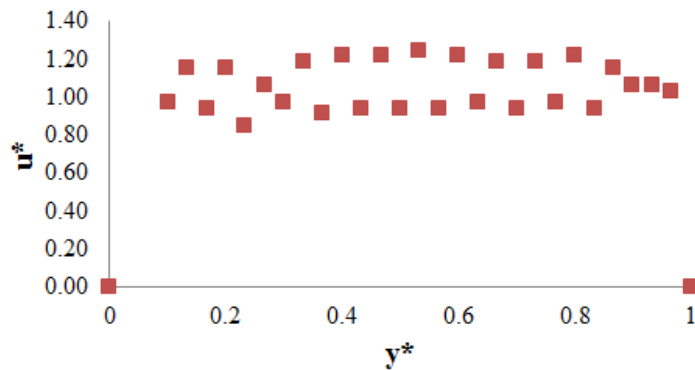


Figure 6.21. A sample measured local velocity distribution in the porous channel ( $x = 500$  mm and  $z = 1400$  mm)

c) Thermocouple wires were fixed by the rods and the temperature measurement terminals were placed in such a way that the measurements were done at the REV centers and at the midpoint of the two adjacent rods as shown in Figure 6.23. The measurements were done at different  $y$  locations at  $z = 1400$  mm to compute the macroscopic temperature values of the REV with a similar procedure used for the computation of macroscopic velocities of the REV.

The temperature and velocity measurements in the porous channel were done for the same mass flow rates (Reynolds numbers) considered for the empty channel.

The validation of the numerically obtained permeability and thermal dispersion coefficient values was done by using the computed macroscopic velocity and temperature values in the following method. The permeability of the porous structure of square rods with porosity of 0.75 was computed numerically by performing the numerical computations explained in Chapter 5. Then, the porous module of Fluent 12 was used with the numerically computed permeability value and the experimental mass flow rates. The macroscopic velocity distribution in a 2D porous channel with height of

300 mm and length of 2500 mm was obtained. By employing porous module of Fluent 12, Eqs. (2.37) and (2.56), which are the governing equations of fluid flow in porous media, were solved for the considered porous channel. Finally, the numerically and experimentally found macroscopic velocity distributions were compared. For thermal dispersion validation, the longitudinal and transverse thermal dispersion coefficients for the corresponding Reynolds numbers were computed, numerically, as explained in Chapter 5. The porous module of Fluent 12 was used with the numerically computed thermal dispersion coefficients for the 2D porous channel that the macroscopic velocity distributions were obtained before. It should be mentioned that the porous module of Fluent 12 requires the effective thermal conductivity values, which are the summation of the equivalent thermal conductivity and thermal dispersion coefficients, in the longitudinal and transverse directions (Eq. 2.57). Eq. (2.59) was used to compute the equivalent thermal dispersion value of the porous channel. Finally, the macroscopic temperature profiles obtained from this numerical computation were compared with the experimentally obtained profiles.

## CHAPTER 7

### RESULTS AND DISCUSSION

In this chapter, the obtained results for permeability, Kozeny constant, interfacial convective heat transfer and thermal dispersion coefficients are presented and discussed. The comparison of results of employed numerical model with the results of reported studies is presented in the first section. The results of the fluid flow and heat transfer computations are presented in the next three sections separately. Finally, the results obtained in the experimental study and experimental validation of numerical model are presented in the last section.

#### 7.1. Comparison of Numerical Model with Literature

Prior to analyze the effects of pore to throat size ratio on the permeability, interfacial convective heat transfer and thermal dispersion coefficients, numerical computations are done for some porous structures reported in the literature and the obtained results are compared with the results of the reported studies.

For the validation of the present numerical model, the obtained velocity and pressure distributions are compared with the results given by researchers. A REV of square rods in inline arrangement with porosity of 0.75 is considered and fluid flow equations are solved for this porous medium. The obtained velocity fields are compared with the results of Lopez Penha et al. (Lopez Penha et al. 2011) for Reynolds numbers of 1 and 100. As seen from Figure 7.1, the resulted streamlines and velocity fields of two studies are well agreed with each other. The identical flow patterns in the upper and lower gaps between the particles are found. The dimensionless pressure drop values (see Eq. 4.8) obtained for the square rods in inline arrangement are compared with the numerical values found by Kuwahara et al. (Kuwahara et al. 1996) (for porosity 0.64 and  $10^{-2} < Re < 10^3$ ) and Saada et al. (Saada et al. 2006) (for porosity 0.3 and  $10^{-2} < Re < 10^2$ ) as displayed in Figure 7.2. The obtained values of the present study and the reported literature values for dimensionless pressure drop are in a good agreement.

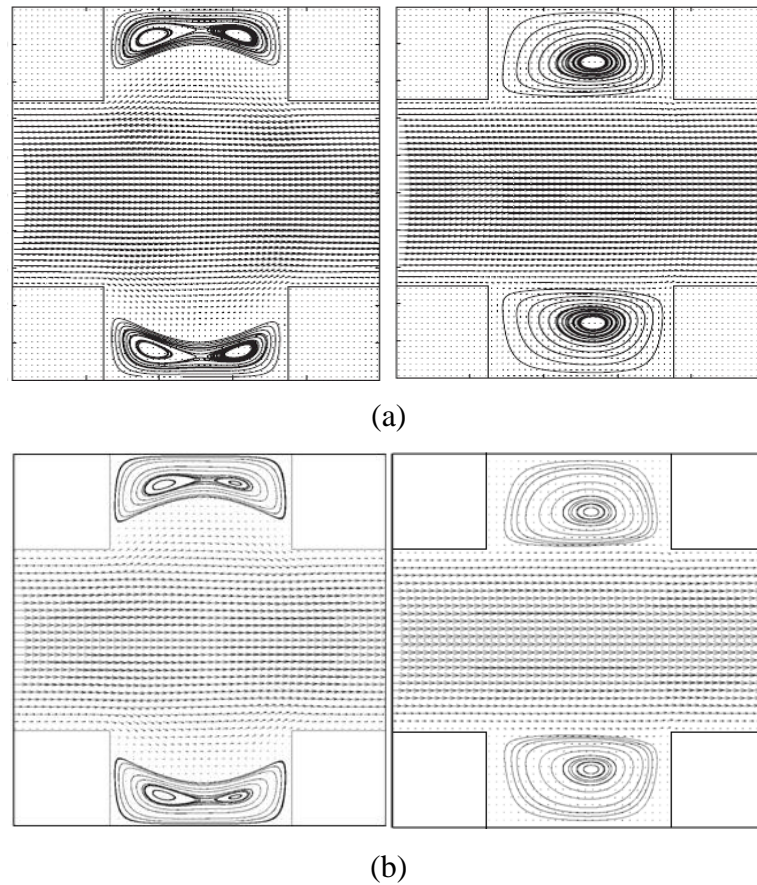


Figure 7.1. Comparison of the results of present study with the results of Lopez Penha et al. for  $Re = 1$  (left) and  $Re = 100$  (right) a) Lopez Penha et al. 2011, b) present study.

The results obtained for the variation of the dimensionless permeability with porosity is compared with the results of Saada et al. (Saada et al. 2006) in Figure 7.3. The obtained results of the present study and the results reported in the study of Saada et al. for the variation of dimensionless permeability are aligning with each other. After validating the numerical results of motion equations, the validation is performed for the computation of the interfacial convective heat transfer coefficient by solving the microscopic energy equation of fluid phase in addition to the Navier-Stokes equations. For the comparison, computations for porous media with square rods in inline arrangement and porosity of 0.75 are made. The interfacial Nusselt numbers found for this porous media are compared with the results of Nakayama et al. (Nakayama et al. 2002), Lopez Penha et al. (Lopez Penha et al. 2012) and Gamrat et al. (Gamrat et al. 2008) and the comparison is displayed in Figure 7.4. As can be seen from Figure 7.4, there is agreement between the results of present study and the literature results for a

wide range of Reynolds number. For low Re, the results obtained in the present study are aligning with the results of Nakayama et al. However, a little difference with the results of Gamrat et al. and Lopez Penha et al. is observed.

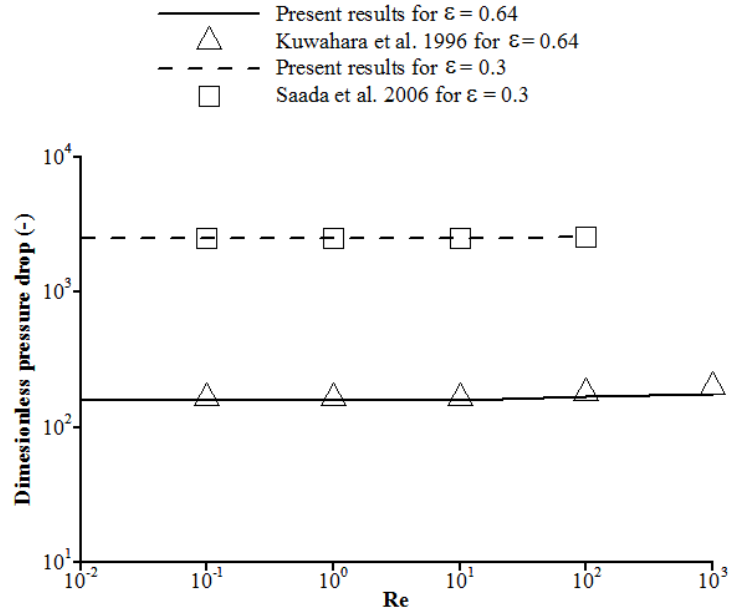


Figure 7.2. Comparison of the results of present study with the results of Kuwahara et al. 1996 and Saada et al. 2006 for the change of dimensionless pressure drop with Re.

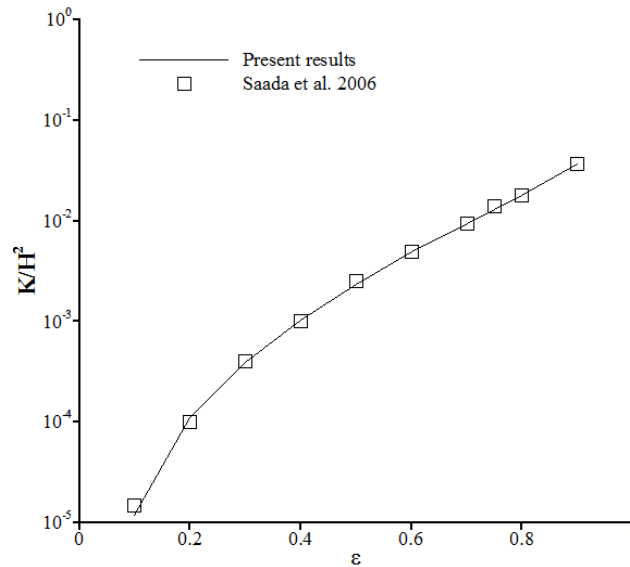


Figure 7.3. Comparison of the obtained results with the study of Saada et al. (Saada et al. 2006) for the change of dimensionless permeability with porosity.

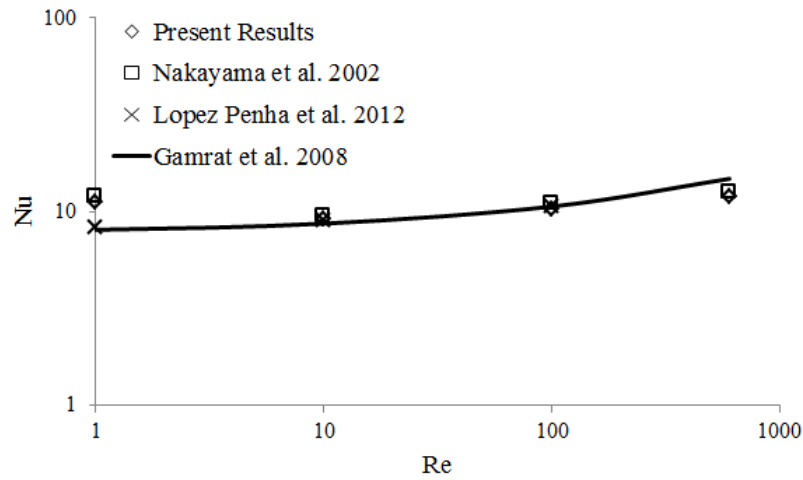


Figure 7.4. Comparison of the obtained results for the change of interfacial Nusselt number with the results of the reported studies.

The validation of the present numerical study continues by the comparison of the obtained numerical results for thermal dispersion coefficients with the reported results in the literature for porous media consisting of square rods in inline arrangement. For comparison of longitudinal effective thermal conductivity, the studies of Kuwahara and Nakayama (Kuwahara and Nakayama 1999), Jeong and Choi (Jeong and Choi 2011), Sahraoui and Kaviany (Sahraoui and Kaviany 1994), Saada et al. (Saada et al. 2006) and Alshare et al. (Alshare et al. 2010) are considered. For the comparison of transverse effective thermal conductivity, the results of Sahraoui and Kaviany (Sahraoui and Kaviany 1994) and Alshare et al. (Alshare et al. 2010) are used. The variation of the effective thermal conductivity ratio ( $k_{eff}/k_f$ , computed by using Eqs. 2.51 and 2.55) in the longitudinal direction with Peclet number is shown in Figure 7.5 for different porosity and solid-to-fluid thermal conductivity ratios. The variation of the effective thermal conductivity ratio in the transverse direction with Pe is displayed in Figure 7.6. The obtained results of the present study are in good agreement with those values reported in the literature.



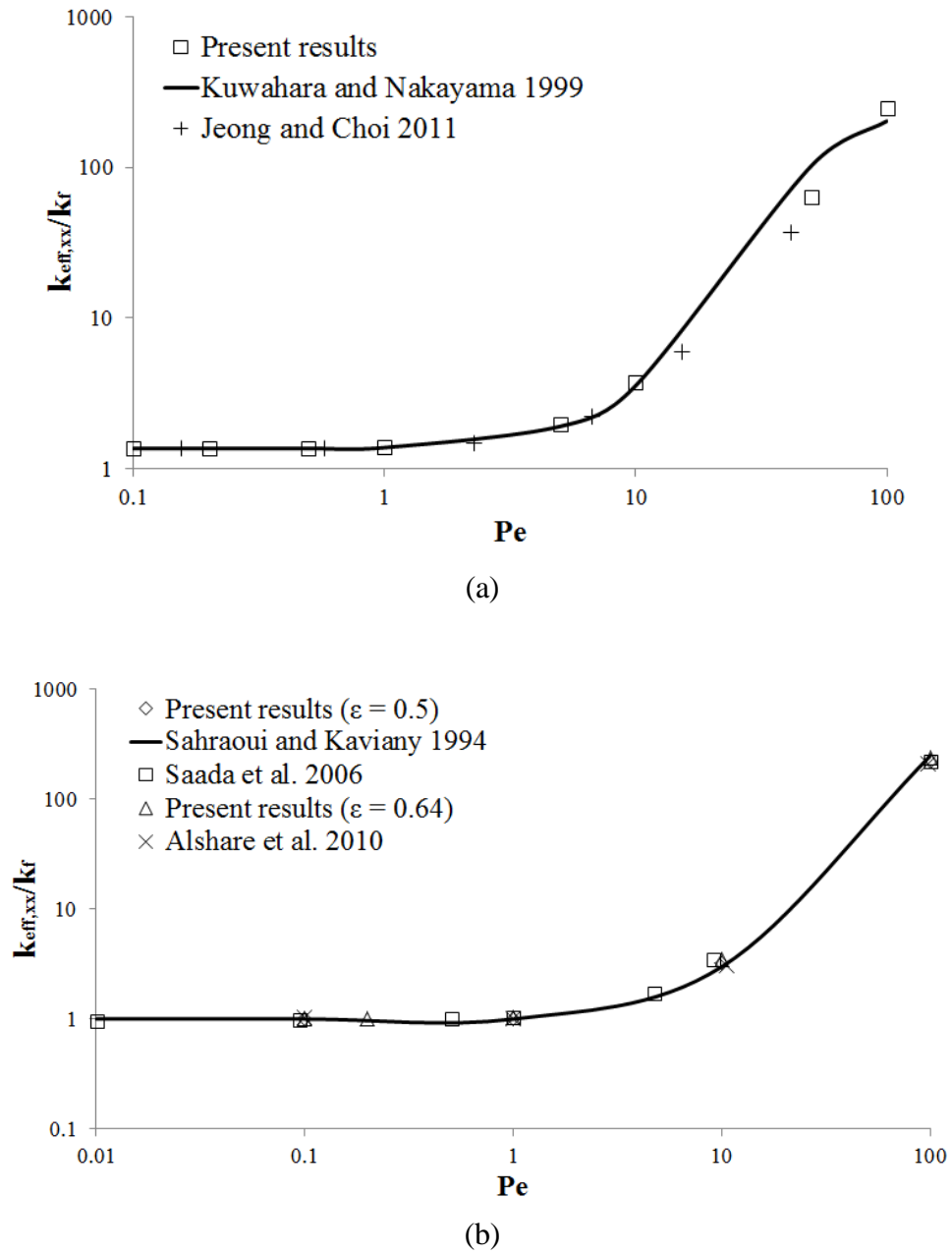


Figure 7.5. Comparison of the present results obtained for the longitudinal effective thermal conductivity with the results of reported studies (a)  $\epsilon = 0.64$  and  $k_s/k_f = 2$  and (b)  $\epsilon = 0.64$  and  $0.5$ ,  $k_s/k_f = 1$ .

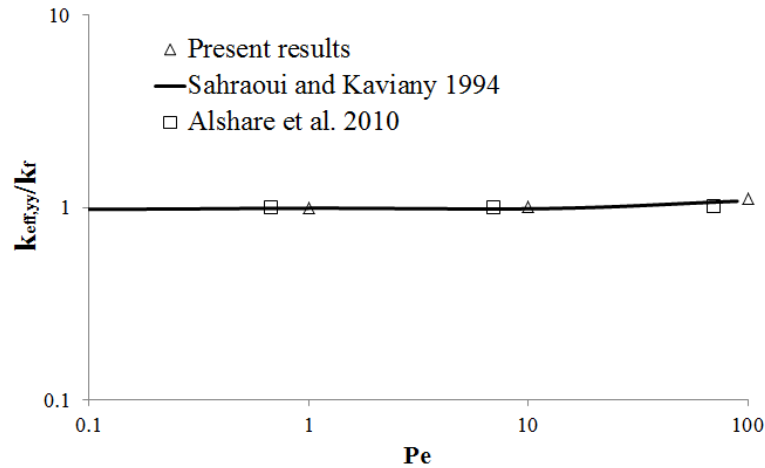


Figure 7.6. Comparison of present results obtained for the transverse effective thermal conductivity with the results of reported studies  $\varepsilon = 0.75$  and  $k_s/k_f = 1$ .

## 7.2. Results for Permeability and Kozeny Constant

In this part of the numerical study, the effects of pore to throat size ratio on the permeability and Kozeny constant are investigated. Numerical study is performed for the array of rectangular rods with different pore to throat size ratios and porosities.

### 7.2.1. Darcy and Non-Darcy Regions

In this part of the study, firstly REV's of the rectangular rods in inline arrangement with porosity of 0.7 are considered to determine the permeability. The pore to throat size ratios between 1.63 and 7.46 are studied and the effects of pore to throat size ratio on the permeability are investigated. The study is performed for Reynolds number from  $10^{-2}$  to  $10^3$ .

The microscopic governing equations with appropriate boundary conditions explained in previous chapters are solved and dimensionless pressure drop values are found according to Eq. (4.8). The change of the dimensionless pressure drop versus Reynolds number for different  $\beta$  values are shown in Figure 7.7. According to the figure, the dimensionless pressure drop increases with increasing of pore to throat size ratio and consequently the permeability value decreases. The dimensionless pressure drop of the porous medium with low value of  $\beta$  approaches to the dimensionless pressure drop of a straight channel flow, as expected. For the flow in the porous

medium with  $\beta = 1.63$ , the dimensionless pressure drop is almost constant and the Darcy's law is valid for the entire studied region. For the flows with  $\beta = 2.21, 3.04, 4.44$  and  $7.46$ , the form drag effect becomes significant in the region of  $Re > 10$ . The effect of the form drag on the fluid flow in the porous medium becomes more important for high values of the pore to throat size ratio (i.e.  $\beta = 7.46$ ). For the pore to throat size ratio of  $7.46$ , the value of the dimensionless pressure drop at  $Re$  of  $1000$  is approximately  $77\%$  greater than the value at  $Re = 0.01$ .

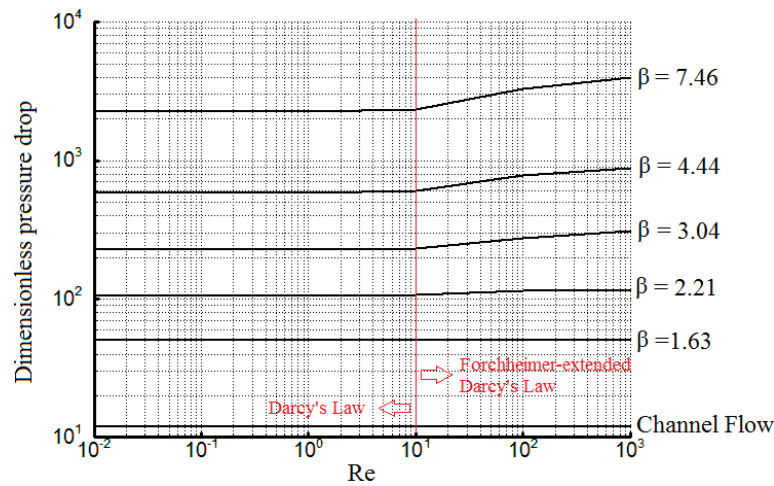


Figure 7.7. The change of dimensionless pressure drop with Reynolds number for porous media with different ratios of pore to throat size ( $\varepsilon = 0.7$ ).

The variation of the dimensionless permeability with the pore to throat size ratio is illustrated in Figure 7.8. The dimensionless permeability decreases with the increase of the pore to throat size ratio and the resistance to flow increases, as expected. The increase of  $\beta$  value from  $1.63$  to  $7.46$  causes the dimensionless permeability decreases from  $0.0198$  to  $0.0004$ .

It is found that the permeability can be considerably different for two porous media with the same porosity, particle arrangement, hydraulic pore and equivalent particle diameters, but different pore to throat size ratios. The porosity, hydraulic diameter and the particle diameter of the studied porous media are presented in Table 4.1. As indicated in the table, for the porous medium with  $\beta = 1.63$  and  $4.44$ , the porosity, hydraulic diameter and the particle diameter are identical (for porosity of  $0.7$ ). Hence the same permeability value for these two structural units is expected if the porosity and the hydraulic diameters are the only required parameters for the

determination of permeability. However, the dimensionless pressure drop (inverse dimensionless permeability) values for these REV's are approximately ten times different from each other (50.44 for  $\beta = 1.63$  and 583.45 for  $\beta = 4.44$ ). This result is important since many correlations for the determination of the permeability are proposed or derived based on porosity and hydraulic or particle diameters (Xu and Yu 2008). However, the present study shows that it is possible to have different permeability for two porous media with the same arrangement, porosity, hydraulic and particle diameters.

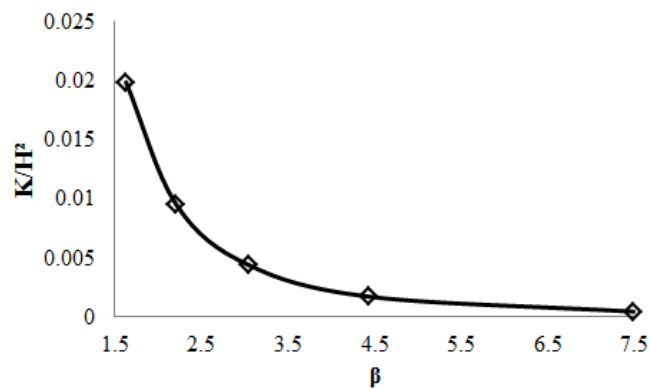


Figure 7.8. The variation of dimensionless permeability with pore to throat size ratio.

### 7.2.2 Effect of Pore to Throat Size Ratio on Kozeny Constant

The analysis of the effects of pore to throat size ratio on fluid flow is extended to investigate its effects on Kozeny constant since Kozeny-Carman permeability equation is an important relation for the determination of permeability in porous media. The applicability of Kozeny-Carman equation for the periodic porous media is investigated and the effects of porosity and pore to throat size ratio on Kozeny constant are studied. The continuity and Navier-Stokes equations are solved to determine the velocity and pressure fields in the voids between the rods. Based on the obtained flow fields, the permeability values for different porosities from 0.2 to 0.9 and pore to throat size ratios values from 1.63 to 7.46 are computed. The minimum porosities for different values of  $\beta$  are shown in Table 7.1. The investigated flows remained in the laminar region and Darcy regime ( $Re < 1$ ).

Table 7.1 Minimum achievable porosities for the considered pore to throat size ratios

$\beta$	Porosity of channel flow
1.63	0.613
2.21	0.452
3.04	0.329
4.44	0.225
7.46	0.134

As mentioned in the literature review chapter, the value of Kozeny constant was proposed as 7.5 by Nakayama et al. (Nakayama et al. 2007) for the array of square rods. Then Kozeny-Carman equation can be written as Eq. (7.1). In this equation, the dimension of the rods is used for the determination of the permeability.

$$K = \frac{\varepsilon^3 D^2}{120(1-\varepsilon)^2} \quad (7.1)$$

In Figure 7.9,  $K/D^2$  values found by numerical computations and the results found from Eq. (7.1) are plotted against  $\varepsilon^3/(1-\varepsilon)^2$  for square rods. Since Kozeny constant has a fixed value in Eq. (7.1), a linear change of  $K/D^2$  with  $\varepsilon^3/(1-\varepsilon)^2$  is observed. However, the numerical results show that Kozeny constant may have a fixed value for a wide range of porosity but it deviates from linear behavior at high porosities. Average value found by our numerical computations for Kozeny constant is approximately 7.5 for the porosities lower than 0.85 as Nakayama et al. proposed. But for higher porosities Kozeny constant increases, rapidly. As mentioned before, Happel and Brenner (Happel and Brenner 1986) also indicated that Kozeny constant increases at high porosities for different types of porous media while a fixed value can be used for lower porosities. This situation was also obtained by various researchers (see Chapter 3).

The change of dimensionless pressure drop with Re for the considered range of  $\varepsilon$  and  $\beta$  values are checked to ensure the validity of Darcy's Law. The plot of the dimensionless pressure drop versus Re for different pore to throat size ratios is given in Figure 7.10. For different values of porosity, the dimensionless pressure drop does not vary with Re for the region of  $Re < 10$  which is Darcy region. The value of dimensionless pressure drop increases with decrease of porosity for a fixed pore to throat size ratio. For instance, the value of dimensionless pressure drop for the porous

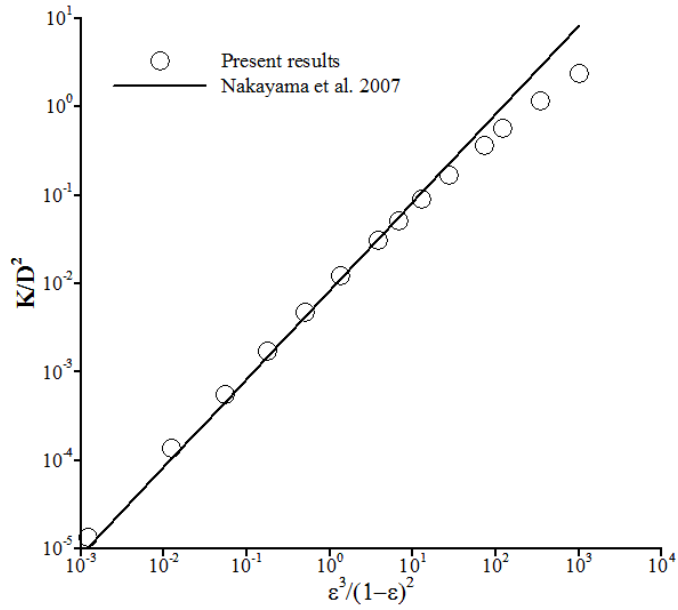


Figure 7.9. The variation of  $K/D^2$  with  $\varepsilon^3/(1-\varepsilon)^2$

media with  $\beta = 7.46$  increases from 1069.4 to 2257.4 by decrease of  $\varepsilon$  from 0.9 to 0.7. It is also observed that the dimensionless pressure drop is much greater for high values of pore to throat size ratios for a fixed porosity value. For example, for the porosity of 0.7, the dimensionless pressure drop is approximately 50.44 for pore to throat size ratio of 1.63 while this value is approximately 2257.4 for the pore to throat size ratio of 7.46.

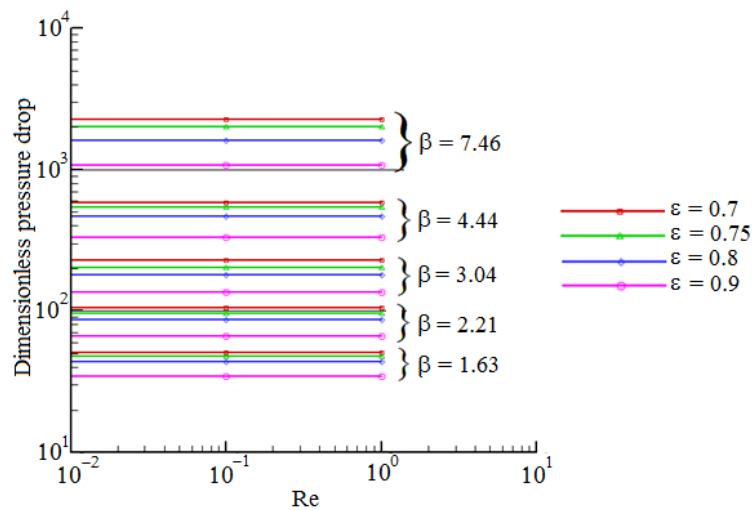


Figure 7.10. The variation of dimensionless pressure drop with Re for various porosity and pore to throat size ratios.

In order to understand the change of flow field in the voids between the rods, the streamlines and the normalized pressure distribution in the REV with  $\beta = 7.46$  are shown in Figure 7.11 for various porosities. The normalized pressure is obtained by dividing the obtained pressure values to the intrinsic averaged inlet pressure. The normalized pressure distributions are presented by colour contours and the legend on the top of the figures is valid for all cases of Figure 7.11. The normalized pressures at the inlets are around 1 for all cases. For pore to throat size ratio of 7.46, porosities as low as 0.2 can be examined and the streamlines are shown for porosities between 0.2 and 0.9. It is revealed in these figures that the pressure drop through the REV decreases with increasing porosity. The highest pressure drop occurs when the porosity of the REV equals to 0.2. Furthermore, the flow in the same REV resembles the channel flow more, as expected. Flow patterns in the figures show variety. Many secondary flows with different shapes at different regions of the REVs are seen. There are many additional flows to the main flow through the REVs. Although the mass flow within the vortices may be very low, their existence cannot be ignored. As can be seen from the figures, pressure drop mainly occurs at the corners of the rods for the high porosity REVs whereas pressure drop through the structural unit is nearly linear for low porosities. The number of vortices in the pore between the rods decreases as porosity increases from 0.2 to 0.4. The flow enters to the bottom and top gaps by the increase of the porosity. The areas occupied by the secondary flows also decrease. There is only one secondary flow between the rods for porosities between 0.4 and 0.6. For porosity of 0.7 the secondary flow in the gap split up into two vortices. There are two secondary flows in the gap for the porosities higher than 0.7. The entrance of the main flow into the top and bottom gaps is such that the top and bottom secondary flows split to two separate vortices for porosity of 0.8 and 0.9, as seen from the figure. These secondary flows become closer to the lower corners of the REVs while porosity increases.

The streamlines and the normalized pressure distributions for different values of pore to throat size ratios are displayed in Figure 7.12 for  $\varepsilon = 0.75$ . Similar to Figure 7.11, the pressure distributions in the REVs are normalized and plotted by colored contours. The legend on the top of Figure 7.12 is valid for all cases of the figure. The values of normalized pressures at the inlets are around 1 for the all the presented cases.

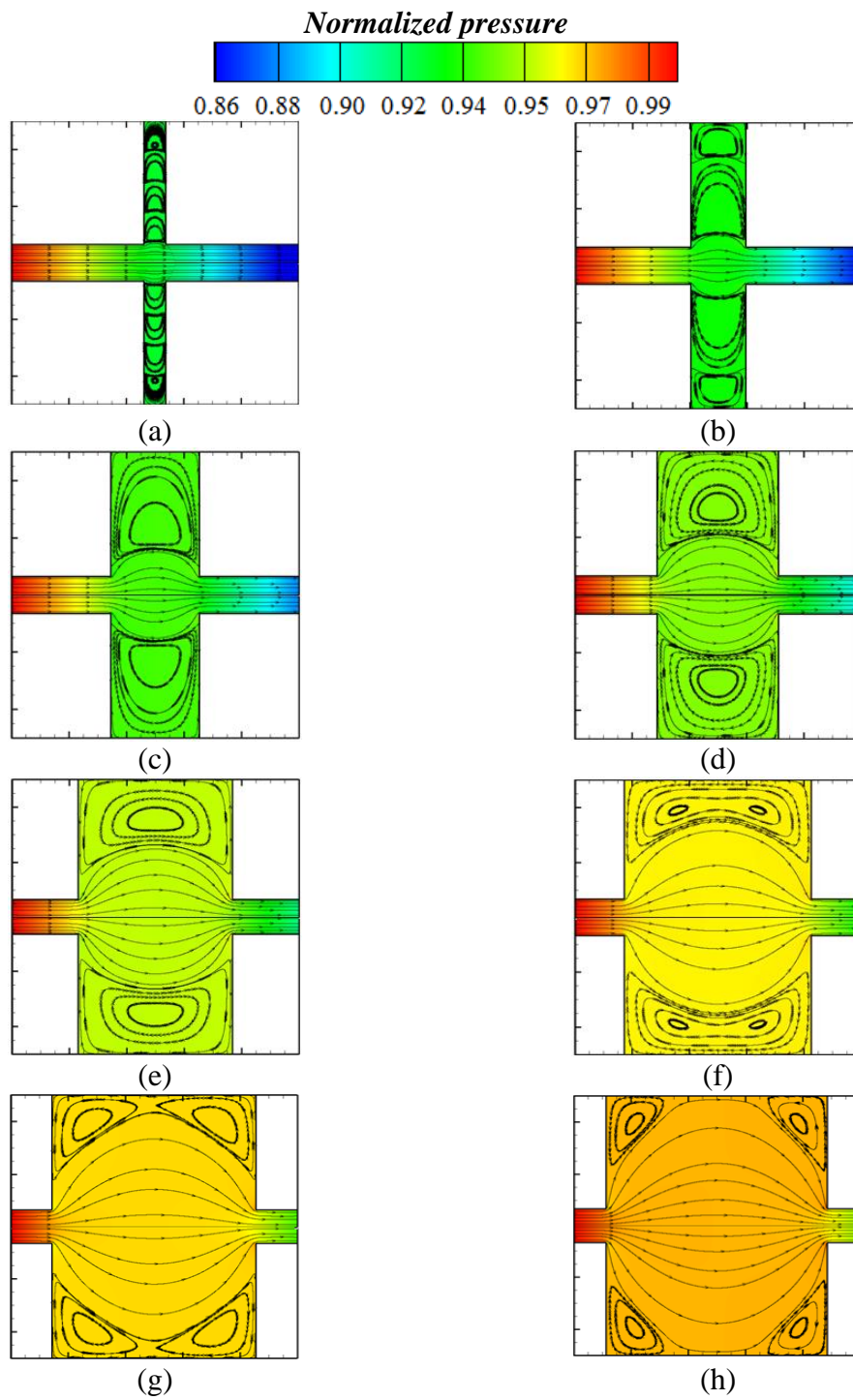


Figure 7.11. Streamlines and pressure contours in the porous media with  $\beta = 7.46$  for porosities of a) 0.2, b) 0.3, c) 0.4, d) 0.5, e) 0.6, f) 0.7, g) 0.8, h) 0.9



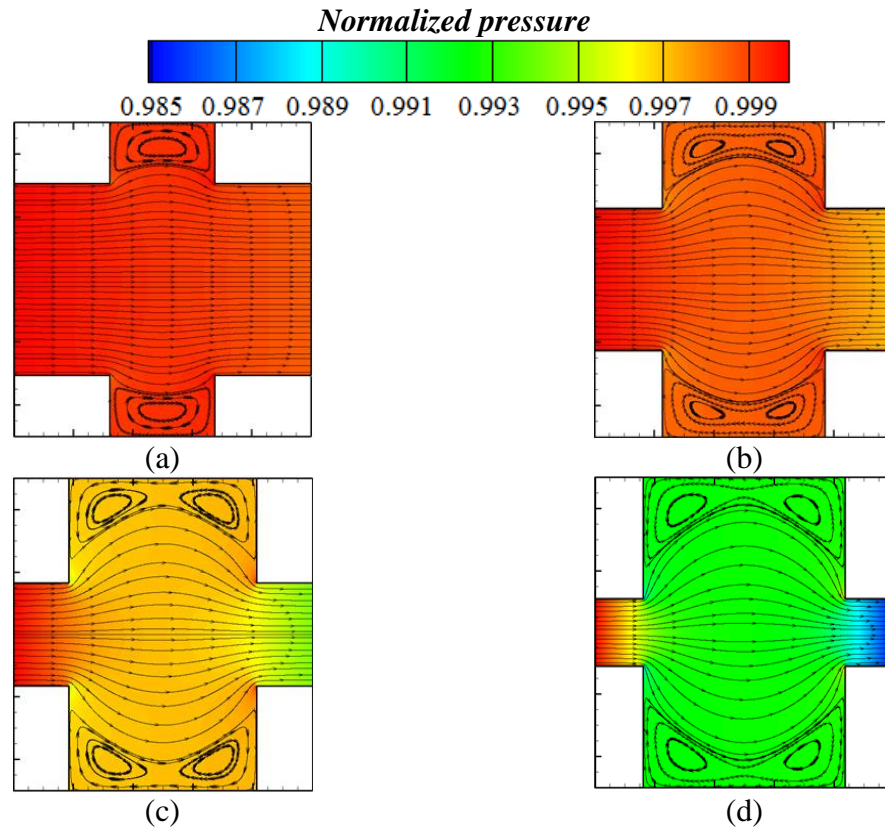


Figure 7.12. Streamlines and normalized pressure contours in porous media with  $\varepsilon = 0.75$  and for pore to throat size ratios of a) 1.63, b) 2.21, c) 3.04, d) 4.44

As can be seen from Figure 7.12, the pressure drop is relatively low for  $\beta = 1.63$ . There are vortices in the top and bottom gaps between the rods. These secondary flows are split up into two vortices except for the case of  $\beta = 1.63$ . The main flow is straight forward and does not enter to the top and bottom gaps between the rods. The pressure drop increases and the main flow penetrate to the top and bottom gaps by the increase of  $\beta$ . Hence the vortices in the secondary flow approach to the rods. There are almost four vortices at the different regions of the REV of porous medium with  $\beta = 4.44$ . There are sudden pressure decrease (expansion) and pressure increase (compression) at the corners of the rods. These pressure changes are higher for lower pore to throat size ratios while the throat effect is getting more significant for high pore to throat size ratios.

The change of dimensionless pressure gradient with porosity for the porous media with different ratios of pore to throat size is shown in Figure 7.13. The limiting values represent dimensionless pressure gradients in the straight channel flows with the same throat sizes. The schematics of the structural units for  $\beta = 1.63$  with different

porosities are also shown in Figure 7.13. For small values of pore to throat size ratio, structural cells with lower porosities are not achievable because of geometrical restrictions. While the pore to throat size ratio increases, REV's with lower porosities can be obtained. The limiting values at low porosities show channel flows with the same throat size. The dimensionless pressure drop values are highest at this flow. It is shown in the figure that the dimensionless pressure drop decreases with increasing porosity for all cases. As mentioned above, the dimensionless pressure drop increases while pore to throat size ratio increases. It means that while the throat size decreases throat effect become influential on the pressure drop through porous media and the pressure drop increases rapidly. As mentioned before, the dimensionless pressure gradient for low Reynolds number flows is equivalent to the inverse of the dimensionless permeability. Since the dimension of the REV is constant, it can be said that the permeability increases with decreasing pore to throat size ratio and increasing porosity.

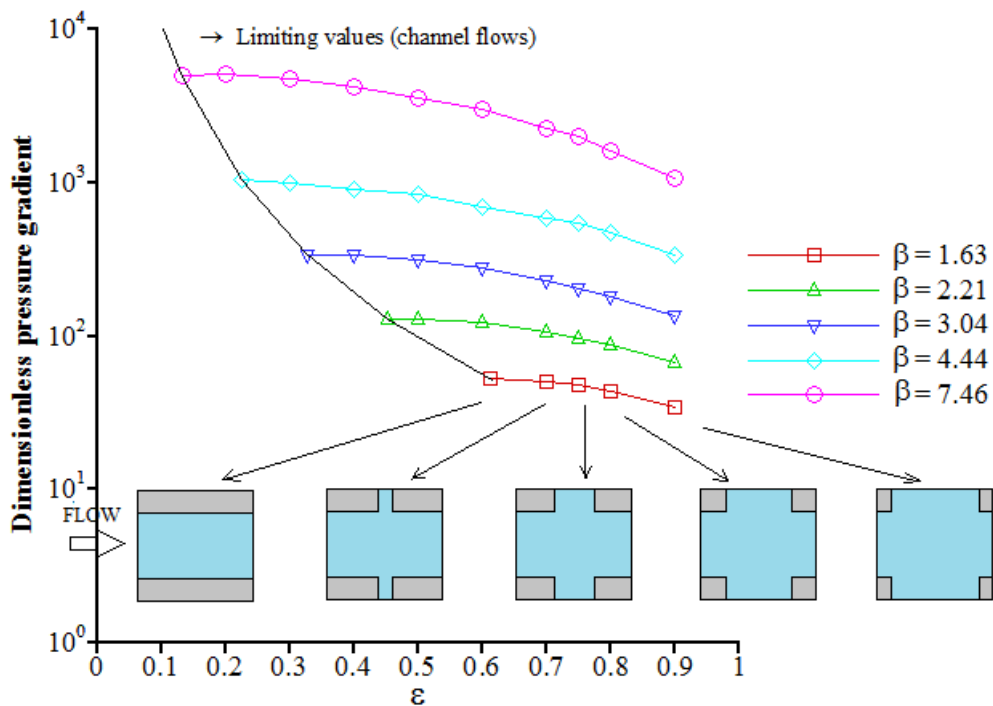


Figure 7.13. The change of dimensionless pressure gradient with porosity for porous media with different pore to throat size ratios.

The variation of  $K/d_h^2$  values with porosity for different ratios of pore to throat size ratios is shown in Figure 7.14. The main form of Kozeny-Carman equation (Eq. 2.14) relates  $K/d_h^2$  with porosity. It is shown in this figure that the pore to throat size

ratio should be taken into consideration while using Kozeny-Carman equation. For the same porosity value, the values for  $K/d_h^2$  are very different from each other for different pore to throat sizes. Hence, porosity alone cannot be sufficient to determine the Kozeny constant.

The dimensionless pressure drop is defined based on the REV dimension (i.e., H). This value is the same for all the studied REVs considered in the present study. However, in order to obtain Kozeny constant values of different REVs, Eq. (2.14) should be used in which the permeability is defined based on the hydraulic diameter of the considered REV. The variation of Kozeny constant with porosity is illustrated in Figure 7.15 for the considered pore to throat size ratios. As can be seen from the figure, the value of Kozeny constant depends on both  $\epsilon$  and  $\beta$ . Almost, a linear variation of Kozeny constant with porosity is observed for the all values of pore to throat size ratio values at low porosities (i.e.,  $\epsilon < 0.7$ ). However, the slope of Kozeny constant with  $\epsilon$  is changed for  $\epsilon > 0.7$ .

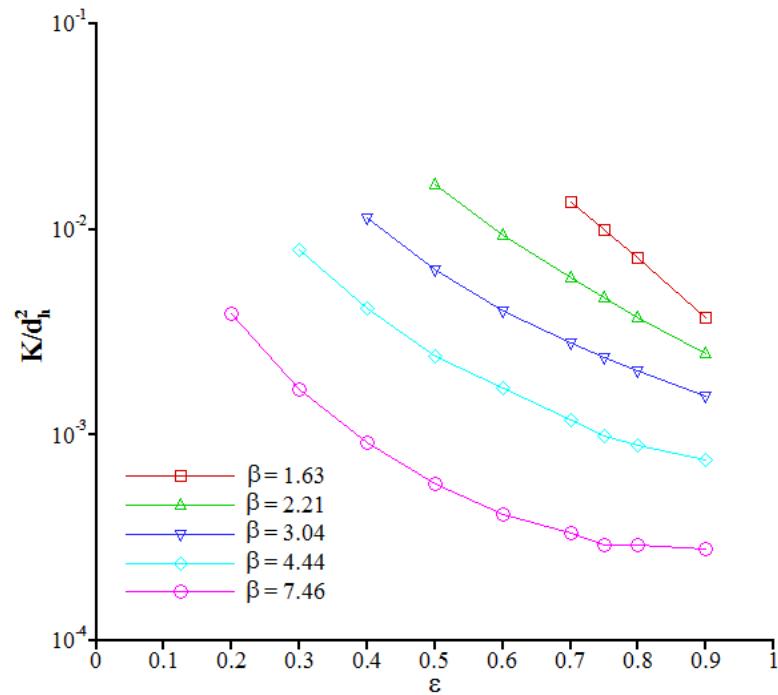


Figure 7.14. The variation of  $K/d_h^2$  with porosity for different pore to throat size ratios

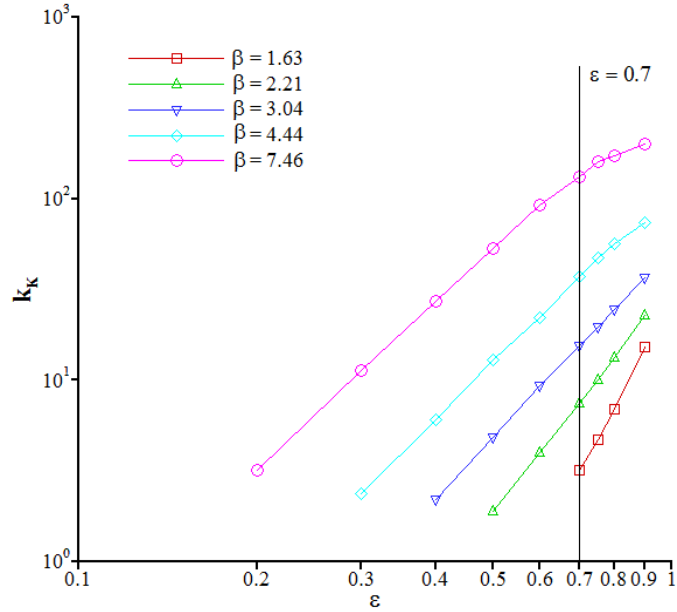


Figure 7.15. The variation of Kozeny constant with porosity for different pore to throat size ratios

An attempt is performed to obtain a general equation for Kozeny constant based on pore to throat size ratio and porosity. As can be seen from Figure 7.15, Kozeny constant generally changes with a power of porosity. Therefore, Eq. (7.2) may be a proper mathematical relationship for the change of Kozeny constant with porosity for  $0.2 < \varepsilon < 0.9$  and  $1.63 < \beta < 7.46$ .

$$k_K = A\varepsilon^B \quad (7.2)$$

where A and B coefficients are functions of pore to throat size ratio and the following equations are proposed to calculate their values.

$$A = C_0\beta^4 + C_1\beta^3 + C_2\beta^2 + C_3\beta + C_4 \quad (7.3)$$

$$B = D_0\beta^4 + D_1\beta^3 + D_2\beta^2 + D_3\beta + D_4 \quad (7.4)$$

Based on the obtained Kozeny constant values, the coefficients of Eqs. (7.3) and (7.4) are calculated and given in Table 7.2 for two different regions separated by the porosity value of 0.7 ( $\varepsilon < 0.7$  and  $\varepsilon \geq 0.7$ ). The coefficient of determination ( $R^2$ ) values

for A and B coefficients are 1 for  $\epsilon < 0.7$  region and 0.9998 and 0.9992 for  $\epsilon \geq 0.7$ , respectively.

Table 7.2. The empirical coefficients for the determination of Kozeny constant

	For $\epsilon < 0.7$	For $\epsilon \geq 0.7$
$C_0$	-0.6372	0.3496
$C_1$	12.358	-5.6485
$C_2$	-72.413	36.482
$C_3$	199.52	-77.519
$C_4$	-172.44	80.773
$D_0$	0.0079	0.0242
$D_1$	-0.1684	-0.4878
$D_2$	1.33	3.6015
$D_3$	-4.7367	-11.958
$D_4$	9.7242	18.028

Based on Eq. (2.14), a linear variation exists between the term of  $16Kk_K/d_h^2$  and  $\epsilon$ . This linear variation with slope of 45 degree can be seen in Figure 7.16 as a solid line. For all cases considered in this study, the values of Kozeny constant, hydraulic diameter and permeability are determined by using Eqs. (2.13), (2.14) and (7.2), then

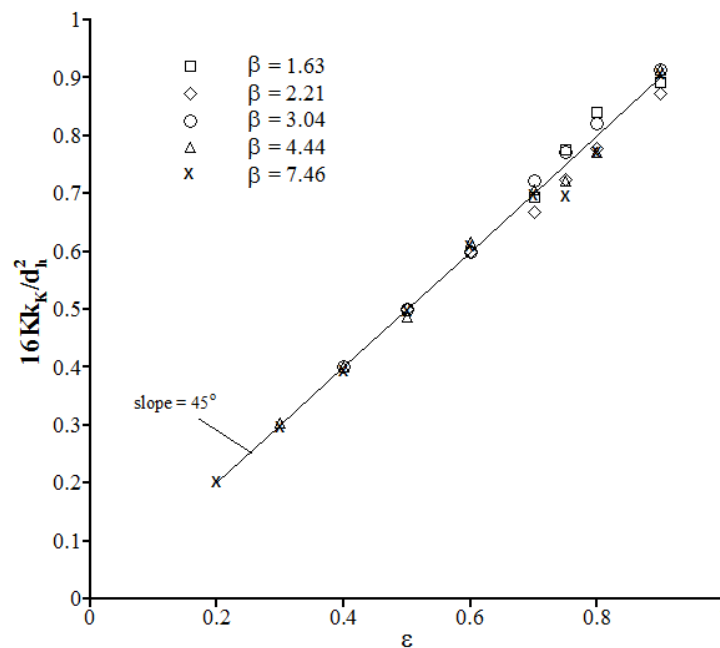


Figure 7.16. The comparison of the predicted  $16Kk_K/d_h^2$  values by using Eqs. (2.13), (2.14) and (7.2) with Kozeny-Carman permeability equation.

the ratio of  $16Kk_{\kappa} / d_h^2$  is determined and plotted with respect to  $\varepsilon$ . As seen from Figure 7.16, the computed results (based on the proposed model) linearly changes with  $\varepsilon$  when  $\varepsilon < 0.7$ . Although the computed values for  $\varepsilon \geq 0.7$  do not fit solid line as well as for  $\varepsilon < 0.7$ , a good agreement can be observed. This linear relationship between the computed values from the proposed model and  $\varepsilon$  exists if only the Kozeny constant is determined as a function of both porosity and pore to throat size ratio. Hence, the suggested relation for the determination of Kozeny constant can gather the effects of both porosity and pore to throat ratio into a single mathematical relation and provides acceptable results for calculation of permeability for wide ranges of porosity and pore to throat size ratio of porous media. It should be mentioned that the proposed relation is valid for a porous medium with rectangular rods in a periodic inline arrangement and square REV.

### **7.3. Results for Interfacial Convective Heat Transfer Coefficient**

In this study, the effects of pore to throat size ratio on the interfacial heat transfer coefficient for a periodic porous media containing inline array of rectangular rods are investigated, numerically. As it was mentioned in the literature review of the studies on the determination of the interfacial heat transfer coefficient, the effects of porosity, Re, particle arrangement and flow direction were widely investigated in the literature. However, the effect of pore to throat size ratios on the interfacial heat transfer coefficient was not studied. In this thesis, the interfacial heat transfer coefficients of porous media with different porosity and pore to throat size ratios are investigated, numerically. The continuity, Navier–Stokes, and energy equations are solved for the representative elementary volume (REV) of the porous media to obtain the microscopic velocity and temperature distributions in the voids between the rods (see Chapter 4 and 5). Based on the obtained microscopic temperature distributions, the interfacial convective heat transfer coefficients and the corresponding interfacial Nusselt numbers are computed. The study is performed for pore to throat size ratios between 1.63 and 7.46, porosities from 0.7 to 0.9, and Reynolds numbers between 1 and 100.

### 7.3.1. Effects of Pore to Throat Size Ratio on Interfacial Nusselt Number

First of all, the effects of pore to throat size ratio on the interfacial Nusselt number is investigated independent of porosity. The streamlines and temperature contours for  $\beta = 1.63$ ,  $\varepsilon = 0.7$  and for different Reynolds numbers are displayed in Figure 7.17. In order to compare different temperature fields, a dimensionless temperature definition is used as:

$$\langle \theta \rangle^f = \frac{\langle T \rangle^f - T_{\min}}{T_{\max} - T_{\min}} \quad (7.5)$$

where  $T_{\min}$  and  $T_{\max}$  are the minimum and maximum temperatures in the REV, respectively. For all presented Reynolds numbers, two types of flow as main and secondary flows are observed. The main flow generally resembles a clear channel flow through the porous medium while the secondary flows occur in the gaps between the particles. The temperature distribution considerably changes with Reynolds number.

For  $Re = 1$ , the fluid slowly passes through the REV (i.e., weak convective transport) and its residence time in the REV is longer. As a result, the fluid temperature can increase to the solid temperature just after the inlet throat and the volume averaged dimensionless fluid temperature is high ( $\langle \theta \rangle^f = 0.862$ ). The local heat transfer coefficient near the inlet section is expected to be very large compared to other surfaces of the solid in REV. As Reynolds number increases to  $Re = 10$ , the convective heat transport becomes stronger and the residence time of the fluid particles in the porous medium diminishes. Furthermore, thermal boundary layers occur on the horizontal surfaces of the solid particles, which create a thermal resistance for the heat flow in the transverse direction of the fluid flow. As a result, a remarkable temperature difference between the center and the solid surface region is observed. The volume averaged dimensionless temperature,  $\langle \theta \rangle^f$  reduces to 0.673. Further increase in Re number ( $Re = 100$ ) causes the decrease of the thermal boundary layer thickness. As Re increases, the convection heat transfer become stronger, the residence time of the fluid in the REV

decreases, and a uniform temperature along the flow direction is observed. For  $Re = 100$ ,  $\langle \theta \rangle^f$  becomes as 0.472.

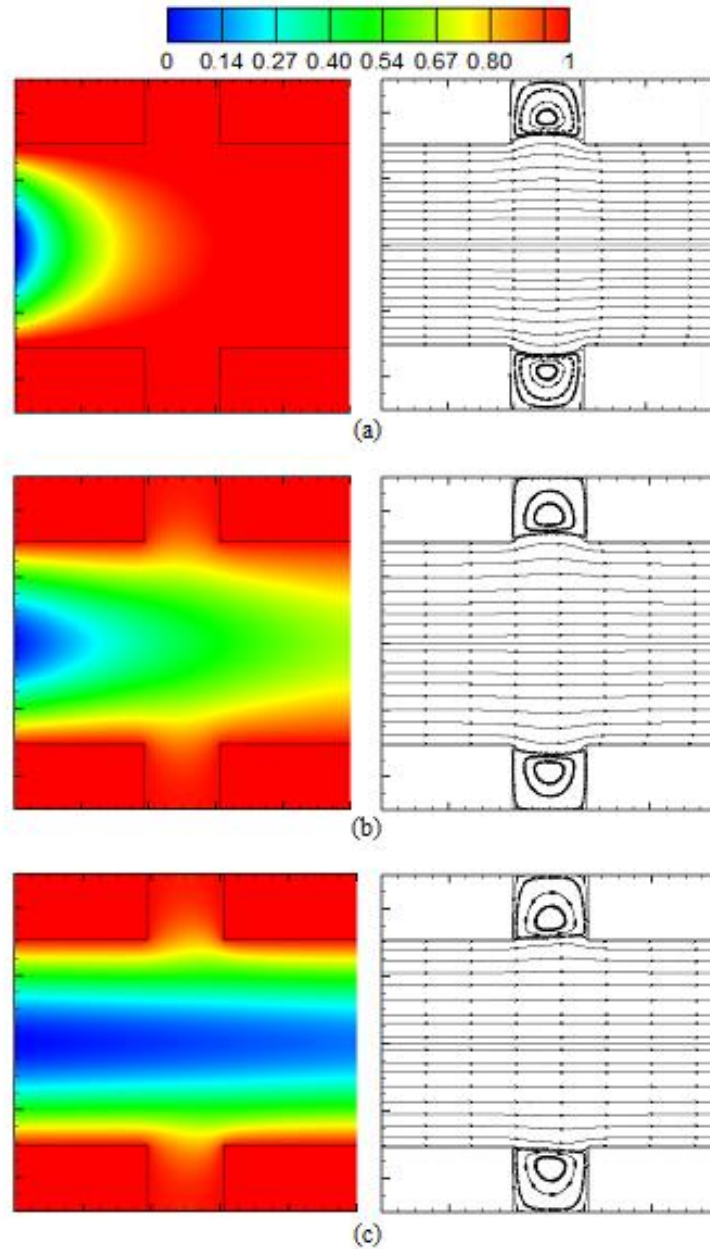


Figure 7.17. The streamlines (on the right) and temperature contours (on the left) for  $\beta = 1.63$  and  $\varepsilon = 0.7$  and (a)  $Re = 1$ , (b)  $Re = 10$ , (c)  $Re = 100$ .

The variation of local interfacial Nusselt numbers along the solid–fluid interface for  $\beta = 1.63$  are displayed in Figure 7.18. The figure indicates that the local interfacial Nusselt number value for  $Re = 1$  is the highest at the inlet of the REV (i.e., point a) and then a sharp decrease is seen toward the edge of the inlet particles (i.e., point b). The



reason of the high value of  $Nu_L$  at the inlet is the long residence time of the fluid in the inlet region due to the low velocity. The convective transport becomes stronger by increase of  $Re$  and consequently the residence time of the fluid and the value of  $Nu_L$  in the inlet region decrease. The stronger convection transport causes the increase of  $Nu_L$  on the interface of the right particles in the REV (d–e and e–f surfaces) since the solid surface touches colder fluid. For  $Re = 100$ , the value of  $Nu_L$  are almost constant at the inlet and outlet throat of the REV (a–b and e–f surfaces). Although  $Nu_L$  values at the interfaces considerably vary with  $Re$  and the location, one may find that the average interfacial Nusselt number (i.e., the area between the curves and x-axis in Figure 7.18) may be close to each other.

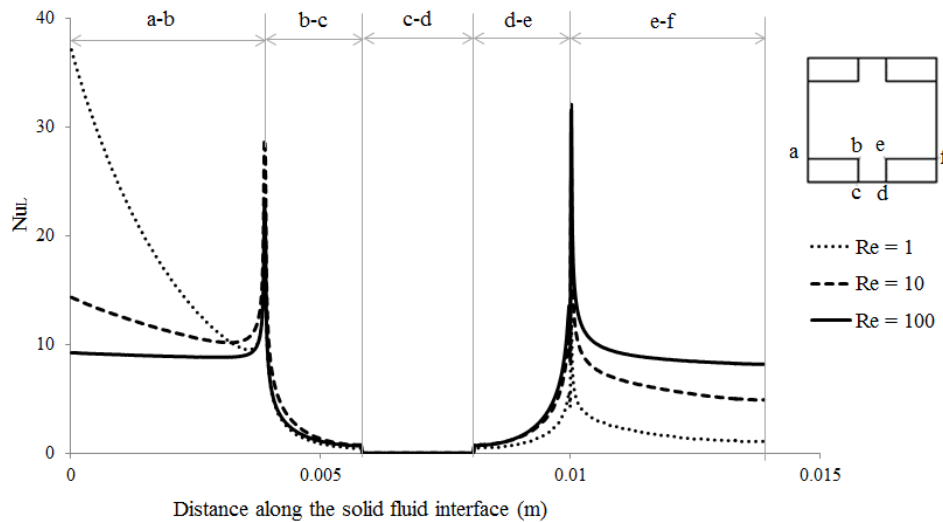


Figure 7.18. The variations of local interfacial Nusselt number along the solid-fluid interface for  $\beta = 1.63$  and  $\varepsilon = 0.7$

For  $\beta = 7.46$ , the corresponding streamlines and the dimensionless temperature contours are displayed in Figure 7.19. As the value of  $\beta$  increases, the vertical distance between the solid particles decreases and the throat effect becomes stronger. Similar to the flows presented in Figure 7.17, there are secondary flows in the top and bottom gaps between the particles. For  $Re = 1$ , the main flow penetrates into the gaps and distorts the secondary flows in such way that two additional vortices occur in the main secondary flows. The temperature distribution is mainly influenced by the conduction heat transfer and the fluid temperature rapidly increases to the solid temperature when the main flow passes through the inlet throat. The residence time of the fluid in the porous structure is

long and  $\langle \theta \rangle^f$  is very close to the dimensionless solid temperature ( $\langle \theta \rangle^f = 0.991$ ). By the increase of Re to 10, the main flow enters into the gaps and the fluid particles crush the vertical walls of the right solid particles of the REV. The thermal boundary layer on the horizontal sides of the inlet solid particles can be seen from the dimensionless

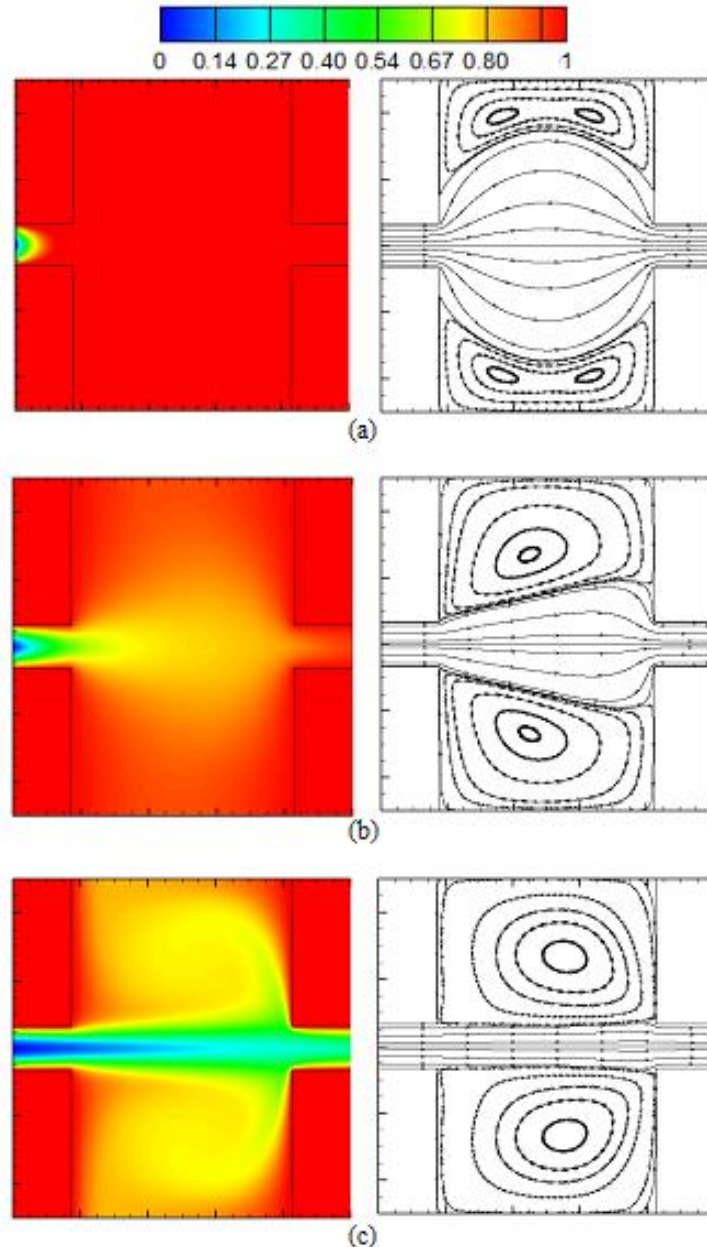


Figure 7.19. The streamlines (on the right) and temperature contours (on the left) for  $\beta = 7.46$  and  $\varepsilon = 0.7$  and (a)  $Re = 1$ , (b)  $Re = 10$ , (c)  $Re = 100$ .

temperature contour of  $Re = 10$ . The influence of fluid inlet temperature is enhanced as Re increases. The value of  $\langle \theta \rangle^f$  decreases to 0.891 for  $Re = 10$ . As Re increases to 100,

the residence time in the REV further decreases. For this Re, the secondary flows play an important role on the temperature distribution in the REV. A strong crush of the fluid with the vertical edges of the outlet solid particles causes the penetration of the heat into the gaps. Due to the strong convective heat transport, the fluid temperature remains smaller than the solid temperature and  $\langle \theta \rangle^f = 0.73$ .

The variations of  $Nu_L$  along the solid–fluid interface for different Re are displayed in Figure 7.20 when  $\beta = 7.46$ . For  $Re = 1$ , the value of  $Nu_L$  in the inlet section of the left is considerably greater than the outlet section. This change of  $Nu_L$  is expected since the temperature gradient in the inlet of the REV is much higher than the remaining part. For  $Re = 10$  and 100, the heat transfer occurs both in the inlet and outlet throats and on the vertical sides of the solid particles (especially at of the right particles). The heat transfer on the surfaces of the inlet particles for  $Re = 10$  considerably decreases while an increase of the heat transfer in the outlet particle of the REV is observed. For  $Re = 100$ , the considerable increase of the heat transfer on the vertical walls of the right particles is due to the strong crush of fluid to the vertical walls. An increase in the interfacial Nusselt number for  $Re = 100$  may be expected.

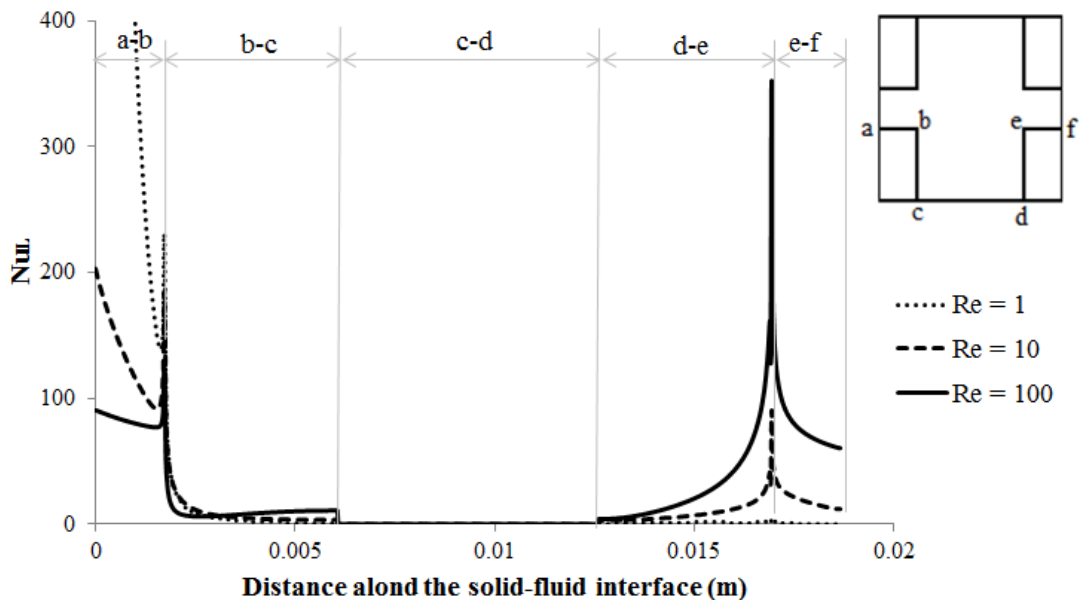


Figure 7.20. The variations of local interfacial Nusselt numbers along the solid-fluid interface for  $\beta = 7.46$  and  $\varepsilon = 0.7$ .

The variations of the interfacial Nu with Reynolds number for the studied pore to throat size ratio values are shown in Figure 7.21 for  $\varepsilon = 0.7$ . Additionally, the

interfacial Nu for the flow in a straight channel with thick walls when  $\varepsilon = 0.7$  is shown on the same figure. The lowest interfacial Nu are obtained for the straight channel flow and it does not change with Re, since the flow is thermally fully developed. For porous structures with  $\varepsilon = 0.7$ , the increase of interfacial Nu with  $\beta$  is observed. The increase of  $\beta$  causes the mixing of the fluid in the voids between the particles. For  $Re = 1$  and  $\beta = 1.63$ , the value of  $\langle \theta \rangle^f = 0.862$  while it is 0.991 for  $\beta = 7.46$  due to the mixing effect. For  $\beta = 1.63$  and 2.21, a small change of the interfacial Nu with Re is observed since the flow is similar to the channel flow. Further increase of  $\beta$  causes a dramatic change of the interfacial Nu with Re. For high  $\beta$  values (e.g.,  $\beta = 7.46$ ), the interfacial Nu decreases along the region of Re between 1 and 10 and takes a minimum value at  $Re = 10$ . The decrease of Nu may be due to the decrease of the residence time of the fluid in the porous media and the formation of the thermal boundary layer on the horizontal surfaces of the inlet solid particles cause the decline of  $Nu_L$  in the inlet region. Further increase of Re from 10 to 100 increases the interfacial Nu. Based on our observation, the reason of the increase of Nu with Re for high values of  $\beta$  for the region of  $Re > 10$  is the crush of the fluid to the vertical wall of the outlet particle, as indicated before. The increase of the  $Nu_L$  at the vertical walls of the right particle for  $Re = 100$  can be observed from Figures 7.19 and 7.20.

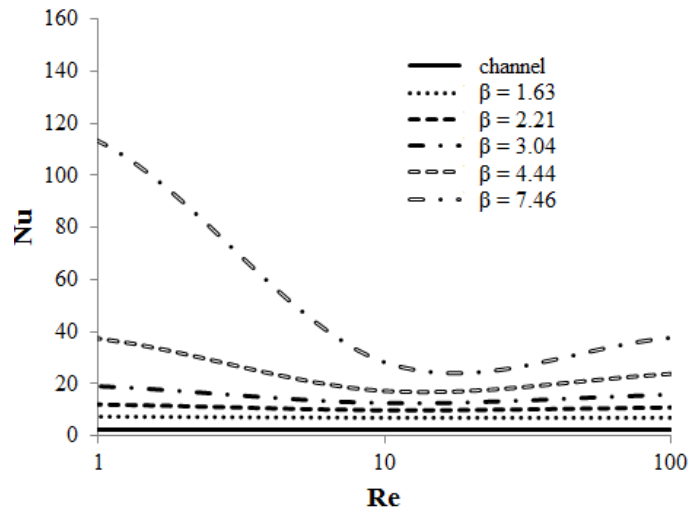


Figure 7.21. The change of interfacial Nusselt number with Reynolds number for porous structure with  $\varepsilon = 0.7$  and different pore to throat size ratios.

As it was mentioned before, the pore hydraulic and equivalent particle diameters of REV's with  $\beta = 1.63$  and  $\beta = 4.44$  are the same as well as their porosity. However, as can be seen from Figure 7.21, the values of interfacial Nu of these two porous media are considerably different for the same Re. Hence, Nu cannot be determined only based on the geometrical parameters such as  $d_h$ ,  $d_p$ , and  $\varepsilon$  along with Re and Pr; the pore to throat size ratio should be taken into consideration in order to develop a general correlation for the determination of interfacial Nusselt number for a porous medium.

### 7.3.2. Effects of Porosity on Interfacial Nusselt Number

For the second part of the study, the effects of porosity on the interfacial convective heat transfer coefficient are investigated for different pore to throat sizes. The change of the local interfacial Nusselt number for  $\beta = 1.63$  and  $Re = 1$  for the porosities from 0.7 to 0.9 is shown in Figure 7.22. As can be seen, the most of the heat transfer between the surfaces of solid particles and the fluid occurs at the inlet throat of the REV's. For low Re, the horizontal surfaces of the particles play an important role on the heat transfer compared to the vertical walls. The comparison of the change of  $Nu_L$

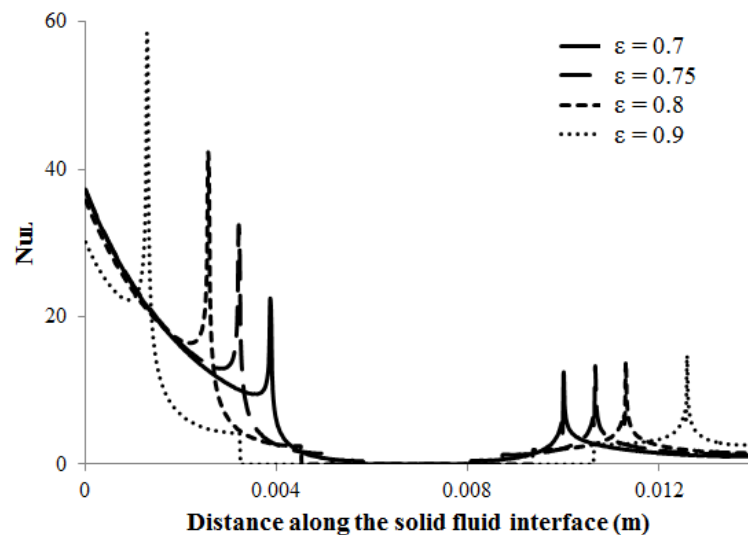


Figure 7.22. The variations of local interfacial Nusselt numbers along the solid-fluid interfaces with porosity for  $\beta = 1.63$  and  $Re = 1$

for  $\varepsilon = 0.7$  and 0.9 shows that the interfacial Nu may not be higher for the porous medium with porosity of 0.7 due to longer surface for  $\varepsilon = 0.7$ . The change of  $Nu_L$  for  $\beta$

= 1.63 and  $Re = 100$  for the studied porosities are displayed in Figure 7.20. The values of  $Nu_L$  of the inlet and outlet regions are comparable and almost have a symmetrical distribution for  $\varepsilon = 0.7$ . The values of  $Nu_L$  increases sharply near the outlet region of the porous medium due to the strike of the fluid to the vertical walls of the right particles in the REV.

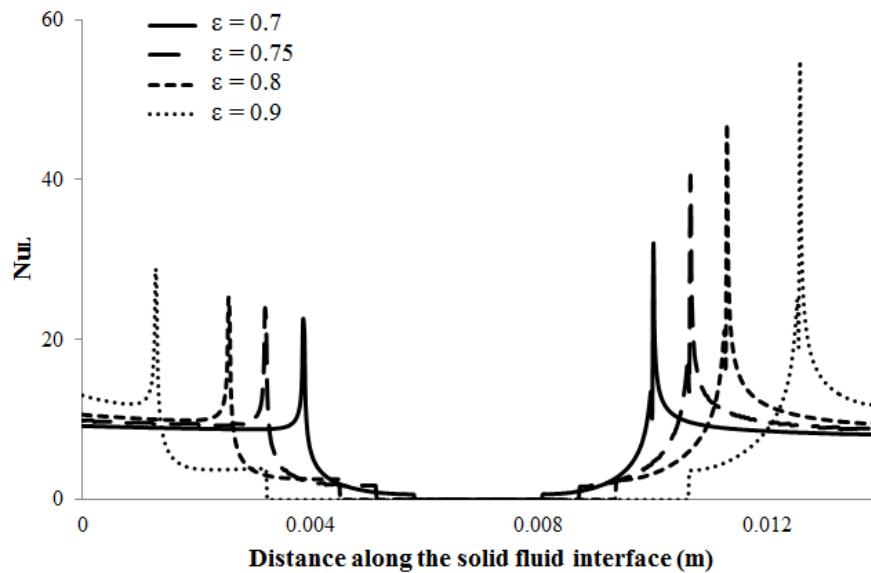


Figure 7.23. The variations of local interfacial Nusselt numbers along the solid-fluid interfaces with porosity for  $\beta = 1.63$  and  $Re = 100$ .

The variation of the interfacial  $Nu$  with  $Re$  for  $\beta = 1.63$  and for different porosities are shown in Figure 7.24. The interfacial  $Nu$  values change between 7 and 10 for the studied porosities when  $\beta = 1.63$ . The interfacial  $Nu$  increases with  $\varepsilon$  due to the increase of the void for proper mixing of the fluid. For porosity of 0.7, the interfacial  $Nu$  is almost constant and similar to the fully developed flow in the channel. For higher porosities,  $Nu$  decreases with the increase of  $Re$  due to the occurrence of the boundary layer on the horizontal surfaces of the solid particles and the decrease of the residence time of the fluid in the REV. However, for  $\varepsilon = 0.8$  and 0.9, an increase of  $Nu$  is observed after  $Re = 10$ . The expansion of the flow after leaving the inlet throat and then the strike of the fluid to the vertical walls of the outlet solid particles in the REV causes the mixing of the fluid in the REV. The effect of the strike of the fluid to the vertical walls of the outlet particles in the REV can be observed by the comparison of the isotherms for  $\varepsilon = 0.7$  and 0.9 when  $\beta = 1.63$  and  $Re = 100$  in Figure 7.25. As can be seen, the strike of the flowing fluid to the vertical walls of the outlet solid particles

causes the entrance of the colder fluid into the top and bottom gaps between the particles. As a result, the heat transfer on the vertical walls of the particles increases.

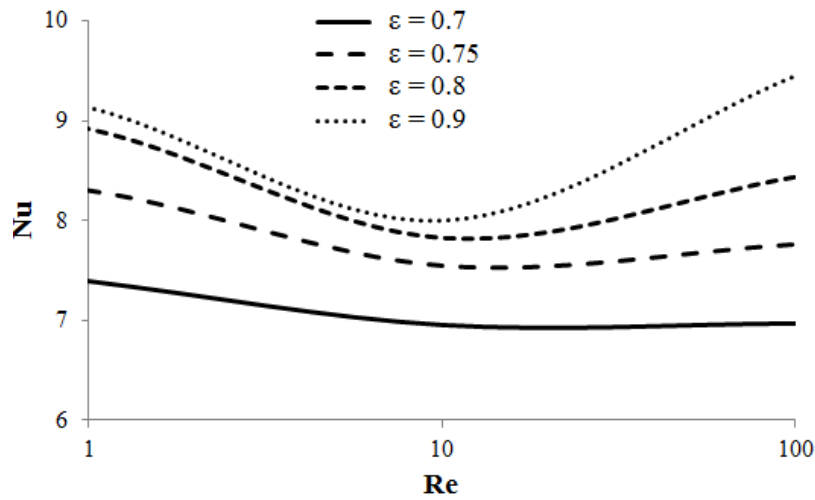


Figure 7.24. The change of interfacial Nusselt number with Re number for  $\beta = 1.63$  and different porosities.

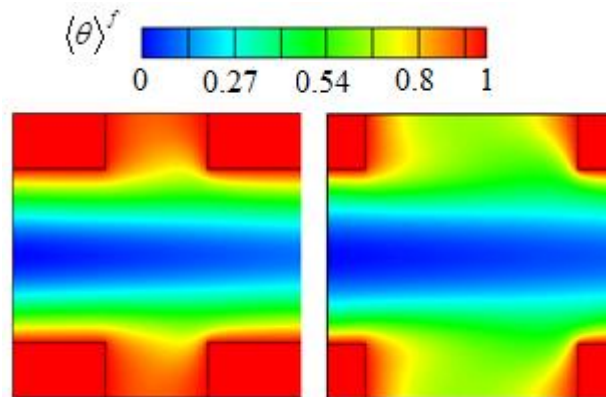


Figure 7.25. The dimensionless temperature contours in porous media with  $Re = 100$ ,  $\beta = 1.63$  and a)  $\varepsilon = 0.75$ , b)  $\varepsilon = 0.9$ .

The change of  $Nu_L$  along the solid–fluid interface for  $\beta = 7.46$ ,  $Re = 1$ , and different porosities are displayed in Figure 7.26. For the flows with low  $Re$ , the heat is mainly transferred from the horizontal surfaces of the inlet solid particles of the REV. Hence, the heat transfer mainly occurs at the inlet throat and it is negligible at the rest of the REV. The value of  $Nu_L$  decreases as  $\varepsilon$  increases due to the decrease of the horizontal surface along the throat length. The change of  $Nu_L$  for  $\beta = 7.46$ , the porosity from 0.7 to 0.9 and  $Re = 100$  is shown in Figure 7.27. The changes of  $Nu_L$  for all porosities are

similar to each other. The strong crush of the fluid to the vertical walls of the right solid particles in the REV and the strong secondary flows in the gap between the particles cause the increase of  $Nu_L$  at the vertical surfaces of the particle in REV.

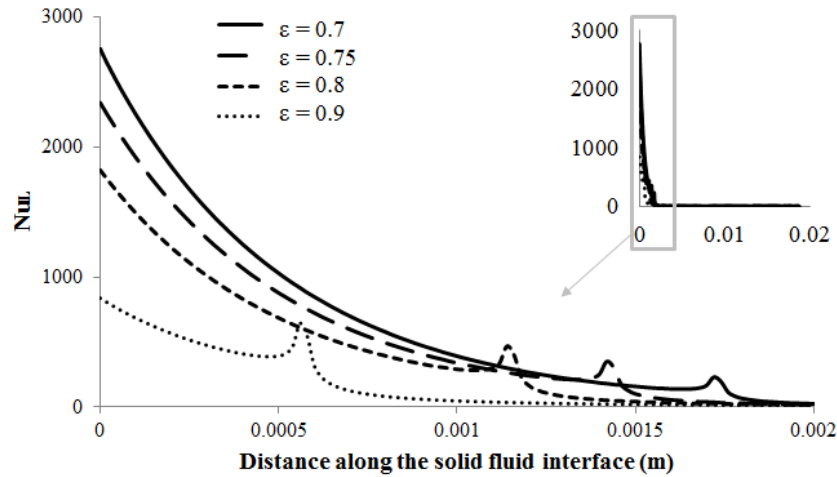


Figure 7.26. The variations of local interfacial Nusselt numbers along the solid-fluid interfaces with porosity for  $\beta = 7.46$  and  $Re = 1$

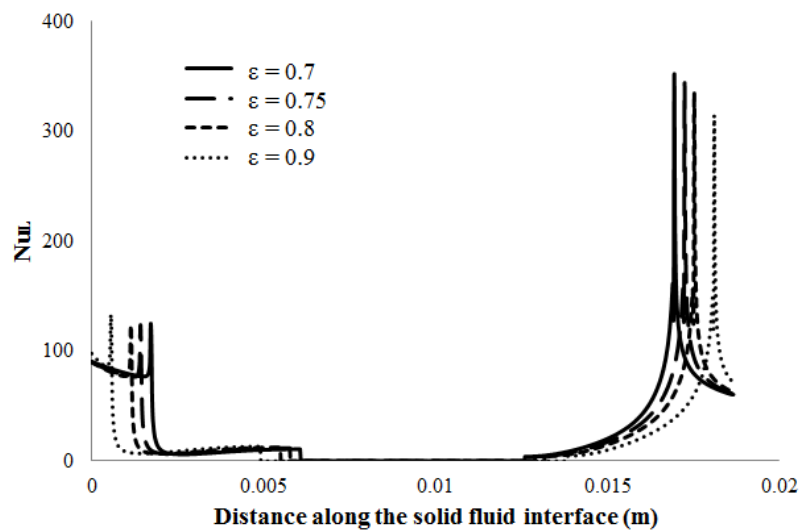


Figure 7.27. The variations of local interfacial Nusselt numbers along the solid-fluid interfaces with porosity for  $\beta = 7.46$  and  $Re = 100$ .

The change of the interfacial  $Nu$  with  $Re$  for  $\beta = 7.46$  is shown in Figure 7.28. The values of  $Nu$  become closer to each other as  $Re$  increases and they are almost the same at  $Re = 100$ . This behavior can be explained by Figure 7.27 where the areas under  $Nu_L$  curves are comparable with each other and additionally, the length of the solid



particles are almost close to each other. It is observed that for high  $\beta$  values (i.e.,  $\beta = 7.46$ ), the increase of  $\varepsilon$  reduces  $Nu$  and this behavior is the reverse of the change of  $Nu$  with  $\varepsilon$  for the low  $\beta$  values (e.g.,  $\beta = 1.63$ ). In the light of the present numerical results, a correlation relating the interfacial Nusselt number with porosity, pore to throat size ratio, and Reynolds and Prandtl numbers is developed for the considered porous media. The proposed correlation is shown in the following equation:

$$Nu = (a_0\varepsilon + a_1) + (a_2\varepsilon + a_3)Re^{0.6} Pr^{1/3} \quad (7.6)$$

where  $a_i$  are functions of  $\beta$  and defined as

$$a_i = a_{i1} + a_{i2}\beta + a_{i3}\beta^2 \quad (7.7)$$

The values of the empirical coefficients are given in Table 7.3.

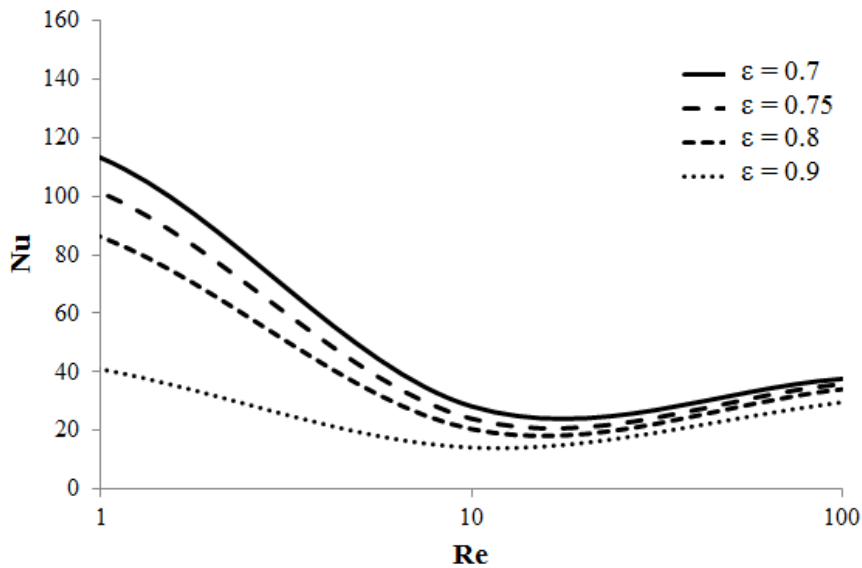


Figure 7.28. The change of interfacial Nusselt number with Re number for porous media with  $\beta = 7.46$ .

Table 7.3. The empirical coefficients of the proposed correlation for the determination of the interfacial Nusselt number.

	Re < 10	Re > 10
a <sub>01</sub>	-12.164	20.96
a <sub>02</sub>	30.362	-13.555
a <sub>03</sub>	-11.581	0.0149
b <sub>01</sub>	19.699	-10.926
b <sub>02</sub>	-28.234	11.771
b <sub>03</sub>	11.551	0.0561
c <sub>01</sub>	8.5755	0.5923
c <sub>02</sub>	-10.652	0.1241
c <sub>03</sub>	2.879	0.0172
d <sub>01</sub>	-8.3585	-0.932
d <sub>02</sub>	10.097	0.2443
d <sub>03</sub>	-2.8843	-0.032

Our observation reveals that the variation of Nu with Re is considerably different for the regions before and after Re = 10. Hence, the coefficients are found for two different regions of Re as can be seen in Table 7.3. The values of the interfacial Nu found from the computational study and the suggested correlation are compared in Figure 7.29. As can be seen, the proposed correlation provides acceptable values for the interfacial Nu of a porous medium consists of rectangular rods.

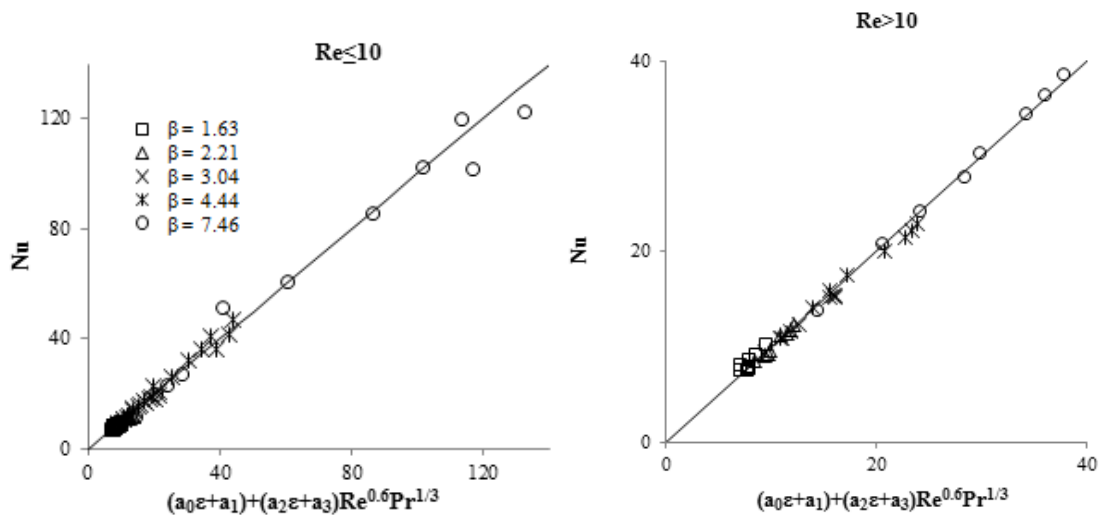


Figure 7.29. The comparison of the obtained numerical values of Nu with the suggested correlation

Additionally, the comparison between the proposed correlation and the results reported in the literature for square rods in inline arrangement ( $\varepsilon = 0.75$  and  $\beta = 2$ ) is shown in Figure 7.30. The interfacial Nusselt numbers found by the present correlation seem to align with the results achieved by other researchers.

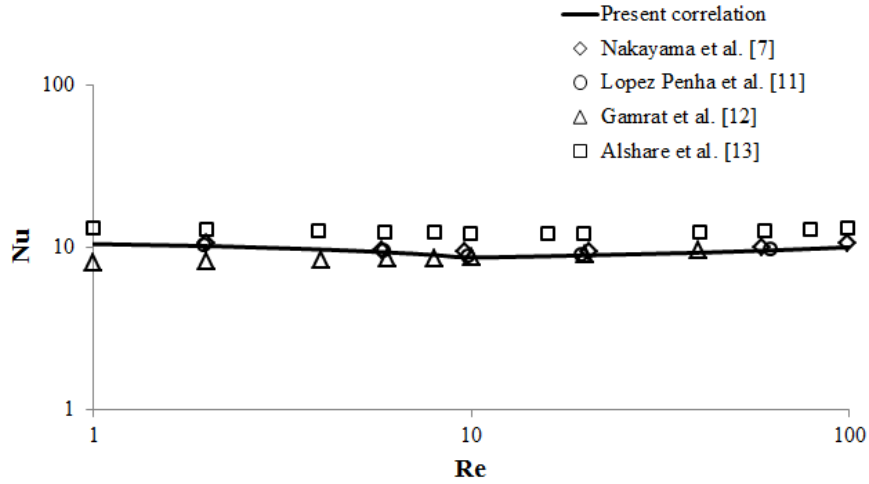


Figure 7.30. The comparison of the suggested correlation with the reported values in literature for  $\varepsilon = 0.75$  and  $\beta = 2$ .

#### 7.4. Results for Thermal Dispersion

In this section the results concerning the effects of pore to throat size on the thermal dispersion coefficients in the longitudinal and transverse directions are presented. By solving the microscopic equations with using the aforementioned boundary conditions, the pore-level velocity and temperature distributions inside the REV are obtained. In order to use the same legend for the presented results, the dimensionless temperature and velocity values are defined as:

$$T^* = \frac{T - T_{\min}}{T_{\max} - T_{\min}} \quad (7.7)$$

$$u^* = \frac{u}{\langle u \rangle} \quad (7.8)$$

where  $T_{\min}$  and  $T_{\max}$  are the minimum and maximum temperature values in the REV. Additionally, a dimensionless value for  $u'T'$  is defined in order to explain the variation of longitudinal thermal dispersion with pore to throat size ratio.

$$(u'T')^* = \frac{u'T'}{\langle u \rangle \Delta T} \quad (7.9)$$

where  $\Delta T$  is macroscopic temperature difference. In Figure 7.31, the streamlines and temperature contours in REV with porosity of 0.7, pore to throat size ratios of 1.63, 3.04 and 7.46 are presented for Reynolds numbers of 1 and 100. As it was mentioned before, the temperature contours show the distribution of dimensionless temperature (*i.e.*,  $T^*$ ) in the REV. Figure 7.31(a) shows the streamlines and dimensionless temperature distributions for the pore to throat size ratio of 1.63, porosity of 0.7 and  $Re = 1$ . As can be seen from the streamline patterns, the main flow along the REV goes straight like a channel flow since the particles (*i.e.* rods) are almost flat in flow direction. A small flow penetration to the gaps between the rods can be observed. There are secondary flows in the upper and lower gaps between particles. Temperature almost linearly drops from the left to the right side of the REV. Figure 7.31(b) presents the streamlines and dimensionless temperature contours for the same REV when  $Re = 100$ . The streamlines in the REV does not change very much, however the strong convection effect in the flow direction can be observed from the isotherms. The streamlines and dimensionless temperature distribution in the porous medium with the same porosity but pore to throat size ratio of 3.04 when  $Re = 1$  are shown in Figure 7.31(c). The main flow penetrates to the upper and lower gaps and compresses the secondary flows in the gaps. The dimensionless temperature distributions in the Figure 7.31(a) and (c) are similar; however, the linearity of the temperature distributions in the flow direction can be observed more clearly in Figure 7.31(c). By increasing  $Re$  from 1 to 100 for the REV shown in Figure 7.31(c), the streamlines and dimensionless temperature distribution considerably change as can be seen from Figure 7.31(d). The main flow resembles the channel flow and the secondary flows cover the entire gaps. Similar to Figure 7.31(b), a strong convection effect can be seen in the center of the REV due to high value of  $Re$ . Furthermore, the strike of the main flow onto the vertical walls of the particles at the right side of the REV causes the entrance of cold fluid to the

gaps between the particles and decreases the temperature inside the gaps. The streamlines and the dimensionless temperature contour in the REV with  $\beta = 7.46$  for the flow with  $Re = 1$  are shown in Figure 7.31(e). The penetration of the main flow into the upper and lower gaps become stronger, the shape of the secondary flows is distorted and the centers of the secondary flows move nearer to the inlet section. The linear temperature gradient along the longitudinal direction is obvious from the temperature distribution.

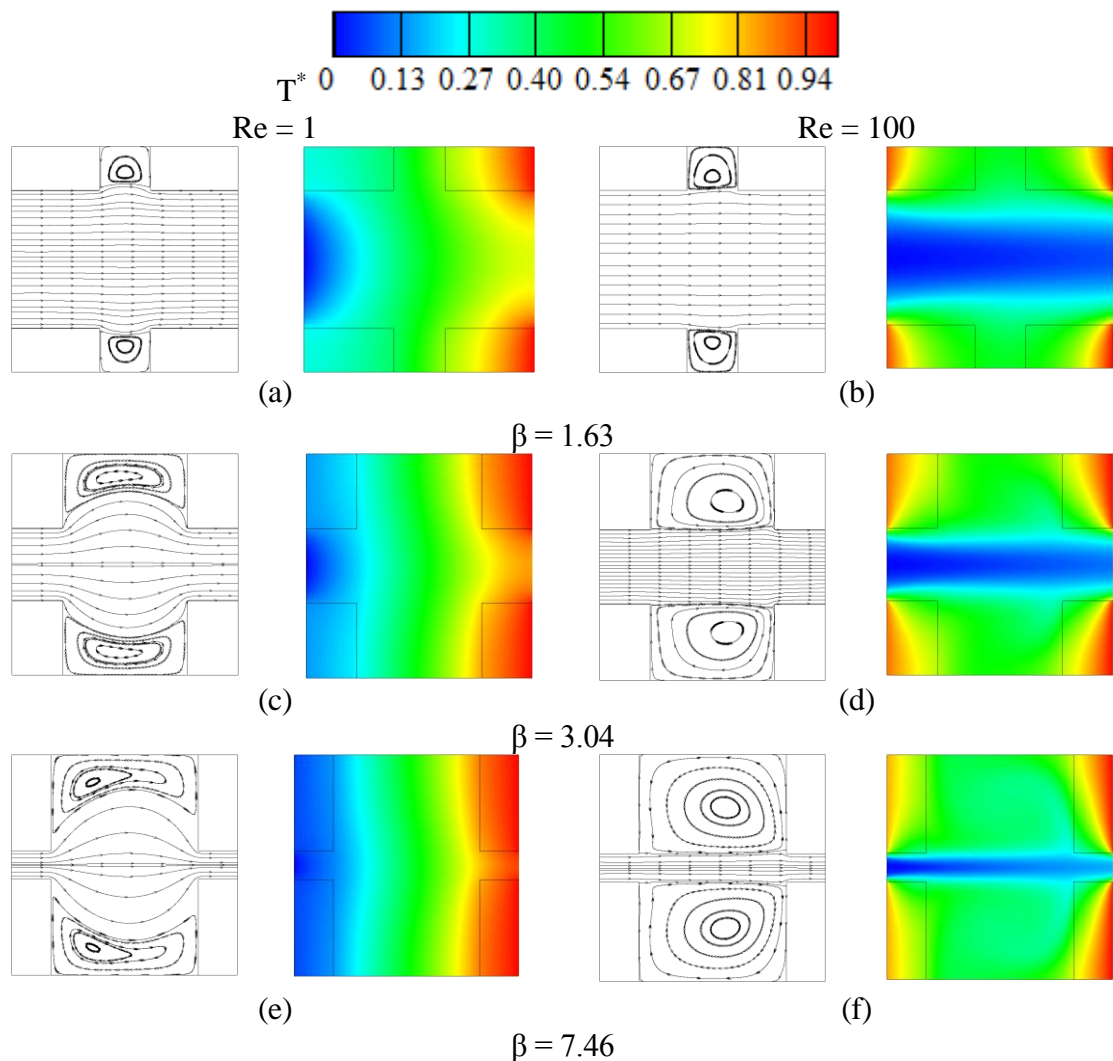


Figure 7.31. The streamlines and dimensional temperature contours with longitudinal temperature gradient

The streamlines and temperature contours are presented in Figure 7.31(f) for  $Re = 100$  of the same REV. Because of high  $Re$  flow, the main flow has nearly straight streamlines through the REV. Similar to the flow in Figure 7.31(d), the strike of the

main flow to the solid particles at the outlet of the REV causes the entrance of fluid particles to the upper and lower gaps. The cooling effect in the gaps is more evident in the temperature contour of Figure 7.31(f). For the all presented figures, the linearity of the temperature gradient is more pronounced for low Re because of the low velocities and consequently low convection effect. Thermal dispersion is resulted due to fluctuations in the pore level temperature and velocity of the porous media. It is seen from Figure 7.31 that the fluctuations of temperature is very low for  $Re = 1$ . Additionally, the magnitude of velocity fluctuations is also small because of the low microscopic velocity values. As Re increases, the temperature non-uniformity in the REV increases and the fluctuation of the temperature become sensible. Furthermore, the magnitude of the velocity fluctuations increases due to the increase of pore-level velocity. Hence, the increase of longitudinal thermal dispersion with Reynolds number is expected.

The change of thermal dispersion with pore to throat size ratio and Reynolds number can be understood better by examining the distribution of dimensionless  $u'T'$  values in the REV. The change of  $(u'T')^*$  in the REVs with pore to throat size ratios of 1.63, 3.04 and 7.46 and for  $Re = 1$  and 100 when  $\varepsilon = 0.7$  are shown in Figure 7.32. The distribution of  $(u'T')^*$  in the REV with  $\beta = 1.63$  and  $Re = 1$  is shown in Figure 7.32(a). The local  $(u'T')^*$  is stronger in the solid particles; however, its direction changes with location (i.e., positive in the right particles and negative in the left ones). This means that the thermal dispersion creates diffusion type heat fluxes with opposite directions. Hence, the integration of  $(u'T')^*$  for the entire of the REV becomes negligible and there is no considerable thermal dispersion for the porous media with  $\beta = 1.63$  when  $Re = 1$ . By increasing of Re to 100, all values of  $(u'T')^*$  become negative in the entire REV (Figure 7.32(b)). Additionally, the magnitude of  $(u'T')^*$  values become greater than those values of  $Re = 1$ . The distribution of  $(u'T')^*$  in the REV with  $\beta = 3.04$  for the flows with  $Re = 1$  and 100 are presented in Figure 7.32(c) and (d). In the REV with  $Re = 1$ , the negative values of  $(u'T')^*$  are observed at the inlet fluid boundary while an opposite transport effect is seen at the outlet fluid boundary. These dispersion effects cancel each other and the magnitude of the thermal dispersion in the longitudinal direction becomes small. For  $Re = 100$ ,  $(u'T')^*$  values are negative in the entire REV and the highest negative values, which contribute greater thermal dispersion, exist at the

core of the main flow in the first half of the REV and also inside the solid particles. When pore to throat size ratio becomes 7.46,  $(u'T')^*$  distribution becomes very different for the flow with  $Re = 1$  (Figure 7.32(e)). Almost whole of the REV has approximately zero  $(u'T')^*$  values except the inlet and outlet throats. The negative values of  $(u'T')^*$  are present at the inlet throat where  $(u'T')^*$  values have opposite direction at the outlet throat. Hence the resulted thermal dispersion coefficient has a small value. For the flow with  $Re = 100$  in the REV with  $\beta = 7.46$  (Figure 7.32(f)), the largest negative value of  $(u'T')^*$  of Figure 7.32 is observed at the inlet throat and then its magnitude decreases along the center of the REV, but still very high negative values are seen. Hence the main flow through the REV highly contributes to the increase of the longitudinal thermal dispersion. The values of  $(u'T')^*$  values in the upper and lower gaps have small positive values. The entrance of the fluid into the gaps results in the mixing effect that decreases the value of the longitudinal thermal dispersion in the gaps. By considering Figure 7.31 and 7.32, it can be seen that for low values of Reynolds number ( $Re = 1$ ), a linear increase of temperature exists in the REV and negative and positive values for  $(u'T')^*$  (which cancel each other) can be observed since the conduction heat transfer is dominant. Furthermore, the magnitude of  $(u'T')^*$  values in the REV is small due to the magnitude of velocity. That's why the thermal dispersion becomes negligible for the low values of  $Re$ . It can also be said that the strike of the fluid particles to the walls of the outlet solid particles and the entrance of the fluid into the gaps at the top and bottom of the REV makes temperature of these regions closer to the REV average temperature and this reduces the magnitude of  $(u'T')^*$  in the gaps. However, high velocity values and consequently high deviations from the average velocity increases the total magnitude of  $(u'T')^*$ .

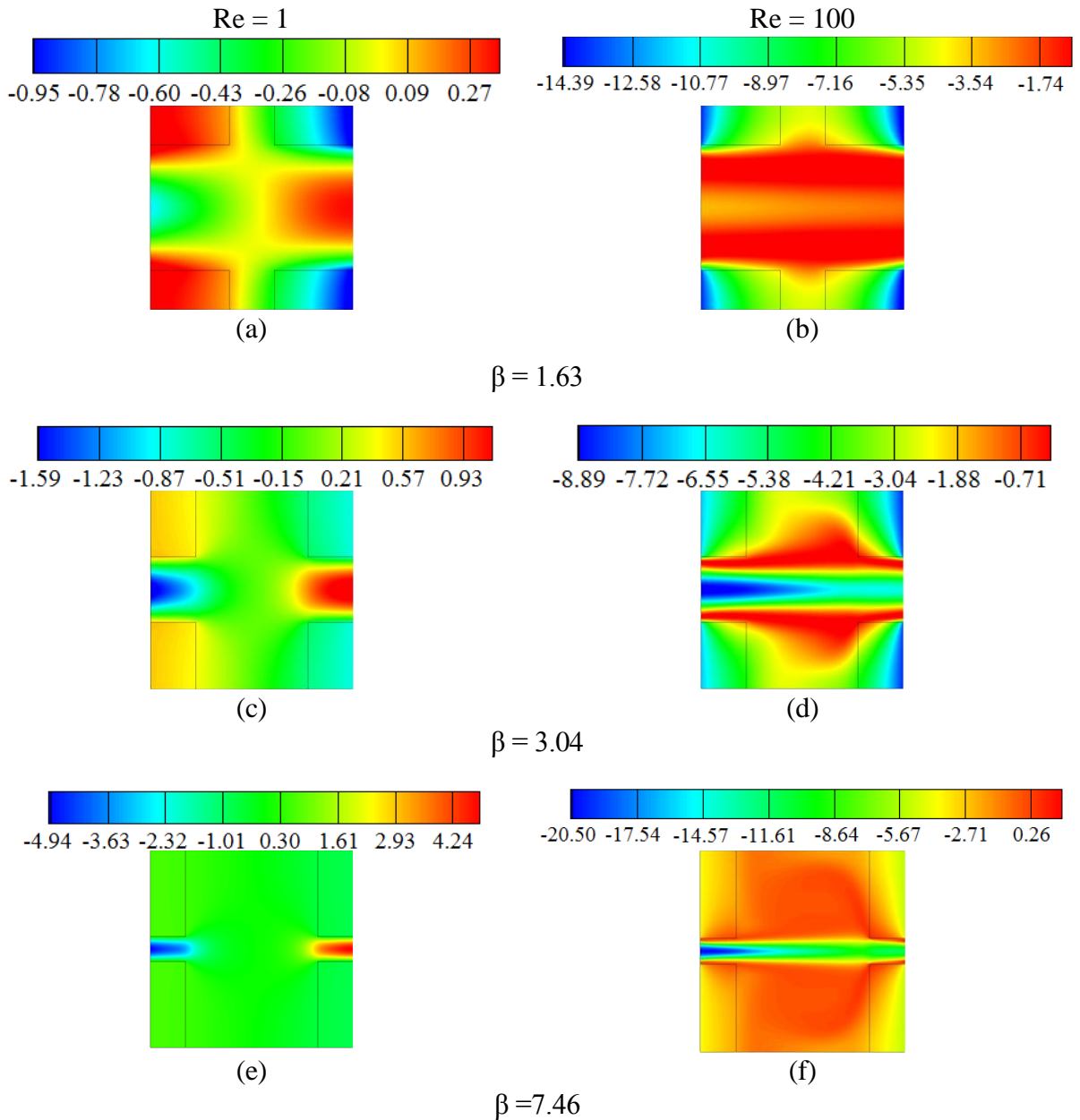


Figure 7.32. The distributions of  $(u'T')^*$  in the REV's

The change of the ratio of the longitudinal thermal dispersion coefficient to the fluid thermal conductivity with the pore to throat size ratio for different Reynolds numbers and for porosities of 0.7, 0.8 and 0.9 are shown in Figure 7.33. As expected, the longitudinal thermal dispersion coefficient is very small for  $Re \leq 10$ , hence the thermal dispersion is negligible for the flows with  $Re \leq 10$ . For higher  $Re$ , the dispersion effect along the longitudinal direction becomes stronger due to the increase of the convective heat transfer, and the value of thermal dispersion coefficient increases. It is observed that for the considered porosities in this study, the longitudinal thermal



dispersion coefficient increases with pore to throat size ratio for the range of  $1.63 \leq \beta \leq 3.04$  and then further increase of  $\beta$  reduces  $k_{dis,xx}$ . By the increase of  $\beta$  from 1.63 to 3.04, the longitudinal thermal dispersion increases almost 43 %. However, by further increasing  $\beta$  to 7.46 causes decrease of the thermal dispersion by 29 %.

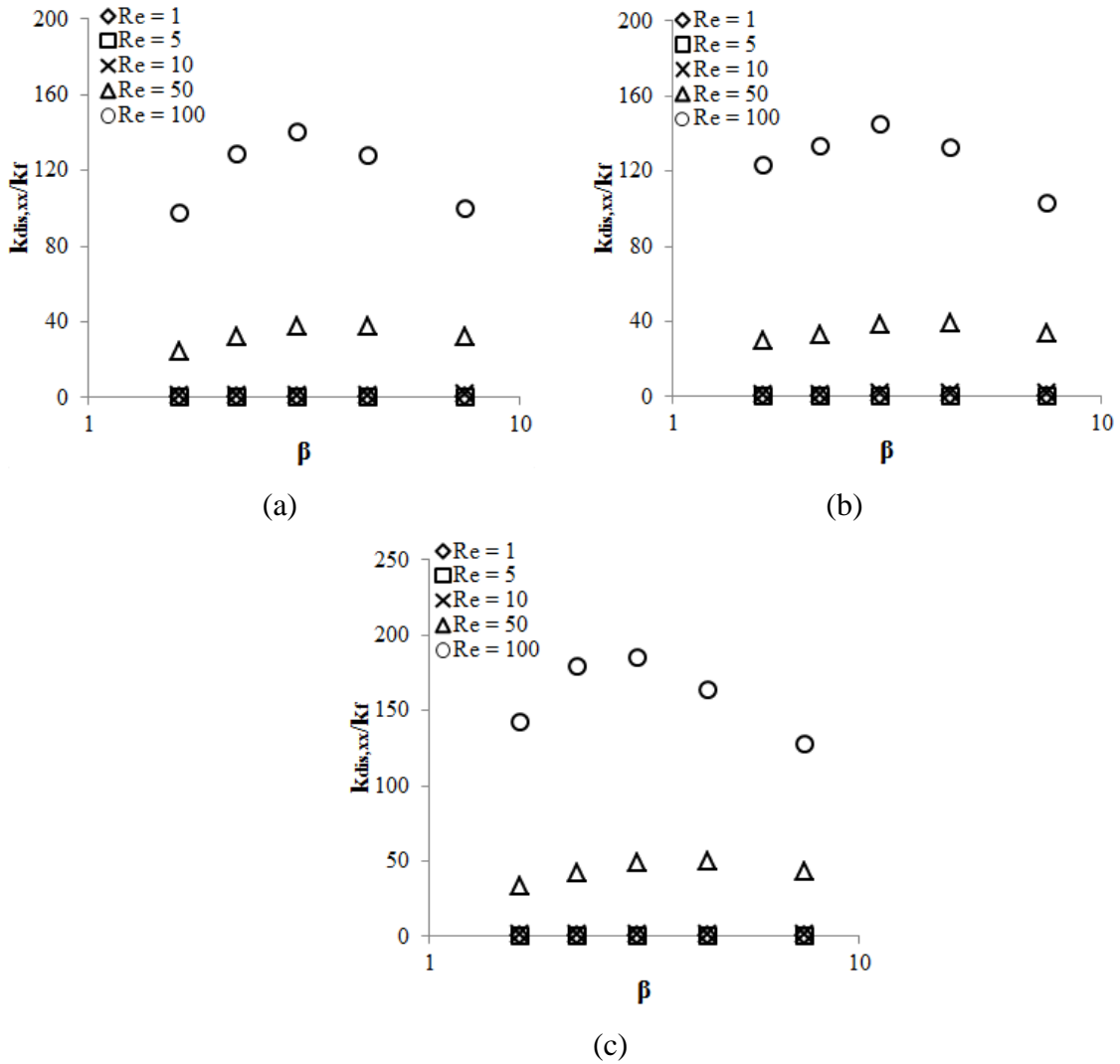


Figure 7.33. The variation of the longitudinal thermal dispersion with  $\beta$  for different Re a)  $\epsilon = 0.7$ , b)  $\epsilon = 0.8$ , c)  $\epsilon = 0.9$

The maximum value of the longitudinal thermal dispersion is found for the REVs with  $\beta = 3.04$ . Hence, it can be said that there is an optimum value of pore to throat size ratio for the maximization of longitudinal thermal dispersion in a porous medium. The largest or narrowest throats have the lowest values of the longitudinal thermal dispersion. When the dimension of the particles in flow direction is slightly smaller than the dimension along the transverse direction, thermal dispersion takes the

greatest value. Figure 7.33 also shows that, the value of the longitudinal thermal dispersion increases with the increase of porosity.

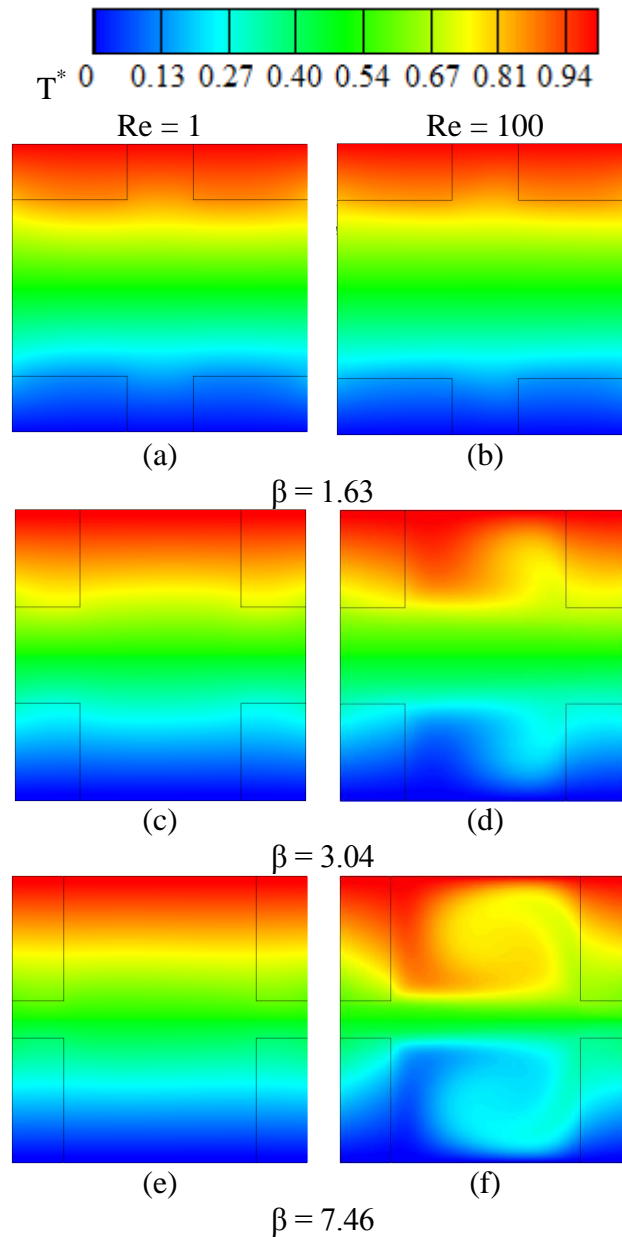


Figure 7.34. The streamlines and dimensional temperature contours with transverse temperature gradient for different REV's and two Reynold numbers.

In order to determine the thermal dispersion in the transverse direction, the macroscopic temperature gradient is applied in y-direction. The temperature profiles at the inlet and outlet of the REV are similar to each other; hence, the dispersion in the longitudinal direction is omitted and only the dispersion in the transverse direction is focused on. The obtained dimensionless temperature contours for the REV's with

porosity of 0.7,  $\beta = 1.63, 3.04$  and  $7.46$ , and for  $Re = 1$  and  $100$  are presented in Figure 7.34. The same flow conditions are employed for the computation of the transverse thermal dispersion coefficient; hence, the streamlines for these flows are the same with the ones that shown in Figure 7.31. For the flows with low Reynolds number (Figure 7.34(a), (c) and (e)) the macroscopically linear temperature gradient is not much disturbed by the flow since the convection effect in transverse direction is weak. For  $Re = 100$  and pore to throat size ratio of  $1.63$  (Figure 7.34(b)) the temperature distribution in the REV is similar to the REVs with  $Re = 1$ . The areas of the gaps between particles in the upper and lower parts are small and there is no strong flow in the transverse direction. That's why; in spite of high Reynolds number, a linear temperature gradient in  $y$  direction is observed. For  $Re = 100$ , as the pore to throat size ratio increases, the main flow strikes to the walls of the solid particles at the right side of the REV and enters to the upper and lower gaps. Because of the mixing of main and secondary flows, the temperature distribution in the upper and lower gaps changes (Figure 7.34(d)). By increasing pore to throat size ratio to  $7.46$ , the mixing of main and secondary flows in the gaps further increases as can be seen from Figure 7.34(f).

The variation of the ratio of the transverse thermal dispersion coefficient to the thermal conductivity of the fluid with Reynolds number is shown in Figure 7.35 for various values of pore to throat size ratio and porosities of  $0.7, 0.8$  and  $0.9$ . The transverse thermal dispersion is computed by using Eqs. (4.31) and (4.33) for the REVs in which a temperature gradient in the transverse direction is created. If Figure 7.33 and 7.35 are compared, it is observed that the transverse thermal dispersion coefficient values are much smaller than the longitudinal thermal dispersion coefficients for the inline arrangement of rectangular rods. As expected, the transverse thermal dispersion increases with the increase of Reynolds number, however the rate of increase depends on the pore to throat size ratio. For low pore to throat size ratios (i.e.,  $\beta = 1.63$ ), the change of transverse thermal dispersion coefficient with  $Re$  is negligible. For high values of  $\beta$ , the transverse thermal dispersion considerably changes with  $Re$ . The transverse thermal dispersion coefficient directly increases with pore to throat size ratio and porosity. For instance, for  $Re = 100$ , the increase of  $\beta$  from  $1.63$  to  $3.04$  causes the enhancement of the thermal dispersion by approximately  $34\%$ . Further increasing  $\beta$  to  $7.46$  increases the thermal dispersion value  $114\%$  more.

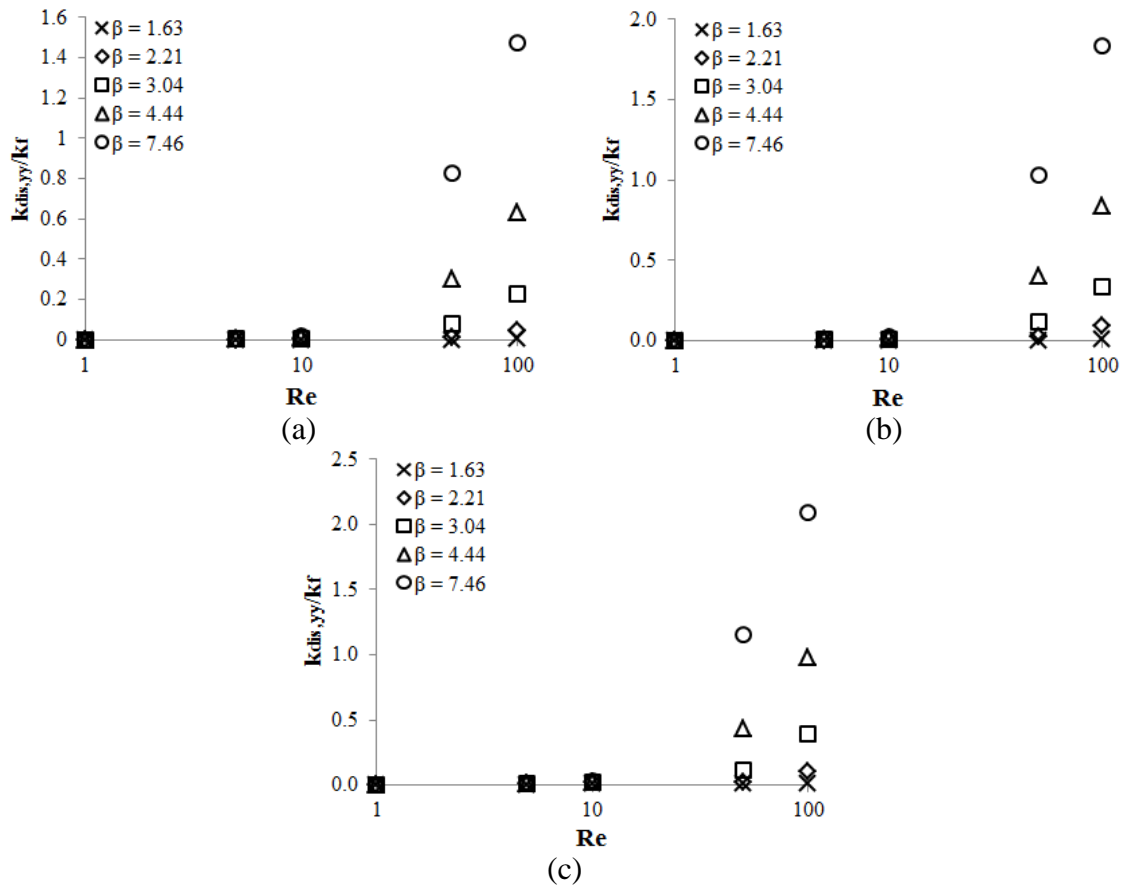


Figure 7.35 The variation of the transverse thermal dispersion with Reynolds number for different  $\beta$  a)  $\epsilon = 0.7$ , b)  $\epsilon = 0.8$ , c)  $\epsilon = 0.9$

Most of correlations suggested for the determination of thermal dispersion are expressed in terms of Reynolds and Prandtl numbers, porosity and solid to fluid thermal conductivity ratio as discussed in Chapter 3. The present study shows that the thermal dispersion of two porous media having the same porosity, hydraulic diameter (or equivalent particle diameter) for the identical working fluid and flow conditions may be considerably different. The thermal dispersion coefficients of the porous media with the same geometrical parameters ( $\beta = 1.63$  and  $4.44$  for  $\epsilon = 0.7$ ) are considerably different. For  $Re = 100$ , the longitudinal and transverse values of  $k_{dis}/k_f$  of porous medium with  $\beta = 1.63$  are  $97.62$  and  $1.22 \cdot 10^{-3}$ , respectively, while for the porous medium with  $\beta = 4.44$ , these values are  $128.15$  and  $0.633$ . Hence, the pore to throat size ratio plays an important role on the mechanism of thermal dispersion and it should be considered in the suggested correlations in order to prevent the possible mistakes in correlations and achieve a relationship that is valid for various geometries of porous media.

## 7.5. Experimental Results

An experimental setup was designed and constructed to validate the numerical model employed in the present study. Detailed explanation of the experimental setup and procedure is presented in Chapter 6. In this section the experimental measurements and obtained results are presented with necessary discussion.

The experimental measurements were done for 3 different mass flow rates. The corresponding Reynolds numbers for these mass flow rates are 192, 329 and 424 (Eq. 6.2). The studied Reynolds numbers and corresponding mass flow rates are shown in Table 7.4. The velocity and temperature measurements for all considered Reynolds numbers were repeated twice on separate days and no considerable change was observed.

Tablo 7.4. The Reynolds number, average velocity and mass flow rate values for the experiments in the empty channel

<b>Re</b>	<b><math>u_m</math> (m/s)</b>	<b><math>\dot{m}</math> (kg/s)</b>
192	0.28	0.1
329	0.48	0.17
424	0.62	0.22

The velocity profiles obtained by the measurements in the empty channel are shown in Figure 7.35, 7.36 and 7.37 for the considered Reynolds numbers. The corresponding coordinate system is shown in Figure 6.15. The velocity profiles at the inlet of empty channel and the outlet of the test section are presented in the dimensionless form made by using the average velocity ( $u^* = u / u_m$ ). In addition to the experimental measurements, numerically computed velocity profiles are shown in the same figures. Numerical velocity profiles are computed for a 2D channel with the height of 300 mm and length of 2500 mm for the same mass flow rates by using Fluent 12. In this computation, the governing equations shown by Eqs. (4.1), (4.2) and (4.3), which are continuity and momentum equations for clear fluid, are solved. As can be seen from the figure, there are small differences between the numerically obtained and experimentally measured velocities at the inlet of the porous channel.

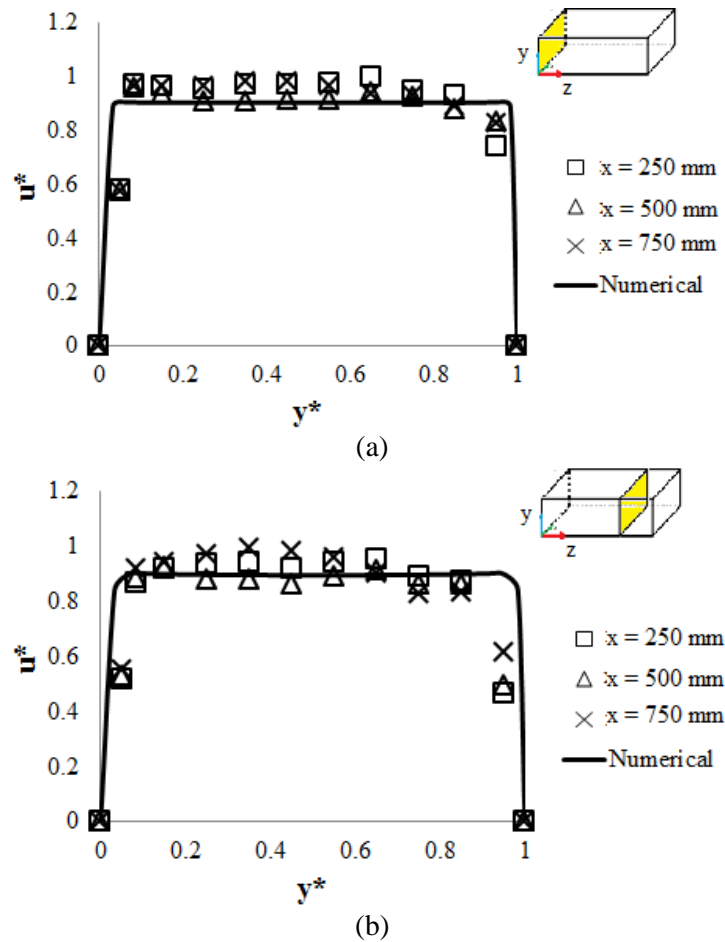


Figure 7.36. Experimental and numerical velocity profiles in empty channel for  $Re = 192$  (a) empty channel inlet ( $z = 0$ ), (b) test section outlet ( $z = 1400$  mm)

In addition to the velocity measurements, temperature measurements in the empty channel were performed. The details of the temperature measurement procedure are explained in Chapter 6. During the experimental measurements for temperature, the temperatures of top and bottom walls of the test section were fixed at  $60$  °C. The obtained dimensionless temperature profiles for different Reynolds numbers are shown in Figure 7.38, 7.39 and 7.40 for the considered Reynolds numbers. The dimensionless temperature is calculated based on Eq. (7.10).

$$T^* = \frac{T - T_{m,i}}{T_w - T_{m,i}} \quad (7.10)$$

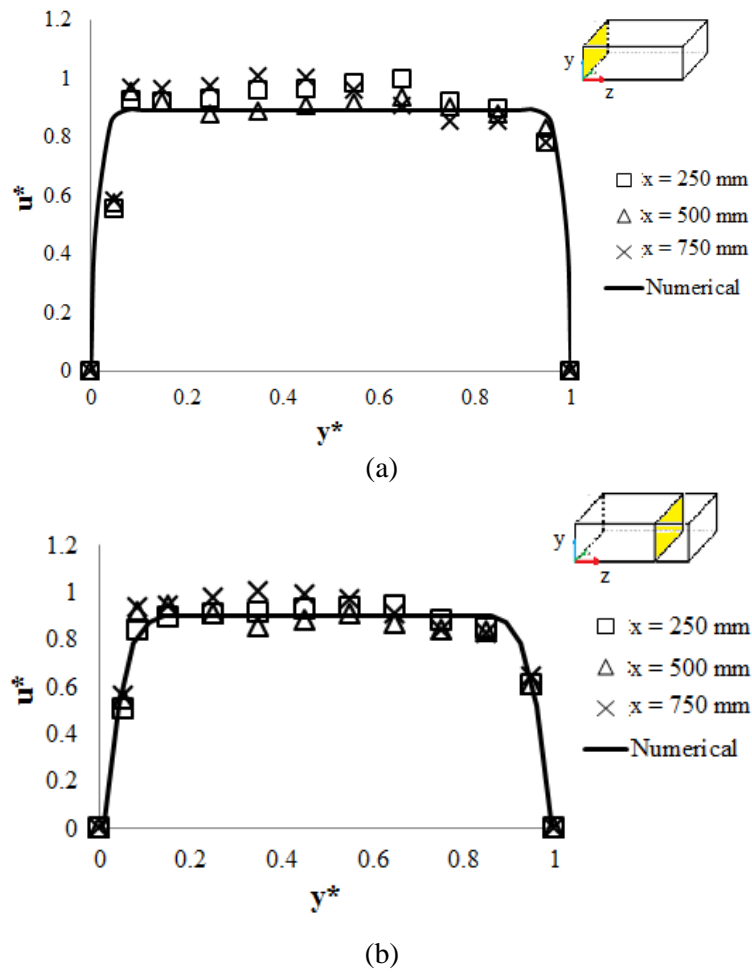
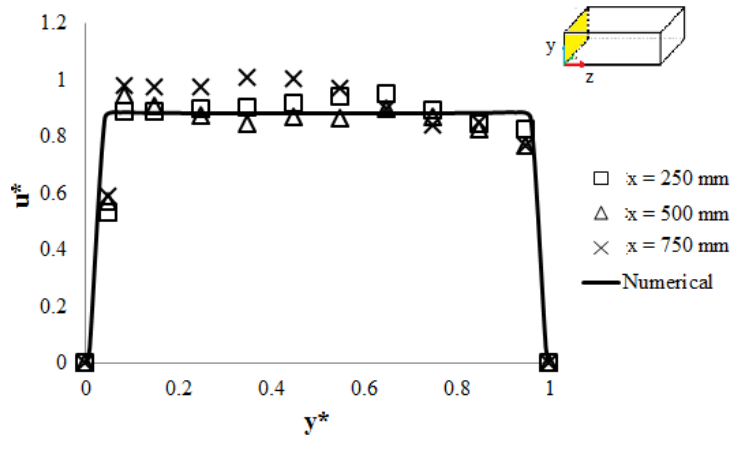
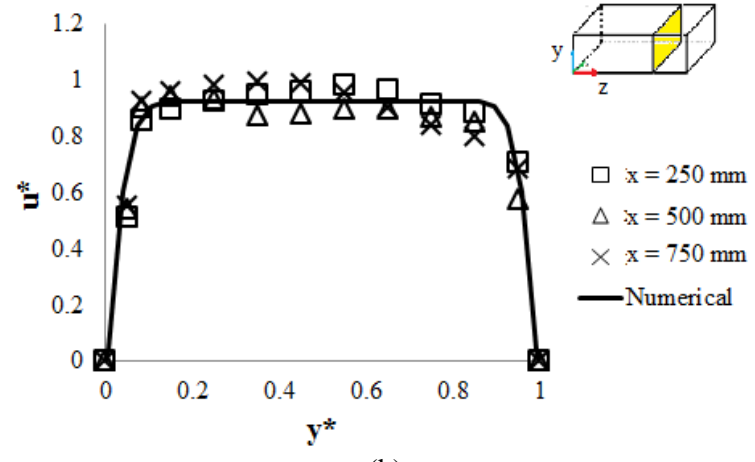


Figure 7.37. Experimental and numerical velocity profiles in empty channel for  $Re = 329$  (a) empty channel inlet ( $z = 0$ ), (b) test section outlet ( $z = 1400$  mm)

where  $T_{m,i}$  is the mass-weighted temperature at the inlet of the empty channel (see Eq. 6.4) and  $T_w$  is the top/bottom wall temperature of the test section ( $60$  °C). Additionally, the obtained temperature profiles from the numerical computations are shown in the same figures. The numerical results for temperature were found for the same 2D channel with the same solver. The top and bottom walls of the test section are taken  $60$  °C and the top and bottom walls of the inlet and outlet sections of channel are taken as insulated. The inlet temperature boundary is given uniform and its value equals to the average inlet temperature of the channel during the experiment. Eq. (4.12), which is the steady form of energy equation for clear fluid, is solved numerically. As can be seen from Figure 7.38, there is a good agreement between the numerical and experimental temperature profiles. The best agreement between experimental and numerical profiles was observed for  $Re = 424$ .



(a)



(b)

Figure 7.38. Experimental and numerical velocity profiles in empty channel for  $Re = 424$  (a) empty channel inlet ( $z = 0$ ), (b) test section outlet ( $z = 1400$  mm)

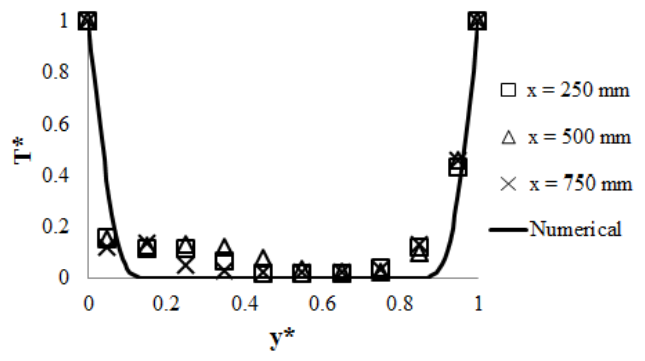


Figure 7.39. Experimental and numerical temperature profiles at the test section outlet in empty channel for  $Re = 192$



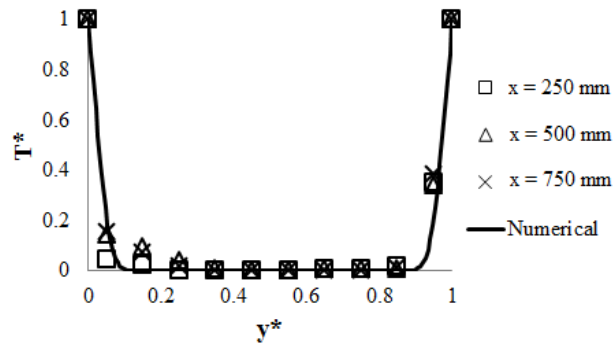


Figure 7.40. Experimental and numerical temperature profiles at the test section outlet in empty channel for  $Re = 329$

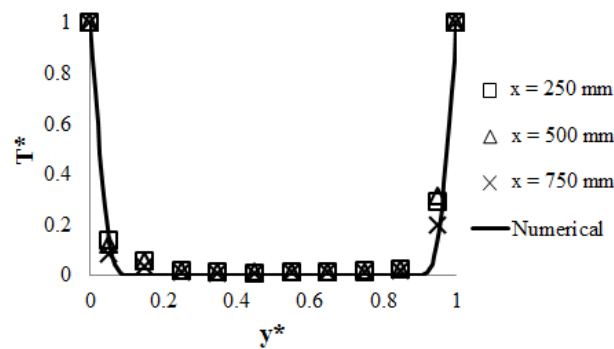


Figure 7.41. Experimental and numerical temperature profiles at the test section outlet in empty channel for  $Re = 424$

After completing the necessary measurements in the empty channel, the aluminium rods were placed into the porous channel as explained in Chapter 6. The velocity and temperature measurements were repeated for the porous channel. Additionally, the velocity measurements were done in the entrance channels to determine the mass flow rate. The same mass flow rate (Reynolds number) values were achieved to compare the velocity and temperature profiles in the porous channel with the empty channel profiles.

The velocity measurements between the rods in the porous channel were performed. The width of channel is larger than the height of channel to reduce the dimensional order of the problem from 3D to 2D. With this assumption, only the velocity profiles on the  $y$ - $z$  plane at  $x = 500$  mm (vertical mid-plane along the flow direction) are needed for the validation of the numerical computations. The velocity measurement points in the porous channel were at the REV center and between the two adjacent rods in the flow direction (see Figure 6.20). The details of measurement

procedure are presented in Chapter 6. The average (macroscopic or Darcian) velocities of the REV's were computed with using the measured velocity values for the corresponding REV, i.e. the volume averaging procedure was applied to the measured velocity. The calculated average velocity profiles for the different Reynolds numbers are shown in Figures 7.41, 7.42 and 7.43 in dimensionless form. These profiles show the average velocities of REV's on y-z plane at  $x = 250, 500$  and  $750$  mm locations. As can be seen from the figures, the average velocity profiles obtained for these 3 sections are very close to each other. Hence the effects of the side walls on these velocity profiles can be neglected and problem can be considered as 2D.

The numerical model is used to obtain the permeability value of the porous channel of the experimental setup with procedure given in Chapter 5. For a REV with square rods in inline arrangement and porosity of 0.75, the permeability is found as  $1.3027 \cdot 10^{-6} \text{ m}^2$ , numerically. For the validation of this value, the porous module of Fluent 12 was employed as explained in Chapter 6. Flow in a 2D channel with the same dimensions of porous channel was analyzed by providing the experimental mass flow rate, porosity and numerical permeability to Fluent software. This means that the steady forms of Eqs. (2.30) and (2.37), which are the governing equations for fluid flow in porous channel, are solved by the computational program. It should be mentioned that for these computation, the drag force is neglected. The drag (Forchheimer) term is very small for the flow through the principal axes of the inline arrangements of square rods and Darcy's law is valid even for high values of Reynolds numbers (Kuwahara et al. 1996, Saada et al. 2006, Steggel 1998). Based on the obtained numerical results, the computed macroscopic velocity profiles are also shown in the Figures 7.41-7.43. As can be seen from three figures, the experimental macroscopic velocity profiles are in good agreement with the numerical macroscopic velocity profiles. Hence, the permeability values obtained this study is validated by the experimental results.

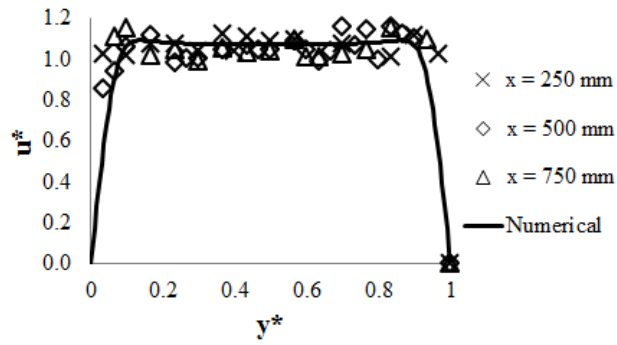


Figure 7.42. The experimental and numerical average velocity profiles in porous channel for  $Re = 192$

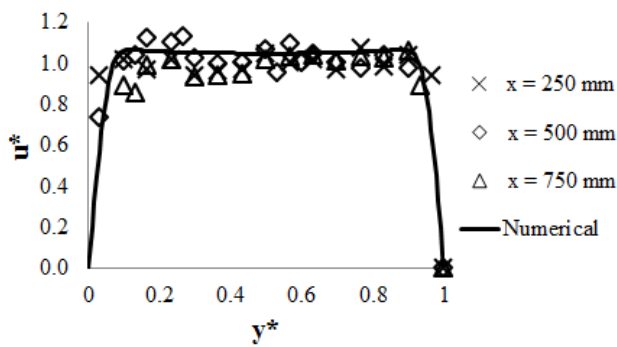


Figure 7.43. The experimental and numerical average velocity profiles in porous channel for  $Re = 329$

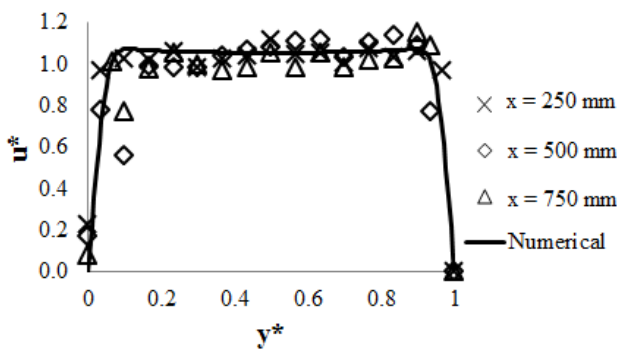


Figure 7.44. The experimental and numerical average velocity profiles in porous channel for  $Re = 424$

The temperature measurements in the porous channel were performed for the considered Reynolds numbers. The temperatures of the top and bottom walls of the test section were fixed at  $60\text{ }^{\circ}\text{C}$  to create the temperature gradient in the porous channel. The thermocouples were distributed in the channel and due to limited number of data logger

channels only the outlet temperature profile in the center of channel at y direction could be measured. The thermocouples were fixed on the rods to measure the temperatures at the REV center and between the two adjacent rods in the flow direction. The measured local temperatures were used to compute the macroscopic temperatures of the REVs by applying the volume averaging method. The obtained macroscopic temperature profiles at the outlet of the test section are shown in Figures 7.44-7.46 in dimensionless form (Eq. 7.10).

The experimentally obtained macroscopic temperature profiles are used to validate the thermal dispersion computation by employing the present numerical model. The transverse and longitudinal thermal dispersion coefficients for the porous channel in the experimental setup were computed, numerically. The details of the numerical model are given in Chapter 5. Again, a REV of the square rods in inline arrangement with porosity of 0.75 was considered for all the studied Reynolds numbers. The computed values of the thermal dispersion coefficients are given in Table 7.5. For the validation of computed thermal dispersion values, steady form of macroscopic energy equation (see Eq. 2.56) along with the macroscopic motion equations was solved with using the porous module of Fluent 12, as explained in Chapter 6. The thermal dispersion coefficients with porosity and experimental mass flow rate values were submitted to the computational program. The obtained macroscopic temperature profiles at the same locations are shown in Figures 7.44-7.46. Because of the arrangement of the rods, the transverse thermal dispersion coefficients were found to be very low and the intended temperature profiles could not be achieved. Nevertheless, the validity of the numerical model for the thermal dispersion computations could also achieved by the aid of the experiments.

Table 7.5. Thermal dispersion coefficients that computed by using the numerical model

Re	$k_{disp,xx}$ (W/mK)	$k_{disp,yy}$ (W/mK)
192	14.141	0.0020
329	39.483	0.0034
424	62.846	0.0042

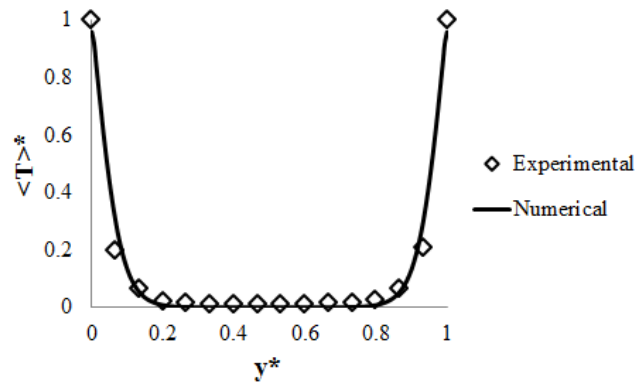


Figure 7.45. The experimental and numerical average temperature profiles in porous channel for  $Re = 192$

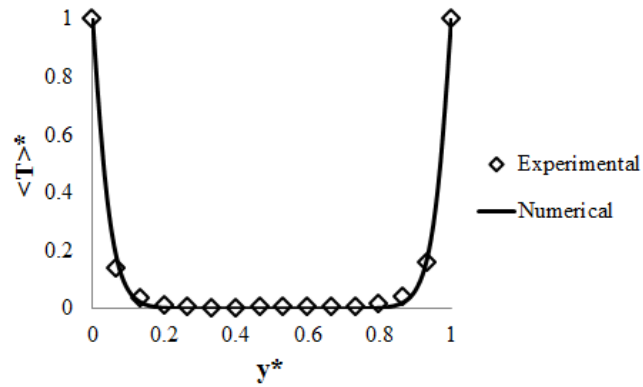


Figure 7.46. The experimental and numerical average temperature profiles in porous channel for  $Re = 329$

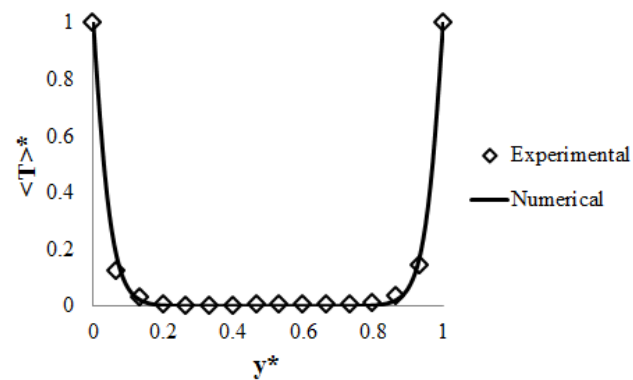


Figure 7.47. The experimental and numerical average temperature profiles in porous channel for  $Re = 424$

## CHAPTER 8

### CONCLUSION

The study is focused on the effects of pore to throat size ratio on the macroscopic transport parameters as permeability, interfacial heat transfer and thermal dispersion coefficients of porous media. The pore to throat size ratio is an important parameter that affects fluid flow and heat transfer in porous media. A parametric study was performed for porous media consisting of rectangular rods in inline arrangement to investigate the effects of pore to throat size ratio on those parameters. An experimental setup was designed and constructed to validate the obtained numerical results. Based on the obtained results the following remarks are achieved.

- The pore to throat size ratio is a very important parameter for the determination of the flow resistance in porous media. The change of the pore to throat size ratio can change flow patterns in the voids between the particles and consequently the permeability changes, considerably. It was found that permeability increases with decrease of pore to throat size ratio since the streamlines become similar to that of straight channel. Furthermore, the permeability increases with increase of porosity.
- The flow in the porous medium with low values of pore to throat size ratio approaches to the straight channel flow and no form drag is observed. However, by the increase of pore to throat size ratio value, the throat effect occurs and this causes the increase of form drag. Our numerical observations showed that the form drag should be taken into account when  $Re > 10$  for porous media with pore to throat size ratio greater than 2.21.
- For two porous media with the same porosity and hydraulic diameter ( $d_h/H = 1.207$ ,  $\varepsilon = 0.7$ ), but different values of pore to throat size ratio (i.e.,  $\beta = 1.63$  and  $3.04$ ), the values of permeability is different. Hence, Kozeny constant does not depend only on porosity and the effect of pore throat size ratio should be taken into account to enhance the applicability of Kozeny-Carman equation for wide ranges of the geometrical parameters.

- An equation for Kozeny constant in terms of porosity and pore to throat size ratio is suggested for the studied periodic structure. The proposed equation provides accurate results for the determination of the permeability for porosity range from 0.2 to 0.9 and pore to throat size ratios values from 1.63 to 7.46.
- The present study reveals that the pore to throat size ratio should also be taken into account for the determination of the interfacial convective heat transfer coefficient. The increase of pore to throat size ratio causes the mixing of the fluid in the voids between the particles and consequently the interfacial Nusselt number increases. For the porous media with the low value of pore to throat size ratio (i.e.,  $\beta = 1.63$ ), the interfacial Nusselt number is almost constant, and the heat transfer in the porous media behaves similar to the fully developed heat transfer in a straight channel. For the porous media with high values of pore to throat size ratio (e.g.,  $\beta = 7.46$ ), the interfacial heat transfer coefficient decreases for the range up to  $Re = 10$  and then it increases with  $Re$ . The strike of the fluid to the vertical walls of the outlet solid particles and the entrance of fluid into the gaps between the particles are the main reasons for the enhancement of heat transfer for the region of  $Re > 10$ .
- Two opposite behaviours are observed for the effect of porosity on the interfacial Nusselt number. For the low pore to throat size ratios, the increase of porosity enhances the Nusselt number because the flow is penetrated deeply into the gaps and the vertical walls of solid particle contribute on the heat transfer. For high pore to throat size ratios, the Nusselt number decreases with the increase of porosity due to the reduction of horizontal surface of solid particles.
- A correlation in terms of porosity, pore to throat size ratio, Reynolds and Prandtl numbers is suggested for the determination of the interfacial Nusselt number in porous media with rectangular rods. The suggested correlation has good agreement with the previously reported correlations however it can be used for the wider range of geometrical parameters of the studied porous structure.
- The effects of pore to throat size ratio on the thermal dispersion coefficients in the longitudinal and transverse directions are investigated. It is found that the longitudinal thermal dispersion coefficient is much higher than the transverse thermal dispersion coefficient for the studied porous structure. Both longitudinal and transverse thermal dispersion coefficients are ignorable for low values of

Reynolds numbers ( $Re \leq 10$ ); however, for flows with  $Re > 10$ , the longitudinal and transverse thermal dispersion coefficients increase with  $Re$  due to the stronger convection effect.

- For the flows with  $Re > 10$ , the effect of the pore to throat size ratio on longitudinal thermal dispersion is noticeable. The longitudinal thermal dispersion increases with pore to throat size ratio for  $\beta < 3.04$  due to strike of the fluid particles to walls of solid particles at the outlet of the REV's and the entrance of fluid into the gaps. However, further increase of pore to throat size ratio causes the penetration of the fluid into the gaps and the increase of mixing effect reduces the longitudinal thermal dispersion. There is an optimum value of pore to throat size ratio for maximum thermal dispersion in the longitudinal direction.
- The transverse thermal dispersion coefficient increases with Reynolds number, however the rate of increase depends on the pore to throat size ratio. For low values of pore to throat size ratio, it does not change with Reynolds number, considerably.
- Both the longitudinal and transverse thermal dispersion coefficients increase with increase of porosity for the studied range of geometrical parameters.
- The numerical model that was used for the determination of the permeability and thermal dispersion coefficients were validated by using the experimental measurements. A good agreement between the numerical and experimental results is observed showing that the employed theoretical models in this study provides accurate results.

For the practical application of the obtained results, following items can be declared:

- The results of the present study can be used for many types of porous media such as metal foams and slotted fin heat sinks since the effects of pore to throat size ratio is important for these kind of porous media as well. The present study provides important hints for prediction of pore to throat size ratio effects on the permeability, interfacial convective heat transfer and thermal dispersion coefficients.
- Narrower throats increases pressure drop and also increases the interfacial heat transfer and transverse thermal dispersion coefficients. Hence, similar to heat



exchanger designs, a conflict between fluid flow and heat transfer exists. For the use of metal foams for enhancement of heat transfer, the value of pore to throat size ratio should be fixed based on the application requirements.

- As it was mentioned before, there is an optimum value of pore to throat size ratio for the maximization of longitudinal thermal dispersion in a porous medium. The largest or narrowest throats have the lowest values of the longitudinal thermal dispersion. When the dimension of the particles in flow direction is slightly smaller than the dimension along the transverse direction, thermal dispersion in the longitudinal direction takes the greatest value.

Future investigations may be done on the relationship between hydraulic tortuosity with porosity and pore to throat size ratio to provide further understanding of the effects of pore to throat size ratio on permeability. The effects of pore to throat size ratio on the thermal tortuosity is also another topic required to be investigated. For the experimental study, it was observed that the transverse thermal dispersion in porous media consisting of square or rectangular rods is very small. Hence obtaining a temperature gradient in transverse direction requires high temperature difference. The experimental setup should resist against the generated high temperature gradient.

## REFERENCES

- Alshare, A.A., Strykowski, P.J., Simon, T.W.. 2010. Modeling of unsteady and steady fluid flow, heat transfer and dispersion in porous media using unit cell scale. *International Journal of Heat and Mass Transfer*. 53: 2294-2310.
- Bauer, R., Schlünder, E.U.. 1977. Die effective radiale Wärmeleitfähigkeit gasdurchströmter Schüttungen. *Verfahrenstechnik*. 11(10): 605-613.
- Bey, O., Eigenberger, G.. 2001. Gas flow and heat transfer through catalyst filled tubes. *International Journal of Thermal Sciences*. 40: 152-164.
- Borkink, J.G.H., Westerterp, K.R.. 1992a. Influence of tube and particle diameter on heat transport in packed beds. *AIChE Journal*. 38 (5): 703-715.
- Borkink, J.G.H., Westerterp, K.R.. 1992b. Significance of axial heat dispersion for the description of heat transport in wall-cooled packed beds. *Chemical Engineering and Technology*. 15: 371-384.
- Borkink, J.G.H., Westerterp, K.R.. 1992c. Determination of effective heat transport coefficients for wall-cooled packed beds. *Chemical Engineering Science*. 47 (9): 2337-2342.
- Bunnell, D.G., Irvin, H.B., Olson, R.W., Smith, J.M.. 1949. Effective thermal conductivities in gas-solid systems. *Industrial and Engineering Chemistry*. 41 (9): 1977-1998.
- Carman, P.C.. 1937. Fluid flow through granular beds. *Chemical Engineering Research & Design: Transactions of the Institution of Chemical Engineers Part A*. 15: 415-421.
- Chen, L., Peterson, G.P. 2006. The effective thermal conductivity of wire screen. *International Journal of Heat and Mass Transfer*. 49: 4095-4105.
- Chen X., Papathanasiou T.D.. 2006. On the variability of the Kozeny constant for saturated flow across unidirectional disordered fiber arrays. *Composites Part A*. 37: 836-846.
- Cheng, G.J., Yu, P., Zulli, A.B.. 1999. Evaluation of effective thermal conductivity from the structure of a packed bed. *Chemical Engineering Science*. 54. 4199-4209.
- Chua, T.H., Ng, C.K., Wang, W., Yap, C., Wang, L.X.. 2004. Transient modeling of a two bed silica gel-water adsorption chiller. *International Journal of Heat and Mass Transfer*. 47: 659-669.

- Clement, K., Jorgensen, S.B.. 1983. Experimental investigation of axial and radial thermal dispersion in a packed bed. *Chemical Engineering Science*. 38(6): 835-842.
- Darcy, H.. 1856. Les fontaines publiques de la ville de Dijon, Paris, Dalmont.
- Davies, L., Dollimore, D.. 1980. Theoretical and experimental values for the parameter  $k$  of the Kozeny–Carman equation as applied to sedimenting suspensions. *Journal of Physics D: Applied Physics*. 13: 2013–2020.
- Dekhtyar, R.A., Sikovsky, D.Ph., Gorine, A.V., Mukhin, V.A.. 2002. Heat transfer in a packed bed at moderate values of the Reynolds number. *High Temperature*. 40(5): 693-700.
- Delgado, J.M.P.Q.. 2007. Dispersion in porous media. *Chemical Engineering Research and Design*. 85(A9): 1245-1252.
- Demir, H., Mobedi, M., Ülkü, S.. 2009. Effects of porosity on heat and mass transfer in a granular adsorbent bed. *International Communications in Heat and Mass Transfer*. 36: 372–377.
- Demirel, Y., Sharma, R.N., Al-Ali, H.H.. 2000. On the effective heat transfer parameters in a packed bed. *International Journal of Heat and Mass Transfer*. 43: 327-332.
- Dias, R.P., Fernandes, C.S., Mota, M., Teixeira, J.A., Yelshin, A.. 2007. Permeability and effective thermal conductivity of bisized porous media, *International Journal of Heat and Mass Transfer*. 50: 1295-1301.
- Dias, R.P., Fernandes, C.S., Teixeira, J.A., Mota, M., Yelshin, A.. 2008. Permeability analysis in bisized porous media: Wall effect between particles of different size. *Journal of Hydrology*. 349: 470-474.
- Dixon, A.G., Cresswell, D.L.. 1979. Theoretical prediction of effective heat transfer parameters in packed beds. *AIChE Journal*. 25(4): 663–676.
- Dixon, A.G., van Dongeren, J.H.. 1998. The influence of the tube and particle diameters at constant ratio on heat transfer in packed beds. *Chemical Engineering and Processing: Process Intensification*. 37: 23-32.
- Drummond, J.E., Tahir, M.I.. 1984. Laminar viscous flow through regular arrays of parallel solid cylinders. *International Journal of Multiphase Flow*. 10: 515-540.
- Dukhan, N., Patel, P.. 2008. Equivalent particle diameter and length scale for pressure drop in porous metals. *Experimental Thermal and Fluid Science*. 32: 1059-1067.
- Dupuit, J.. 1863. Etudes theoretiques et pratiques sur le mouvement des eaux, Dunond, Paris.

- Eidsath, A., Carbonell R.G., Whitaker S., Herrmann L.R.. 1983. Dispersion in pulsed systems-III: Comparison between theory and experiments for packed beds. *Chemical Engineering Science*. 38: 1803-1816.
- Elsari, M., Hughes, R.. 2002. Axial effective thermal conductivities of packed beds. *Applied Thermal Engineering*. 22: 1969-1980.
- Ergun, S.. 1952. Fluid flow through packed columns, *Chemical Engineering Progress*. 48: 89-94.
- Forchheimer, P.H.. 1901. Wasserbewegung durch Boden. *Z. Ver. Dtsch. Ing.*. 45. 1782-1788.
- Gamrat, G., Favre-Marinet, M., Le Person, S.. 2008. Numerical study of heat transfer over banks of rods in small Reynolds number cross-flow. *International Journal of Heat and Mass Transfer*. 51: 853-864.
- Gunn, D.J., de Souza, J.F.C.. 1974. Heat transfer and axial dispersion in packed beds. *Chemical Engineering Science*. 29: 1363-1371.
- Gunn, D.J., Khalid, M.. 1975. Thermal dispersion and wall heat transfer in packed beds. *Chemical Engineering Science*. 30: 261-267.
- Han, K.K., Lee, C.W., Rice, B.P.. 2000. Measurements of the permeability of fiber performs and applications. *Composites Science and Technology*. 60: 2435-2441.
- Happel, J., Brenner, H.. 1986. Low Reynolds Number Hydrodynamics. Martinus Nijhoff Publishers. Dordrecht.
- Heijs, A.W.J., Lowe, C.P.. 1995. Numerical evaluation of the permeability and the Kozeny constant for two types of porous media. *Physics Review E*. 51: 4346-4352.
- Hsu, C. T.. 2000. Conduction in Porous Media, Handbook of Porous Media, K. Vafai, ed., CRC Press, Boca Raton, FL.
- Jeong, N., Choi, D.H.. 2011. Estimation of the thermal dispersion in a porous medium of complex structures using a lattice Boltzmann method. *International Journal of Heat and Mass Transfer*. 54: 4389-4399.
- Jorge, L.M.M., Jorge, R.M.M., Giudici, R.. 2010. Experimental and numerical investigation of dynamic heat transfer parameters in packed bed. *Heat and Mass Transfer*. 46: 1355-1365.
- Kandula, M.. 2011. On the effective thermal conductivity of porous packed beds with uniform spherical particles. *Journal of Porous Media*. 14: 919-926.
- Karimian, S.A.M., Straatman, A.G.. 2008. CFD study of the hydraulic and thermal behavior of spherical-void-phase porous materials. *International Journal of Heat and Fluid Flow* 29: 292-305.

- Kaviany, M.. 1995. Principles of Heat Transfer in Porous Media, 2nd Edition, New York, Springer-Verlag.
- Koponen, A., Kataja, M., Timonen, J.. 1997. Permeability and effective porosity of porous media. *Physics Review E*. 56: 3319-3325.
- Kozeny, J.. 1927. Ueber kapillare Leitung des Wassers im Boden. *Sitzungsber Akad. Wiss*. 136: 271-306
- Krupiczka, R.. 1967. Analysis of thermal conductivity in granular materials. *International Journal of Chemical Engineering*. 7: 122-144.
- Kunii, D., Smith, J.M.. 1961. Heat transfer characteristics of porous rocks. *AIChE Journal*. 7: 29-34.
- Kuwahara, F., Mitsuhiro, S., Nakayama, A.. 2001. A numerical study of interfacial convective heat transfer coefficient in two-energy equation model for convection in porous media. *International Journal of Heat and Mass Transfer*. 44: 1153-1159.
- Kuwahara, F., Nakayama, A.. 1999. Numerical determination of thermal dispersion coefficients using a periodic porous structure, *Journal of Heat Transfer*. 121: 160-163.
- Kuwahara, F., Nakayama, A., Koyama, H.. 1996. A numerical study of thermal dispersion in porous media, *Journal of Heat Transfer*. 118: 756-761.
- Kuwahara, F., Shirota, M., Nakayama, A.. 2001. A numerical study of interfacial convective heat transfer coefficient in two-energy equation model for convection in porous media. *International Journal of Heat and Mass Transfer*. 44: 1153-1159.
- Kwong, S.S., Smith, J.M.. 1957. Radial heat transfer in packed beds, *Industrial and Engineering Chemistry*. 49(5): 894-903.
- Kyan, C.P., Wasan, D.T., Kintner, R.C.. 1970. Flow of single-phase fluids through fibrous beds. *Industrial and Engineering Chemistry Fundamentals*. 9: 596-603.
- Levec, J., Carbonell, R.G.. 1985. Longitudinal and lateral thermal dispersion in packed beds. *AIChE Journal*. 31(4): 591-602.
- Li J., Gu Y.. 2005. Coalescence of oil-in-water emulsions in fibrous and granular beds. *Separation and Purification Technology*. 42: 1-13.
- Liu, H.L., Hwang, W.R.. 2012. Permeability prediction of fibrous porous media with complex 3D architectures. *Composites Part A*. 43: 2030-2038.
- Liu, J., Sano, Y., Nakayama, A.. 2009. A simple mathematical model for determining the equivalent permeability of fractured porous media. *International Communications in Heat and Mass Transfer*. 36: 220-224.

- Liu, S., Masliyah, J.H.. 2005. Dispersion in Porous Media. Handbook of porous media edited by Vafai, K., 2nd edition, Taylor&Francis, Boca Raton.
- Lopez Penha, D.J., Geurts, B.J., Stolz, S., Nordlund, M.. 2011. Computing the apparent permeability of an array of staggered square rods using volume-penalization. *Computers and Fluids*. 51: 157-173.
- Lopez Penha, D. J., Stolz, S., Kuerten, J. G. M., Nordlund, M., Kuczaj, A. K., and Geurts, B. J.. 2012. Fully-Developed Conjugate Heat Transfer in Porous Media With Uniform Heating. *International Journal of Heat and Fluid Flow*. 38: 94–106.
- Mathavan, G.N., Viraraghavan, T.. 1992. Coalescence/filtration of an oil-in-water emulsion in a peat bed. *Water Research*. 26: 91–98.
- Metzger, T., Didierjean S., Maillet, D.. 2004. Optimal experimental estimation of thermal dispersion coefficients in porous media. *International Journal of Heat and Mass Transfer*. 47: 3341-3353.
- Nakayama, A.. 1995. PC-Aided numerical heat transfer and convective flow, CRC Press.
- Nakayama, A., Kuwahara, F.. 2005. Algebraic model for thermal dispersion heat flux within porous media. *AIChE Journal*. 51: 2859-2864.
- Nakayama, A., Kuwahara, F., and Hayashi, T.. 2003. Numerical Modeling for Three-Dimensional Heat and Fluid Flow Through a Bank of Cylinders in Yaw. *Journal of Fluid Mechanics*. 498: 139–159.
- Nakayama, A., Kuwahara, F., Sano, Y.. 2007. Concept of equivalent diameter for heat and fluid flow in porous media. *AIChE Journal*. 53: 732-736.
- Nakayama, A., Kuwahara, F., Umemoto, T., Hayashi, T.. 2002. Heat and fluid flow within an anisotropic porous medium. *Journal of Heat Transfer*. 124: 746-753.
- Nield, D.A., Bejan, A.. 2006. Convection in porous media, 3rd edition, Springer, U.S.
- Nooruddin, H.A., Hossain, M.E.. 2012. Modified Kozeny-Carmen correlation for enhanced hydraulic flow unit characterization. *Journal of Petroleum Science and Engineering*. 80: 107-115.
- Özdemir, M., Özgüç, A.F.. 1997. Forced convective heat transfer in porous medium of wire screen meshes. *Heat and Mass Transfer*. 33: 129-136.
- Özgümüş, T., Mobedi, M., Özkol, Ü., Nakayama, A.. 2013. Thermal dispersion in porous media – A review on the experimental studies for packed beds. *Applied Mechanics Review*. 65: 031001.

- Pacella, H.E., Eash, H.J., Frankowski, B.J., Federspiel, W.J.. 2011. Darcy permeability of hollow fiber bundles used in blood oxygenation devices. *Journal of Membrane Science*. 382: 238-242.
- Paek, J.W., Kang, B.H., Kim, S.Y., Hyun, J.M.. 2000. Effective thermal conductivity and permeability of aluminum foam materials, *International Journal of Thermophysics*. 21: 453-464.
- Papathanasiou, T.D., Markicevic, B., Dendy, E.D.. 2001. A computation evaluation of the Ergun and Forchheimer equations for fibrous porous media. *Physics of Fluids*. 13: 2795-2804.
- Pathak, M.G., Ghiaasiaan, S.M.. 2011. Convective heat transfer and thermal dispersion during laminar pulsating flow in porous media. *International Journal of Thermal Sciences*. 50: 440-448.
- Pedras, M., de Lemos, M.. 2001. Simulation of turbulent flow in porous media using a spatially periodic array and a low Re two-equation closure, *Numerical Heat Transfer Part A*. 39: 35-39.
- Pedras, M.H.J., de Lemos, M.J.S.. 2008. Thermal dispersion in porous media as a function of the solid-fluid conductivity ratio. *International Journal of Heat and Mass Transfer*. 51: 5359-5367.
- Petrasch, J., Meier, F., Friess, H., Steinfeld, A.. 2008. Tomography based determination of permeability, Dupuit-Forchheimer coefficient, and interfacial heat transfer coefficient in reticulate porous ceramics. *International Journal of Heat and Fluid Flow*. 29: 315-326.
- Plessis, J.P., Woudberg, S.. 2008. Pore-scale derivation of the Ergun equation to enhance its adaptability and generalization. *Chemical Engineering Science*. 63: 2576-2586.
- Quintard, M., and Whitaker, S.. 1995. Local thermal equilibrium for transient heat conduction: Theory and comparison with numerical experiments. *International Journal of Heat and Mass Transfer*. 38(15): 2779-2796.
- Rahli, O., Tadrist, L., Miscevic, M., Santini, R.. 1997. Fluid flow through randomly packed monodisperse fibers: the Kozeny-Carman parameter analysis. *Journal of Fluids Engineering*. 119: 188-192.
- Rodriguez, E., Gacomelli, F., Vazquez, A.. 2004. Permeability-porosity relationship in RTM for different fibreglass and natural reinforcements. *Journal of Composite Materials*. 38: 259-270.
- Saada, M.A., Chikh, S., Campo, A.. 2006. Analysis of hydrodynamic and thermal dispersion in porous media by means of a local approach. *Heat and Mass Transfer*. 42: 995-1006.

- Sahraoui, M., Kaviany, M.. 1992. Slip and no-slip temperature boundary conditions at the interface of porous plain media. *International Journal of Heat and Mass Transfer*. 35 (4): 927-943.
- Sahraoui, M., Kaviany, M.. 1994. Slip and no-slip temperature boundary conditions at the interface of porous, plain media: convection. *International Journal of Heat and Mass Transfer*. 37 (6): 1029-1044.
- Saidi, M.S., Rasouli, F., Hajaligol, M.R.. 2006. Heat transfer coefficient for a packed bed of shredded materials at low Peclet numbers. *Heat Transfer Engineering*. 27(7): 41-49.
- Saito, M. B., de Lemos, M. J. S.. 2005. Interfacial Heat Transfer Coefficient for Non-Equilibrium Convective Transport in Porous Media. *International Communications in Heat and Mass Transfer*. 32(5): 666–676.
- Saito, M. B., de Lemos, M. J. S.. 2006. A Correlation for Interfacial Heat Transfer Coefficient for Turbulent Flow Over an Array of Square Rods. *Journal of Heat Transfer*. 128(5): 444–452.
- Sano, Y., Noguchi, K., Kuroiwa, T.. 2009. An experimental investigation into the effective permeability of porous media whose matrices are composed of obstacles of different sizes. *The Open Transport Phenomena Journal*. 1: 15-19.
- Schröder, E., Class, A., Krebs, L.. 2006. Measurements of heat transfer between particles and gas in packed beds at low to medium Reynolds numbers. *Experimental Thermal and Fluid Science*. 30: 545-558.
- Shah, R.K., London, A.L.. 1978. Laminar Flow Forced Convection in Ducts. Academic Press.
- Singh, M., Mohanty, K.K.. 2000. Permeability of spatially correlated porous media. *Chemical Engineering Science*. 55: 5393-5403.
- Smirnov, E.I., Kuzmin, V.A., Zolotarskii, I.A.. 2004. Radial thermal conductivity in cylindrical beds packed by shaped particles. *Chemical Engineering Research and Design*. 82(A2): 293-296.
- Smirnov, E.I., Muzykantov, A.V., Kuzmin, V.A., Kronberg, A.E., Zolotarskii, I.A.. 2003a. Radial heat transfer in packed beds of spheres, cylinders and Raschig rings – Verification of model with a linear variation of  $\lambda_{er}$  in the vicinity of the wall. *Chemical Engineering Journal*. 91: 243-248.
- Smirnov, E.I., Muzykantov, A.V., Kuzmin, V.A., Zolotarskii, I.A., Koning, G.W., Kronberg, A.E.. 2003b. Radial heat transfer in packed beds of shaped particles. *Chemistry for Sustainable Development*. 11: 293-296.
- Sparrow, E.M., Loeffler, A.L.. 1959. Longitudinal laminar flow between cylinders arranged in regular array. *AIChE Journal* 5: 325–330.



- Steggel, N.. 1998. A numerical investigation of the flow around rectangular cylinders. School of Mechanical and Materials Engineering, The University of Surrey, UK. Doctor of Philosophy.
- Sullivan, R.R.. 1942. Specific surface measurement on compact bundles of parallel fibers. *Journal of Applied Physics* 13: 725–730.
- Tamayol, A., Bahrami, M.. 2009. Analytical determination of viscous permeability of fibrous porous media. *International Journal of Heat and Mass Transfer*. 52: 2407-2414.
- Teruel, F. E., and Diaz, L.. 2013. Calculation of the Interfacial Heat Transfer Coefficient in Porous Media Employing Numerical Simulations. *International Journal of Heat and Mass Transfer*. 60: 406–412.
- Teruel, F.E., Rizwan-uddin. 2009. Characterization of a porous medium employing numerical tools: Permeability and pressure drop from Darcy to turbulence. *International Journal of Heat and Mass Transfer*. 52: 5878-5888.
- Testu, A., Didierjean, S., Maillet, D., Moyne, C., Metzger, T., Niass, T.. 2007. Thermal dispersion for water or air flow through a bed of glass beads. *International Journal of Heat and Mass Transfer*. 50: 1469-1484.
- Testu, A., Didierjean, S., Maillet, D., Moyne, C., Niass, T.. 2005. Experimental estimation of thermal dispersion coefficients in granular media through which a gas is flowing: porous versus non porous grain. *Proceedings of the 5th International Conference on Inverse Problems in Engineering*, Cambridge, UK.
- Thomeo, J.C., Freire, J.T.. 2000. Heat transfer in fixed bed: a model non-linearity approach. *Chemical Engineering Science*. 55: 2329 – 2338.
- Vafai, K., Tien, C.L.. 1981. Boundary and inertia effects on flow and heat transfer in porous media. *International Journal of Heat and Mass Transfer*. 24: 195-203.
- Vidal, D., Ridgway, C., Pianet, G., Schoelkopt, J., Roy, R., Bertrand, F.. 2009. Effect of particle size distribution and packing compression on fluid permeability as predicted by lattice-Boltzmann simulations. *Computers and Chemical Engineering*. 3: 256-266.
- Vortmeyer, D., Adam, W.. 1984. Steady-state measurements and analytical correlations of axial effective thermal conductivities in packed beds at low gas flow rates. *International Journal of Heat and Mass Transfer*. 27(9): 1465-1472.
- Vortuba, J., Hlavacek, V., Marek, M.. 1972. Packed bed axial thermal conductivity. *Chemical Engineering Science*. 27: 1845-1851.
- Wakao, N., Kaguei, S., Nagai, H.. 1978. Effective diffusion coefficients for fluid species reacting with first order kinetics in packed bed reactors and discussion on evaluation of catalyst effectiveness factors. *Chemical Engineering Science*. 33: 183-187.

- Wen, D., Ding, Y.. 2006. Heat transfer of gas flow through a packed bed. *Chemical Engineering Science*. 61: 3532-3542.
- Whitaker, S.. 1999. The Method of Volume Averaging. Kluwer Academic. Dordrecht, The Netherlands.
- Wu, J., Yu, B.. 2007. A fractal resistance model for flow through porous media. *International Journal of Heat and Mass Transfer*. 50: 3925-3932.
- Xu, J., Lu, T.J., Hodson, H.P., Fleck, N.A.. 2010. Analysis of thermal dispersion in an array of parallel plates with fully-developed laminar flow. *International Journal of Heat and Fluid Flow*. 31: 57-69.
- Xu, P., Yu, B.. 2008. Developing a new form of permeability and Kozeny-Carman constant for homogeneous porous media by means of fractal geometry. *Advances in Water Resources*. 31: 74-81.
- Yagi, S., Kunii, D., Wakao, N.. 1960. Studies on axial effective thermal conductivities in packed beds. *AIChE Journal*. 6: 543-546.
- Yang, C., Nakayama, A.. 2010. A synthesis of tortuosity and dispersion in effective thermal conductivity of porous media. *International Journal of Heat and Mass Transfer*. 53: 3222-3230.
- Yang, J., Wang, J., Bu, S., Zeng, M., Wang, Q., Nakayama, A.. 2012. Experimental analysis of forced convective heat transfer in novel structured packed beds of particles. *Chemical Engineering Science*. 71: 126-137.
- Yang, J., Wang, Q., Zeng, M., Nakayama, A.. 2010. Computational study of forced convective heat transfer in structured packed beds with spherical or ellipsoidal particles. *Chemical Engineering Science*. 65: 726-738.
- Yazdchi, K., Srivastava, S., Luding, S.. 2011. Microstructural effects on the permeability of periodic fibrous porous media. *International Journal of Multiphase Flow*. 37: 956-966.
- Yu, B.. 2008. Analysis of flow in fractal porous media. *Applied Mechanics Review*. 61: 050801.

# APPENDIX A

## CALIBRATION OF PID CONTROLLERS AND DATA LOGGER

In order to ensure the accuracy of measured temperature, the calibration of the measurement devices was performed. A heating equipment was established to calibrate the temperature measurements of PID controllers and data logger. A container was put on a electrical heater device to heat the water inside. The surfaces of container were strongly insulated except the bottom touching the surface of electrical heater. The power of the electrical heater is adjustable. The accurate temperature of the water inside the container was measured by two thermometers. Firstly, a glass thermometer whose sensitive part is inside the container was used to measure the water temperature. The sensitivity of the glass thermometer is 1 °C. Secondly, a thermocouple calibrator (Fluke 714) with sensitivity of 0.1 °C was used for measuring of the water temperature. The setup is shown in Figure A.1.



Figure A.1. Temperature calibration setup

The thermocouples used in the experiments were inserted into the water filled container. The temperature of the water was measured both by glass type thermometer, calibrator and thermocouples which were connected to random PID controllers. The measurements were done with ten minute time intervals and temperature was changed from 20 °C to 80 °C. It was observed that the temperature values taken from the PID

controllers were about 2.5 °C higher than the values measured by the calibrator. Hence the measured temperatures were revised such that  $T_{PID} = T_{measured} - 2.5$  to achieve the exact temperature value. Figure A.2 shows the difference between the calibrator and PID controller temperatures. The difference between the revised temperature of PID and calibrator is generally within  $\pm 0.5$  °C.

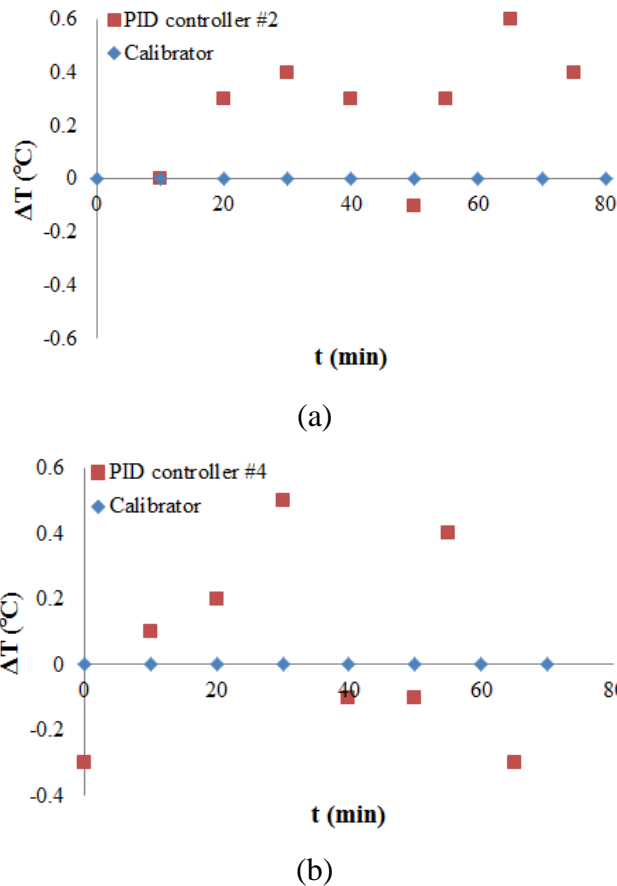


Figure A.2. Modified temperature differences of PID controller with calibrator for random PID controllers. a) PID controller #2, b) PID controller #4.

For calibration of data logger, the same procedure was followed. The temperature measurements were taken with an average of 5 measurements in 1 second (data collecting frequency of 5 Hz) for randomly selected channels. It was observed there is a difference between the measured temperature of data logger and calibrator. The measured temperature by data logger were revised as  $T_{dtlg} = T_{measured} + 0.5$ . Figure A.3 was presented for the modified temperatures. As can be seen from the figure, modified temperature differences are in the acceptable interval which is  $\pm 0.5$  °C.

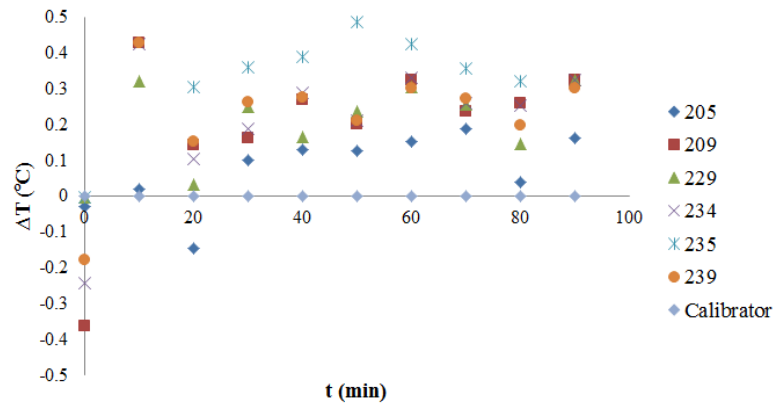


Figure A.3. Modified temperature differences of channels of the data logger with calibrator with measurements taken with 5 Hz.

# VITA

## PERSONAL

**Date of Birth:** 23.10.1982  
**Place of Birth:** Ankara

## EDUCATION

**2015** Izmir Institute of Technology, Mechanical Engineering, PhD.  
**2009** TOBB University of Economics and Technology, Mechanical Engineering, MSc.  
**2006** Hacettepe University, Nuclear Engineering, BSc.

## PUBLICATIONS

Aktas, M.K., Ozgumus, T.. 2009. Heat transfer enhancement by irregular acoustic streaming in a shallow enclosure. *Proc. ASME Summer Heat Transfer Conf. 2*: 735-744.  
Aktas, M.K., Ozgumus, T.. 2010. Nonzero mean oscillatory flow in symmetrically-heated shallow enclosures: An analysis of acoustic streaming. *Numer. Heat Transfer A.57*: 869-891.  
Aktas, M.K., Ozgumus, T.. 2010. The effects of acoustic streaming on thermal convection in an enclosure with differentially heated horizontal walls. *International Journal of Heat and Mass Transfer. 53*: 5289-5297.  
Aktas, M.K., Ozgumus, T.. 2011. A numerical investigation of the effects of a transverse temperature gradient on the formation of regular and irregular acoustic streaming in an enclosure. *Proceedings of the Institution of Mechanical Engineers Part C – Journal of Mechanical Engineering Science. 225*: 132-144.  
Ozgumus, T., Mobedi, M., Ozkol, U., Nakayama, A.. 2013. Thermal dispersion in porous media—A review on the experimental studies for packed beds. *Appl. Mec. Rev.. 65*: 031001.  
Ozgumus, T., Mobedi, M., Ozkol, U.. 2014. Determination of Kozeny constant based on porosity and pore to throat size ratio in porous medium with rectangular rods. *Engineering Applications of Computational Fluid Mechanics. 8*: 308-318.  
Ozgumus, T., Mobedi, M.. 2014. Effect of pore to throat size ratio on interfacial heat transfer coefficient of porous media. *Journal of Heat Transfer. 137*: 012602.

## PRESENTATIONS

Aktas, M.K., Ozgumus, T.. Computational study of irregular acoustic streaming flows in an enclosure subject to a transverse temperature gradient. *International. Symposium on Convective Heat and Mass Transfer in Sustainable Energy*. Tunisia, April 2009.  
Özgümüş, T., Aktaş, M.K.. Kapalı bir ortamda akustik etkiyle oluşturulan ikinci mertebe girdapların sayısal olarak incelenmesi, *17. Ulusal Isı Bilimi Tek. Kong.*, Turkey, June 2009.  
Ozgumus, T., Mobedi, M., Ozkol, U., Nakayama, A.. Thermal dispersion in porous media – A review on approaches in experimental studies. *6th International Advanced Technologies Symposium*. Turkey. May 2011.  
Ozgumus, T., Mobedi, M., Ozkol, U.. Effect of pore to throat size ratio on interfacial convective heat transfer coefficient. *5<sup>th</sup> International Conference on Applications of Porous Media*. Romania. August 2013.  
Özgümüş, T., Mobedi, M., Özkol, Ü.. A numerical study on the determination of the effects of pore to throat size ratio on permeability and interfacial heat transfer coefficient. *19. Ulusal Isı Bilimi ve Tekniği Kongresi*. Samsun. September 2013.